New Molecular Precursors for Metal Sulfides

A thesis submitted to the University of Manchester for the Degree of Doctor of Philosophy in the Faculty of Engineering and Physical Sciences

2010

Karthik Ramasamy

School of Chemistry, The University of Manchester, Oxford Road

Manchester, M13 9PL

List of figures

List of tables

Abbreviations

CVD	Chemical vapour deposition
AACVD	Aerosol-assisted chemical vapour deposition
MOCVD	Metal organic chemical vapour deposition
LPCVD	Low-pressure chemical vapour deposition
PVD	Physical vapour deposition
CBD	Chemical bath deposition
MBE	Molecular beam epitaxy
ALD	Atomic layer deposition
fcc	Face-centered cubic
bcc	Body-centered cubic
SSP	Single source precursors
MR	Magnetoresistance
Me	Methyl
Et	Ethyl
^{i}Pr	Isopropy
Ph	Phenyl
THF	Tetrahydrofuran
TOP	Trioctylphosphine
DCM	Dichloromethane
PXRD	Powder X-ray diffraction
ICDD	The International center for diffraction data
SEM	Scanning electron microscopy
TEM	Transmission electron microscopy
SAED	Selected area electrondiffraction
EDX	Energy dispersive X-ray spectroscopy
FEG	Field emission gun

MS	Mass spectroscopy
GC	Gas chromatography
NMR	Nuclear magnetic resonance
UV/Vis	Ultra violet/ visible
FFT	Fast fourier transform
mpt	Melting point
mmol	Milli mole
mL	Milli liter
eV	Electron Volt
KeV	Kilo electron Volt
K	Kelvin
Eg	Bandgap
et al	Et alia
etc	Et cetra
e.g	Exempli gratia
ca	Circa
TGA	Thermogravimetry analysis
FFT	Fast fourier transform
ZFC	Zero field cooling
FC	Field cooling

Abstract

Metal sulfide thin films are important class of materials which have applications in photovoltaics, microelectronics and displays. Chemical vapour deposition (CVD) is well known method for the deposition of high quality thin films. Very few classes of single source precursors (eg: dithiocarbamates, xanthates) were successful for the deposition of good quality metal sulfide films by MOCVD. This limited choice was due to the difficulties of finding precursors with suitable physico-chemical properties. Hence, it is important to develop precursors with suitable volatility, solubility and being able to deposit films with little or no contamination.

This work describes the synthesis of a series of metal (Fe, Co, Ni, Zn, Cd) complexes of thio- and dithio-biuret ligands, their structural and spectroscopic characterization and thermal decomposition. The complexes were used as single source precursors for the deposition of iron, cobalt, nickel, zinc, cadmium and zinc cadmium sulfide thin films by AACVD. The effect of alkyl groups, coordinating atoms, deposition temperatures on phases and morphology of the films were studied. The deposited films were characterised by powder X-ray diffraction (PXRD), scanning electron microscopy (SEM), energy dispersive X-ray spectroscopy (EDX), transmission electron microscopy (TEM), selected area electron diffraction (SAED), and atomic force microscopy (AFM).

The complex $[Fe(SON(CN^{i}Pr_2)_2)_3]$ gave hexagonal troilite FeS films with small amount of tetragonal pyrrhotites $Fe_{1-x}S$ at 300 °C, whereas only troilite FeS was deposited at 350, 400 or 450 °C. Complexes $[Fe_2(\mu\text{-}OMe)_2(SON(CNEt_2)_2)_2]$ and $[Fe(SON(CNEt_2)_2)_3]$ deposited a mixture of hexagonal troilite FeS and cubic pyrite FeS_2 films at all temperatures. $[Fe(SON(CNMe_2)_2)_3]$ deposited very thin films of FeS at all temperatures as troilite.

Complexes $[Co(N(SCNMe_2)_2)_3]$ and $[Co(N(SCNEt_2)_2)_3]$ deposited hexagonal $Co_{1-x}S$ films at all temperatures of 350-500 °C, whereas $[Co(SON(CN^{i}Pr_2)_2)_2]$ gave mixture of cubic and hexagonal Co_4S_3 films at 280-400 °C.

Thiobiuret complex $[Ni(SON(CNMe_2)_2)_2]$ gave orthorhombic Ni_7S_6. Complexes $[Ni(SON(CNMe_2CNEt_2))_2]$ and $[Ni(SON(CNEt_2)_2)_2]$ gave mixtures of hexagonal $Ni_{17}S_{18}$ and orthorhombic Ni_7S_6. In contrast, $[Ni(SON(CN^{i}Pr_2)_2)_2]$ gave orthorhombic Ni_9S_8. Dithiobiuret complexes $[Ni(N(SCNMe_2SCNEt_2))_2]$ and $[Ni(N(SCNEt_2)_2)_2]$ gave hexagonal $NiS_{1.03}$ at 360 and 400 °C, orthorhombic Ni_7S_6 phase at 440 and 480 °C.

The zinc complexes $[Zn(N(SCNMe_2)_2)_2]$ and $[Zn(SON(CN^{i}Pr_2)_2)_2]$ deposited cubic ZnS at 300 and 350 °C, whereas at 400 and 450 °C hexagonal ZnS were apparent $[Zn(N(SCNEt_2)_2)_2]$ gave hexagonal ZnS films at all deposition temperatures. Cadmium complexes $[Cd(N(SCNMe_2)_2)_2]$, $[Cd(N(SCNEt_2)_2)_2]$ and $[Cd(SON(CN^{i}Pr_2)_2)_2]$ gave hexagonal CdS films at all deposition temperatures.

Declaration

I hereby declare that no part of this thesis has been submitted in support of an application for any degree or qualification of the University of Manchester or any other University or Institution of Learning

---

Karthik Ramasamy

Copyright

To

Family,

Friends and Teachers

Acknowledgement :

I have immense pleasure in thanking my supervisor Professor Paul O'Brien for giving me the opportunity to pursue my doctoral degree with his group in a renowned university. I would like to thank him for his valuable guidance and encouragement throughout my course. I am grateful to The University of Manchester for the financial support. I would like to thank Dr. M. Azad Malik for his discussions and valuable comments. I am thankful to Professor Neerish Revaprasadu, University of Zululand, South Africa for his guidance and the chance he gave me to spend two months with his group in South Africa. I also thank Prof D. D. Sarma, Indian Institute of Science for being a gracious host during my short visit to India.

My gratitude to Ms. Judith Shackleton, Mr. Mike Faulkner, Mr. Alan Harvey, Andrew Forrest for training me in XRD, SEM, TEM and AFM. Special thanks to Dr. James Raftery and Dr. Madeleine Helliwell for solving the crystal structures, Dr. Paul Wincott for carringout XPS measurement and Dr. Floriana Tuna for doing magnetic measurement studies. Very special thanks to mass spectrometry, elemental analysis team and Mr. David Gordon (Glassblower). I also thank Ms. Laura, Mrs. Christiane Taylor, Mrs. Loraine Bishoff (late).

I would like to thank Dr. Gopal Kandasamy, Dr. Venkat Ulaganathan, Dr. Arunkumar Panneerselvam and Dr. P. John Thomas for being there unconditionally and for their constant encouragement throughout the PhD course. I am grateful to Dr. Weerakanya Maneeprakorn (Pui) and Mr. Ahmed for their help in TEM. Special thanks to all POB group members and their friendship.

I am very grateful to all my teachers in school, undergraduation and masters. Thanks to all my friends in Orchid Chemicals Chennai. My special thanks to Mr.

Eswar for always helping me perform better. I sincerely thank Mr. Singaraselvan (cousin) for his financial help and encouragement. I am glad to acknowledge to all my friends in India, UK and South Africa for their love and support.

Last but not the least my very special thanks and love to my mother (R. Tamil Selvi), father (Ramasamy) and brother (Sridhar), for being the reason of my presence and whose unconditional love which has been strongest pillar of support to help me become the person I am today.

Chapter 1

General Introduction

1.1 Semiconductors

Semiconductors and insulators are two categories of solid–state materials that differ primarily in that insulators have larger bandgap – the energy that an electron must acquire to be free to move from atom to atom. The conductivity value of semiconductors (10^4 to 10^{-8} Ω cm^{-1}) lies between the conductivity value of metals (10^8 to 10^4 Ω cm^{-1}) and insulators (less than 10^{-8} Ω cm^{-1}). In semiconductors, at room temperature, very few electrons gain enough thermal energy to jump the energy gap from the valence band to conduction band, which is necessary for electrons (or holes) to be available for electric current conduction. For this reason, pure semiconductors and insulators in the absence of applied electric field have roughly similar resistance.[1]

1.1.1 Band Structure

The band structure of a solid describes ranges of energy that an electron is "forbidden" or "allowed" to have. It is due to the diffraction of the quantum mechanical electron waves in the periodic crystal lattice. The band structure of a material determines several characteristics, in particular its electronic and optical properties. The electrons of a single free-standing atom occupy atomic orbitals, which form a discrete set of energy levels. If several atoms are brought together into a molecule, their atomic orbitals split, as in a coupled oscillation. This produces a number of molecular orbitals proportional to the number of atoms. When a large number of atoms (of order 10^{20} or more) are brought together to form a solid, the number of orbitals becomes exceedingly large, and the difference in energy between them becomes very small, so the levels may be considered to form continuous bands of energy rather than the discrete energy levels of the atoms in isolation. However, some intervals of energy contain no orbitals, no matter how many atoms are aggregated, forming bandgap.

1.1.2 Band structure in different types of solids

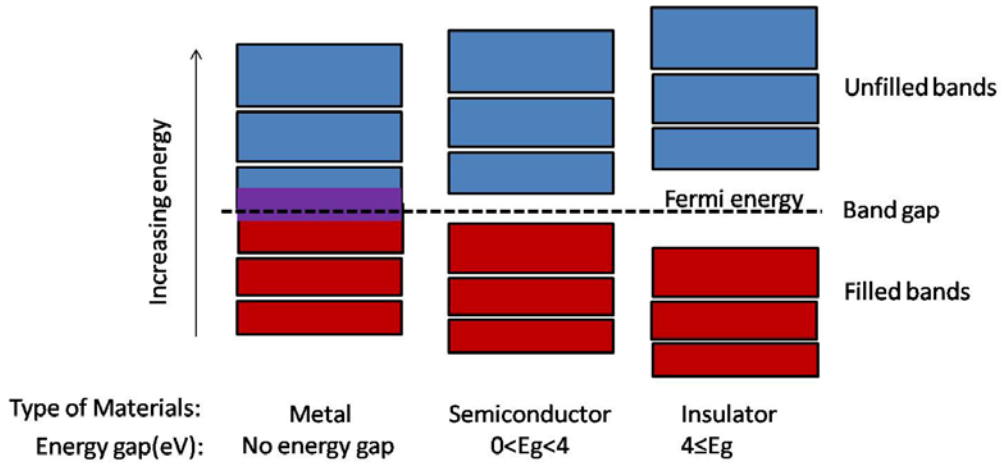

Fig. 1.1 Simplified diagram of the electronic band structure of metals, semiconductors and insulators

Metals contain a band that is partly filled and partly empty regardless of temperature, therefore they have very high conductivity. The lowermost, almost fully occupied band in an insulator or semiconductor is called the valence band by analogy with the valence electrons of individual atoms. The uppermost, almost unoccupied band is called the conduction band because only when electrons are excited to the conduction band can current flow in these materials. The difference between insulators and semiconductors is only that the forbidden bandgap between the valence band and conduction band is larger in an insulator (Fig. 1.1), generally upwards of 4 eV, so that fewer electrons are found there and the electrical conductivity is lower. Thus, semiconductors have bandgaps of somewhat less than 4 eV and often within the range of IR-Vis-UV region. One of the main mechanisms for electrons to be excited to the conduction band is due to thermal energy.

1.1.3 Intrinsic and extrinsic semiconductors

The conductivity of semiconductors is not only affected by temperature but is also changed by the level of impurities and defects in crystal lattice. An intrinsic semiconductor is also called an undoped semiconductor. The property of electrical

conductivity can be due to crystal lattice defects or thermal excitation. In an intrinsic semiconductor the number of electrons (n) and the number of holes (p) created by excitation of electron is equal i.e. (n=p). Examples of intrinsic semiconductors include elemental semiconductors, such as Si and Ge, and compound semiconductors such as CdS, GaAs or $CuInS_2$. An extrinsic semiconductor is a semiconductor that has been doped. Doping involves adding dopant atoms to an intrinsic semiconductor, which changes the electron and hole carrier concentrations of the semiconductor at thermal equilibrium. During doping, impurity atoms are introduced to an intrinsic semiconductor. Impurity atoms are atoms of an element different from the intrinsic semiconductor atoms. Impurity atoms act as either donors or acceptors to the intrinsic semiconductor, changing the electron and hole concentrations of the semiconductor. Impurity atoms are classified as donor or acceptor atoms based on the effect they have on the intrinsic semiconductor. Donor impurity atoms have more valence electrons than the atoms they replace in the intrinsic semiconductor lattice. Donor impurities "donate" their extra valence electrons to a semiconductor's conduction band, providing excess electrons to the intrinsic semiconductor. Excess electrons increase the electron carrier concentration (n_0) of the semiconductor, making it n-type. Acceptor impurity atoms have fewer valences electron than the atoms they replace in the intrinsic semiconductor. They "accept" electrons from the semiconductor's valence band. This provides excess holes to the intrinsic semiconductor. Excess holes increase the hole carrier concentration (p_0) of the semiconductor, creating a p-type semiconductor.

n-Type doping

An example of n-type doping is arsenic in silicon. Arsenic has five valence electrons whereas silicon has four. This extra electron creates donor electron levels just below the conduction band (Fig. 1.2).

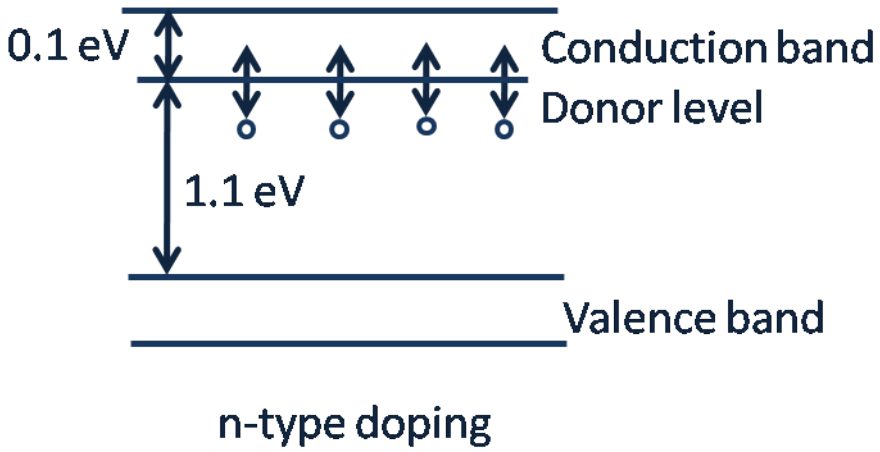

Fig. 1.2 The result of n-type doping on band structure

Thermal excitation can cause electrons to move from the new donor levels (rather than the valence band) into the conduction band. The donor levels do not display band-like qualities and electrons are not free to move. Conduction is caused by movement of the promoted electrons in the partially filled conduction band. Due to the proximity of donor levels and the conduction band, electrons can move from one to the other more easily than in pure silicon. The bandgap for silicon is 1.1 eV whereas for arsenic doped silicon the donor level energy is less than 0.1 eV below the conduction band. Less thermal energy is required for arsenic doped silicon to reach the same conductivity level as pure silicon.

p-Type doping

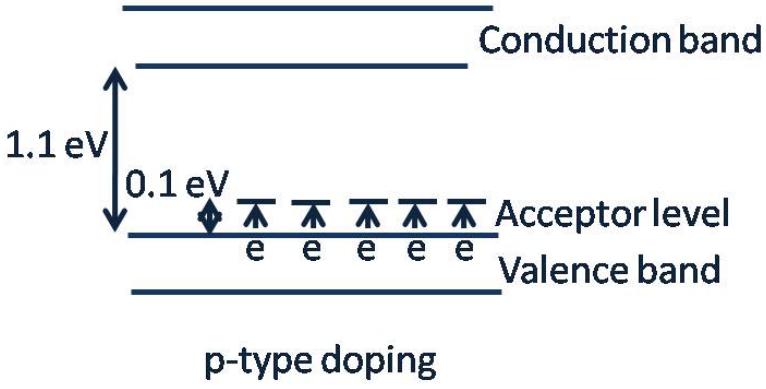

Fig. 1.3 The result of p-type doping on band structure

An example of p-type doping is gallium in silicon. Gallium has three valence electrons whereas silicon has four, and the resulting material is therefore deficient by one electron. Acceptor levels form just above the valence band. Thermal excitation causes electrons to move from the valence band to the new acceptor levels (rather than to the conduction band). Similar to the donor levels in n-type materials, the acceptor levels in p-type materials do not display band-like qualities and electrons are not free to move (i.e. they are localized energy levels). The movement of electrons from the valence band to the acceptor levels causes positively charged holes to be left behind in the valence band. The movement of these holes in the valence band causes the conduction of the material. Due to the proximity of the valence band and acceptor levels, electrons can move from one to the other more easily than in the pure silicon. In gallium-doped silicon the acceptor level energy is ~ 0.1 eV above the valence band (compared to the 1.1 eV bandgap of silicon)

1.1.4 Carrier concentrations and the position of the Fermi level

The position of the Fermi level is different for intrinsic n-type and p-type semiconductors. In intrinsic semiconductors the Fermi level is always mid-bandgap (i.e. $E_f = E_g/2$) and is temperature independent. The number of holes in the valence band is always equal to the number of electrons in the conduction band. The Fermi level in n-type materials is temperature dependent and it is just above the donor level energy (E_d) slightly below the conduction band. At low temperature all the electrons are in the donor levels. In this material there are more electrons present in the conduction band than there are holes in the valence band. In the p-type extrinsic semiconductor the Fermi level is located slightly below the acceptor energy level (E_a), and just above the valence band. In this type of material there are more holes present in the valence band than electrons in the conduction band.

1.1.5 Direct and indirect semiconductors

Semiconductors can be further characterized according to their electronic structure by the type of electrons transferred from valence to conduction band. The kinetic energy of electrons is described by the equation:

$$E = k^2 / 2m_n \quad (1.1)$$

Where m_n is the effective mass and k is the crystal momentum

In some semiconductors, such as GaAs, electron promotion from the valence to the conduction band requires no change in crystal momentum (vibrational energy); these are termed direct bandgap semiconductors (Fig 1.4). However, in many semiconductor materials, promotion from valence band to the conduction band must be accompanied by a change in crystal momentum; which are termed indirect bandgap semiconductors (Fig 1.4) because the lowest energy electronic transition occurs by an indirect process. In indirect semiconductors, such as Si or Ge, energy equal to the bandgap (E_g) is not sufficient to promote electrons from the valence to conduction band; extra energy is required in the form of lattice

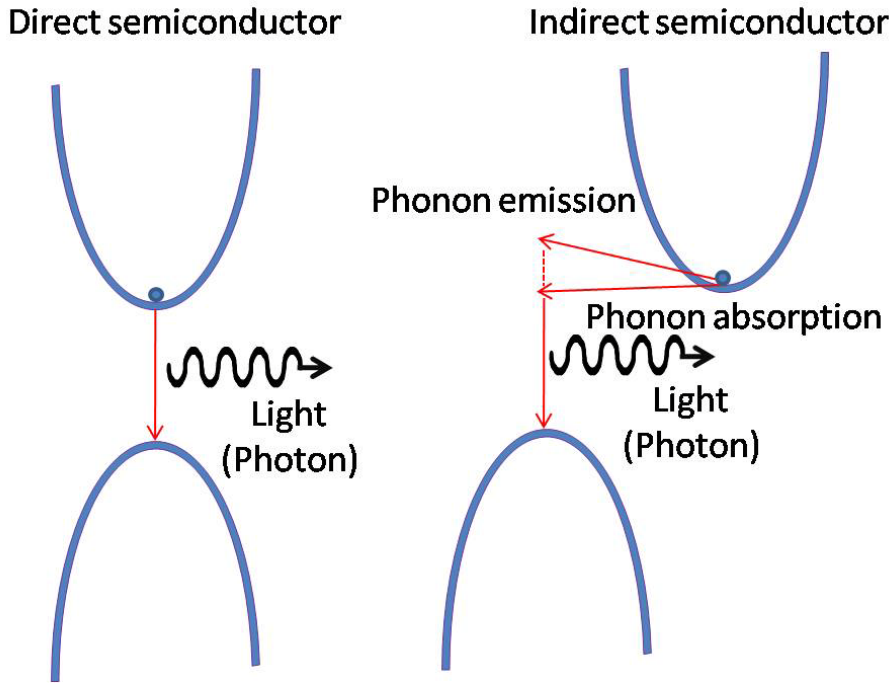

Fig. 1.4 Example of bandgap in direct and indirect semiconductors

vibrational energy (phonons). Therefore, with energy $h\nu = E_g + E_{phonon}$, an electron can undergo the required change in crystal momentum for an indirect transition to be possible.

1.1.6 Classification and applications of semiconductors

Semiconductor materials can be classified based on their type. Semiconductors have widely been used in electronic and optoelectronic applications.[2] Summaries of applications listed in Table 1.1.

Table 1.1 Classification and applications of semiconductors

Type	Example	Applications
IV Elemental semiconductors	Si, Ge, Diamond	Microchips, solar cells
IV- IV Semiconductors	SiC, SiGe	Lightning arrestors, blue LED, Schottky diodes
III-V Semiconductors	AlN, AlAs, AlP, BN, BP, BAs, GaSb, GaAs, GaN, GaP, InSb, InSb, InN,InP	Light emitting diodes
III-V Ternary semiconductor alloys	AlGaAs, InGaAs, InGaP, AlInAs, AlInSb, GaAsP, AlGaN, AlGaP, InGaN, InAsSb, InGaSb	IR photo detectors, red emitting diodes, solar cells
III-V Quaternary semiconductor alloys	GaInNAsSb, GaInAsSbP	Light emitting diodes
II- VI Semiconductors	CdSe, CdS, CdTe, ZnO, ZnSe, ZnS, ZnTe	Solar cells, Solid state lasers
II-VI Ternary semiconductor alloys	CdZnTe,HgCdTe, HgZnTe, HgZnSe	IR detectors
IV-VI Semiconductors	PbSe, PbS, PbTe, SnS, SnTe	Thermal imaging, IR detectors
IV-VI Ternary semiconductor alloys	PbSnTe, Tl_2SnTe_5, Tl_2GeTe_5	IR detectors
V-VI Semiconductors	Bi_2Te_3	Thermoelectric materials
II-V Semiconductors	CdP, Cd_3As_2, Cd_3Sb_2, ZnP, Zn_3As_2, Zn_3Sb_2	IR detectors, magneto resistors

1.2 Thin films

1.2.1 Thin film semiconductor materials

Thin films can be deposited on a substrate by physical or chemical deposition methods, e.g: Sputtering, laser ablation, MOCVD etc.

1. The formation of films from any deposition technique starts with a random nucleation process followed by nucleation and growth stages
2. Nucleation and growth stages are dependent upon various deposition conditions, such as growth temperature, growth rate, substrate and precursors
3. The nucleation stage can be modified significantly by external influences, such as electron or ion bombardment.
4. Film microstructure, associated defect structure and film stress depend on the deposition conditions at the nucleation stage.
5. The crystal phase and the orientation of the films are governed by the deposition conditions.
6. Thin films exhibit unique properties that cannot be observed in bulk materials:

Unique material properties resulting from the atomic growth process, size effects, including quantum size effects characterized by the thickness, crystalline orientation and multilayer aspects.

1.2.2 Fabrication of thin film semiconductor materials

Semiconductor materials can be fabricated by various techniques which fall into four general categories: deposition, removal, patterning and modification of electrical properties

Deposition: Deposition is a process that grows, coats or transfers a material onto the substrate: e.g, Physical Vapour Deposition (PVD), Chemical Vapour Deposition (CVD), Electro Chemical Deposition (ECD), Molecular Beam Epitaxy (MBE) and Atomic Layer Deposition (ALD).

Removal: Removal processes are any that remove material from the wafer either in bulk or selective form. These include etching and chemical-mechanical planarization among others.

Patterning: The series of processes that shape or alter the existing shape of deposited materials and are generally referred to as lithography.

Modification of electrical properties: The process consisting of doping transistor sources and drains originally by diffusion furnaces and later by ion implantation.

1.2.3 Chemical vapour deposition (CVD)

Chemical vapour deposition is a chemical process used to produce high purity and high performance thin film materials. In a typical CVD process the substrate is exposed to one or more volatile precursors which react and/or decompose on the substrate to produce the desired deposit.

1.2.3.1 Types of chemical vapour deposition

A number of forms of CVD are in wide use and are frequently referenced. These processes differ in the means by which chemical reactions are initiated (activation process) and process condition. The types of CVD include:

Atmospheric pressure CVD (APCVD) – CVD process at atmospheric pressure.

Low-pressure CVD (LPCVD) – CVD process at sub-atmospheric pressures. Reduced pressure tends to reduce unwanted gas-phase reactions and improves film uniformity across the wafer.

Aerosol assisted CVD (AACVD) – CVD process in which the precursors are transported to the substrate by means of a liquid/gas aerosol, which can be generated ultrasonically. This technique is suitable for use with involatile precursors.

Direct liquid injection CVD (DLICVD) – CVD process in which the precursors are in liquid form. Liquid solutions are injected in a vapourization chamber towards reactors. Then the precursor vapours are transported to the substrate as in classical

CVD process. This technique is suitable for use on liquid or solid precursors. High growth rates can be reached using this technique.

Plasma – Enhanced CVD (PECVD) – CVD process that utilize plasma to enhance chemical reaction rates of the precursors. PECVD processing allows deposition at lower temperatures, which is often critical in the manufacture of semiconductors.

Remote plasma-enhanced CVD (RPECVD) – CVD process similar to PECVD except that the wafer substrate is not directly in the plasma discharge region. Removing the wafer from the plasma region allows processing temperatures down to room temperature.

Atomic layer CVD (ALCVD) – Deposits successive layers of different substances to produce layered crystalline films.

Hot wire CVD (HWCVD) – Also known as Catalytic CVD or hot filament CVD (HWCVD) uses a hot filament to chemically decompose the source gases.

Metalorganic chemical vapour deposition (MOCVD) – CVD process based on metalorganic precursors.

Hybrid physical chemical vapour deposition (HPCVD) – Vapour deposition process, that involve chemical decomposition of precursor gas and vapourization of solid a source.

Rapid thermal CVD (RTCVD) – CVD process that uses heating lamps or other methods to rapidly heat the wafer substrate. Heating only the substrate rather than the gas or chamber walls helps reduce unwanted gas phase reactions that can lead to particle formation.

1.2.3.2 The process of chemical vapour deposition

CVD processes are extremely complex and involve a series of gas phase and surface reactions. The basic steps in an overall CVD reaction are shown in Fig. 1.5.

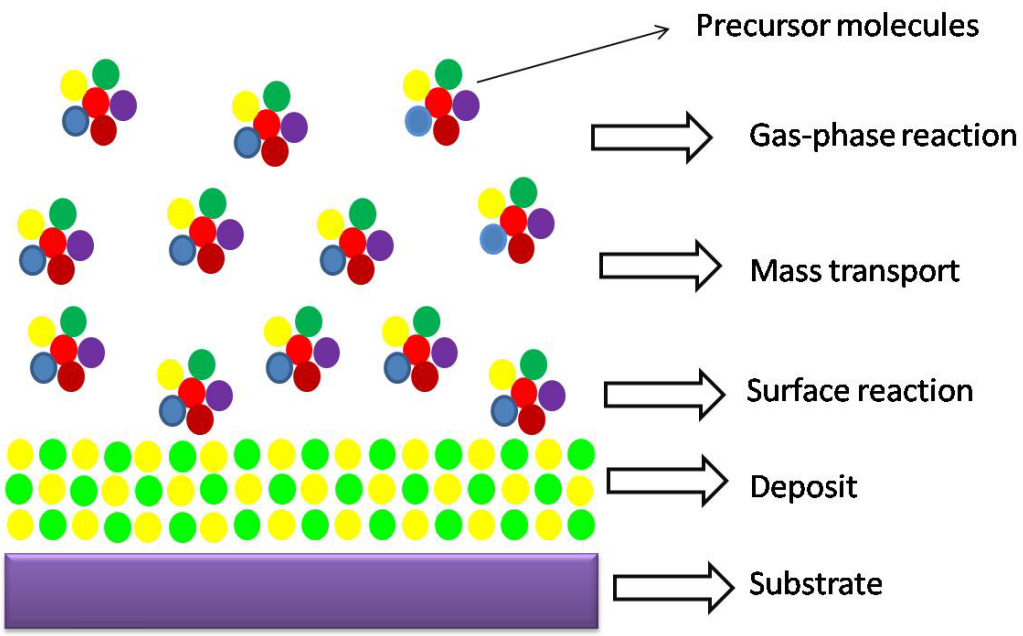

Fig. 1.5 Process of chemical vapour deposition

Step 1: Evaporation and transport of reagents (precursors) in the bulk gas flow region into the reactor

Step 2: Gas phase reactions of precursors in the reaction zone to produce Intermediates

Step 3: Mass transport of reactants to the substrate surface

Step 4: Nucleation and surface chemical reactions leading to film formation

Step 5: Mass transport of remaining fragments of the decomposition away from the reaction zone

1.2.4 Precursors for chemical vapour deposition

A major part of tailoring material properties resides in the proper choice of the molecular precursors, whose nature strongly affects the nature and morphology of the final product. It is most important to design the precursors that have a combination of certain characteristics that make them suitable precursor for preparation of high quality thin films. The characteristics of an ideal CVD precursor can be explained as follows:

- The main requirement of any precursor is that it should be readily volatile at a temperature well below that of its decomposition temperature
- Its thermal stability is also a crucial factor in determining the suitability of a precursor for CVD
- Pure precursors play an important role in preparing high purity semiconductor thin films and help to prevent contamination with undesirable side products
- The precursors should be easily available and preparation should be cost effective
- Clean decomposition without the incorporation of residual impurities
- Compatibility with other precursors or solvents during the growth of complex materials
- Precursor should be non-toxic to reduce the environmental effects during the CVD process.

1.2.5 Issues in using conventional precursors for CVD

The uses of conventional precursors for the CVD process involve some issues which include:

- The highly pyrophoric nature of metal alkyls and the high toxicity of hydride gases such as H_2S, H_2Se, NH_3, PH_3, AsH_3, SiH_4 and the like. In addition, the reactivity of the metal alkyls means that trace amounts of air and moisture may lead to the formation of alkoxides and result in the incorporation of oxygen impurities on the films
- Prereactions within the reactant molecules in MOCVD reactor. Such reactions affect the morphology and stoichiometries of the final product
- A large imbalance in the mole ratios of the precursors in the feed gas is usually needed with conventional precursors to control and maintain the stoichiometry of the thin films

1.2.6 Advantages of the single source precursors

The uses of single source precursors for the CVD process have advantages over the conventional precursors which are:

- Control of the coordination numbers at the metal by the formation of adducts or aggregates can decrease the sensitivity towards the air and moisture
- Use of single source precursors can minimise the use of toxic gases
- Prereactions may be limited
- Easy to maintain the stoichiometries of metal and ligand compositions
- The decomposition temperature is also controllable by design of the precursor consequently film growth at low temperature can be achieved
- It may also overcome the problem of incompatibility between the different precursors occasionally found in the conventional multiple source methods

1.3 Single source precursors for metal chalcogenide thin films

1.3.1 Precursors for II-VI semiconductor materials

1.3.1.1 Adducts as precursors

Amine or ether adducts of the alkyls of zinc and cadmium are found to be good candidates for the growth of II-VI semiconductors by CVD. Use of such adducts have several potential advantages: (1) the vapour pressure of these complexes are reduced compared to those of simple dialkyls (2) the reaction before the precursors reach the hot zone of the reactor may be reduced (3) layers may have improved electrical properties due to the purification of the alkyl moiety during the preparation of the adduct. Lewis bases form isolable adducts of the composition Me_2ML_2, where L is furan, tetrahydrofuran, thiophene, tetrahydrothiophene, triethylamine or L_2 is 1,4-dioxane, 1,4-thioxane or tetramethylethylenediamine[3,4] as in example shown below. Amine adducts are more effective than ethers or thioethers in suppressing prereactions (Fig. 1.6).Good quality films of ZnS, ZnSe and ZnTe[5-7] were grown using $[Me_2Zn(NEt_3)_2]$ at 300-350°C whereas the prereactions were more difficult to suppress in the case of cadmium.

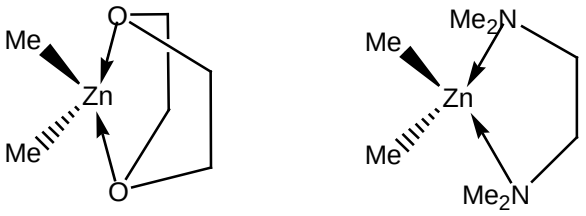

Fig. 1.6 Structures of 1, 4-dioxane and tetramethylethylenediamine adduct of dimethyl zinc

$Me_2Cd(SC_4H_8)_2$ gave cleaner growth with H_2S and H_2Se and better quality films than $CdMe_2$.[8] Initially observation led to the idea that Lewis bases as good n-donor ligands blocked coordination sites on the metal dialkyl and suppressed the binding of the chalcogenide component to the metal center by shifting the equilibrium to the left in equation 1.2.

$$Me_2M{:}L + H_2S \rightleftharpoons Me_2M{:}SH_2 + L \qquad (1.2)$$

M = Zn or Cd

However, spectroscopic studies showed that in the gas-phase the adducts $Me_2M{:}L$ completely dissociate even at room temperature. This observation suggests that the Lewis base reacted with certain reaction intermediates and not with metal dialkyls.

1.3.1.2 Chalcogenolates as precursors

The group 12 metal chalcogenolates are generally non-volatile and polymeric. These complexes are promising in several aspects: they can deliver both the metal and chalcogenide element in a defined ratio, avoiding any mixing problems;

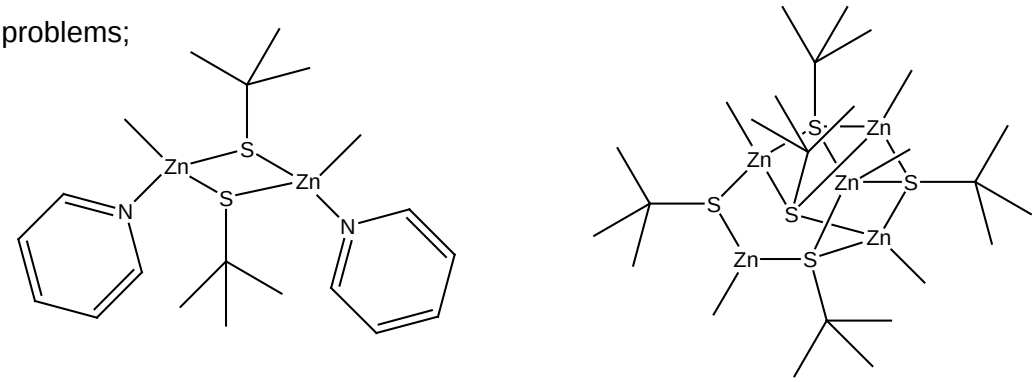

Fig. 1.7 Structures of $[MeZn(S^tBu)(Py)]_2$ and $[MeZn(S^tBu)]_5$

they are not prone to pre-reactions; they are also stable, less toxic, non-pyrophoric and easier to handle. The structures of alkylzinc thiolates are often oligomeric, e.g. $[RZn(SR')]_n$: such as $[MeZn(S^tBu)]_5$ is a pentamer,[9,10] $[MeZn(S^iPr)]_8$ is an octamer and $[EtZn(SEt)]_{10}$ is a decamer with a wurtzite-like cluster frame work.[11] It is evident that such clusters provide models for the gas-phase nucleation process involved in prereaction in CVD (Fig 1.7). It is also known that donor ligands are able to split μ-thiolato bridges. Arene thiolato complexes of zinc and cadmium $M(SC_6X_5)_2$ (X = F,Cl) suggested that these compounds were polymeric high melting solids, and were soluble in polar solvents such as methanol and acetone.[12] The structure of $[Cd(SCH_2CO_2Et)_2]_\infty$ consists of one dimensional thiolato bridged chains in which each cadmium center is bound to four sulfurs, with additional weak contacts to four carboxylate oxygens.[13] The structure of $[Zn(SPh)_2]$ may be regarded as the prototype for sterically less hindered chalcogenolato complexes: The compound consists of $[Zn_4(SPh)_8]$ adamantoid cages linked to each other via μ-SPh bridges.[14] The structure of $[Cd(SPh)_2]_\infty$ also shows the similar coordination.[15] The supermesityl complexes exhibit many of the properties ideal for MOCVD precursor: they are fairly air stable, can be obtained in high yield and purity, and also sublime under reduced pressure without any residues. A series of volatile compounds of general formula: $[M(ESi(SiMe_3)_3)_2]$ (E = Te) have been examined by Arnold and co-workers. They form dimers in the solid state, with two bridging and two terminal E atoms.[16,17] In a preliminary study, thin films of ZnTe and CdTe were grown from $[M(TeSi(SiMe_3)_3)_2]$ M= Zn or Cd at temperature between 250 and 350 °C. Based on analysis of by-products obtained during the film growth, the following decomposition path way was suggested.[16]

$$[M(TeSi(SiMe_3)_3]_2)_2] \text{ (Solid)} \longrightarrow 2M[TeSi(SiMe_3)_3]_2 \text{ (gas)} \quad (1.3)$$

$$M(TeSi(SiMe_3)_3)_2 \longrightarrow MTe + Te(Si(SiMe_3)_3)_2 \quad (1.4)$$

Bochmann and co-workers[17, 18] have developed a range of precursors based on 2,4,6-tri-tert-butylphenylchalcogenolate for the deposition of II–VI materials. The single crystal structure of $[Cd(SC_6H_2{}^tBu_3\text{-}2,4,6)_2]_2$ showed that the complex is a dimer. Polycrystalline CdS thin films were deposited at 450 °C by low pressure MOCVD using $[Cd(SC_6H_2{}^tBu_3\text{-}2,4,6)_2]_2$ as precursor. During the deposition diarylsulfide was detected as a residual pyrolysate. The mercury analogues readily decomposed *via* a reductive elimination path to from atomic Hg and diaryl chalcogenide, which indicates that these compounds may be more suited for photo-assisted rather than thermal MOCVD method.[19] The general preparation method of one such complex is shown in scheme 1.5, 1.6 and 1.7.

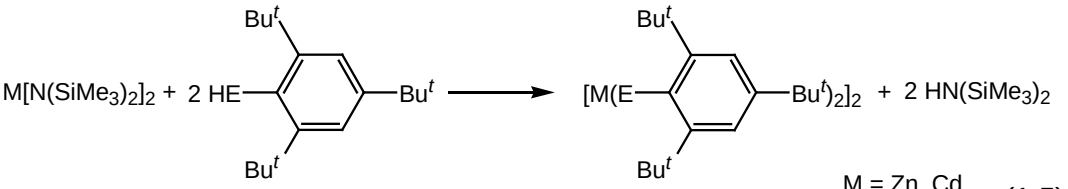

(1.5)

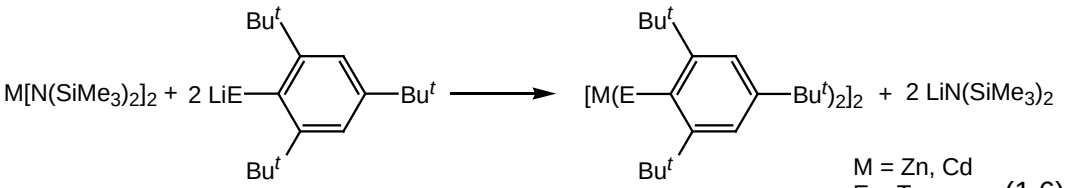

(1.6)

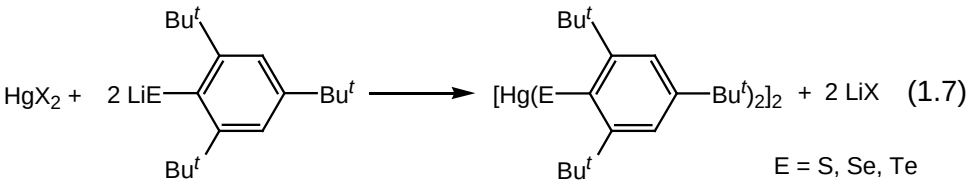

(1.7)

1.3.1.3 Chalcogeno-urea complexes as precursors

Cadmium sulfide films were grown by spray pyrolysis using aqueous mixtures of cadmium chloride and thiourea. The single-molecule precursor was formed by reacting the parent compounds directly in the spray solution. Depending

upon the pH, molar ratio and whether anhydrous or hydrated cadmium chloride was used, $[Cd(SC(NH_2)_2)_2]Cl_2$, $[Cd(SC(NH_2)_2]Cl_2$, and $[Cd(H_2O)(SC(NH_2)_2)]Cl_2$ intermediates have been claimed.[20-22] Niinisto *et al.* have confirmed the formation of $[Cd(SC(NH_2)_2)_2]Cl_2$, which contains a terahedrally coordinated cadmium complex with quite complex thermal behaviour in air and under the conditions of spray pyrolysis,[23] from which they concluded that it is not possible to produce CdS thin films without significant amounts of chlorine and other impurities.[24] Similar results have also been obtained for the preparation of CdSe thin films using cadmium chloride and N,N-di-methylselenourea.

1.3.1.4 Dialkyldichalcogenocarbamato complexes as precursors

Dialkyldichalcogenocarbamate complexes of group 12 metals have been employed widely for the preparation of II-VI material thin films by MOCVD. It is well known that the solid state pyrolysis of dithiocarbamate complexes under inert atmosphere generally give the corresponding metal sulfide. However, the stoichiometry and phase of the metal sulfide deposited are strongly dependent on the pyrolysis condition.[25] Their general formulae are $[M(E_2CNR_2)_2]$ or $[M(E_2CNR^1R^2)_2]$, according to whether they symmetrically or asymmetrically substituted. Crystal structure determinations of various dialkyldichalcogenocarbamates, either symmetrically as $[Zn(S_2CNR_2)_2]$ with R = Me,[26] Et,[27] or ^{i}Pr[28] and in $[Cd(S_2CNR_2)_2]$,[29] $[Zn(Se_2CNEt_2)_2]$[30] $[Cd(Se_2CNEt_2)_2]$ or unsymmetrically substituted as in $[Zn(S_2CNMeR)_2]$ with R = Et, ^{n}Pr, ^{i}Pr, or ^{n}Bu, have shown dimeric associations $[M(E_2CNR)_2]_2$ (E = S, Se; M = Zn, Cd) in the solid-state (Fig. 1.8), but are apparently monomeric in the vapour phase, as confirmed by mass spectra.[31] Saunders *et al.* pioneered the use diethyldithiocarbamate complexes of Zn and Cd as single source precursor for the deposition of ZnS, CdS by low-pressure MOCVD. Polycrystalline and hexagonal cadmium sulfide films were grown by MOCVD on glass, but thin epitaxial layers were obtained on InP (100) and GaAs

(100). Such compounds may open up the possibility of the low-cost preparation of photovoltaic materials.[32] The quality of the ZnS films was generally lower than that of the CdS films as seen by Frigo *et al.* in a hot wall reactor.[33] The use of metal diethyldiselenocarbamates to deposit ZnSe and CdSe on glass plates, under the same conditions, resulted in the deposition of elemental selenium,[31] whereas unsymmetrical selenocarbamates such as zinc and cadmium complexes of methyl(n-hexyl)diselenocarbamates gave corresponding metal selenide thin films by LP-MOCVD at 200-250°C for zinc 400-450°C for cadmium selenide. By changing the alkyl group on parent amine of the diselenocarbamate from the symmetric diethyl to asymmetric methyl(n-hexyl) derivative, the formation of diethyl diselenide is hindered, and thus the deposition of selenium during film growth is inhibited.[34]

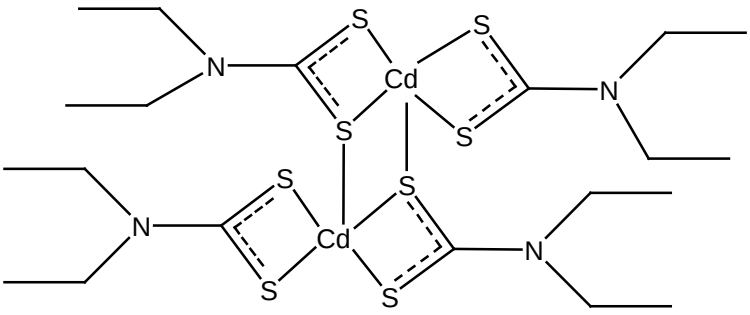

Fig. 1.8 Structure of cadmium diethyldithiocarbamate

Wold and co-workers reported the elaborate study of the deposition of zinc sulfide films by MOCVD using toluene solution of diethyldithiocarbamate in a sonicated spray evaporator. The effects of various factors on the crystalline form of the ZnS deposited were discussed, and the epitaxial growth of cubic ZnS could be observed on GaAs (100) substrates at growth temperatures of 460-520°C. The thermal decomposition path of the precursor was also investigated by pyrolysis GC-MS at pyrolyser temperature 400-500°C. These volatile pyrolysates are consistent with results of earlier thermogravimetric (TG) studies of the decomposition of dithiocarbamates. The decomposition path is shown in Scheme (1.8) and (1.9).[35]

$$Zn(S_2CNEt_2)_2 \longrightarrow ZnS + EtNCS + Et_2NCS_2Et \quad (1.8)$$

$$Et_2NCS_2Et \longrightarrow Et_2NH + CS_2 + C_2H_4 \quad (1.9)$$

Nomura *et al.* grew the cubic β-ZnS zinc blende phase epitaxially on Si (111) by OMPVE, using $[Zn(S_2CN(Et)_2)_2]$ in a cold wall horizontal reactor. The important point is that depositions conducted without carrier gas resulted in hexagonal α-ZnS of poor crystallinity and morphology. The introduction of carrier gas (N_2) improved the morphology and allowed (111)-oriented β-ZnS to grow strongly.[36] Motevalli *et al.*[31] studied the deposition behavior of the zinc complexes of unsymmetrically substituted dithiocarbamato ligands. In trial volatilization experiments it was shown that at *ca*. 150°C, unsymmetrically substituted $[Zn(S_2CN(Me)Et)]_2$, $[Zn(S_2CN(Me)^nPr)]_2$ and $[Zn(S_2CN(Me)^nBu)]_2$ sublime above their melting points, whereas $[Zn(S_2CNEt_2]_2$ sublimes as a solid. $[Zn(S_2CN(Me)^nBu)]_2$ was used successfully to grow ZnS on glass, in a cold wall, low-pressure MOCVD reactor, with the source at 150°C and with a substrate temperature range of 450-490°C. A film of hexagonal phase with a high degree of preferred (0001) orientation was obtained in a two hour run at 470°C. A similar comparative study of $[Cd(SCNEt_2)_2]$ and $[Cd(SCN(Me)^nBu)_2]$ has established the latter to be by far the more volatile.[37]

1.3.1.5 Mixed alkyl/dialkyldichalcogenocarbamato complexes as precursors

The volatility of dichalcogenocarbamate complexes has been increased by making associates of alkyl ligand, so as to form heteroleptic complexes of general formula $[M(R)(E_2CNR'_2)]$, (Me)Zn(diethyldithiocarbamate)[38] and (Me)Zn (diethyldiselenocarbamate)[39] have been shown to be dimers, with $[EZn(\mu\text{-}E)]_2$ cores, in the solid state. These compounds were first prepared by Noltes[40] using the insertion reactions (1.10) and (1.11).

$$2\ MeZn(NEt_2) + 2CS_2 \longrightarrow [MeZn(S_2CNEt_2)]_2 \qquad (1.10)$$

Conproportionation also provides a convenient synthesis for these compounds

$$Me_2Zn + Zn(S_2CNEt_2)_2 \longrightarrow [MeZn(S_2CNEt_2)]_2 \qquad (1.11)$$

Complexes with general formula $[M(R)(E_2CNR'_2)]$ (R or R' = Me or Et, M = Zn; R = Me, R' = Et, M = Cd) have been shown to sublime under mild conditions (100-150°C). Films of ZnS, ZnSe, CdSe and $Zn_{0.5}Cd_{0.5}Se$ have been grown by LP-MOCVD on glass plates at 450°C from $[(R)Zn(S_2CNEt_2)]_2$ with (R = Me,[38] Me_3C and Me_3CCH_2),[41] $[(Me)Cd(Se_2CNEt_2)]_2$ and $[(Me)Zn_{0.5}Cd_{0.5}(Se_2CNEt_2)]_2$ in a hot wall reactor. In a comparative study, $[(Me)Zn(S_2CNEt_2)]_2$, $[(Me)Cd(Se_2CNEt_2)]_2$, and $[(Me_3CCH_2)Cd(S_2CNEt_2)]_2$ were also used to deposit films of the respective metal chalcogenides on both glass and GaAs (100), using a cold wall reactor under vacuum.[42] CdS films were grown at 425°C from $[(Me)Cd(S_2CNEt_2)]_2$ were of better quality than those grown from $[(Me_3CCH_2)Cd(S_2CNEt_2)]_2$.

Heteroleptic bis(dialkyldithiocarbamate) complexes of general formula $[LM(R_2NCS_2)_2]$ (M = Zn, Cd, Mn, Mn:Zn, or Zn:Cd and L = 1, 10 –phenanthroline or 2,2'-bipyridine or 4,4'bipyridine) adducts were used as single source precursors for the deposition of ZnS, CdS, (ZnCd)S, or (Zn,Mn)S films by MOCVD.[43,44]

1.3.1.6 Metal complexes of xanthates as precursors

Zink *et al.*studied the growth of ZnS films from zinc xanthate (bis(O-isopropyldithiocarbonato)zinc(II)) by thermal and photolytic MOCVD comparatively. Both series of experiments were carried out under low pressure, with glass plates and silicon wafers as substrates, the precursor being vapourised at 120°C. Thermal depositions were effected at 350°C. They produced polycrystalline, highly (0002) oriented, hexagonal ZnS-films. Photolytic depositions were run at an overall temperature of 120°C using a XeCl excimer laser which produced pure hexagonal ZnS films in contrast to the thermal CVD mathod.[45]

1.3.1.7 Metal complexes of monothiocarboxylates as precursors

Hampden-Smith co-workers studied the deposition CdS, ZnS and $Cd_xZn_{1-x}S$ films from the precursors of general formula $M(SOCR)_2$ (tmeda) (tmeda = N,N,N,N-tetramethylehylenediamine), R being a methyl[46] or a tert-butyl[47] group, by aerosol-assisted CVD (AA-CVD). Single crystal structure of $[Zn(SOCCH_3)_2(tmeda)]$ and $[Cd(SOCCH_3)_2(tmeda)]$ revealed that they are isostructural, monomeric with the metal atom in a distorted tetrahedral coordination environment comprising two nitrogens and two sulfurs. Highly oriented, crystalline films of CdS and ZnS have been grown from toluene solutions of these complexes at temperatures as low as 125°C. $Cd_xZn_{1-x}S$ films were grown at 175°C from solutions of the precursors mixed in Cd/Zn ratios of 6:4, 5:5, 4:6 and 2.5:7.5. Compared to the solutions, the films appeared Cd-deficient by ca. 5-10% under deposition conditions. Thermally more-stable complexes of thiopivalate analogues of $[M(SOCC(CH_3)_3)_2$ (tmeda)] (M = Zn, Cd) were used to grow films of $Cd_xZn_{1-x}S$ with the stoichiometry of the solution (Cd/Zn =1).[48]

1.3.1.8 Metal complexes of chalcogenophosphinates as precursors

Chalcogenophosphinates are another class of compound that has been studied as single-source precursors for the deposition of II-IV thin materials. CdS thin films were grown using dimethylthiophosphinates, and it was found that doping of excess phosphorus on n-type CdS films would lead to highly compensated semi insulating material.[49] Thin films of ZnS and CdS were grown from $[M(S_2P^iBu_2)_2]_2$ (M=Zn, Cd) using homemade cold-wall low-pressure reactor.[50] The cadmium complex has classic C_i symmetric two–step ladder structure (chair) which is in contrast to the C_2 (boat) geometry observed for closely related isopropoxide complex $[Cd_2((i\text{-}C_3H_7O)_2PS_2)_4]$.[51] The geometry of cadmium is severely distorted tetrahedral. Similar geometry was also obtained in zinc complex with $Zn_2S_8P_4$ core. It has previously been postulated that a reason for a change from C_i symmetry chair

conformation to C_2 symmetry boat conformation for the central eight membered metallocyclic ring for phosphinodithioates/dithiocarbamates is a consequence of the packing requirements of the different sized R groups. O'Brien *et al.*[52, 53] recently reported the series of metal complexes of selenophosphinates general formula $[M(R_2PSe_2)_n]$ (M = Zn, Cd, Pb, In, Ga, Cu, Bi, Ni; R = ^{i}Pr, Ph) for the deposition of metal selenide thin films. The synthesis involves reaction of NEt_3 with $^iPr_2PCl$ or $^iPr_2PCl$ and $HSiCl_3$ in cold toluene as given in reaction Scheme (1.12) and (1.13). This compound was then reacted with different metal salts in methanolic solution to give the metal complexes as precipitates. The complexes are soluble in chloroform, toluene or dichloromethane. All are stable at room temperature under open atmosphere for several months, making them useful precursors for the deposition of metal selenide thin films.

$$R_2PCl + HSiCl_3 + NEt_3 \xrightarrow[6h,\ rt]{Toluene} R_2PSiCl_3 + (HNEt_3)Cl \qquad (1.12)$$

$$R_2PSiCl_3 + 3Se \xrightarrow[20h,\ reflux]{Toluene} [R_2PSe_2]_2Se + Si_2Cl_6 \qquad (1.13)$$

1.3.1.9 Metal complexes of dichalcogenoiminophosphinates as precursors

Cadmium complex of diselenodiisopropyliminophosphinates are prepared by Woolins *et al.*from diisopropylphosphine *via* a two step strategy as shown in (1.14), (1.15) and (1.16). The $NH(SeP^iPr_2)_2$ ligand is more thermally stable than bulky selenolate ligands, such as $[SeSi(SiMe_3)_3]$, and thermolysis of its complexes produces cleaner products with reduced contamination which makes them suitable precursors for the deposition of CdSe thin films.[54] The complex $[MeCd((SeP^iPr_2)_2N)]_2$ was prepared by conproportionation of Me_2Cd and $[Cd((SeP^iPr_2)_2N)_2]$ in toluene. The single-crystal structure of the complex showed dimeric nature of the molecule; each diselenoimidodiohosphinate chelates to one cadmium atom and bridges to next, each cadmium is four coordinate and bound to three selenium atoms and one carbon.[55]

$$NH(SiMe_3)_2 + {}^{i}Pr_2PCl \longrightarrow NH(P{}^{i}Pr_2)_2 + 2ClSiMe_3 \quad (1.14)$$

$$NH(P{}^{i}Pr_2)_2 \xrightarrow{E = S, Se} NH(EP{}^{i}Pr_2)_2 \quad (1.15)$$

$$2NH(EP{}^{i}Pr_2)_2 \xrightarrow[MeOH]{NaOMe,\ MCl_2} M[(EP{}^{i}Pr_2)_2N]_2 + 2NaCl \quad (1.16)$$

The Te analogue of $[Cd((SeP{}^{i}Pr_2)_2N)_2]$ could not be prepared by direct reaction of $NH(P{}^{i}Pr_2)_2$ with tellurium. An alternative method has been introduced by Chivers *et al.* which involves metallation of $NH(PR)_2$ with NaH prior to reaction with tellurium, which facilitates the preparation of $Na[N(TePR_2)_2]$ (R = Ph, ^{i}Pr).[56] This reagent was then used in metathetical reactions with metal halides to generate homoleptic complexes of the type $[M((TeP{}^{i}Pr_2)_2N)_2]$ (M =Cd,Hg) as shown in scheme (1.17) and (1.18)

$$Na((P{}^{i}Pr_2)_2N) + 2Te \xrightarrow[TMEDA]{Hot\ Toluene} (tmeda)Na(NTeP{}^{i}Pr_2)_2) \quad (1.17)$$

$$MX_2 + 2\ (tmeda)Na(N(TeP{}^{i}Pr_2)_2) \xrightarrow[-2\ NaX,\ -tmeda]{Hot\ Toluene} [M((TeP{}^{i}Pr_2)_2N)_2] \quad (1.18)$$

M = Cd, Hg
X = I, Cl
tmeda = tetramethylethanediamine

AACVD experiment using $[Cd((TeP{}^{i}Pr_2)_2N)]_2$ gave mixture of cubic and hexagonal CdTe films at 375°C, whereas at 425 and 475°C cubic CdTe films with excess of Te were obtained. A similar compound of mercury analogues $[Hg((TeP{}^{i}Pr_2)_2N)_2]$ gave only hexagonal tellurium.[57]

1.3.2 Precursors for III-VI semiconductor materials

1.3.2.1 Metal complexes of chalcogenolates as precursors

Nomura *et al.*[58] successfully prepared volatile precursors of alkyl indium chalcogenolates $[(^{n}Bu)_2In(S{}^{i}Pr)]$ and $[(^{n}Bu)In(S{}^{i}Pr)_2]$, which are liquids at room temperature. Low-pressure CVD experiments using these precursors gave tetragonal β-In_2S_3 on (111)-Si or quartz substrates. β-In_2S_3 was obtained amorphous at 300°C and crystalline in the range 350-400°C with strong (103)-

orientation, on (111)-Si at 400 °C. At 450°C, a mixture of In_6S_7 and β-In_2S_3 was obtained with predominantly In_6S_7. Gysling and co-workers[59] prepared metastable phases of indium selenide films on (100)-GaAs by spraying a toluene solution of either [$In(SePh)_3$] or [$Me_2In(SePh)$]. The former gave films of hexagonal In_2Se_3. The latter gave either a new cubic face-centered phase at 365 °C and below whereas in a temperature range of 400 – 476 °C hexagonal InSe phase with small quantities of the new cubic phase was obtained. The most striking evidence of the potential to control film stoichiometry and phase, including the possibility of stabilizing phases that are metastable in bulk was given by Barron and co-workers. They have deposited a novel metastable cubic GaS phase from the $[^tBuGaS]_4$ cube, at temperatures in the region of 400 °C; in this case it is tempting to draw a correlation between the cubic phase observed and the cubane structure of the precursor.[60] In a comparative MOCVD experiment three structurally distinct precursors, dimeric $[(^tBu)_2Ga(\mu_2\text{-}S^tBu)]_2$, tetrameric $[(^tBu)Ga(\mu_3\text{-}S)]_4$ and heptameric $[(^tBu)Ga(\mu_3\text{-}S)]_7$ were used as precursors in order to gain further inside into phase control by molecular design. As expected, $[(^tBu)Ga(\mu_3\text{-}S)]_4$ yielded the cubic GaS at about 400°C. At the same temperature $[(^tBu)_2Ga(\mu_2\text{-}S^tBu)]_2$ gave poorly crystalline films of hexagonal GaS.[61]

1.3.2.2 Metal complexes of chalcogenocarbamates as precursors

O'Brien and co-workers explored the precursor chemistry of chalcogenocarbamates[62] to deposit III-VI materials. Indium sulfide thin films were grown from dimethyl-, diethyl- or dineopentyl-indium diethyldithiocarbamates [$R_2In(S_2CNEt_2)$] with (R = Me, Et, or Np) on GaAs substrate, using a cold wall low-pressure reactor. The phases deposited from $Me_2InS_2CNEt_2$ were either β-In_2S_3 at 325°C, In_6S_7 at 350°C and 375°C or InS + In_6S_7 at 400°C and 425°C. [$Et_2In(S_2CNEt_2)$] yielded β-In_2S_3 at 350 °C and 400°C, whereas [$Np_2In(S_2CNEt_2)$] gave In_6S_7 at 375 and 400°C. The ethyl complex differs from the other two, both by

its aptitude for *β*-H elimination, and the production of single phase cubic β-In_2S_3 over the entire temperature range studied. The analogous gallium precursors proved less effective to produce gallium sulfide thin films. Unsymmetrically substituted indium tris-chelate complexes of dichalcogenocarbamate [$In(E_2CN(Me)R)_3$] were E = S or Se, R = n-butyl or n-hexyl[63] have been used as precursors for the deposition of In_2S_3 on glass, (100)-GaAs or (111)-InP using cold wall reactor under low pressure at 450-500 °C. Similarly mixtures of cubic and hexagonal In_2Se_3 films were produced from the methylhexyldiselenocarbamate of indium complex.

1.3.2.3 Metal complexes of xanthates and monothiocarboxylates as precursors

Highly (111) direction oriented-cubic α-In_2S_3 films were grown on glass using [$In(S_2CO^iPr)_3$] at 210°C.[64] Hampden-Smith and co-workers have taken the facile elimination of thioacetic anhydride from polyether adducts of group 2 metal thioacetates and applied it to adducts of gallium and indium thioacetates.[65] Two gallium complexes, [$Ga(SCOMe)_2(CH_3)(dmp)$] and [$Ga(SCOMe)_3(dmp)$] (dmp = 3,5-dimethylpyridine),[66] and an ionic complex, $[Hdmp]^+[In(SCOCH_3)_4]^-$ have been employed in aerosol-assisted MOCVD experiments to prepare thin films of the metal sesquisulfides.[67] The respective proposed decomposition pathways for the gallium complexes are shown in Schemes (1.19)-(1.22).

$$2\ Ga(SCOMe)_2(CH_3)(dmp) \longrightarrow 2\ dmpy + [MeC(O)SC(O)Me] + 2(Me_2CO) + Ga_2S_3 \quad (1.19)$$

$$2\ Ga(SCOMe)_3(dmp) \longrightarrow 2\ dmpy + 3[MeC(O)SSC(O)Me] + Ga_2S_3 \quad (1.20)$$

Two step decomposition pathway for indium complex

$$2\ [Hdmp]^+\ [In(SCOMe)_4]^- \longrightarrow 2\ HSOCMe + 2\ (dmp)In(SOMe)_3 \quad (1.21)$$

$$(dmp)In(SOMe)_3 \longrightarrow 2\ (dmpy) + 3[MeC(O)SC(O)Me] + In_2S_3 \quad (1.22)$$

1.3.2.4 Metal complexes of chalocogenophosphinates and iminochalcogenophosphinates as precursors

Diselenophosphinates of indium and gallium complexes have been prepared by O'Brien and co-workers and used as single-source precursors for the deposition of indium selenide, gallium selenide by aerosol assisted chemical vapour deposition.[68] The single crystal structure of indium complex shows the expected tris chelate octahedral geometry. All three diselenophosphinate ligands are chelating to form three 4-membered rings (Se-P-Se-In) with In-Se bond distances of 2.729(6)-2.768(6) Å. In contrast, gallium complex [Ga(^{i}Pr$_2$PSe$_2$)$_3$] has four-coordinate around gallium. The structure consists of one chelating and two pendant di-isopropyldiselenophosphinate ligands in a distorted tetragonal geometry (Fig. 1.9).

Similarly, thin films of hexagonal In_2Se_3 and cubic Ga_2Se_3 were deposited by AACVD and LPCVD using dialkyldiselenoiminophosphinates of indium or gallium [$R_2M(SeP^iPr_2)_2N$] (M = In or Ga; R = Me, Et) as single source precursors.[69] [M(μ-Te)(N(^{i}Pr$_2$PTe)$_2$)]$_3$ (M = In, Ga) have been employed to deposit to prepare M_2Te_3 films onto glass and Si(100) substrate at 325-475 °C.[70] The indium complex gave cubic In_2Te_3 exclusively, whereas the gallium complex yielded mixture of cubic Ga_2Te_3, monoclinic GaTe and hexagonal Te.

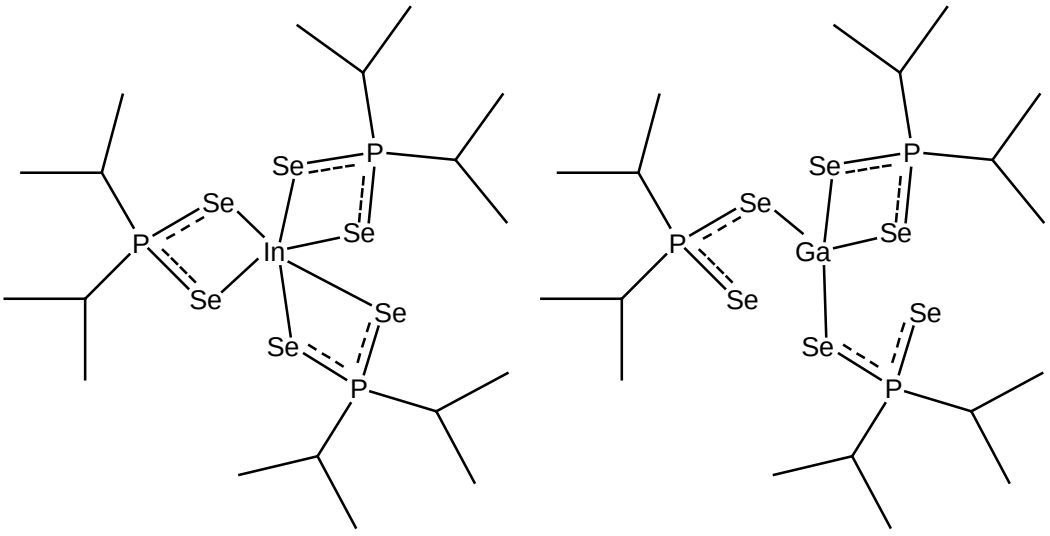

Fig. 1.9 Structures of (a) [In(^{i}Pr$_2$PSe$_2$)$_3$] and (b) [Ga(^{i}Pr$_2$PSe$_2$)$_3$]

1.3.3 Precursors for IV-VI semiconductor materials

Tin and lead chalcogenates are narrow bandgap semiconductor materials. It's only recently that attempts have been made to grow them as thin films from single-source precursors. Cubic PbS thin films have been prepared from lead dithiocarbamates: $[Pb(S_2CNEt_2)_2]$ gave PbS films in the temperature range of 425 - 500°C by LPCVD and in the temperature range of 230-300°C, by remote plasma-enhanced MOCVD.[71] Trindade and O'Brien selected $[Pb(S_2CN^nBu_2)_2]$ to deposit PbS films on glass and (100) Si, in the temperature range of 400-600 °C, in a cold wall, low-pressure MOCVD reactor.[72] Similarly Afzaal *et al.* prepared a series of lead dithiocarbamate complexes of general formula $[Pb(S_2CNRR')_2]$ (R = Me, Et; R' = ^{i}Pr, ^{n}Bu) and used them to deposit cubic PbS films by AA and LPCVD on glass substrates.[73]

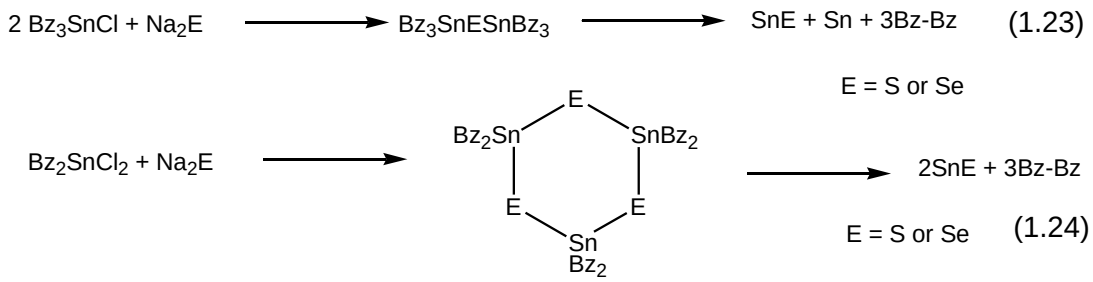

The benzyl-substituted tin chalcogenides $[(R_3Sn)_2S]$, $[R_2SnS]_3$, $[(R_3Sn)_2Se]$ and $[R_2SnSe]_3$ have been synthesized and investigated as single-source precursors to tin sulfide or tin selenide.[74] Compounds were prepared from the corresponding benzyltin chloride and anhydrous sodium chalcogenide, according to Scheme (1.23) and (1.24). Pyrolysis of compounds at 450°C yielded gray or black powders and dibenzyl as the major products. The powders produced were analyzed as SnS and SnSe with some contamination from elemental tin. Solid solutions of the type $Sn(S_xSe_{1-x})$ were prepared by the co-pyrolysis of precursors $[(R_3Sn)_2S]$ and $[(R_3Sn)_2Se]$.

Thin films of SnTe were deposited from $[\{(Me_3Si)_2CH\}_2Sn(\mu\text{-}Te)]_2$ by MOCVD at 400°C. The SnTe films were free of carbon contamination and were crystalline. In contrast, the selenium analogue $[\{(Me_3Si)_2CH\}_2Sn(\mu\text{-}Se)]_2$ was thermally stable and no deposition was observed.[75] Thermal decomposition of $[Ph_2Sn(S_2CN(CH_2)_4)_2]$ and $[Ph_3Sn(S_2CN(CH_2)_4)]$ resulted in the formation of a mixture of orthorhombic Sn_2S_3 and SnS.[76] Similarly APCVD of $[Me_2Sn(S_2CN(C_4H_9)CH_3)]$ and $[BuSn(S_2CN(C_4H_9)CH_3)_3]$ at 350–550°C in the presence of H_2S, afforded SnS and Sn_2S_3 films on glass.[77] In an attempt to develop a mild, low-temperature route to the formation of SnS thin films, the APCVD reaction of $[^nBu_3SnO_2CCF_3]$ with H_2S has been studied. Tin(II) sulfide films were deposited at 350–600°C under nitrogen, and no contamination from fluorine was observed in the resulting films.[78]

1.3.4 Precursors for transition metal chalcogenide materials

Titanium and molybdenum chalcogenide have applications as lubricant coatings, electrode materials or catalysts. TiS_2 and MoS_2 thin films were deposited using $[M(S^tBu)_4]$ as the precursor through conventional hot wall LP-MOCVD. The precursor was heated to 45°C and the substrate in the range 150-270°C for TiS_2 and 110-350°C for MoS_2.[79] Winter *et al.* have prepared TiS_2 and $TiSe_2$ using adducts of titanium tetrachloride with cycloalkanethiols and alkylselenium, $[TiCl_4(HSC_6H_{11})_2]$. The films were grown on silicon and glass substrates in a hot wall reactor using sublimation temperature of 50°C and deposition temperatures in the range 200-600°C. The films were almost exclusively (001)- oriented at 400°C and above.[80] Similarly (001)-oriented $TiSe_2$ films were grown at 500 and 600°C using $[TiCl_4(Se(C_2H_5)_2)_2]$.[81] $[(\eta^5\text{-}C_5H_5)_2Ti(S^tBu)_2]$ and $[(\eta^5\text{-}C_5H_5)_2Ti(SEt)_2]$ have been tested in hot wall LP-MOCVD experiments with helium as the carrier gas, the films had S/Ti atomic ratios in the range of 0.5-1.5, depending on the precursor and deposition temperature which was varied from 400-650°C.[82] Volatile

phosphinochalcogenoic amidato complexes of general formulae $[M(^tBu)_2P(E)NR]_2$ with E = Se, Te, have been prepared for 3-d transition metal elements from chromium to nickel.[83] Thermolysis studies under hot wall LP-MOCVD conditions have resulted in the growth of several metal chalcogenides thin films on glass substrate at 300-400°C. While the tellurides had Te/M atomic ratios equal to 2 ($MnTe_2$, $FeTe_2$, $CoTe_2$), the selenides had Se/M ratios close to equal to 1 ($Cr_{0.68}Se$, MnSe, FeSe, Co_3Se_4, NiSe, Ni_6Se_5). No phosphorus contamination was observed. Thin films of nickel sulfide and palladium sulfide have been prepared from metal complexes of bis(isopropylxanthate) $[M(S_2COCHMe_2)_2]$ (M = Ni or Pd).[84] The precursors were sublimed at 95°C (Ni) and 110°C (Pd) under 10^{-2} Torr and depositions occurred on glass or silicon wafers at 300°C for NiS and 350°C for PdS. Highly oriented rhombohedral γ-NiS and polycrystalline tetragonal PdS films were deposited. Dithiocarbamate complexes of a number of transition metals including Fe, Co, Ni and Cu have been used as precursors for metal sulfide thin films. Nomura *et al.* have grown copper-deficient $Cu_{1.96}S$ films by LP-MOCVD from copper(II) bis(diethyl-dithiocarbamate) $[Cu(S_2CNEt_2)_2]$ using N_2 as the carrier gas with source temperature of 200°C and deposition temperature of 400°C on a silica substrate.[85] The same precursor has been employed in RPECVD experiments to grow Cu_2S films at the deposition temperature range of 200-400 °C under helium.[86] Films deposited on fused silica were a mixture of hexagonal and cubic phases, whereas films grown on silica were in the cubic phase. O'Brien and co-workers have claimed the deposition of high-purity Cu_2S and Cu_2Se thin films from the $[Cu(E_2CN(Me)Hex)_2]$ (E = S or Se) precursors respectively.[87] Pyrite FeS_2 thin films have been deposited using symmetrical and unsymmetrical dialkyl dithiocarbamate complexes of iron $[Fe(S_2CNRR')_3]$ R = Me, ^{n}Bu; R' = ^{i}Pr, ^{n}Bu by AACVD in the temperature range of 375-450°C.[88] Cubic manganese sulfide thin films were deposited from $[Mn(S_2CN(Me)Hex)_3]$ on a glass substrate under an argon flow rate of 200 sccm in the temperature range of 475-500°C.[89] Similarly thin films of cobalt

sulfides were deposited from cobalt complex of methylhexyldithiocarbamate in the temperature range of 375-475°C on glass substrate by AACVD and obtained mixture of $Co_{1-x}S$, CoS_2 and Co_3S_4.[89] O'Brien *et al.* achieved deposition of nickel selenide and nickel phosphide thin films using imido-bis-(diisopropylthioselenophosphinate) of nickel(II), $[Ni(^{i}Pr_2P(S)NP(Se)^{i}Pr_2)_2]$, complex (Fig. 1.10) in the temperature range of 375-475°C by cold wall LP-MOCVD on glass. Nickel phosphide films were deposited in the temperatures between 475 and 425°C. Nickel selenide films were deposited in the temperature between 375 and 400°C.[90]

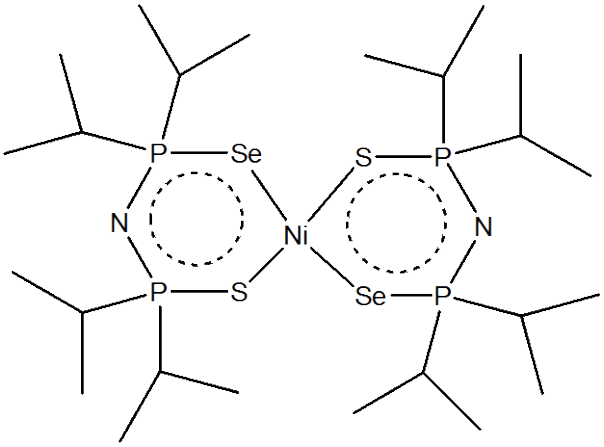

Fig. 1.10 Structure of $[Ni(^{i}Pr_2P(S)NP(Se)^{i}Pr_2)_2]$

1.4 Scope of the present study

The aim of the present investigation is to synthesize new single-source precursors for the deposition of metal sulfide thin films, in order to overcome the difficulties such as solubility, volatility and incorporation of phosphorus impurities in the final products by the use of previously studied precursors. Thio- and dithio-biuret metal complexes have not yet been well studied. There are no reports of their use as single-source precursors for metal sulfide thin films by any methods. Our interest in such ligands led us to synthesise a series of metal complexes with the potential technologically important metals of Co, Ni, Fe, Zn, Cd, In and Cu and use them as single source precursors for the deposition of metal sulfide thin films by CVD.**1.5 References**

1. C. Kittel, *Introduction to solid state physics*, 2002, John Wiley & sons, Inc., Singapore.
2. A. C. Jones, P. O'Brien, *CVD of compound semiconductors: precursor synthesis, development and applications,*1997 Vch: Weinheim, Germany; Cambridge.
3. a) P. O'Brien in: *Inorganic Materials*, 1992, Wiley, Chichester, UK. b) P. O'Brien, *Chemtronics,* 1991, **5**, 61. c) A. C. Jones, P.J. Wright, B. Cockayne, *Chemtronics,* 1988, **3**, 35.
4. a) P. J. Wright, B. Cockayne, A. J. Williams, A. C. Jones, E. D. Orrell, *J. Cryst. Growth.*, 1987, **84**, 552. b) B. Cockayne, P. J. Wright, A. J. Armstrong, A. C. Jones, E. D. Orrell, *J. Cryst. Growth.*, 1988, **91**, 57.
5. a) W. Kuhn, A. Naumov, H. Stanzl, S. Bauer, K. Wolf, H. P. Wagner, W. Gebhardt, U. W. Pohl, A. Krost, W. Richter, U. Dümichen, K. H. Thiele, *J. Cryst. Growth.,* 1992, **123**, 605. b) G. Sato, T. Numai, M. Hoshiyama, I. Suemune, H. Machida, N. Shimoyama, *J. Cryst. Growth.,* 1995, **150**, 734.

6. a) P. J. Wright, P. J. Parbrook, B. Cockayne, A. C. Jones, E. D. Orrell, K. P. O'Donnell, B. Henderson, *J. Cryst. Growth.*, 1989, **94**, 441.
7. T. Cloitre, N. Briot, O. Briot, B. Gil, R. L. Aulombard, *J. Cryst. Growth.*, 1993, **133**, 101.
8. A. C. Jones, S. A. Rushworth, P. J. Wright, B. Cockayne, P. O'Brien, J. R. Walsh*, J. Cryst. Growth.,* 1989, **97**, 537.
9. a) G. E. Coates, D. Ridley, *J. Chem. Soc*., 1965, 1870. b) G. W. Adamson, *Acta Crystallogr. B.,* 1982, **38**, 462.
10. M. A. Malik, M. Motevalli, J. R. Walsh, P. O'Brien, A. C. Jones, *J. Mater. Chem.,* 1995, **5**, 731.
11. a) G. W. Adamson, H. M. M. Shearer, *J. Chem. Soc., Chem. Comm*., 1969, 897. b) D. H. Zeng, M. J. Hampden-Smith, E. N. Duesler, *Inorg. Chem*., 1994, **33**, 5376.
12. a) M. E. Peach, *Can. J. Chem*., 1968, **46**, 2699. b) C. R. Lucas, M. E. Peach, *Inorg. Nucl. Chem. Lett*., 1969, **5**, 73. c) M. E. Peach, *Can. J. Chem.,* 1970, **48**, 1869.
13. I. G. Dance, M. L. Scudder, R. Secomb, *Inorg. Chem*., 1983, **22**, 1794.
14. I. G. Dance, *J. Am. Chem. Soc.,* 1980, **102**, 3445.
15. D.C. Craig, I. G. Dance, R. Garbutt, *Angew. Chem., Int. Ed. Engl*., 1986, **25**, 165.
16. C. C. Landry, L. K. Chetham, J. J. Graham, A. R. Barron, *J. Mater. Res.,* 1991, **1**, 143.
17. M. Bochmann, K. Webb, M. Harman, M. B. Hursthouse, *Angew. Chem. Int. Ed. Engl*., 1990, **29**, 638.
18. M. Bochman, K. J. Webb, M. B. Hursthouse, M. Mazid, *J. Chem. Soc., Dalton Trans*., 1991, 2317.
19. M. Bochman, K. J. Webb, *J. Chem. Soc., Dalton Trans*., 1991, 2325.

20. V. N. Semyonov, E. M. Averbach, L. A. Michalyeva, *Zh.Neorg. Khim*. 1979, **24**, 911.
21. K. V. Kerm, A. O. Tilling, J. A. Varvas, *Proc. Tallinn Tech. Univ.* 1980, **479**, 101.
22. F. Dutault, J. Lahaye, *Bull. Soc. Chim. Fr*., 1979, **5-6**, 145.
23. M. Nardelli, L. Cavalca, M. Braibanti, *Gazz. Chim.Ital*., 1957, **87**, 137.
24. M. Krunks, J. Madarasz, L. Hiltunen, R. Mannonen, E. Mellikov, L. Niinisto, *Acta Chem. Scan.,* 1997, **51**, 294.
25. A. K. Sharma, *Thermochim. Acta*, 1986, **104**, 339.
26. H. P. Klug, *Acta Cryst*., 1966, **21**, 536.
27. M. Bonamico, G. Mazzone, A. Vaciago, L. Zambonelli, *Acta Cryst*., 1965, **19**, 898.
28. H. Miyame, M. Ito, H. Iwasaki, *Acta Cryst*., 1979, **B35**, 1480.
29. A. Domenicano, G. Mazzone, A. Vaciago, L. Zambonelli, *J. Chem. Soc. A.,* 1968, 1351.
30. M. Bonamico, G. Dessy, *J. Chem. Soc. A.,* 1971, 264.
31. M. Motevalli, P. O'Brien, J. R. Walsh, I. M. Watson, *Polyhedron,* 1996, **15**, 2801.
32. A. Saunders, A. Vecht, G. Tyrell, *Chem. Abstr*., 1988, **108**, 66226h.
33. D. M. Frigo, O. F. Z. Khan and P. O'Brien, *J. Cryst. Growth.*, 1989, **96**, 989.
34. M. Chunggaze, J. McAleese, P. O'Brien, D. J. Otway, *Chem. Comm.,* 1998, 833.
35. R. D. Pike, H. Cui, R. Kershaw, K. Dwight, A. Wold, T. N. Blanton, A. A. Wernberg, H. J. Gysling, *Thin Solid Films,* 1993, **224**, 221.
36. R. Nomura, T. Murai, T. Toyosaki, H. Matsuda, *Thin Solid Films,* 1995, **271**, 4.
37. P. O'Brien, J. R. Walsh, I. M. Watson, L. Hart, S. R. P. Silva, *J. Cryst. Growth.,* 1996, **167**, 133.
38. M. B. Hursthouse, M. A. Malik, M. Motevalli, P. O'Brien, *Organometallics,* 1991, **10**, 730.
39. M. B. Hursthouse, M. A. Malik, M. Motevalli, P. O'Brien, *J. Mater. Chem*., 1992, **2**, 949.

40. J. G. Noltes, *Recl. Trav. Chim. Pays-Bas.*, 1965, **84**, 126.
41. M. A. Malik, M. Motevalli, J. R. Walsh, P. O'Brien, *Organometallics,* 1992, **11**, 3136.
42. M. A. Malik, P. O'Brien, *Adv. Mater. Opt. Electron*., 1994, **3**, 171.
43. S. M. Zemskova, E. I. Berus, L. A. Glinskaya, R. F. Klevtsova, S. A. Gromilov, V. B. Durasov, S. V. Larianov, *in Proc. XIII Int. CVD Conf*, Electrochemical Society, Pennington, NJ 1996, Vol.**96-25**, p.267.
44. S. M. Zemskova,S. V. Sysoev, L. A. Glinskaya, R. F. Klevtsova, S. A. Gromilov, S. V. Larianov, in *Proc. XIV Int. CVD Conf. and EUROCVD* 11, Electrochemical Society, Pennington, NJ 1997, Vol.**97-25**, p.1429.
45. J. Cheon, D. S. Talaga, J. I. Zink, *J. Am. Chem. Soc.,* 1997, **119**, 163.
46. M. Nyman, M. J. Hampden-Smith, E. Duesler, *Chem. Vap. Deposition.*, 1996, **2**, 171.
47. M. Nyman, K. Jenkins, M. J. Hampden-Smith, T. T. Kodas, E. N. Duesler, A. L. Rheingold, M. L. Liable-Sands, *Chem. Mater*., 1998, **10**, 914.
48. C. Xu, M. J. Hampden-Smith, T. T. Kodas, *Chem. Mater*., 1995, **7**, 1539
49. Y. Takahashi, R. Yuki, M. Sugiura, S. Motojima and K. Sugiyama, *J. Cryst. Growth.*, 1980, **50**, 491.
50. C. Byrom, M. A. Malik, P. O'Brien and A. White, *Polyhedron*, 2000, **19**, 211.
51. S. L. Lawton and G. T. Kokotailo, *Inorg. Chem*., 1969, **8**, 2410.
52. C. Q. Nguyen, A. Adeogun, M. A. Malik and P. O'Brien, *Chem. Commun*., 2006, 2179.
53. C. Q. Nguyen, A. Adeogun, M. A. Malik and P. O'Brien, *Chem. Commun*., 2006, 2182.
54. M. Afzaal, S. M. Aucott, D. Crouch, P. O'Brien, J. D. Woolins and J. H. Park, *Chem. Vap. Deposition.,* 2002, **8**(5), 187.
55. M. Afzaal, D. Crouch, M. A. Mailk, M. Motevalli, P. O'Brien and Jin-Ho Park, *J. Mater. Chem.*, 2003, **13**, 639.

56. G. G. Briand, T. Chivers and M. Parvez, *Angew. Chem., Int. Ed*., 2002, **41**, 3468.
57. S. S. Garje, J. S. Ritch, D. J. Eisler, M. Afzaal, P. O'Brien and T. Chivers, *J. Mater. Chem*., 2006, **16**, 966.
58. (a) R. Nomura, S. Fujii, K. Kanaya, H. Matsuda, *Polyhedron,* 1990, **9**, 361. (b) R. Nomura, K. Konishi, H. Matsuda, *Thin Solid Films,* 1991, **198**, 339.
59. H. J. Gysling, A. A. Wernberg, *Chem. Mater.* 1992, **4**, 900.
60. A. N. MacInnes, M. B. Power and A. R. Barron, *Chem. Mater*., 1992, **4**, 11.
61. A. N. MacInnes, M. B. Power and A. R. Barron, *Chem. Mater*., 1993, **5**, 1344.
62. P. O'Brien, D. J. Otway, J. R. Walsh, *Chem. Vap. Deposition.,* 1997, **3**, 227.
63. P. O'Brien, D. J. Otway, J. R. Walsh, *Thin Solid Films,* 1998, **315**, 57.
64. V. G. Bessergenev, E. N. Ivanova, Y. A. Kovalevskaya, S. A. Gromiliv, V. N. Kirichenko, S. V. Larionov, *Inorg. Mater*., 1996, **32**, 592.
65. K. Kunze, L. Bihry, P. Atansova, M. J. Hampden-Smith, E. N. Duesler, *Chem. Vap. Deposition.,* 1996, **2**, 105.
66. G. Shang, M. J. Hampden-Smith, E. N. Duesler, *Chem. Commun*. 1996, 1733.
67. G. Shang, K. Kunze, M. J. Hampden-Smith, E. Duesler, *Chem. Vap. Deposition.,* 1996, **2**, 242.
68. C. Q. Nguyen, M. Afzaal, M. A. Malik and P. O'Brien, unpublished result
69. J. H. Park, M. Afzaal, M. Helliwell, M. A. Malik, P. O'Brien, J. Raftery, *J. Chem. Mater*., 2003, **15**, 4205.
70. S. S. Garje, M. C. Copsey, M. Afzaal, P. O'Brien and T. Chivers, *J. Mater. Chem.*, 2006, **16**, 4542.
71. N. I. Fainer, M. L. Kosinova, Y. M. Rumyantsev, E. G. Salman, F. A. Kuznetsov, *Thin Solid Films,* 1996, **280**, 16.
72. T. Trindade, P. O'Brien, *Chem. Vap. Deposition.,* 1997, **3**, 75.
73. M. Afzaal, K. Ellwood, N. L. Pickett, P. O'Brien, J. Raftery and J. Waters, *J. Mater. Chem*., 2004, **14**, 1310.

74. P. Boudjouk, D. J. Seidler, D. Grier, G. McCarthy, *J. Chem. Mater*.,1996, **8**, 1189.
75. P. Boudjouk, M. P. Remington, D. J. Seidler, B. R. Jarabek, D. G. Grier, B. E. Very, R. L. Jarabek, G. McCarthy, J. Mater. Res. Bull. 1999, 34, 2327.
76. D. C. Menezes, G. M. de Lima, A. O. Porto, C. L. Donnici, J. D. Ardisson, A. C. Doriguetto, J. Ellena, *Polyhderon,* 2004, **23**, 2103.
77. A. T. Kana, T. G. Hibbert, M. F. Mahon, K. C. Molloy, I. P. Parkin, L. S. Price, *Polyhedron,* 2001, **20**, 2989.
78. L. S. Price, I. P. Parkin, M. N. Field, A. M. E. Hardy, R. J. H Clark, T. G. Hibbert, K. C. Molloy, *J. Mater. Chem*., 2000, **10**, 527.
79. J. Cheon, J. E. Gozum, G. S. Girolami, *Chem. Mater.,* 1997, **9**, 1847.
80. C. H. Winter, T. S. Lewkebandara, J. W. Proscia, A. L. Rheingold, *Inorg. Chem*., 1993, **32**, 3807.
81. P. J. McKarns, T. S. Lewkebandara, G. P. A. Yap, L. M. Liable-Sands, A. L.Rheingold, C. H. Winter, *Inorg. Chem.,* 1998, **37**, 418.
82. F. Senocq, N. Viguier, A. Gleizes, *Eur. J. Solid State Inorg. Chem.,* 1996, **33**, 1185.
83. M. Bochmann, *Chem. Vap. Deposition.,* 1996, **2**, 85.
84. J. Cheon, D. S. Talaga, J. I. Zink, *Chem. Mater.,* 1997, **9**, 1208.
85. R. Nomura, K. Miyawaki, T. Toyosaki, H. Matsuda, *Chem. Vap. Deposition.,* 1996, **2**, 174
86. Y. M. Rumyantsev, N. I. Fainer, M. L. Kosinova, B. M. Ayupov, N. P. Sysoeva, *J. Phys. IV*, 1999, **9**, 777.
87. P. O'Brien, D. J. Otway, *Chem. Vap. Deposition.,* 1998, **4**, 94.
88. P. O' Brien, D. J. Otway, J. H. Park, *Mat. Res. Soc. Symp. Proc*, 2000, ***606***, 133.
89. F. Srouji, M. Afzaal, J. Waters, P. O'Brien, *Chem. Vap. Deposition*., 2005, ***11***, 91.

90. A. Panneerselvam, M. A. Malik, M. Afzaal, P. O'Brien and M. Helliwell, *J. Am. Chem. Soc.*, 2008, **130**, 2420.

Chapter 2

Iron Sulfide Nanostructured Thin Films*

2.1 Summary

This chapter describes the synthesis of several iron(III) complexes of the 1,1,5,5-tetraalkyl-2-thiobiurets ([$Fe(SON(CN^iPr_2)_2)_3$] (**1**), [$Fe_2(\mu\text{-}OMe)_2(SON(CNEt_2)_2)_2$] (**2**), [$Fe(SON(CNEt_2)_2)_3$] (**3**) and [$Fe(SON(CNMe_2)_2)_3$] (**4**)) and the determination of single crystal X-ray structures of (**1**), (**2**) and (**4**). The magnetic properties of complex (**2**) as a function of temperature and field were studied. Thermogravimetric analysis (TGA) of complexes (**1**)-(**4**) showed the decomposition in one major step to iron sulfide residues. All four complexes were used as single-source precursors for the deposition of iron sulfide thin films by aerosol assisted chemical vapour deposition (AACVD). Complex (**1**) gave hexagonal troilite FeS films with a small amount of tetragonal pyrrhotites $Fe_{1-x}S$ at 300°C, whereas only troilite FeS was deposited at 350, 400 or 450°C. Complexes (**2**) and (**3**) deposited a mixture of hexagonal troilite FeS and cubic pyrite FeS_2 films at all temperatures. Complex (**4**) deposited very thin films of FeS at all temperatures as troilite. Scanning Electron Microscopy (SEM) images of the films deposited from all complexes showed that the morphology consisted of plates, granules, rods and sheet-like crystallites. The size and the shapes of these crystallites were dependent on the growth temperature and the precursor used. This is the first time that iron(III) thio-biuret complexes have been used as single source precursors for iron sulfide thin films.

*Part of the work has been published in *Dalton Trans.,* 2010, **39**, 1460 and *Inorg. Chem.,* 2010, **49**, 8495

2.2 Introduction

Iron sulfides are an interesting class of materials with many different forms, which includes: pyrite (cubic-FeS_2), marcasite (calcium chloride structure-FeS_2), troilite (FeS), mackinawite ($Fe_{1+x}S$), pyrrhotite ($Fe_{1-x}S$, Fe_7S_8), smythite (hexagonal-Fe_3S_4) and greigite (cubic spinel-Fe_3S_4).[1-3] Although there is considerable phase diversity, the situation is less complicated than the related oxides and related hydrolysed species which include: wüstite (FeO), magnetite (Fe_3O_4), haematite (α, β-Fe_3O_2), maghemite (γ-Fe_3O_2), goethite (α-FeOOH), akaganéite (β-FeOOH), lepidocrocite (γ-FeOOH), feroxyhyte (δ-FeOOH) and ferrihydrite ($Fe_5HO_8{\cdot}4H_2O$).[4]

Pyrite is a promising solar cell material because of its very high optical absorption coefficient of ≈ 5 x 10^5 cm^{-1} and useful band gap of 0.95 eV; it is also a cheap and relatively not-toxic material.[5] Its optical absorption coefficient is two orders of magnitude higher than that of crystalline silicon;[6] hence only a thin layer is required in solar cell applications.[7] It has also been used in commercial lithium primary cells,[8,9] high-temperature thermal batteries[10] and has been studied for use in secondary lithium cells.[11] Various methods have been employed to produce different phases of iron sulfide nanoparticles including: high energy mechanical milling combined with mechanochemical processing for FeS and FeS_2,[12] sulfur reducing bacteria for $Fe_{1-x}S$ and Fe_3S_4,[13,14] dendrimer stabilised FeS,[15] the laser pyrolysis of iron complexes for FeS,[16] reverse micelles for FeS_2,[17] solvothermal synthesis of Fe_3S_4,[18] polymer-stabilized wet chemical synthesis of FeS[19] and the decomposition of single source precursors for FeS_2,[20] Fe_3S_4 and Fe_7S_8.[21,22]

Thin films of iron sulfide have also been prepared by the techniques of atmospheric and low-pressure metal-organic chemical vapour deposition AP or LP-MOCVD (FeS_2),[23-26] the sulfurization of iron oxides (FeS_2),[27,28] flash evaporation (FeS_2),[29] ion beam and reactive sputtering (FeS_2),[30] plasma-assisted sulfurization of iron (FeS_2),[31] vapour transport (FeS_2),[32] chemical spray pyrolysis (FeS_2)[33] and

vacuum thermal evaporation (FeS_2).[34] Amongst the methods used, MOCVD is one of considerable potential technological importance. Iron disulfide (FeS_2) thin films were prepared by Schleigh *et al.* using iron pentacarbonyl [$Fe(CO)_5$], hydrogen sulfide and tert-butyl sulfide as precursors by LPCVD.[23] Meester *et al.* also prepared iron disulfide (FeS_2) using iron(III) acetylacetonate, [$Fe(acac)_3$], tert-butyl disulfide and hydrogen.[35] There has been very limited number of iron complexes employed as single-source precursors for the deposition of iron sulfide as $Fe_{1+x}S$, FeS_2 and $Fe_{1-x}S$ thin films, which include: dithiocarbamatoiron complexes [$Fe(S_2CNRR')_3$] (R, R' = Et, Et,[36] Me, ^{i}Pr[37]) and the sulfur-bridged binuclear iron carbonyl complex [$Fe_2(CO)_6(\mu\text{-}S_2)$].[38]

To the best of our knowledge there are no reports for the use iron thio-biuret complexes as a single source precursor for the preparation of iron sulfide thin films or nanoparticles. In this chapter the synthesis of four iron(III) complexes with 1,1,5,5-tetraalkyl-2-thiobiuret (R = methyl, ethyl and isopropyl) and the single crystal X-ray structures of complexes (**1**), (**2**) and (**4**) and their use as single source precursors for the deposition of iron sulfide (FeS and FeS_2) thin films by AACVD are reported

2.3 Experimental

2.3.1 Synthesis of [Fe(SON(CN^{i}Pr$_2$)$_2$)$_3$] (1)

A solution of di-*iso*-propylcarbamoyl chloride (1.0 g, 6 mmol) and sodium thiocyanate (0.49 g, 6 mmol) in acetonitrile (25 mL) was heated to reflux with continuous stirring for 1 h, during which time a fine precipitate of sodium chloride formed. To the cooled reaction mixture was added di-*iso*-propylamine (1.49 mL, 12 mmol) followed by stirring for 30 min and addition of methanolic solution (10 mL) of iron nitrate (0.82 g, 2 mmol). The crude product was precipitated as red powder and recrystallized from tetrahydrofuran to give shiny red needles which were identified

as (**1**). Yield 0.95 g (15 %), mpt: 160 °C, IR (ν_{max} /cm^{-1}): 2956(w), 1494(s), 1425(s), 1353(s), 1278(s), 1142(s), 1060(s), 1038(s). Elemental analysis: Calc. for $C_{42}H_{84}N_9S_3O_3Fe$: C, 55.1; H, 9.1; N, 13.7; S, 10.5; Fe, 6.1 %. Found: C, 54.8; H, 8.9; N, 13.2; S, 9.9; Ni, 5.9 %.

2.3.2 Synthesis of $[Fe_2(\mu\text{-}OMe)_2(SON(CNEt_2)_2)_2]$ (2)

The above procedure was used to prepare (**2**) but used diethylamine (1.26 mL, 12 mmol) and obtained dark brown crystals of (**2**). Yield 0.80 g, (11 %) Mpt: 140 °C, IR (ν_{max} /cm^{-1}): 2974(w), 2925(w), 1503(m), 1470(s), 1417(s), 1397(s), 1350(s), 1253(s), 1123(m), 1076(s), 1040(s). Elemental analysis: Calc. for $C_{42}H_{66}N_{12}S_4O_6Fe_2$: C, 46.9; H, 6.1; N, 15.6; S, 11.9; Fe, 10.4 %. Found: C, 46.5; H, 6.4; N, 15.3; S, 11.4; Fe, 10.2 %.

2.3.3 Synthesis of $[Fe(SON(CNEt_2)_2)_3]$ (3)

The procedure for (**1**) was used to prepare (**3**) but used excess diethylamine (3.78 mL, 36 mmol) and obtained dark red powder of (**3**). Yield 1.20 g, (25 %) Mpt: 131 °C, IR (ν_{max} /cm^{-1}): 2971(w), 2929 (w), 1497(s), 1424(s), 1396(s), 1349(s), 1254 (s), 1125(s), 1075(s), 1048(s). Elemental analysis: Calc. for $C_{30}H_{60}N_9S_3O_3Fe$: C, 45.3; H, 7.5; N, 15.8; S, 24.1; Fe, 7.0 %. Found: C, 45.1; H, 7.7; N, 15.4; S, 23.7; Fe, 7.2 %.

2.3.4 Synthesis of $[Fe(SON(CNMe_2)_2)_3]$.4/3 THF (4) and $[Fe(SON(CNMe_2)_2)_3]$ (4a)

The process for (**1**) was followed but using dimethylamine in water (0.92 mL, 12 mmol) and followed by recrystallisation from THF gave a dark red powder of (**4**). Yield 0.82 g, (19 %) Mpt: 155 °C, IR (ν_{max} /cm^{-1}): 2851(w), 1529(s), 1465(s), 1378(s), 1341(s), 1192(m), 1112(s), 1022(s). Elemental analysis: Calcd. for $C_{23.33}H_{46.67}N_9S_3O_{4.33}Fe$: C, 41.4; H, 6.9; N, 18.6; S, 14.2; Fe, 8.2 %. Found: C, 40.8; H, 6.5; N, 18.2; S, 13.5; Fe, 8.5 %.

The same experiment with dimethylamine in methanol (0.92 mL, 12 mmol) instead of water gave a dark red powder (**4a**). Yield 0.61 g, (17 %) MPt: 148 °C, IR (ν_{max} /cm^{-1}): 2851(w), 1529(s), 1465(s), 1378(s), 1341(s), 1192(m), 1112(s), 1022(s). Elemental analysis: Calcd. For $C_{18}H_{36}N_9S_3O_3Fe$: C, 37.3; H, 6.2; N, 21.8; S, 16.6; Fe, 9.6 %. Found: C, 37.1; H, 6.4; N, 21.1; S, 16.3; Fe,9.3 %.

2.4 Results and discussion

The reaction of di-*iso*-propylcarbamoyl chloride, sodium thiocyanate and di-*iso*-propyl amine followed by addition of a methanolic solution of iron(III) nitrate gave a red crystalline powder of complex (**1**), whereas the same reaction with diethyl

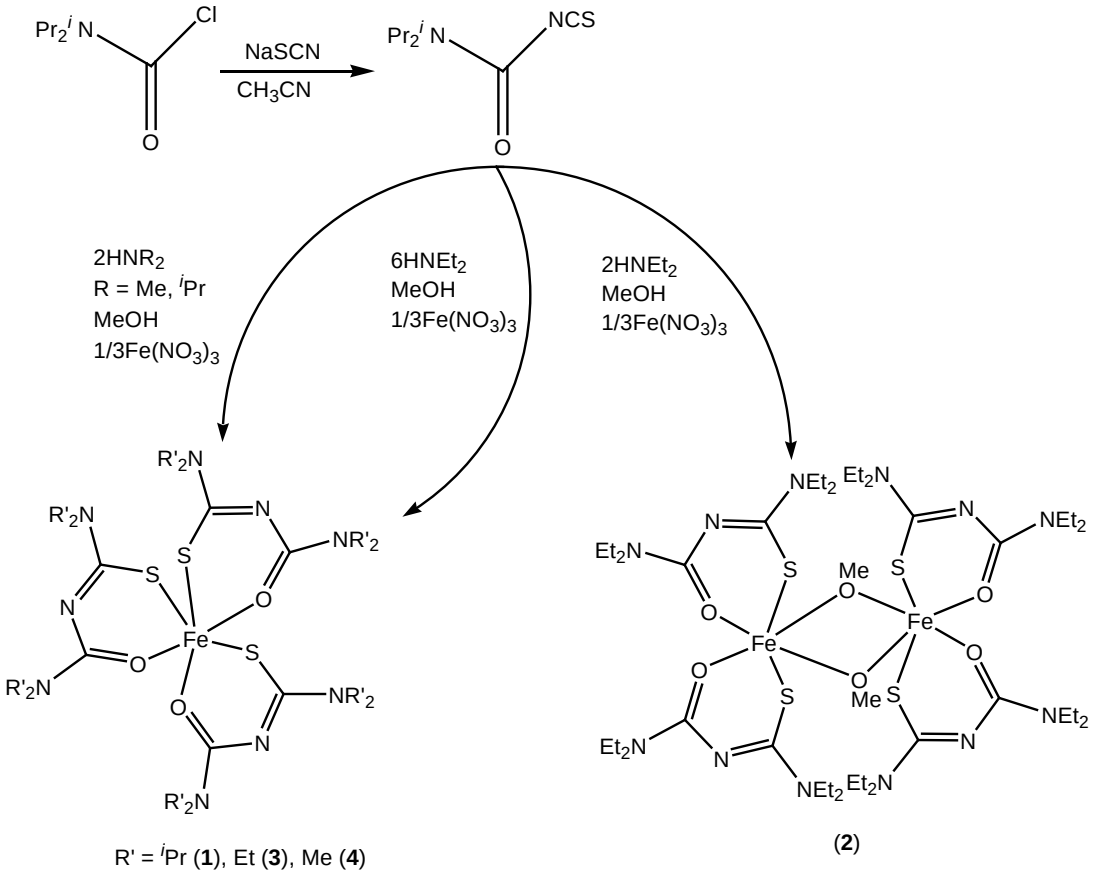

Scheme. 2.1 Schematic representation of synthesis of ligands and complexes

Amine gave dark brown crystals of complex (**2**). Similarly, the reaction with an excess of diethylamine gave a dark red powder of complex (**3**). Complex (**4**) was isolated as powder after evaporation of solvent. A representation of the syntheses is

given in Scheme 2.1. All four complexes are low melting solids, air and moisture stable for several weeks. Complexes (**1**)-(**4**) are soluble in most organic solvents (toluene, tetrahydrofuran, chloroform and dichloromethane) which makes them suitable for the AACVD. The synthesis of complex (**2**) was repeated many times under varying reaction conditions; for example, the addition of water and /or using twice as much diethylamine in the reaction mixture did not stop the methoxy-bridged compound from forming. However, when the reaction was carried out with three-fold excess of diethylamine the monomer formed, but all attempts to crystallize this complex for X-ray single crystal studies were unsuccessful. The reason for this unusual but reproducible behaviour are not at this time clear to us.

2.4.1 Single crystal X-ray structure of $[Fe(SON(CN^{i}Pr_2)_2)_3]$ (1)

The single crystal X-ray structure of complex (**1**) (Fig. 2.1) shows the iron(III) ion in distorted octahedral environment with S_3O_3 donor set. The donor atoms, three sulfur and oxygen atoms, are in a facial arrangement. The *fac*-isomer is statistically preferred and often predominates in systems of this type with S_3O_3 sets at iron(III).[40,41] The bite angles of O1-Fe1-S1, O2-Fe1-S2 and O3-Fe1-S3 are 86.54(5), 86.40(5) and 85.90(5) indicate a distorted octahedron geometry on iron(III). Each thiobiuret ligand chelates to form three six membered rings (NC_2OS-Fe) with Fe-S bond distances ranging from 2.412(8) to 2.418(8) Å and Fe-O bond distances ranging from 1.972(2) to 1.986(2) Å. This is somewhat longer than the bond length of M-S and M-O observed for cobalt and nickel complexes of same ligand.[39] Structure refinement data are given in Table A1 and selected bond lengths and angles given in caption to Fig. 2.1

2.4.2 Single crystal X-ray structure of $[Fe_2(\mu\text{-}OMe)_2(SON(CNEt_2)_2)_2]$ (2)

The complex crystallizes in the monoclinic space group $P2_1/c$. Each iron ion is chelated by two bidentate ligands and bridged by two methoxide ions and is in distorted octahedral coordination with an S_2O_4 donor set. The two sets of ligands

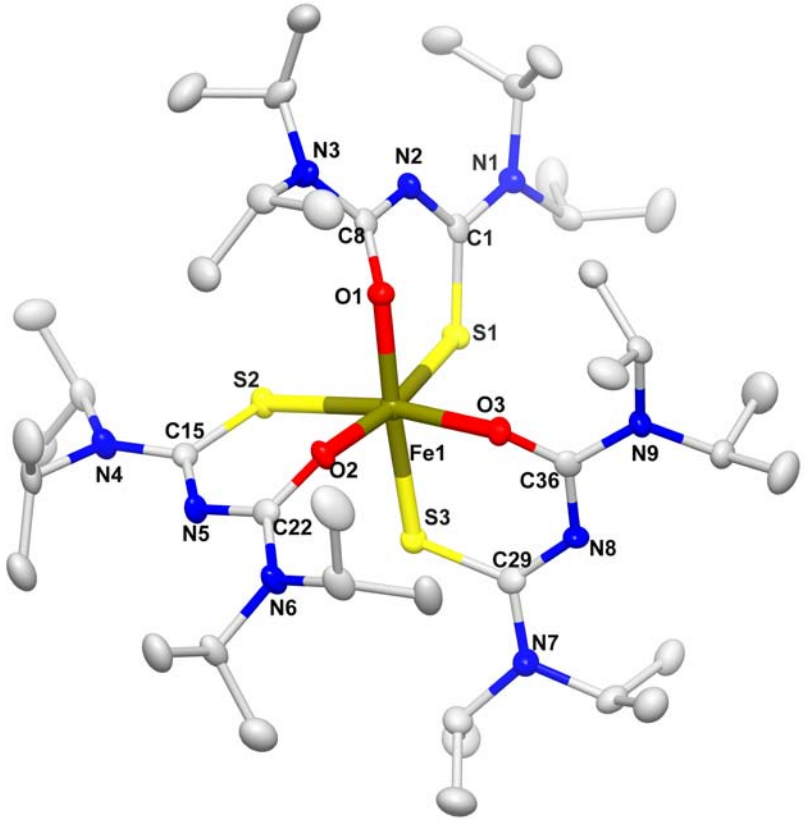

Fig. 2.1 Single crystal X-ray structures of [Fe(SON(CN^{i}Pr$_2$)$_2$)$_3$] (**1**): Selected bond lengths (Å) and bond angles (°) Fe(1)-O(1) 1.986(2), Fe(1)-O(2) 1.979(2), Fe(1)-O(3) 1.972(2), Fe(1)-S(1) 2.418(8), Fe(1)-S(2) 2.416(8), Fe(1)-S(3) 2.412(8), O(1)-C(8) 1.276(3), S(3)-C(29) 1.746(3), O(3)-Fe(1)-S(3) 85.90(5), C(1)-N(2)-C(8) 123.8(2), O(1)-C(8)-N(2) 126.3(2).

coordinated to each iron(III) are *trans*. Within each of the two thiobiuret ligands, the four atoms of the urea or thiourea groups are close to being coplanar. Both thiobiuret ligands on each unit are chelating to form two six membered rings (NC_2OS-Fe) with Fe-S bond distances ranging from 2.424(8) to 2.450(9) Å and Fe-O bond distances ranging from 1.993(2) to 2.011(2) Å. The Fe1-O3 distance 1.988(2) Å is similar to that for [$Fe_2(\mu$-$OCH_3)_2(HL)_4$] (where H_2L is 2-salicyloylhydrazono-1,3-dithiolane) (1.974(2) Å) reported.[42] The pattern of bond distances in all four ligands indicates that the formal negative charge is predominantly localized on the S atom. The relatively long C-S and short C-O average bond lengths of 1.753(8) and 1.282(3) Å are consistent with mostly single and double–bond character, respectively, and this bond localization is also reflected

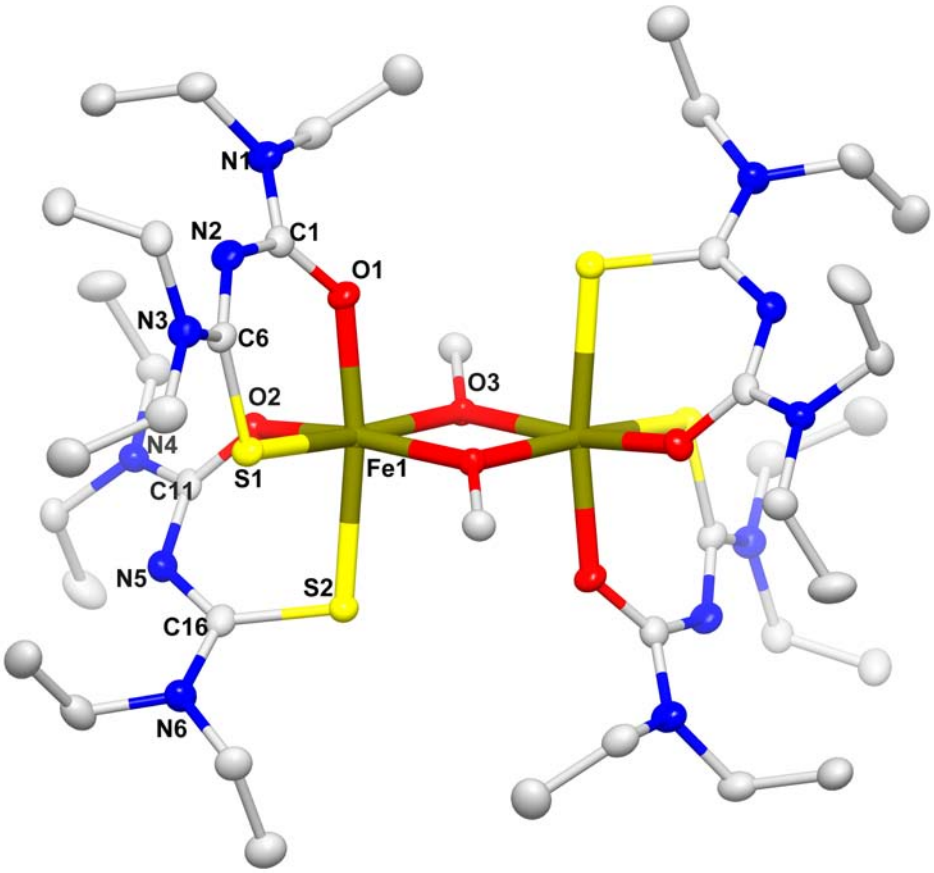

Fig. 2.2 Single crystal X-ray structures of $[Fe_2(\mu\text{-}OMe)_2(SON(CNEt_2)_2)_2]$ (**2**), Selected bond lengths (Å) and bond angles (°) Fe(1)-O(1) 1.993(2), Fe(1)-O(3) 1.988(2), Fe(1)-S(1) 2.424(8), S(1)-C(6) 1.753(3), O(3)-Fe(1)-O(1) 100.94(8), O(3)-Fe(1)-S(1) 94.85. Unlabeled atoms are symmetrically related to labeled atoms.

in the average C-N bond distances to the central N2 atom: 1.323(4) Å in the (iso)thiourea group and 1.336(4) Å in the urea group (Fig 2). Structure refinement data are given in Table A1 and selected bond lengths and angles given in caption to Fig. 2.2

2.4.3 Single crystal X-ray structure of $[Fe(SON(CNMe_2)_2)_3]$ (4) and $[Fe(SON(CNMe_2)_2)_3]$ (4a)

The Single crystal X-ray structure of complex (**4**) reveals a distorted octahedral geometry at iron(III) ion through three sulfur and three oxygen atoms of the thiobiuret ligands (Fig. 2.3). The complex crystallizes in two forms depending on the method of synthesis and recrystallisation. Orthorhombic crystals (*Pna2*(1)) of

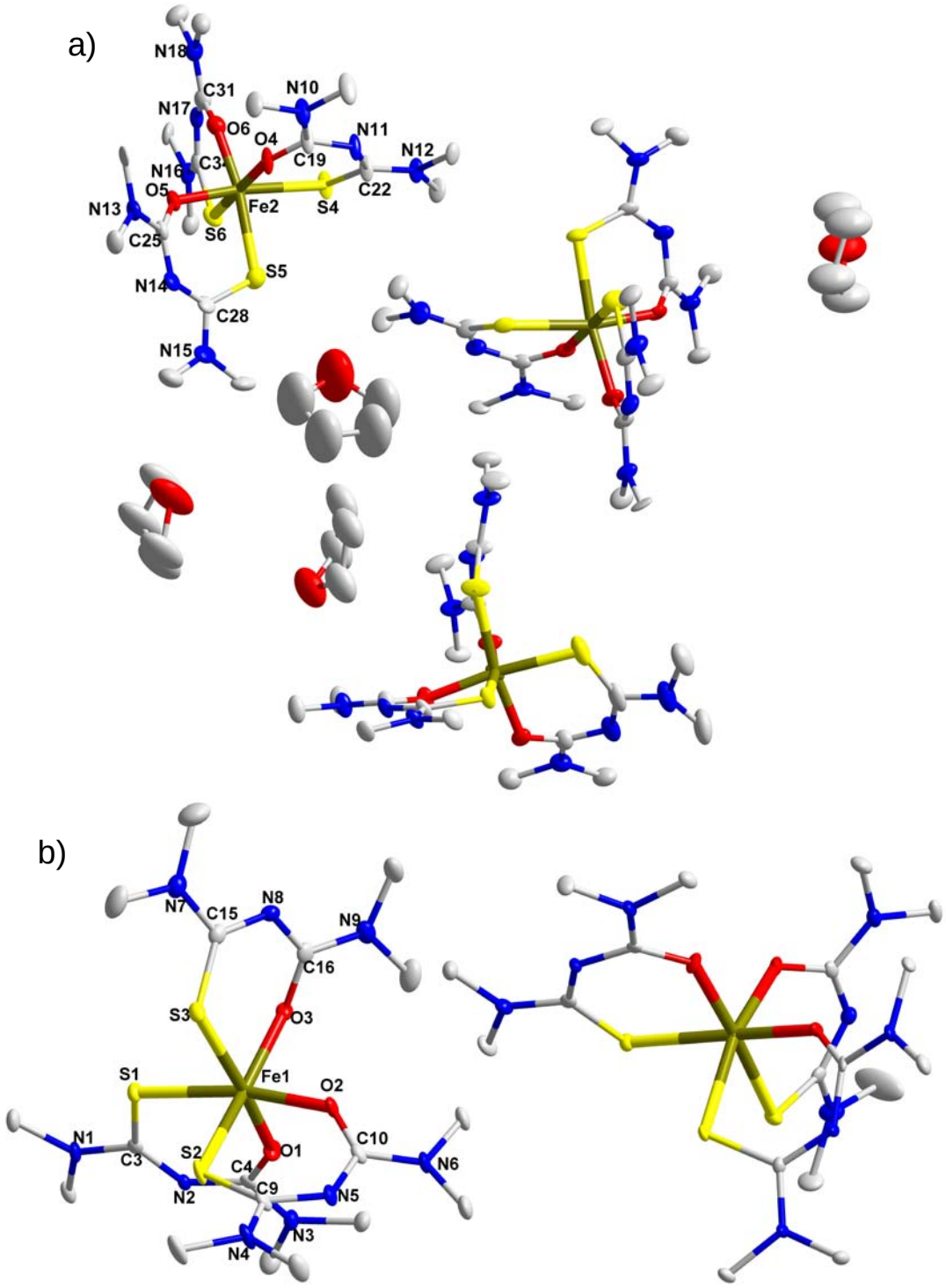

Fig. 2.3 Single crystal X-ray structures of $[Fe(SON(CNMe_2)_2)_3]$ (**4**). a) Orthorhombic system, selected bond lengths (Å) and bond angles (°): Fe(1)-O(1) 1.990(1), Fe(1)-O(3) 2.053(1), Fe(1)-S(1) 2.421(5), S(1)-C(4) 1.700(2), O(1)-Fe(1)-S(1) 85.5(3), C(1)-N(1)-C(2) 119.6(1). b) Tetragonal system, selected bond lengths (Å) and bond angles (°): Fe(1)-O(1) 1.961(1), Fe(1)-O(3) 2.018(9), Fe(1)-S(1) 2.413(3), S(1)-C(3) 1.729(9), O(1)-Fe(1)-S(1) 86.5(2), C(3)-N(1)-C(1) 123.0(8).

$[Fe(SON(CNMe_2)_2)_3].4/3THF$ (**4**) were obtained when the reaction carried was out using dimethylamine in water followed by recrystallisation from tetrahydrofuran. In this form three molecules of the complex were present in the unit cell along with four molecules of tetrahydrofuran solvent. Whereas tetragonal crystals (P4/n) of $[Fe(SON(CNMe_2)_2)_3]$ (**4a**) were obtained when the reaction was carried out using dimethylamine in methanol instead of water. There are no significant differences in atomic separations between complexes (**4**) or (**4a**) and complex (**1**). Structure refinement data are given in Table A2 and selected bond lengths and angles given in caption to Fig. 2.3.

2.4.4 Thermogravimetric analysis (TGA)

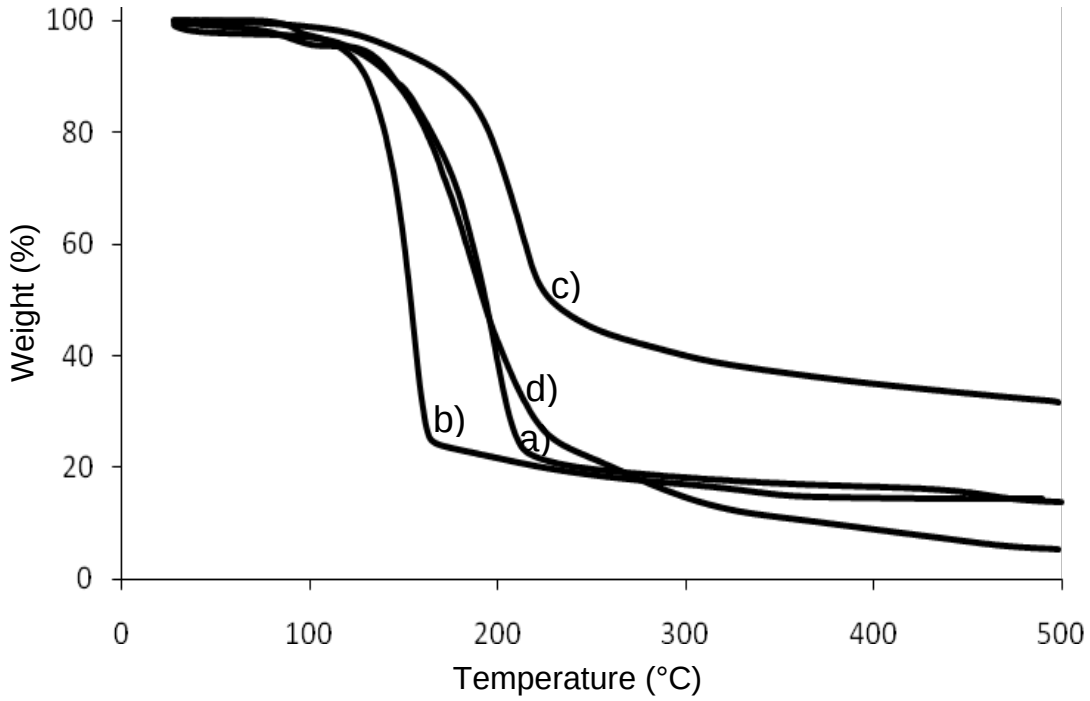

Fig. 2.4 Thermogravimetric analysis (TGA) of complexes (a) $[Fe(SON(CN^iPr_2)_2)_3]$ (**1**), (b) $[Fe_2(\mu\text{-}OMe)_2(SON(CNEt_2)_2)_2]$ (**2**), (c) $[Fe(SON(CNEt_2)_2)_3]$ (**3**) and (d) $[Fe(SON(CNMe_2)_2)_3]$ (**4**)

Thermogravimetric analysis (TGA) provides an understanding of the decomposition process and the volatility of the complexes. TGA of the complexes $[Fe(SON(CN^iPr_2)_2)_3]$ **(1),** $[Fe(SON(CNEt_2)_2)_3]$ **(3)** and $[Fe(SON(CNMe_2)_2)_3]$ **(4)**

indicates single step decomposition with a rapid weight loss between 128-208 °C, 117-312 °C and 113-309 °C respectively (Fig. 2.4). The solid decomposition residue amounts to 20.0 % for (**1**) which is in fair agreement with the calculated value of 22.7% for Fe_2S_3. Similarly the observed final residue of 27.1 for (**3**) is in agreement with the calculated value of 27.7 for Fe_2S_3 and the weight of final residue is 13.0 % for (**4**) close to the calculated value of 15.0% for FeS. Whereas complex (**2**) decomposes in two steps with rapid weight losses at temperatures between 117-195 °C and 195-245 °C. The weight loss of 5.9 % in first step is in good agreement with that calculated for two units of methoxides (6.0%). The remaining residue amounts to 17.2 % which is close to calculated value of 18.9 % for Fe_2S_3.

2.4.5 Magnetic measurement on the $[Fe_2(\mu\text{-}OMe)_2(SON(CNEt_2)_2)_2]$ (2)

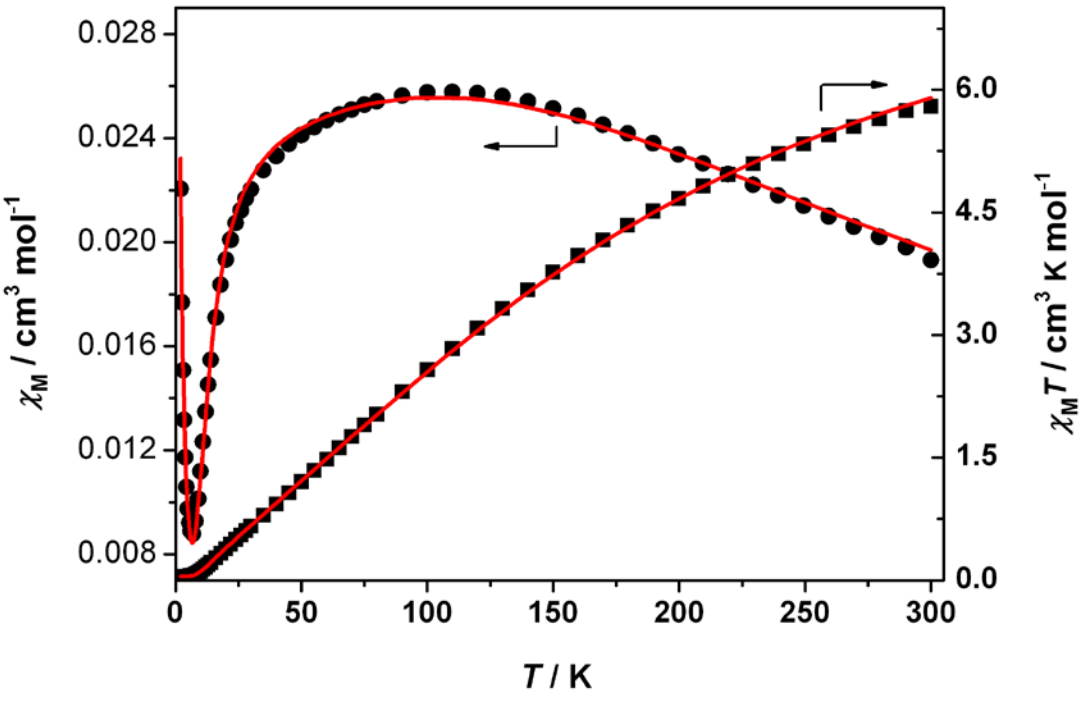

Fig. 2.5 χ_M (circles) and $\chi_M T$ (boxes) as a function of temperature for complex (**2**). Full line corresponds to the fit of the $\chi = f(T)$ curve and to the corresponding $\chi_M T$ product

The investigation of the magnetic properties of a polycrystalline sample of compound (**2**), which is a di-μ-methoxo bridged iron(III) dinuclear complex, over the

temperature range 1.8 – 300 K under applied magnetic fields of 1, 5 and 10 kOe. The temperature dependence of χ_M and $\chi_M T$ (where χ_M represents the molar magnetic susceptibility) of (**2**) recorded with a magnetic field of 1 kOe is presented in Fig. 2.5. The $\chi_M T$ value at room temperature is 5.79 cm^3 K mol^{-1}, which is well below the spin-only value of 8.75 cm^3 K mol^{-1} (assuming g = 2) expected for two non-interacting high-spin Fe(III) metal ions. Upon cooling, the $\chi_M T$ product decreases continuously down to almost zero (0.03 cm^3 K mol^{-1} at 1.8 K). This indicates relatively strong antiferromagnetic coupling between metal centers, leading to a diamagnetic (S = 0) spin ground state. And indeed, the susceptibility curve reaches a maximum value of 0.026 cm^3 mol^{-1} at 100 K, and decreases upon further cooling to approach zero (χ_M = 0.0087 cm^3 mol^{-1}) at 7 K. Below 7 K, however, the susceptibility curve increases again to reach 0.022 cm^3 mol^{-1} at 1.8 K, suggesting the presence of a small amount of paramagnetic impurity. In order to quantify the intramolecular antiferromagnetic coupling between the two iron(III) centers, the experimental susceptibility data were analysed by means of the Van-Vleck equation **(1):**[45]

$$\chi_M = \frac{2Ng^2\beta^2}{k_B T}\frac{e^x + 5e^{3x} + 14e^{6x} + 30e^{10x} + 55e^{15x}}{1 + 3e^x + 5e^{3x} + 7e^{6x} + 9e^{10x} + 11e^{15x}}(1-\rho) + \frac{35Ng^2\beta^2}{6k_B T}\rho$$

(where x = $2j$ / k_BT), **(1)**

which is derived from the spin Hamiltonian $H = -2JS_{Fe1}S_{Fe2} + g\beta HS$, where J is the exchange coupling parameter, ρ represents the proportion of a paramagnetic impurity considered to be an uncoupled Fe(III) species (S_{impur} = 5/2), and the spin operator S is defined as $S = S_{Fe1} + S_{Fe2}$. The least-squares fitting to equation **(1)** leads to J = -13.32 cm^{-1}, g = 2.04, ρ = 0.005, with an excellent reliability factor of 7.8 x 10^{-6}, defined as $R(\chi_M) = \Sigma(\chi_M^{obs} - \chi_M^{calc})^2/\Sigma(\chi_M^{obs})^2$. Same set of parameters reproduce very well the $\chi_M T$ data plotted in Fig. 2.5. The negative sign of J confirms

the occurrence of antiferromagnetic interactions in this compound. The size of the exchange coupling constant is in good agreement with the values reported in the literature for di-μ-methoxo bridged diiron(III) complexes with similar structural features.[44]

2.4.6 The AA-CVD deposition of iron sulfide thin films from [Fe(SON(CN^{i}Pr$_2$)$_2$)$_3$] (1)

Deposition was carried out on glass substrates and heated to temperatures in the range 300-450°C at intervals of 50°C, with an argon flow rate of 160 sccm.

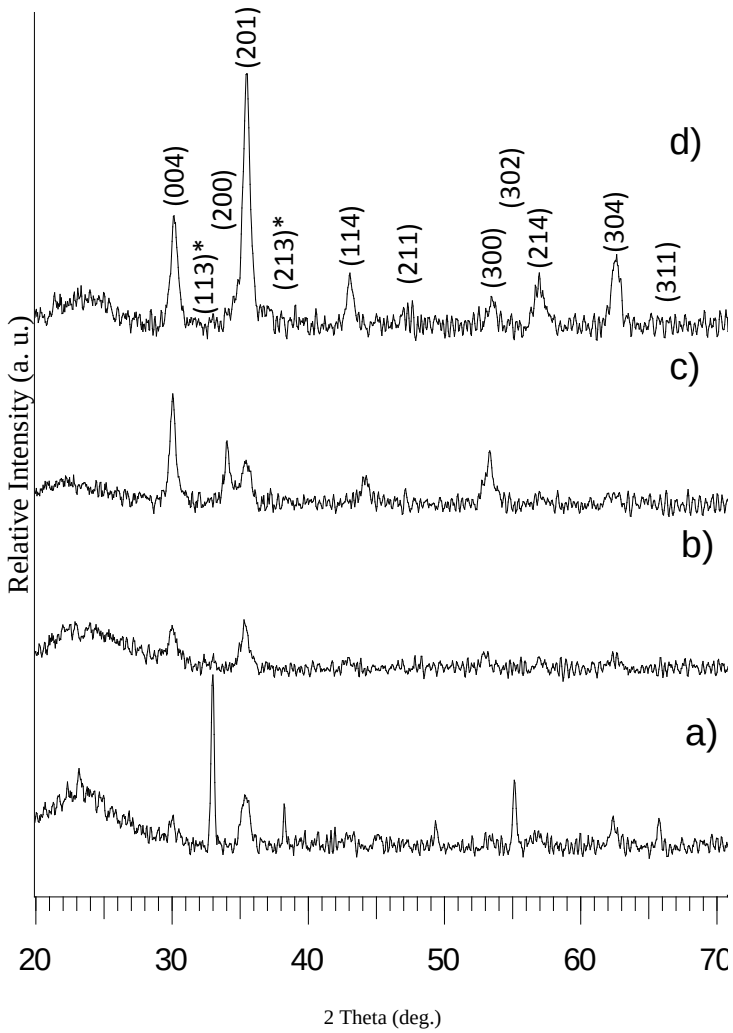

Fig. 2.6 Powder X-ray diffraction of troilite (FeS) thin films deposited from [Fe(SON(CN^{i}Pr$_2$)$_2$)$_3$] (**1**) on glass at a) 300 b) 350 c) 400 and d) 450 °C, (*) symbol denotes the pyrrhotite

No deposits were obtained below 300 °C. Reflective dark brown uniform films were deposited at 300 and 350 °C and black uniform films were obtained at 400 and 450°C. The PXRD pattern of the deposited films at 300- 450°C (Fig. 2.6), show films of hexagonal troilite-2H FeS (ICDD No: 037-0477) with a smaller amount of tetragonal pyrrhotite $Fe_{1-x}S$ (ICDD No: 024-0079). At the lowest deposition temperature (300 °C) the diffraction pattern of hexagonal troilite-2H planes of (112), (200), (302) and (304) were dominant along with peak at 38.9*(2θ)* corresponding to (213) plane of tetragonal pyrrhotite. At the higher deposition temperature 450°C diffraction peaks of (004), (201), (114), (214) and (304) planes from troilite become dominant. The X-ray photoelectron spectra from the thin film deposited at 400 °C show both unoxidized and oxidized forms of iron sulfide. The binding energy of Fe 2p 3/2 peak is fitted with two components iron oxide at 710.8 eV and iron sulfide at 707 eV. The peaks at 161.3 eV can be attributed to S 2p as sulfide and at 168 eV can be sulfur as sulfate.[44]

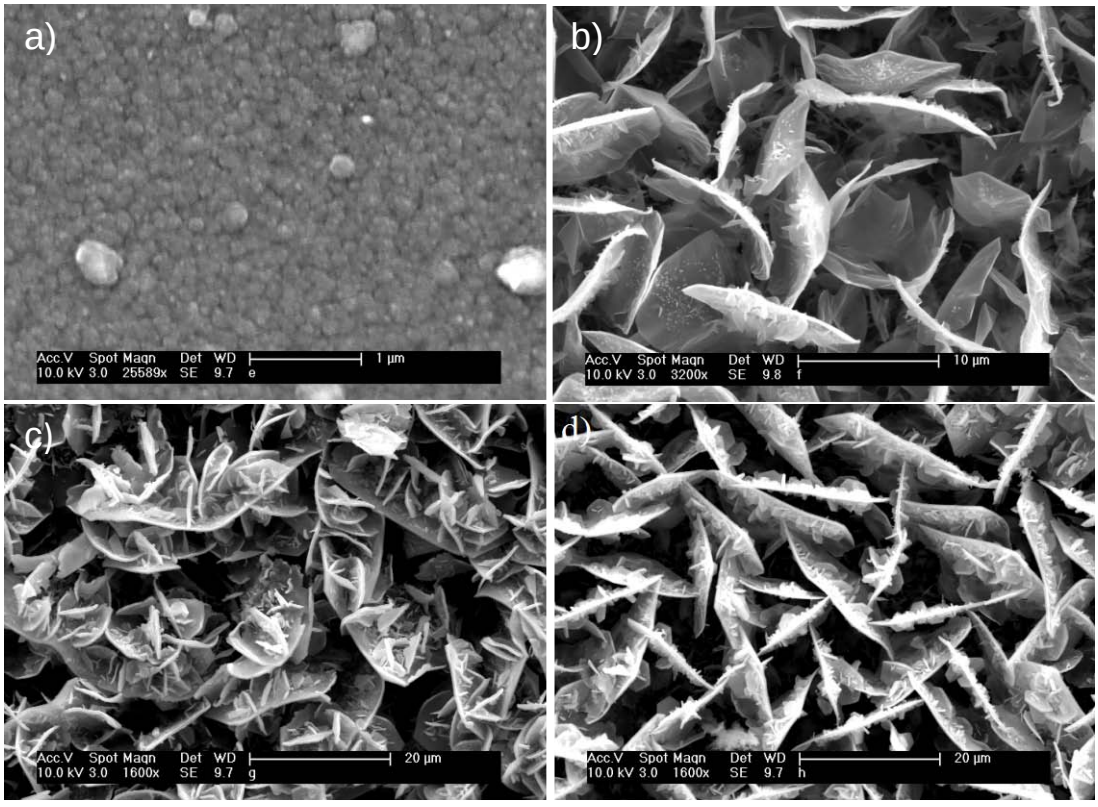

Fig. 2.7 SEM images of iron sulfide (FeS) films deposited from $[Fe(SON(CN^{i}Pr_2)_2)_3]$ (**1**) on glass at a) 300 b) 350 c) 400 and d) 450 °C

The presence of oxides is expected because of handling the sample in open atmosphere. The presence of unoxidized iron sulfide suggests that the oxide is likely covered only to the film surface with a thickness less than Fe 2p and S 2p electron escape depths (< 2 nm). The SEM images in Fig. 2.7, show that the growth of smaller individual granular crystallites (size 300-400 nm) at 300 °C and layer like crystallites at 350 °C whereas plates of crystallites (size 20–25 µm) were formed at 400 and 450 °C. EDX analysis shows that the films are composed of iron: sulfur 51: 49 (300 °C), 52: 48 (350 °C), 55: 45 (400 and 450 °C).

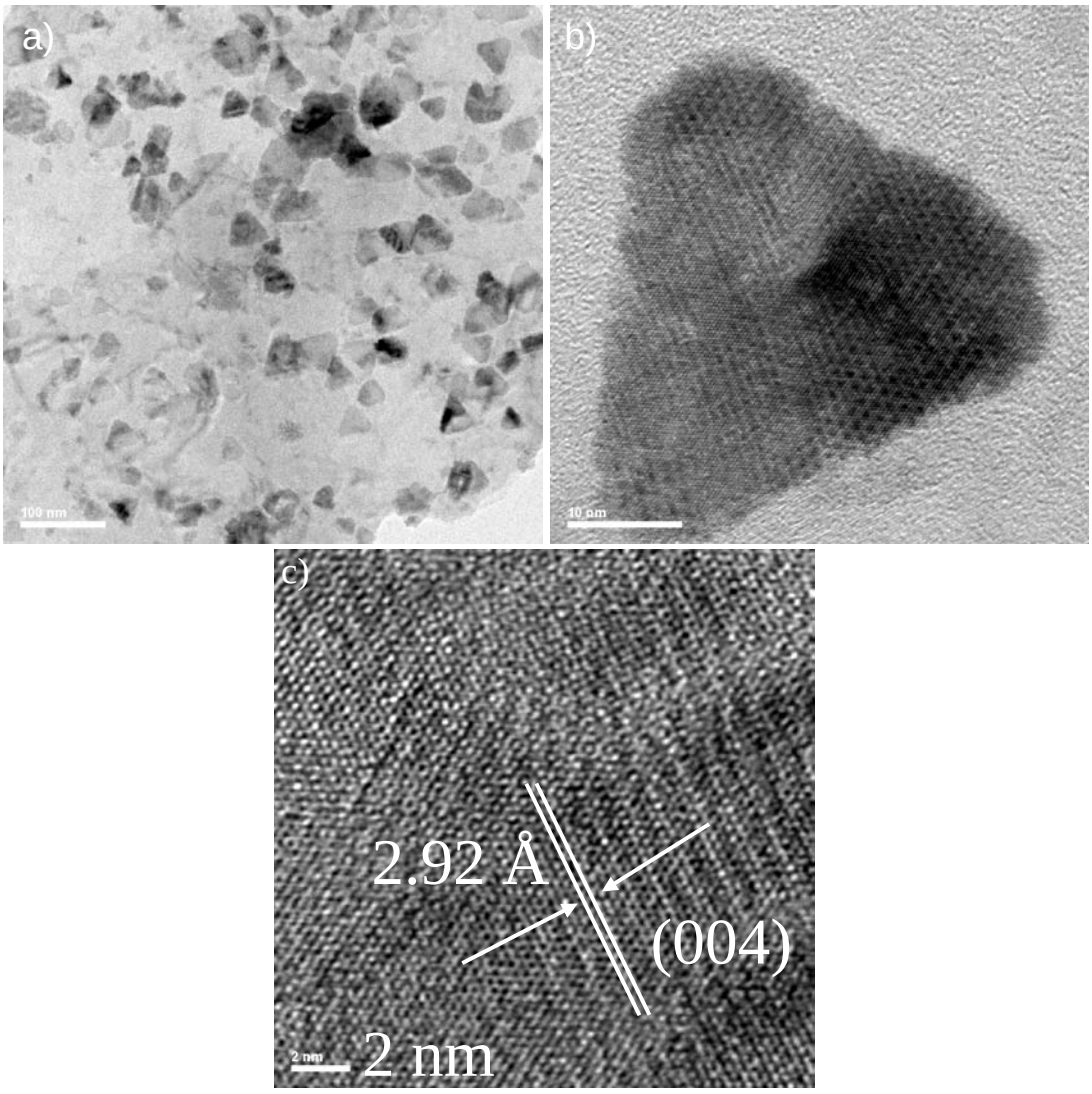

Fig. 2.8 a) Lower b) higher magnification TEM images of the FeS thin films deposited from [Fe(SON(CN^{i}Pr$_2$)$_2$)$_3$] (**1**) at 400 °C c) HRTEM image

The Fe:S ratio is closer to 1:1 in the films deposited at 300 °C. Further insight into the morphology and microstructure of the films was gained by TEM. The TEM images from the scratched sample of films grown at 400 °C show that the films consist of trigonal plates with the size ranging from 35-45 nm, and also clearly exhibits the primary trigonal structures attached together towards the regular manner to form secondary bigger crystallites (Fig. 2.8(a)). The higher magnified TEM image in Fig. 2.8(b) shows smaller trigonal crystallites with the size of 2-3 nm self assembling to form trigonal crystals of larger size.

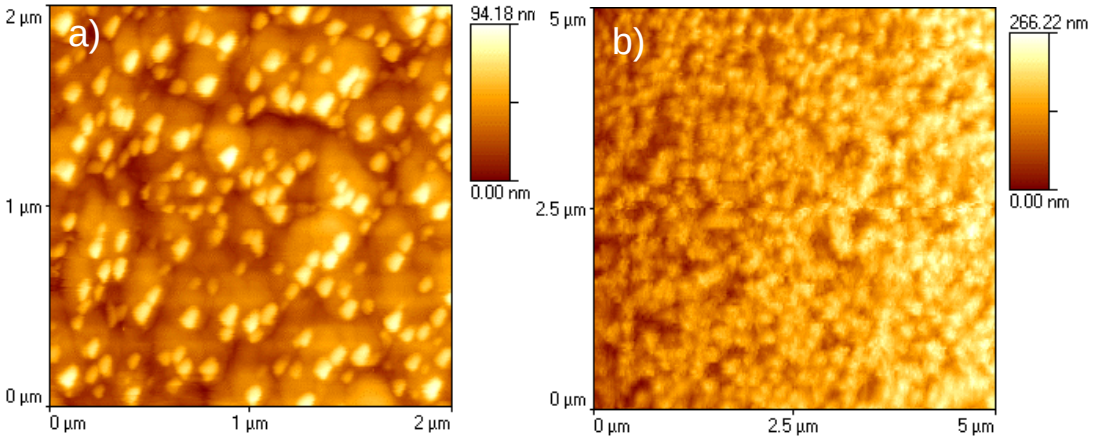

Fig. 2.9 2D-AFM images a) FeS deposited at 300 °C from $[Fe(SON(CN^{i}Pr_2)_2)_3]$ (**1**), b) FeS deposited at 350 °C from $[Fe_2(\mu\text{-}OMe)_2(SON(CNEt_2)_2)_2]$ (**2**)

HRTEM image of the trigonal plates (Fig. 2.8(c)) shows the lattice fringes with a d-spacing 0.29 nm corresponding to (004) reflection of hexagonal FeS. The surface topography of the films analysed by 2D-AFM image (Fig. 2.9(a)) of films deposited at 300 °C shows well interconnected globular crystallites. The average roughness value ranged from 16 to 26 nm from the films deposited at 300 to 450 °C. The increase in surface roughness with increasing deposition temperature is associated with increase of grain size. As the grain grew bigger, the density of grain boundaries decreased and the grain growth took place with a large variation in the height of the grain on the film surface. Therefore it is apparent that the deposition temperature of the films changes the grain sizes as well as the surface roughness.

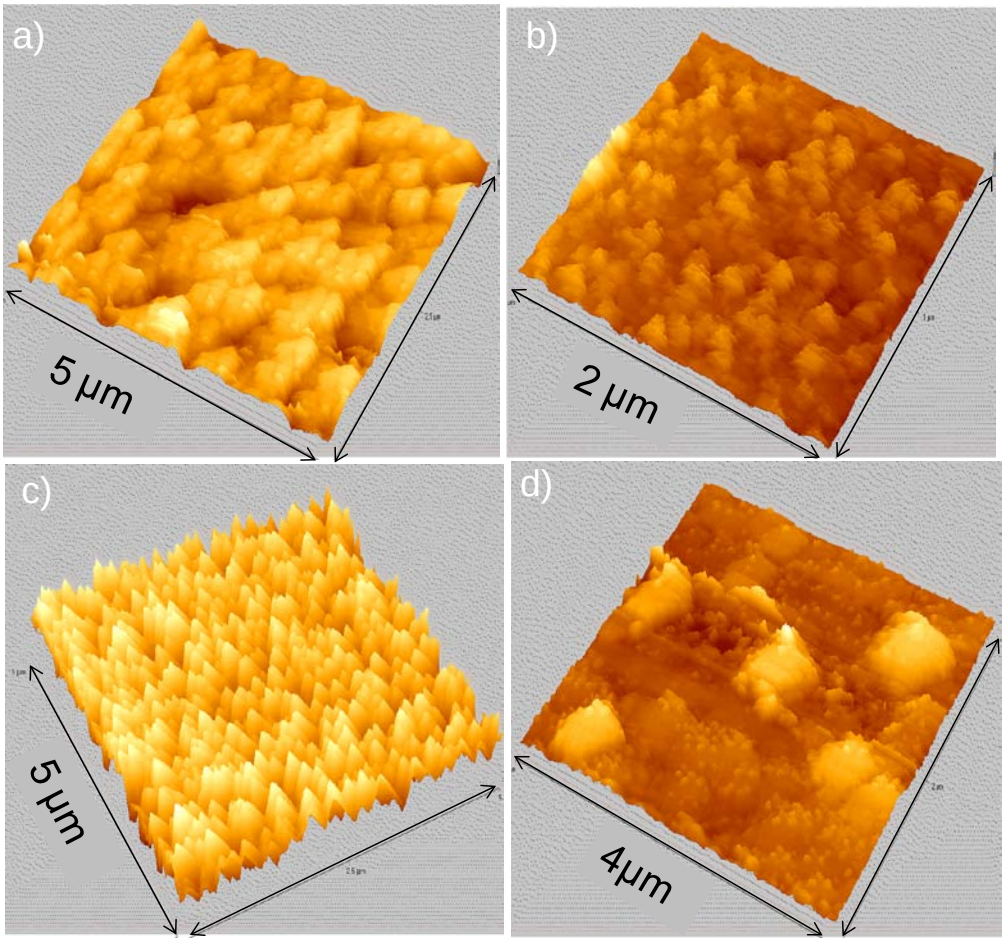

Fig. 2.10 3D-AFM images a) – d) FeS films deposited complexes (**1**) – (**4**)

2.4.7 The AA-CVD deposition of iron sulfide thin films from [$Fe_2(\mu\text{-}OMe)_2(SON(CNEt_2)_2)_2$] (2)

Iron sulfide thin film deposition was carried out at substrate temperature between 250 and 400 °C with argon flow rate of 160 sccm using complex (**2**). No deposition was obtained below 250 °C and above 400 °C. Reddish reflective, uniform films were deposited at 250 and 300 °C whereas dark brown films were deposited at 350 and 400 °C. XRD pattern of as deposited films at 250 - 400 °C in Fig. 2.11 shows that the films consist of hexagonal troilite-2H FeS (ICDD No: 037-0477) and cubic pyrite FeS_2 (ICDD No: 042-1340). At the lowest deposition temperature (250 °C) only pyrite diffraction peaks were observed whereas hexagonal troilite peaks become predominant at 300 °C. At 350 and 400 °C almost

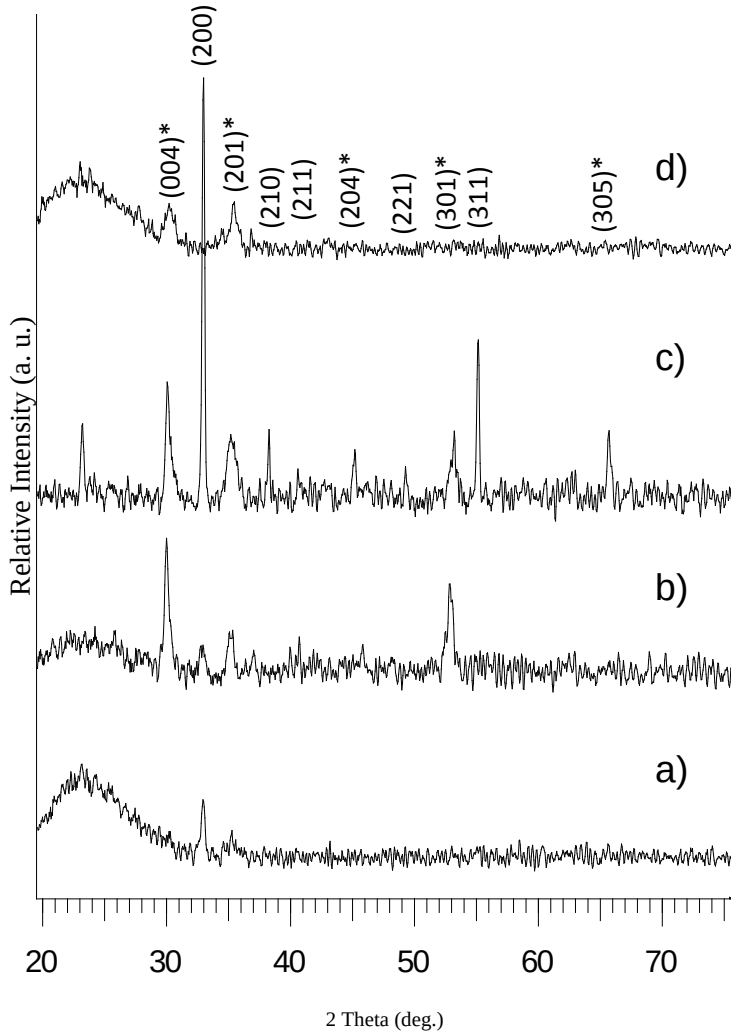

Fig. 2.11 Powder X-ray diffraction of pyrite iron sulfide thin films deposited from $[Fe_2(\mu\text{-}OMe)_2(SON(CNEt_2)_2)_2]$ (**2**) on glass at a) 250 b) 300 c) 350 and d) 400 °C, (*) symbol denotes the troilite-2H

equal amounts of troilite and pyrite were observed. This suggests loss of sulfur at higher deposition temperature leads to formation of troilite FeS predominantly. The major diffraction peaks can be assigned to (200), (210), (211) and (311) of cubic pyrite and (004), (201), (204) and (301) of hexagonal trolite-2H phase.

The morphology of the deposited films was investigated by scanning electron microscope as shown in Fig. 2.12. At 250 °C smaller cluster like crystallites with size ranging from 200–300 nm were obtained, whereas cross-linked network-like sheets (5-7 µm) were obtained at 300 °C. Flower-like crystallites with size range

of 10 -15 µm deposited at 350 and 400 °C. EDX analysis shows that the films are composed of iron: sulfur 52: 48 (250 and 300 °C), 55: 45 (350 and 400 °C).

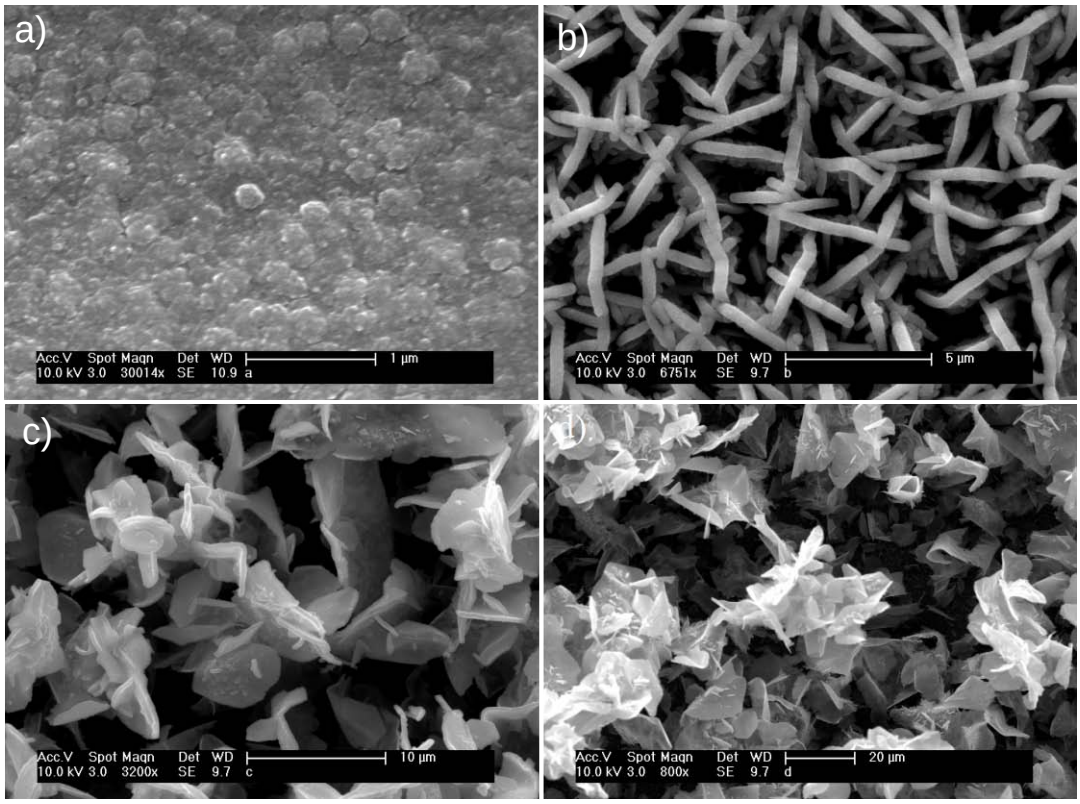

Fig. 2.12 SEM images of pyrite iron sulfide films deposited from [$Fe_2(\mu\text{-}OMe)_2(SON(CNEt_2)_2)_2$] (**2**) on glass at a) 250 b) 300 c) 350 and d) 400 °C

The TEM images from the scratched sample of films grown at 300 °C show that the films consist of plates with sizes ranging from 25-35 nm. HRTEM image of the plates (Fig. 2.13(b)) shows the lattice fringes with a d-spacing 0.27 nm corresponding to (200) reflection of cubic FeS_2. AFM image of films deposited from complex (**2**) on glass substrate in Fig. 2.9(b), shows highly packed crystallites. The average roughness of the films ranged from 14 to 31 nm from the films deposited at 250 to 400 °C

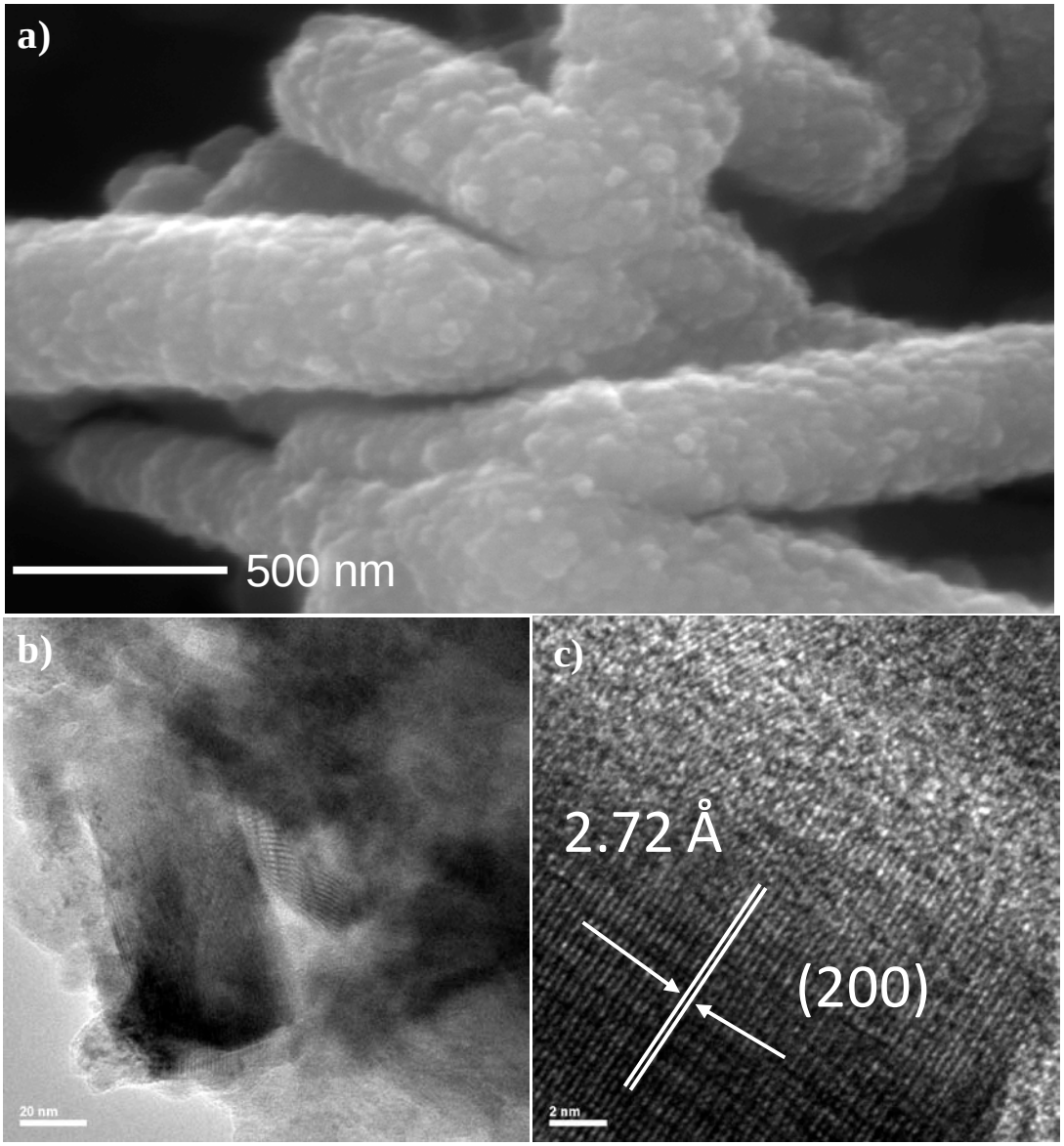

Fig. 2.13 a) HRSEM image iron sulfide films deposited at 300 °C, b) TEM images of the thin films deposited from $[Fe_2(\mu\text{-}OMe)_2(SON(CNEt_2)_2)_2]$ (**2**) at 300 °C b) HRTEM image

2.4.8 The AA-CVD deposition of iron sulfide thin films from $[Fe(SON(CNEt_2)_2)_3]$ (3)

Thin films of iron sulfide were deposited from complex (**3**) on glass substrate temperature between 300 and 450 °C. Brownish films were deposited at 300 °C whereas black films were deposited at 350, 400 and 450 °C. The films were characterized by powder X-ray diffraction.

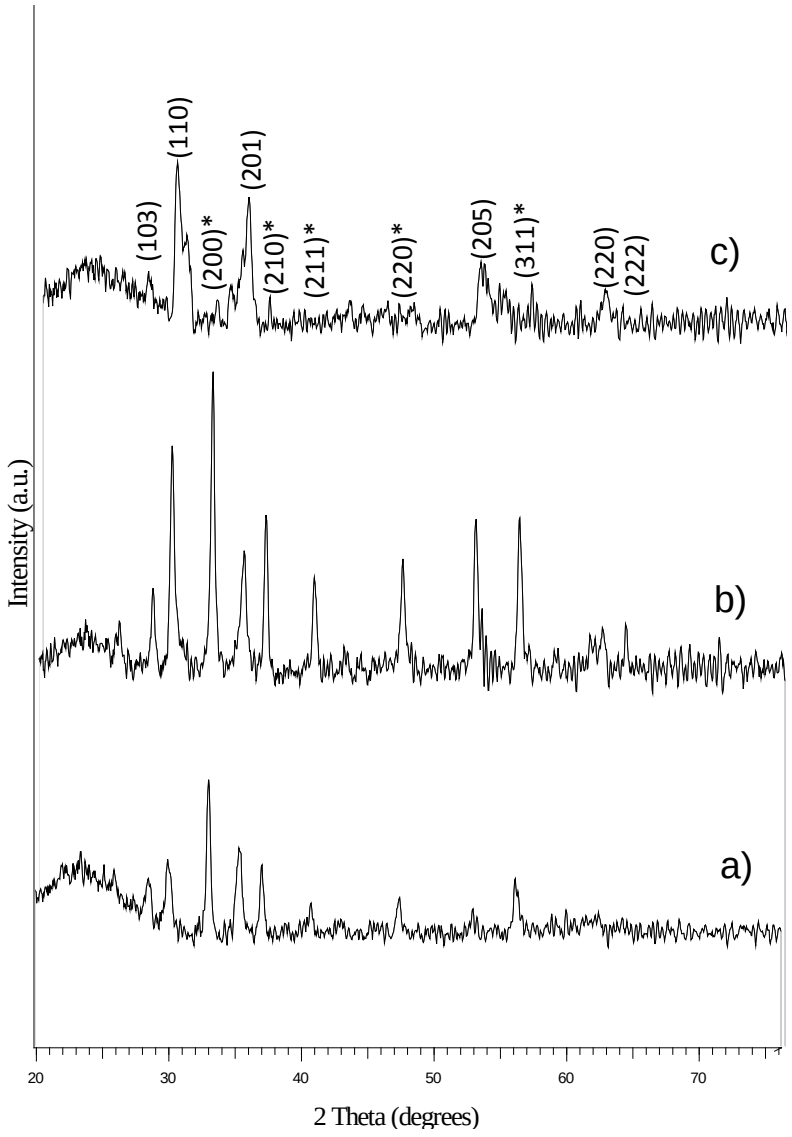

Fig. 2.14 Powder X-ray diffraction of troilite (FeS) iron sulfide thin films deposited from $[Fe(SON(CNEt_2)_2)_3]$ (**3**) on glass at a) 350 b) 400 and c) 450 °C, (*) symbol denotes the pyrites.

It shows deposition of mixture of troilite (ICDD No: 037-0477) and pyrite phases (ICDD No: 042-1340) at all temperatures though the pyrite diffraction peaks are dominant at 400 °C. The major diffraction peaks could be indexed as (103), (110), (201), (205) and (220) of troilite and (200), (210), (211), (220) and (311) of pyrite (Fig. 2.14).

SEM images of films deposited at 300 °C shows granular crystallites with an average size of 500-700 nm, mixture of granular crystallites and hexagonal plates

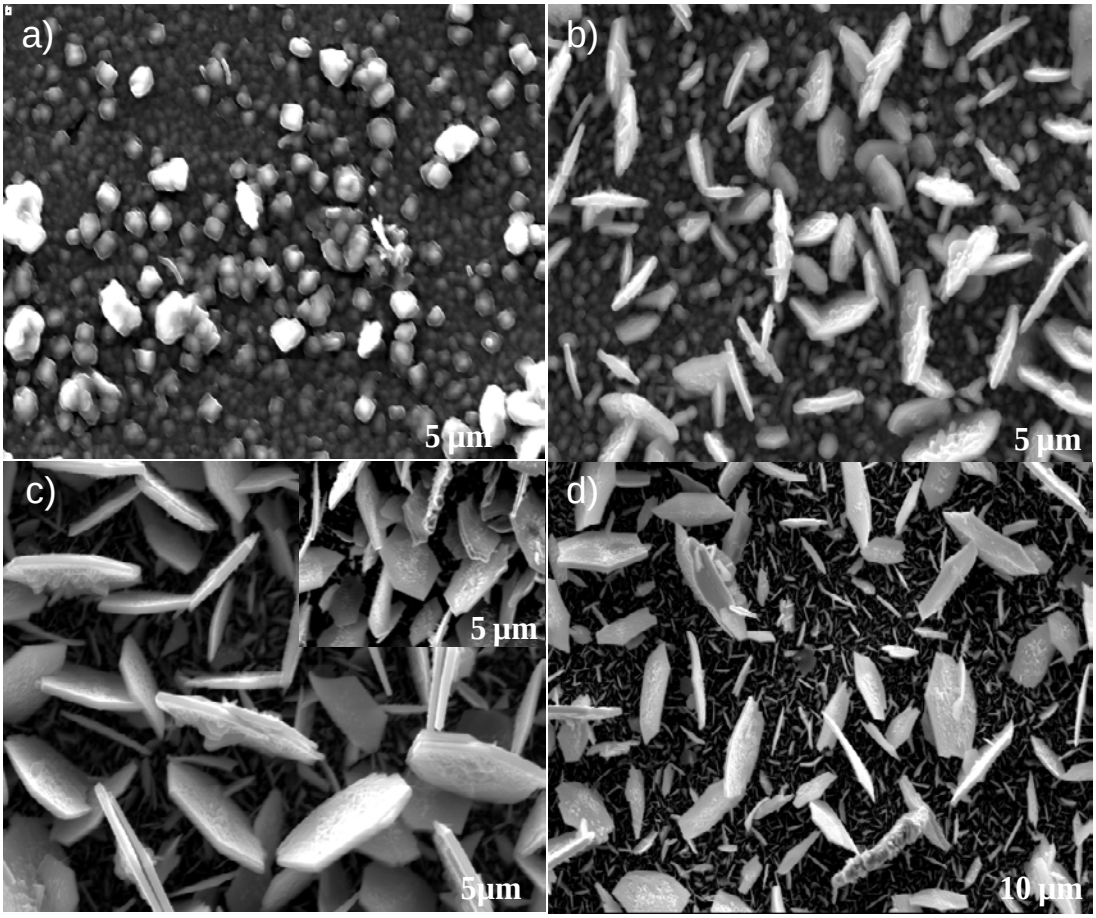

Fig. 2.15 SEM images of troilite(FeS) iron sulfide films deposited from $[Fe(SON(CNEt_2)_2)_3]$ (**3**) on glass at a) 300 b) 350 c) 400 d) 450 °C and onset 45° tilt image of film deposited at 400 °C

were deposited at 350 °C whereas hexagonal plates were deposited in the *c*-direction of glass substrate at 400 and 450 °C with an average size of 5-7 µm (Fig. 2.15). EDX analysis shows that the films are composed of iron: sulfur 51: 49 (300 °C), 52: 48 (350 °C), 55: 45 (400 and 450 °C). TEM images from the scratched sample of films grown at 400 °C further confirm deposition of plate-like crystallites (Fig. 2.16). The AFM image in Fig. 2.10(c), shows growth of closely packed crystallites on glass substrate with an average roughness of 19-23 nm (300-450 °C).

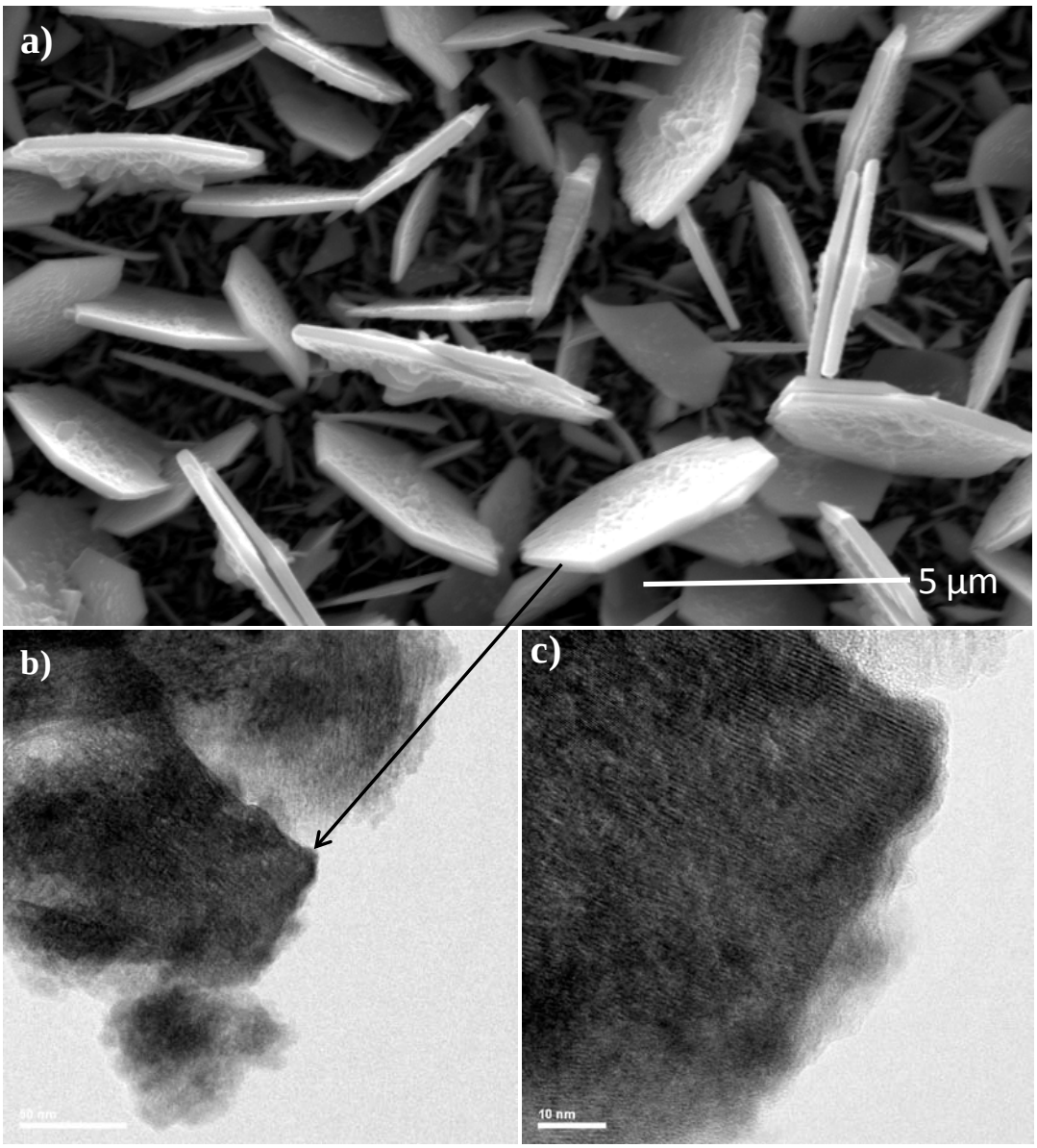

Fig. 2.16 a) Higher magnification SEM image , b) lower and c) higher magnification TEM images of the thin films deposited from $[Fe(SON(CNEt_2)_2)_3]$ (**3**) at 400 °C

2.4.9 The AA-CVD deposition of iron sulfide thin films from $[Fe(SON(CNMe_2)_2)_3]$ (4)

Reddish uniform reflective iron sulfide thin films were deposited from complex (**4**) at 350 and 400 °C. The films deposited were very thin so that the XRD pattern could not be obtained. SEM images in Fig. 2.17, shows deposition of granular crystallites with size of 100 -150 nm at 350 whereas granular and rods of

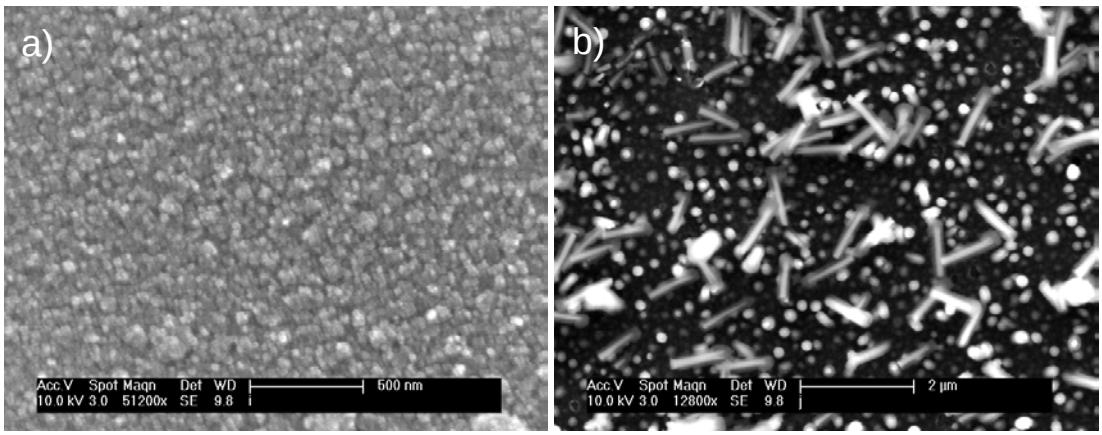

Fig. 2.17 SEM images of iron sulfide films deposited from $[Fe(SON(CNMe_2)_2)_3]$ (**4**) on glass at a) 350 b) 400 °C

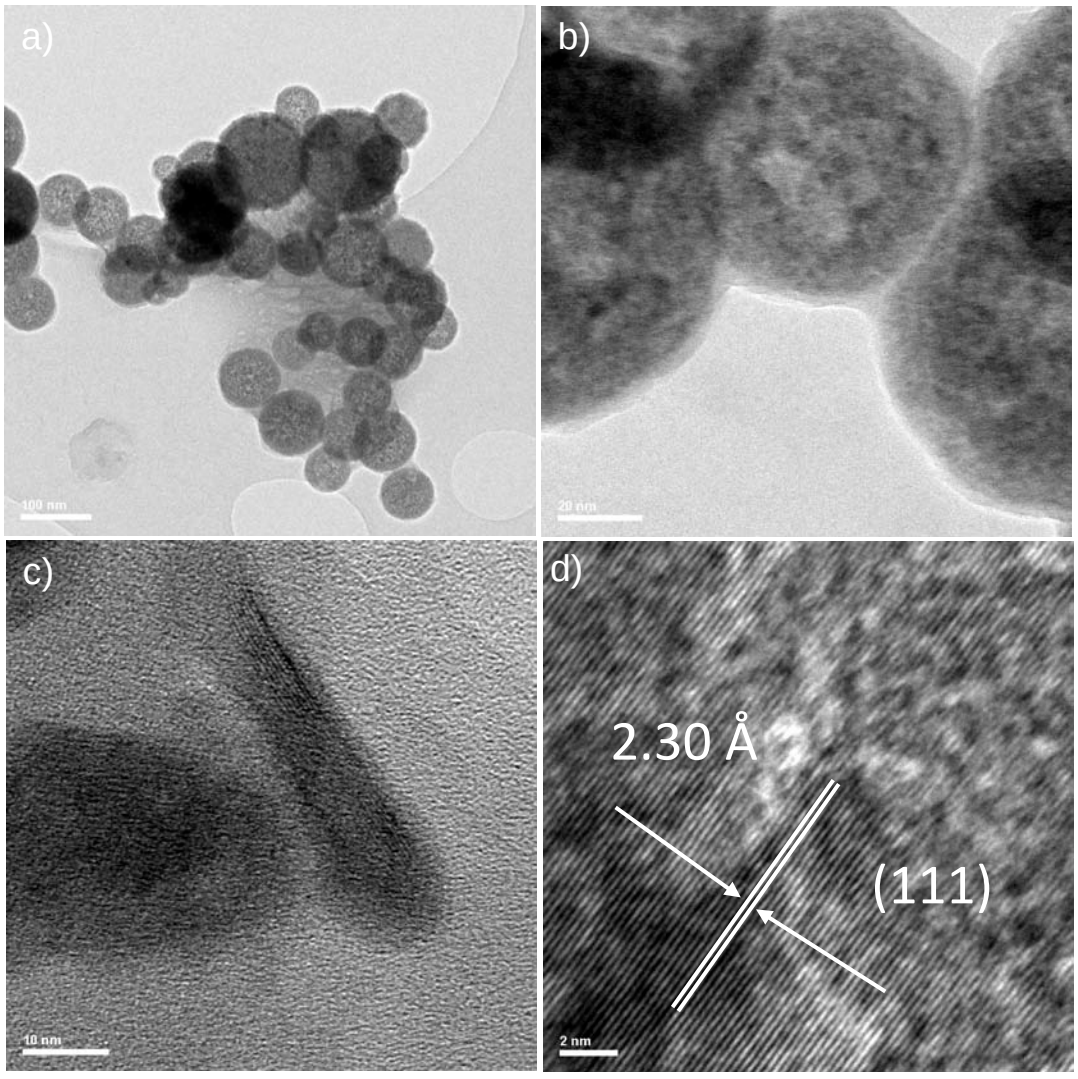

Fig. 2.18 TEM images of the thin films deposited from $[Fe(SON(CNMe_2)_2)_3]$ (**4**) at 400 °C a) lower b) higher magnification images of nanospheres c) nanorod and d) HRTEM image of nanosphere

crystallites obtained at 400 °C. EDX analysis shows that the films are composed of iron: sulfur 53: 47 (350 °C), 56: 44 (400 °C). TEM images of scratched films deposited at 400 shows nano spheres with an average size of 100–150 nm (Fig. 2.18(a)) and nanorods width of 10 nm (Fig. 2.18(c)). HRTEM image of the spherical crystallites (Fig. 2.18(d)), shows the lattice fringes with a d-spacing 0.23 nm corresponding to (111) reflection of tetragonal FeS. The surface topography of the films was further analysed by AFM. The 3D-AFM image in Fig. 2.10(d), shows the growth of irregular granular crystallites on glass substrate at 300 °C. The average roughness of films is 13 nm at 350 °C and 16 nm at 400 °C.

2.5 Conclusion

The synthesis, structures and magnetic properties of some new Fe(III) complexes of 1,1,5,5-tetraalkyl-2-thiobiurets have been reported. The synthesis is straight forward from the reaction of di-*iso*-propylcarbamoyl chloride, sodium thiocyanate and iron(III) nitrate in the presence of dialkylamine produced new monomeric complexes, however in the case of diethylamine a methoxide bridged binuclear iron(III) complex was formed. Single crystal X-ray structure of complexes (**1**), (**2**) and (**4**) showed a distorted octahedral geometry on iron(III) ion. Magnetic measurement for complex (**2**) confirmed its antiferromagnetic behavior. Thermogravimetric analysis showed the single step decomposition of complexes (**1**), (**3**), (**4**) and double step decomposition of complex (**2**). The newly synthesized complexes were used as single source precursors for the deposition of iron sulfide thin films by AACVD.

The relative stabilities of various phases of iron sulfide are shown in Fig. 2.19, using a plot similar to that developed by Vaughan and Lennie.[1] The height of the pyramid on the negative z- axis represents the free energy of formation of each

phase. The solid line represents thermodynamic stability and connects the stable phases FeS (troilite) and FeS_2 (pyrite).[1]

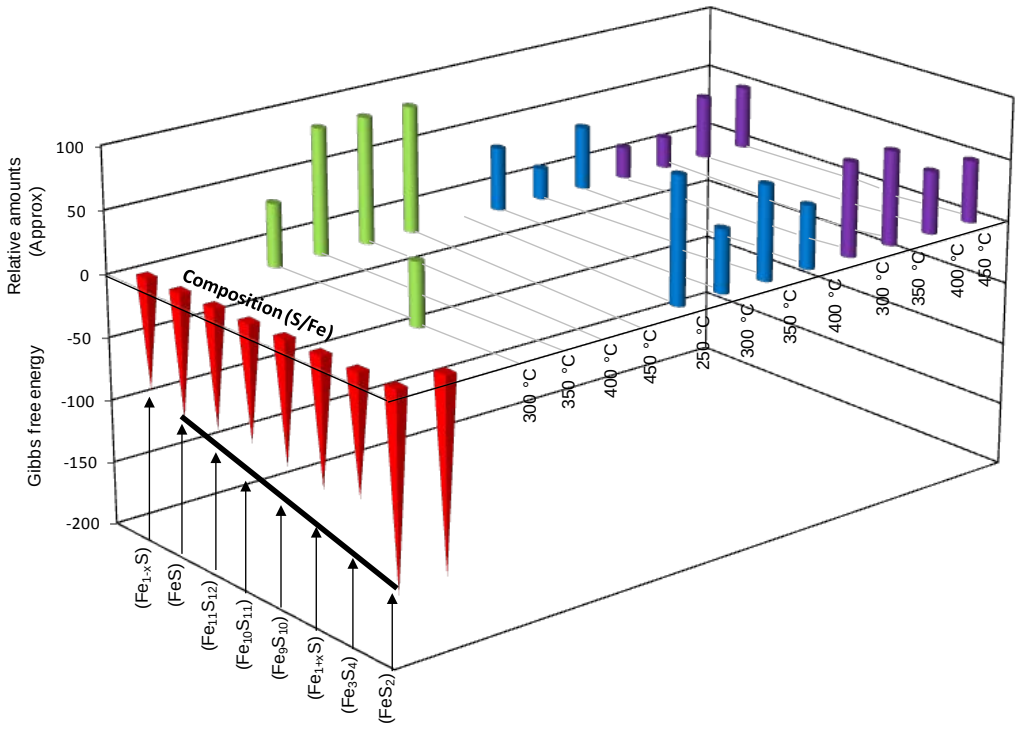

Fig. 2.19 The phases iron sulfide films deposited in CVD experiments from precursor (**1**) green, (**2**) blue and (**3**) violet. Relative amounts of each phase are represented by the height of the cylinders small (25 %), medium (50 %) and large (75%) only one phase (100%) these are approximation based on PXRD results. Compared to the relative thermodynamic stabilities of the various phases of iron sulfides (-ve *z*-axis) and phases after Vaughan.[1]

In this CVD work, almost always only the two most stable phases were seen, with the exception of Fe_7S_8 (pyrrhotites) at 300 °C from complex (**1**). This may suggest a reaction leading to predominantly thermodynamic products, *i.e* once the system is sufficiently sulfide-rich for FeS_2 to form only this phase or its mixtures with FeS are seen from films deposited using precursors (**1**), (**2**) and (**3**). There are apparently two known exceptions[36,38] to this rule in the CVD of FeS_x along with Fe_7S_8 from complex (**1**) at 300 °C. This behaviour is in contrast with that observed in the deposition of iron sulfide from solution, sometimes, occurring as particles with critical dimensions of the order of nanometers. It is interesting that solution

deposition, possibly because of the lower temperatures involved can allow the formation of less stable phases such as mackinawite, although the stoichiometry is the subject of controversy[1,3] ($Fe_{1+x}S$),[13,44] pyrrhotite ($Fe_{1-x}S$),[21,22,45] and greigite (Fe_3S_4)[14,18] which must form under kinetic control (Fig. 2.20). Indeed there are many examples of such FeS phases in biology notably in magnetotactic bacteria.[13,14,46,47]

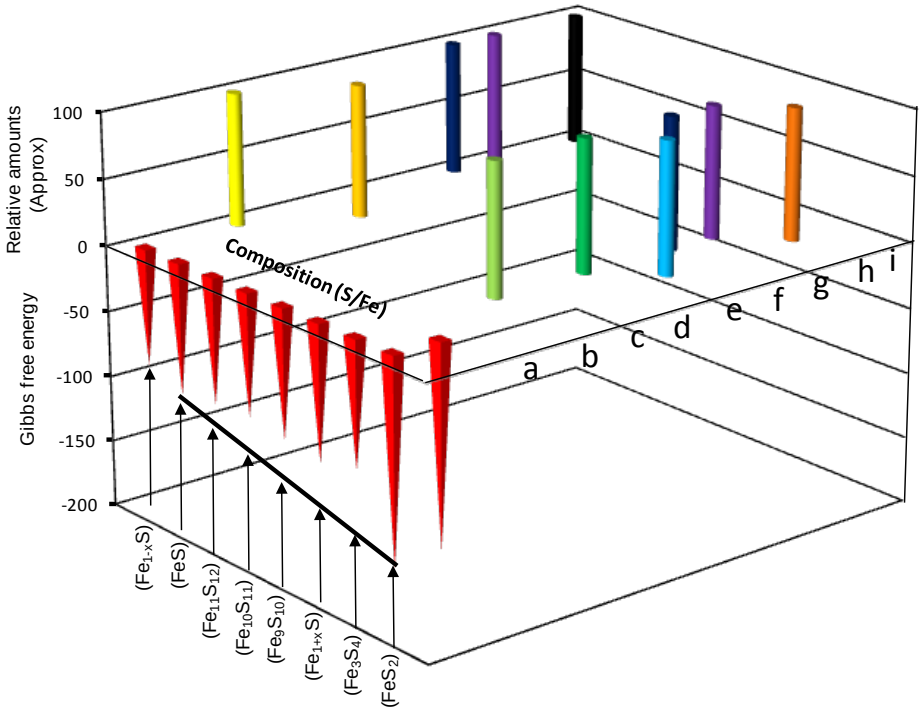

Fig. 2.20 The phases of iron sulfide nanoparticles reported by solution methods in the literature, compared to the relative thermodynamic stabilities of the various phases of iron sulfides and phases after Vaughan.[1] (a) $Fe_{1-x}S$, sulfate reducing bacteria (Ref. 13), (b) Fe_3S_4, sulfate reducing bacteria (Ref. 14), (c) Dendrimer stabilized FeS (Ref. 15), (d) Fe_3S_4, $FeSO_4$, L-cysteine, solvothermal (Ref. 18), (e) FeS_2, single source precursor, hydrothermal (Ref. 20), (f) Fe_3S_4, Fe_7S_8, single source precursors (Ref. 21), (g) Fe_3S_4, Fe_7S_8, single source precursor (Ref. 22), (h) FeS_2, single source precursors, hydrothermal (Ref. 44), (i) $Fe_{1-x}S$, iron oleate, 1-octadecanethiol (Ref. 45).

2.6 References

1. D. J. Vaughan, A. R. Lennie, *Sci. Progr. Edinburgh*. 1991, **75**, 371.

2. J. B. Goodenough, *Mat. Res. Bull.,* 1978, **13**, 1305.

3. C. N. R. Rao, K. P. R. Pisharody, *Prog. Solid State Chem.,*1975, **10**, 207.

4. R. M. Cornell, U. Schwertmann, 1996, Vch, Weinheim, Newyork.

5. C. Hopfner, K. Ellmer, A. Ennaoui, C. Pettenkofer, S. Fiechter, H. Tributsch, *J. Cryst. Growth*, 1995, **151**, 325.

6. A. Ennaoui, S. Fiechter, C. Pettenkofer, N. Alonso-Vante, K. Büker, C. Hopfner, H. Tributsch, *Sol. Energy Mater. Sol. Cells,* 1993, **29**, 289.

7. J. Oertel, K. Ellmer, W. Bohne, J. Röhrich, H. Tributsch, *J. Cryst. Growth,* 1999, **198**, 1205.

8. D. A. Tryk, S. Kim, Y. Hu, X. Xing, D. A. Scherson, M. R. Antonio, V. Z. Leger, G. E. Blomgren, *J. Phys. Chem.,* 1995, **99**, 3732.

9. Y. Shao-Horn, S. Osmialowski, C. Horn Quinn, *J. Electrochem. Soc*., 2002, **149**, A1499.

10. G. L. Henriksen, D. R. Vissers, A. A. Hilenskas, *J. Power Sources,* 1995, **54**, 134.

11. D. Golodnitsky, E. Peled, *Electrochim. Acta*, 1999, **45**, 335.

12. P. P. Chin, J. Ding, J. B. Yi, B. H. Liu, *J. Alloys Compounds,* 2005, **390**, 255.

13. J. H. P. Watson, B. A. Cressey, A. P. Roberts, D. C. Ellwood, J. M. Charnock, A. K. Soper, *J. Magn. Magn Mater*., 2000, **214**, 13.

14. J. H. P. Watson, D. C. Ellwood, A. K. Soper, J. M. Charnock, *J. Magn. Magn Mater.,* 1999, **203**, 69.

15. X. Shi, K. Sun, L. P. Balogh, J. R. Jr Baker, *Nanotech*., 2006, **17**, 4554.

16. X. X. Bi, P. C. Eklund, *Mater. Res. Soc. Symp. Proc.,* 1993, **286**, 161.

17. J. P. Wilcoxon, P. P. Newcomer, G. A. Samara, *Solid State Commun.,* 1996, **98**, 581.

18. F. Cao. W. Hu, L. Zhou, W. Shi, S. Song, Y. Lei, S. Wang, H. Zhang, *Dalton Trans.,* 2009, 9246.
19. K. M. Paknikar, V. Nagpal, A. V. Pethkar, J. M. Rajwade, *Sci. Tecnol. Adv. Mater.,* 2005, **6**, 370.
20. X. Chen, Z. Wang, X. Wang, J. Wan, J. Liu, Y. Qian, *Inorg. Chem.,* 2005, **44**, 951.
21. P. V. Vanitha, P. O'Brien, *J. Am. Chem. Soc.,* 2008, **130**, 17256.
22. W. Han, M. Gao, *Cryst. Growth Des*., 2008, **8**,1023.
23. D. M. Schleigh, H. S. W. Chang, *J. Cryst. Growth,* 1991, **112**, 737.
24. B. Thomas, C. Hoepfner, K. Ellmer, S. Fiechter, H. Tributsch, *J. Cryst. Growth,* 1995, **146**, 630.
25. B. Thomas, T. Cibik, C. Hoepfner, D. Diesner, G. Ehlers, S. Fiechter, K. Ellmer, *J. Mat. Sci*., 1998, **9**, 61.
26. B. Meester, L. Reijnen, A. Goossens, J. Schoonman, *J. Phys.,* 1999, **9**, Pr8-613.
27. G. Smestad. E. Ennaoui, S. Fiechter, H. Tributsch, W. K. Hofman, M. Birkholz, S*ol. Energy. Mater.,* 1990, **20**, 149.
28. B. Ouertani, J. Ouerfelli, M. Saadoun, B. Bessais, H. Ezzaouia, J. C. Bernede, *Mater. Charact.,* 2005, **54**, 431.
29. I.J. Ferrer, C. J. Sanchez, *Appl. Phys*., 1991, **70**, 2641.
30. M. Birkholz, D. Lichtenberger, C. Hoepfner, S. Fiechter, *Sol. Energy Mater. Sol. Cells,* 1992, **27**, 243.
31. S. Bausch, B. Sailer, H. Keppner, G. Willeke, E. Bucher, G. Frommeyer, *Appl.*

*Phys. Lett.,*1990, **25**, 57.

32. A. Ennaoui, G. Schlichtlorel, S. Fiechter, H. Tributsch, *Sol. Energy Mater. Sol. Cells.,* 1992, **25**, 169.
33. G. Smestad, A. Da Silva, H. Tributsch, S. Fiechter, M. Kunst, N. Meziani, M. Birkholz, *Sol .Energy Mater*., 1989, **18**, 299.
34. B. Rezig, H. Dalma, M. Kanzai, *Renewable Energy,* 1992, **2**, 125.
35. B. Meester, L. Reijnen, A. Goossens, J. Schoonman, *Chem. Vap. Deposition,* 2000, **6**, 121.
36. J. M. Soon, L. Y. Goh, K. P. Loh, Y. L. Foo, L. Ming, J. Ding, *Appl. Phys. Lett.,* 2007, **91,** 084105.
37. P. O' Brien, D. J. Otway, J. H. Park, *Mat. Res. Soc. Symp. Proc.,* 2000, **606**, 133.
38. S. G. Shyu, J. S. Wu. C. C. Wu, S. H. Chuang, K. M. Chi, *Inorg. Chim. Acta,* 2002, **334**, 276.
39. K. Ramasamy, M. A. Malik, P. O'Brien, J. Raftery, *Dalton Trans.,* 2010, **39**, 1460.
40. J. Ahmed, J. A. Ibers, *Inorg.Chem*., **1977**, *16*, 935.
41. B. F. Hoskins, C. D. Pannan, *Inorg. Nucl. Chem. Lett.*, **1975**, *11*, 409.
42. N. Bouslimani, N. Clement, G. Rogez, P. Turek, M. Bernard, S. Dagorne, D. Martel, H. N. Cong, R. Welter, *Inorg Chem.,* 2008, **47**, 7623.
43. O. Khan, Molecular Magnetism, 1993, VCH, Newyork,
44. C. Wadia, Y. Wu, S. Gul, S. k. Volkman, J. Guo, P. Alivisatos, *Chem Mater*., 2009, **21**, 2568.
45. H. Y. Lai, C. J. Chen, *J. Crys. Growth*, 2009, **311**, 4698.
46. M. Posfai, P. R. Buseck, D. A. Bazylinski, R. B. Frankel, *Am. Mineral*., 1998, **83**, 1469.

47. M. Posfai, P. R. Buseck, D. A. Bazylinski, R. B. Frankel, *Science*, 1998, **280**, 880.

Chapter 3

Cobalt Sulfide Nanostructured Thin Films*

3.1 Summary

This chapter describes the synthesis of cobalt(III) complexes of 1,1,5,5-tetramethyl- and 1,1,5,5-tetraethyl-2,4-dithiobiuret, and the cobalt(II) complex of 1,1,5,5-tetra-*iso*-propyl-2-thiobiuret. The determination of the single crystal X-ray structure of the thiocyanate (**1**) and tetrachlorocobaltate (**2**) complexes of the parent cyclised ligand, together with complexes $[Co(N(SCNMe_2)_2)_3]$ (**3**), $[Co(N(SCNEt_2)_2)_3]$ (**4**) and $[Co(SON(CN^iPr_2)_2)_2]$ (**5**) are discussed. The thermal decompositions of (**3**), (**4**) and (**5**) were studied. The complexes were used as single-source precursors for the deposition of cobalt sulfide thin films by aerosol assisted chemical vapour deposition (AACVD). The powder X-ray diffraction (XRD) of the deposited films showed hexagonal $Co_{1-x}S$ from complex (**3**) and (**4**) whereas complex (**5**) gave a mixture of cubic and hexagonal Co_4S_3. The morphology of the films were characterized by scanning electron microscopy (SEM), and showed rod like crystallites from (**3**), granular crystallites from (**4**) and stalagmitic structures from (**5**) was achived. Transmission electron microscopy (TEM) of the samples obtained from thin films from (**3**) and (**4**) show that the films are composed of hexagonal nanoplates and nanocubes were obtained from (**5**). Magnetic measurements showed the para or ferro-magnetic behavior from the crystallites. The mechanism for decomposition of precursors to the cobalt sulfide was studied by pyrolysis gas chromatography (Py-GC-MS).

*Part of the work has been published in *Dalton Trans.,* 2010, **39**, 1460 and *Chem. Mater.,* 2010, **22**, 4919.

3.2 Introduction

Magnetic semiconductors, especially cobalt sulfides, have attracted considerable attention in recent years as; solar energy absorbers,[1] ultra high-density magnetic recording,[2] anodes for Li-ion batteries[3] and catalysts for hydrodesulfurization or dehydrodearomatization.[4,5] Cobalt sulfide exists as various crystalline phases: Co_4S_3, Co_9S_8, CoS, $Co_{1-x}S$, Co_3S_4, Co_2S_3 and CoS_2.[6,7] Considerable effort has been focused on depositing cobalt sulfide thin films by various methods such as chemical bath deposition (CBD),[8] chemical vapor deposition (CVD),[9] electrochemical deposition (ECD)[3] and Langmuir-Blodgett (LB)[10] methods. Previously, O'Brien *et al.* have studied methyl n-hexyl dithiocarbamates $[Co(S_2CNMe^nHex)_3]$ as single source precursor for the growth of cobalt sulfide films, and they have reported the deposition of $Co_{1-x}S$, CoS_2 and Co_3S_4.[11] Recently, Co_9S_8 thin films have been deposited by AACVD using iminobisthiophosphinate complex of cobalt as the single-source precursor.[12] More recently, the synthesis of $Co_{1-x}S$ and Co_4S_3 nanoparticles using thio- and dithio-biuret cobalt complexes was reported.[13,14] To the best of our knowledge no other cobalt complexes have been used as single-source precursors for the phase selective deposition of cobalt sulfide thin films. In this chapter the synthesis and structures of ligands (**1**), (**2**) and their cobalt complexes (**3**), (**4**) and (**5**), and their use as single source precursors for phase selective deposition of $Co_{1-x}S$ and Co_4S_3 thin films by AACVD method are reported.

3.3 Experimental

3.3.1 Synthesis of $[N(SCNMe_2)_2]SCN$ (1)

A mixture of dimethylthiocarbamoyl chloride (1.23 g, 10 mmol) and sodium thiocyanate (0.81 g, 10 mmol) in acetonitrile (40 mL) was refluxed with continuous

stirring for 1 h, during which time a fine precipitate of sodium chloride formed. To the cooled reaction mixture was added 60 % aqueous dimethylamine (1.49 mL, 20 mmol) followed by stirring for 30 min. The mixture was left at room temperature to give colorless needles of the product. Yield 0.72 g (37.8 %), MS (EI/CI) major fragments: m/z = [M+] 190, [$N(SCNMe_2)_2$] 190. ^{1}H NMR (300 MHz; $CDCl_3$; Me_4Si): 2.3 (s, 6 H). Elemental analysis: Calc. for [$C_7H_{12}N_4S_3$]: C, 33.8; H, 4.8; N, 22.5; S, 38.7 % Found C, 33.2; H, 4.9; N, 21.7; S, 37.8 %.

3.3.2 Synthesis of [$Co(N(SCNMe_2)_2)_3$] (3)

A solution of dimethylthiocarbamoyl chloride (1.23 g, 10 mmol) and sodium thiocyanate (0.81 g, 10 mmol) in acetonitrile (40 mL) was heated at reflux with continuous stirring for 1 h, during which time a fine precipitate of sodium chloride formed. To the cooled reaction mixture was added 60 % aqueous dimethylamine (1.49 mL, 20 mmol) followed by stirring for 30 min and addition of cobalt(II) chloride hexahydrate (1.193 g, 5 mmol). The crude product was precipitated as a red powder and recrystallised from chloroform and then by tetrahydrofuran to get suitable quality crystals for X-ray crystallography. Yield 1.89 g (30 %), MS (APCI) major fragments: m/z = [M+] 631, [$Co(N(SCNMe_2)_2)_3$] 631, [$N(SCNMe_2)_2$] 190. IR (ν_{max} /cm^{-1}): 2928(w), 1468(s), 1380(m), 1306(s), 1104(s), 906(s). Elemental analysis: Calc. for $C_{18}H_{36}N_9S_6Co$: C, 34.1; H, 6.1; N, 19.9; S, 30.3; Co, 9.3 %. Found: C, 34.9; H, 6.0; N, 19.7; S, 28.9; Co, 9.1 %

3.3.3 Synthesis of [$Co(N(SCNEt_2)_2)_3$] (4)

Compound (**4**) was synthesized by the same method as described for (**3**) but using diethylthiocarbamoyl chloride (1.51 g, 10 mmol) and diethylamine (1.91 mL, 20 mmol). The crude product was precipitated as a black crystalline powder and recrystallised from chloroform to give black needles. Yield 1.90 g (25 %), MS (APCI), major fragments: m/z = [M+] 796, [Co ($N(SCNEt_2)_2)_3$] 796, [$N(SCNMe_2)_2$]

246. IR (ν_{max} /cm^{-1}): 2971(w), 2924(w), 1473(s), 1422(s), 1403(m), 1341(s), 1247(s), 1116(s), 996(s). Elemental analysis: Calc. for $C_{30}H_{60}N_9S_6Co$: C, 45.2; H, 7.5; N, 15.8; S, 24.0; Co, 7.3 %. Found: C, 44.9; H, 7.5; N, 15.7; S, 23.7; Co, 7.3 %

3.3.4 Synthesis of [Co(SON(CN^{i}Pr$_2$)$_2$)$_2$] (5)

Compound (**5**) was synthesized by the same method as described for (**3**) but using di-*iso*-propylcarbamoyl chloride (1.0 g, 6 mmol) and di-*iso*-propylamine (1.49 mL, 12 mmol). The crude product was precipitated as blue powder and recrystallized from tetrahydrofuran to get shiny crystals of blue needles which were identified as (**5)**. Yield 1.89 g (30 %), MS (APCI) major fragments: m/z = [M+] 631, [Co(N(SOCN^{i}Pr$_2$)$_2$)$_2$], [NSO(CN-*i*-Pr$_2$)$_2$] 284. IR (ν_{max} /cm^{-1}): 2963(s), 1499(s), 1434(s), 1353(s), 1208(m), 1144(m). Elemental analysis: Calc. for $C_{28}H_{56}N_6S_2O_2Co$: C, 53.2; H, 8.8; N, 13.3; S, 10.1; Co, 9.3 %. Found: C, 53.2; H, 9.0; N, 13.2; S, 9.9; Co, 9.0 %

3.4 Results and discussion

The reaction of N,N'-dimethylcarbamoyl chloride, sodium thiocyanate and dimethylamine produced a cyclised ligand cation stabilized by a thiocyante ion. Addition of cobalt(II) chloride to this reaction gave a mixture of compound (**2**) and (**3**). Compound (**2**) was unexpectedly identified as consisting of two cyclised ligand cations stabilized by a tetrachlorocobaltate anion, whereas the compound (**3)** was identified as the expected cobalt complex but of cobalt(III). A schematic representation of the reaction is shown in Scheme. 3.1. The cyclisation of the ligand as observed in compound (**2**) had been discussed by Pellacani *et al.*[15] in dithiomalonamide

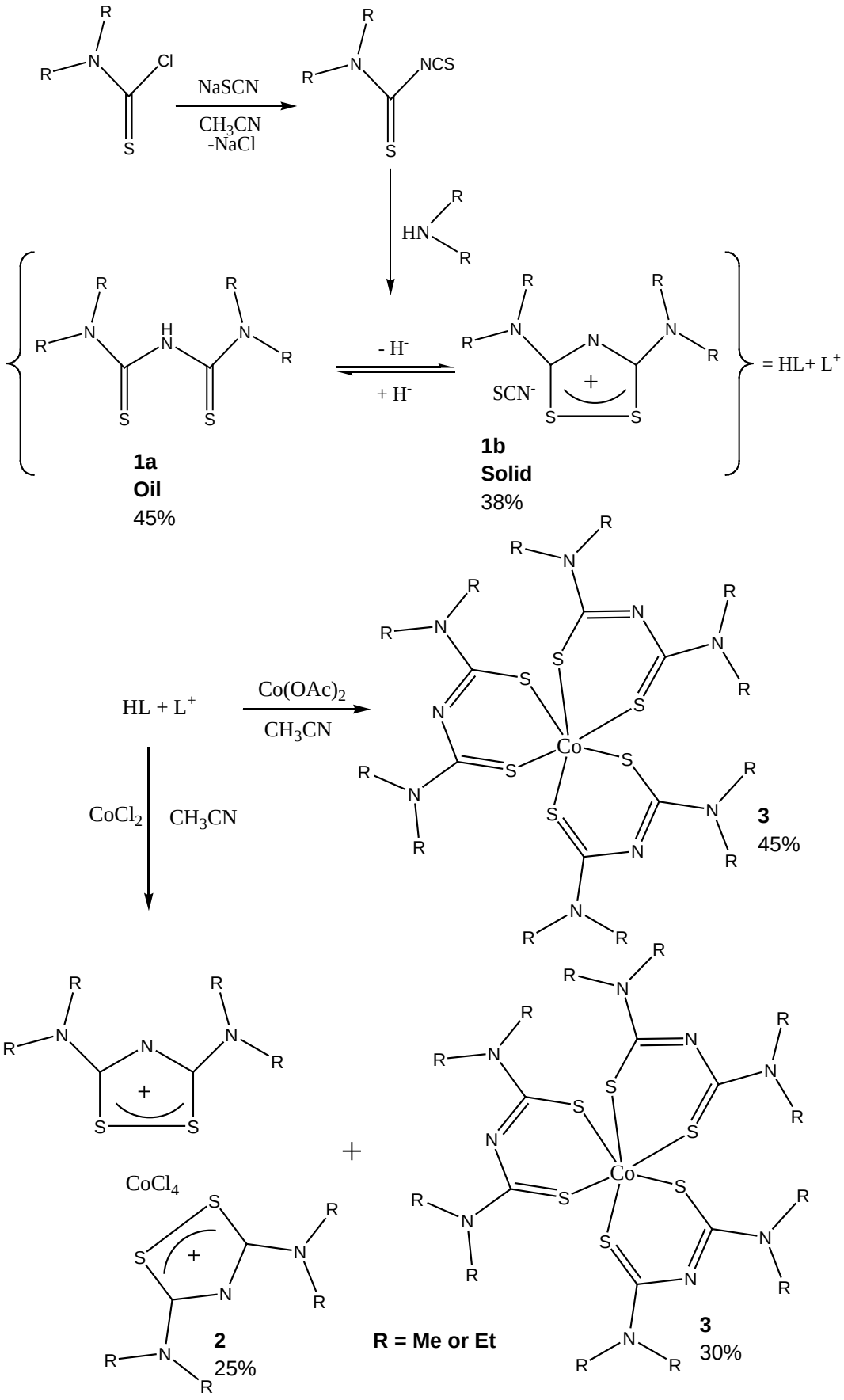

Scheme. 3.1 Schematic representation of the synthesis of ligand and complexes

systems and proposed mechanism for formation of dithiolium salts based on polarographic investigations. Köhler *et al.*[16] observed the same for dithiazolium tetrachloroniccolate. The reaction of N,N'-diethylcarbamoyl chloride, sodium thiocyanate and neat dithiazolium tetrachloroniccolate. The diethylamine followed same behavior as explained above. All three complexes are air and moisture-stable for several months and soluble in most organic solvents (toluene, tetrahydrofuran, chloroform, dichloromethane), which makes them suitable for AACVD.

3.4.1 Single crystal X-ray structure of $[N(SCNMe_2)_2]SCN$ (1)

The single crystal X-ray structure of (**1**) shows a planar five-membered disulfide ring with bite angles of N(2)C(4)S(2)-120.1(3)° and C(4)N(2)C(3)-114.6(4)° which are slightly smaller than for trigonal planar. The bond lengths of C(4)-S(2) 1.758(4) Å, and S(1)-S(2) 2.0568(15) Å indicate partial charge delocalisation over the atoms. Structure refinement data are given in Table A3, selected bond angles and bond distances are given in the caption to Fig. 3.1. The crystal packing diagram in Fig. 3.1(b), shows weak interactions between thiocyanate and sulfur in the range 2.935-3.022 Å which gives a supramolecular chain like network by linking each thiocyanide ion with two molecules of cyclised ligand.

3.4.2 Single crystal X-ray structure of $[N(SCNMe_2)_2]_2[CoCl_4]$ (2)

The single crystal X-ray structure shown in Fig. 3.2(a), shows a tetrahedral geometry of cobalt. The ligand bite angles of 109.68(4)º and 111.29(4)º are somewhat larger than perfect tetrahedral coordination. Weak interactions connect the cyclised ligand cation through sulfur atom with $[CoCl_4]^{2-}$ by 3.221-3.531Å distance another unit of ligand connects $CoCl_4^{2-}$ unit by 2.930Å through methyl hydrogen of dimethylamine. Structure refinement data are given Table A3, selected bond angles and bond distances are given in caption to Fig. 3.2. The crystal packing

diagram Fig. 3.2(b), shows weak interactions which gives a double packed chain network and each $[CoCl_4]^{2-}$ unit connects four units of the ligand.

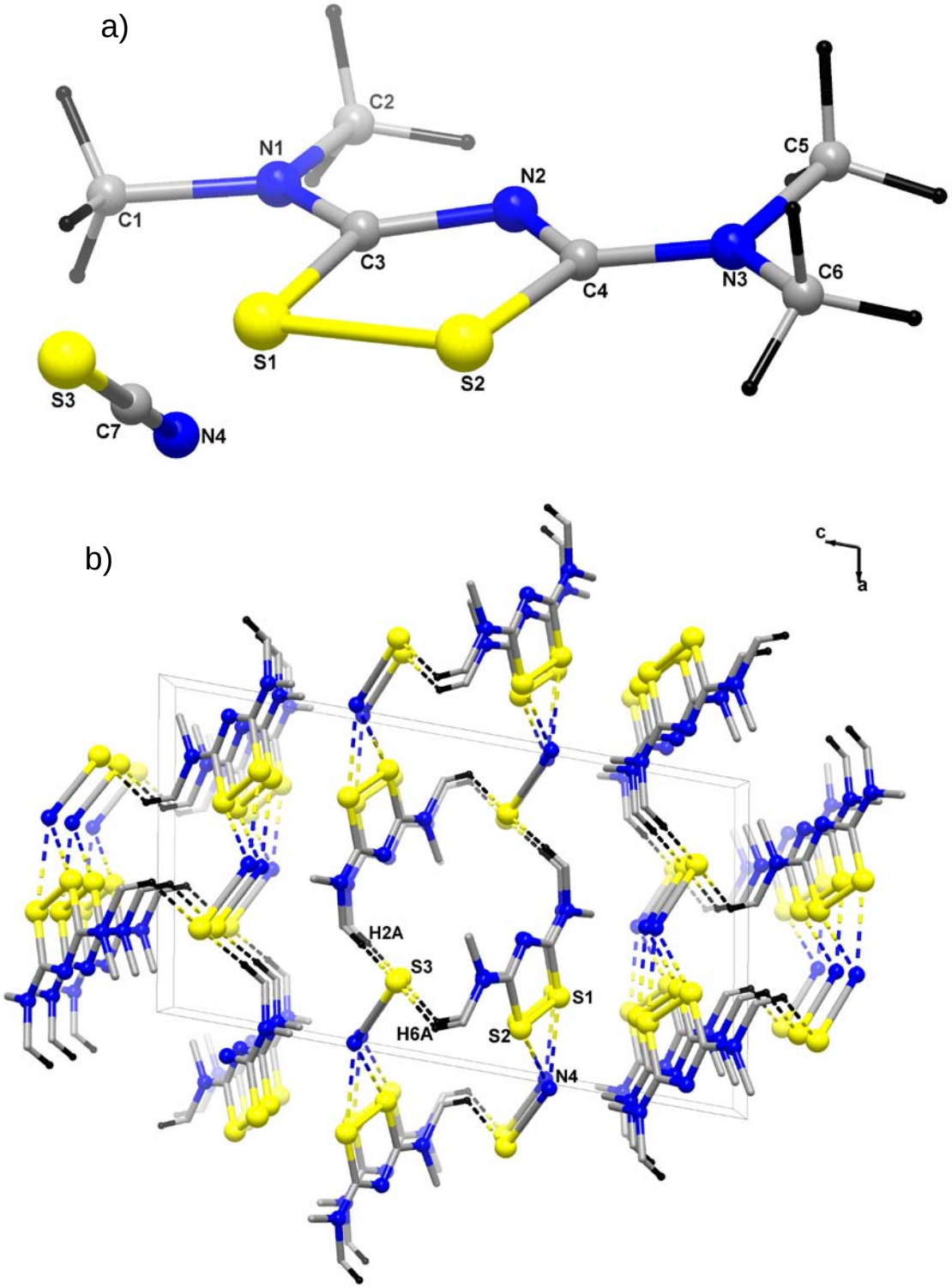

Fig. 3.1 (a) X-ray structure of (**1**). Selected bond lengths (Å) and bond angles (°): C1-N1 1.465(5), C2-N1 1.471(5), C3-S1 1.768(4); N2-C4-S2 120.1(3), C4-S2-S1 92.9(1). (b) View showing the supramolecular network mediated by C-H---S and C-N---S interactions

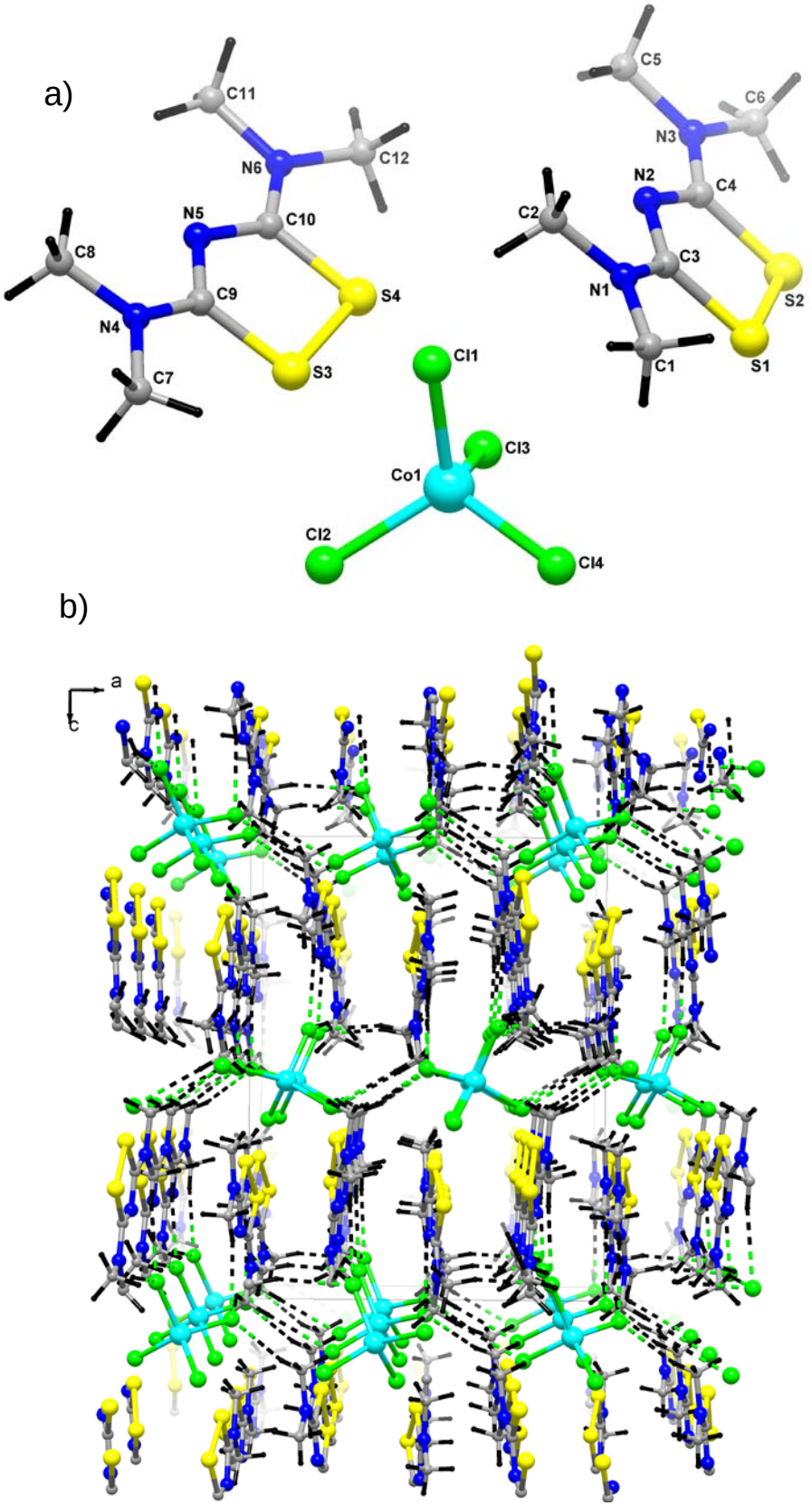

Fig. 3.2 (a) X-ray structure of (**2**).Selected bond lengths (Å) and bond angles (°) C1-N1 1.457(4), C3-S1 1.770(3), S1-S2 2.064(1); N3-C4-N2 122.5(3), Cl4-Co1-Cl1 107.3(4). (b) View showing the supramolecular network mediated by C-H---Cl and Co-Cl---S interactions

3.4.3 Single crystal X-ray structure of $[Co(N(SCNMe_2)_2)_3]$ (3)

The single crystal X-ray structure of $[Co(N(SCNMe_2)_2)_3]$ (**3**) (Fig. 3.3(a)) shows cobalt in an octahedral geometry with the ligand bite angles of 93.98(6)°, 94.29(6)° and 94.34(6)° which are slightly larger than those for perfect square planar configuration. The bond lengths between C(8)-S(3) 1.718(5) Å are shorter than for the cyclised ligand 1.758(4) Å which may be due to partial delocalization of positive charge over the atoms in cyclised ligand. Structure refinement data are given in Table A4 and selected bond angles and bond lengths are given in caption to Fig. 3. 3(a).

3.4.4 Single crystal X-ray structure of $[Co(N(SCNEt_2)_2)_3]$ (4)

The single crystal X-ray structure of $[Co(N(SCNEt_2)_2)_3]$ (**4)** in (Fig. 3.3(b)) shows cobalt in octahedral geometry with the ligand bite angles of 93.37(4)°, 92.58(4)° and 91.73(4)°. The separations C(5)-S(1) 1.734(4) Å are intermediate between the values found for cyclised ligand cation 1.758(4) Å and complex (**3**) 1.718(5) Å this may be due to stronger electron donating nature of diethyl amine. Structure refinement data are given in Table A4, selected bond angles and bond lengths are given in caption to Fig. 3.3(b).

3.4.5 Single crystal X-ray structure of $[Co(SON(CN^{i}Pr_2)_2)_2]$ (5)

The single crystal X-ray structure of $[Co(SON(CN^{i}Pr_2)_2)_2]$ (**5**) shows cobalt(II) ion is tetrahedral with an S_2O_2 donor set. Within each of the two thiobiuret ligands, the four atoms of the urea or thiourea groups are close to being coplanar. However, overall, the two thiobiuret ligands all show significant deviation from planarity due to twisting about the central N atom; The dihedral angles between the two pairs of urea and thiourea are 124.2 (1) and 122.5 (2)°. In both ligands, the pattern of bond

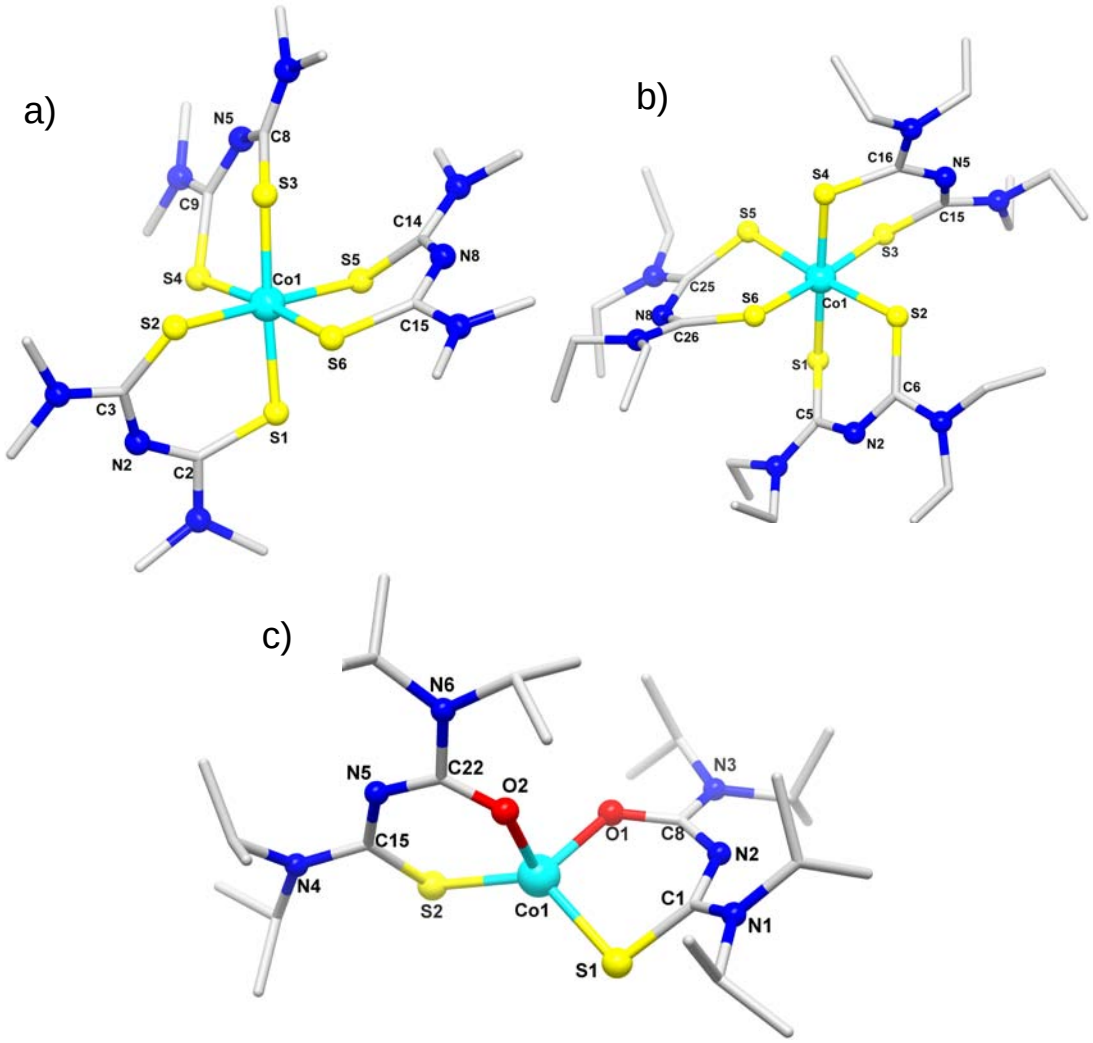

Fig. 3.3 (a) X-ray structure of (**3**). Selected bond lengths (Å) and bond angles (°): C1-N1 1.458(6), C2-S1 1.723(5), Co1-S4 2.231(1); C2-N2-C3 127.7(5), S4-Co1-S3 94.3(6). (b) X-ray structure of (**4**). Selected bond lengths (Å) and bond angles (°) C1-N1 1.454(4), C6-S2 1.723(4), C16-S4 1.737(4); N2-C5-S1 127.9(3), S2-Co1-S1 91.7(4). (c) X-ray structures of (**5**). Selected bond lengths (Å) and bond angles (°): Co(1)-O(1) 1.918 (7), Co(1)-S(2) 2.149, N(2)-C(8) 1.261(1), N(2)-C(1) 1.336(1); O(1)-Co(1)-S(1) 96.7 (2), C(8)-N(2)-C(1) 124.2 (1).

distances indicates that the formal negative charge is predominately localized on the S atom. The relatively long C-S and short C-O average bond lengths of 1.749(1) and 1.300(2) Å are consistent with mostly single and double bond character, respectively, and this bond localization is also reflected in the average C-N bond

distances to the central N atom: 1.336(2) Å in the (iso)thiourea group and 1.261 (2) Å in the urea group. One of the ligands is disordered over two sites and has been modelled using a ratio of 47:53. Structure refinement listed in Table A3. Selected bond angles and bond lengths are listed in caption to Fig. 3.3(c)

3.4.6 Thermogravimetric analysis (TGA)

Thermogravimetric analysis of complexes (**3**), (**4**) and (**5**) show that the complexes decomposed in a single step between 228-320, 210-329 and 140-230 °C, respectively with the observed final residue of 20.0% for complex (**3**) in good agreement with the calculated 19.5% for cobalt disulfide. The observed final residue 14.5% for complex (**4**) is close to the calculated 15.4% for cobalt disulfide and from complex (**5**) also observed final residue of 18.0% is close to the calculated value of 19.5% for cobalt disulfide

3.4.7 The AA-CVD deposition of cobalt sulfide thin films from $[Co(N(SCNMe_2)_2)_3]$ (3)

Film deposition was carried out at substrate temperature in the range 350-500°C with argon flow rate at of 160 sccm. No deposition was obtained below 350 °C. Films deposited at 350°C or 400°C were black in colour, not uniform, but adherent, whereas reflective black films were deposited at 450°C or 500°C. The XRD pattern of the deposited films at 350-500°C show formation of cobalt sulfide films indexed to NiAs type-hexagonal phase of $Co_{1-x}S$ (Fig. 3.4). No characteristic XRD peaks arising from possible impurities were detected. The intensity of the peaks increased with increasing deposition temperature. This observation suggests the formation of bigger crystallites at higher temperatures. The dominant peaks can be assigned to the (100), (101), (102) and (110) reflections of hexagonal $Co_{1-x}S$ as shown in Fig. 3.4. The SEM images of the films (Fig. 3.5) show that the morphology of the cobalt sulfide depends on the growth temperature.

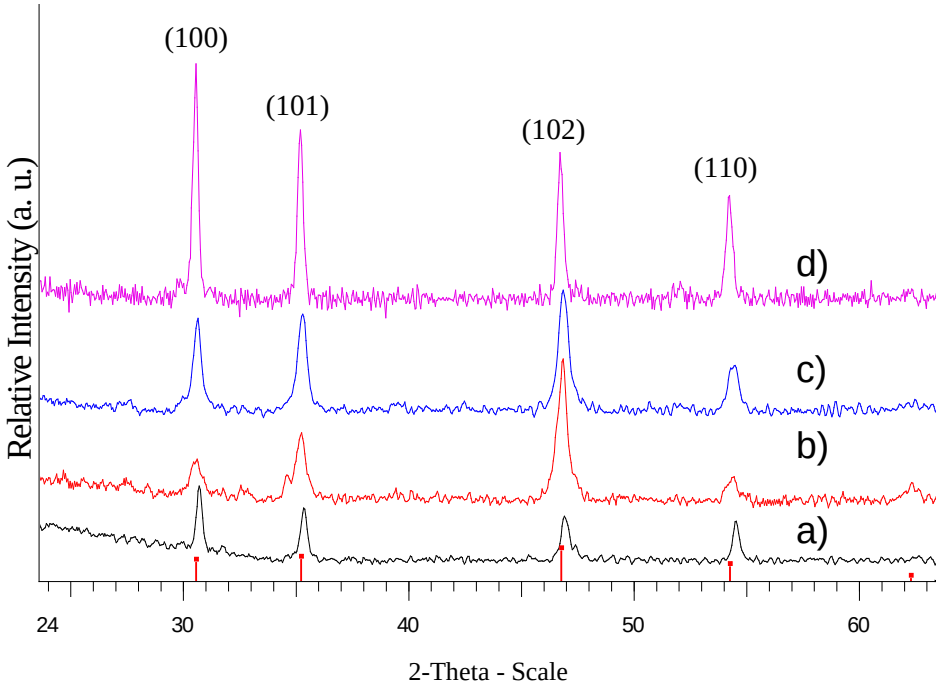

Fig. 3.4 XRD pattern of CoS films deposited on glass at (a) 350 °C (b) 400 °C (c) 450 °C and (d) 500 °C from $[Co(N(SCNMe_2)_2)_3]$ Solid lines are for hexagonal $Co_{1-x}S$ (ICDD-042-0826)

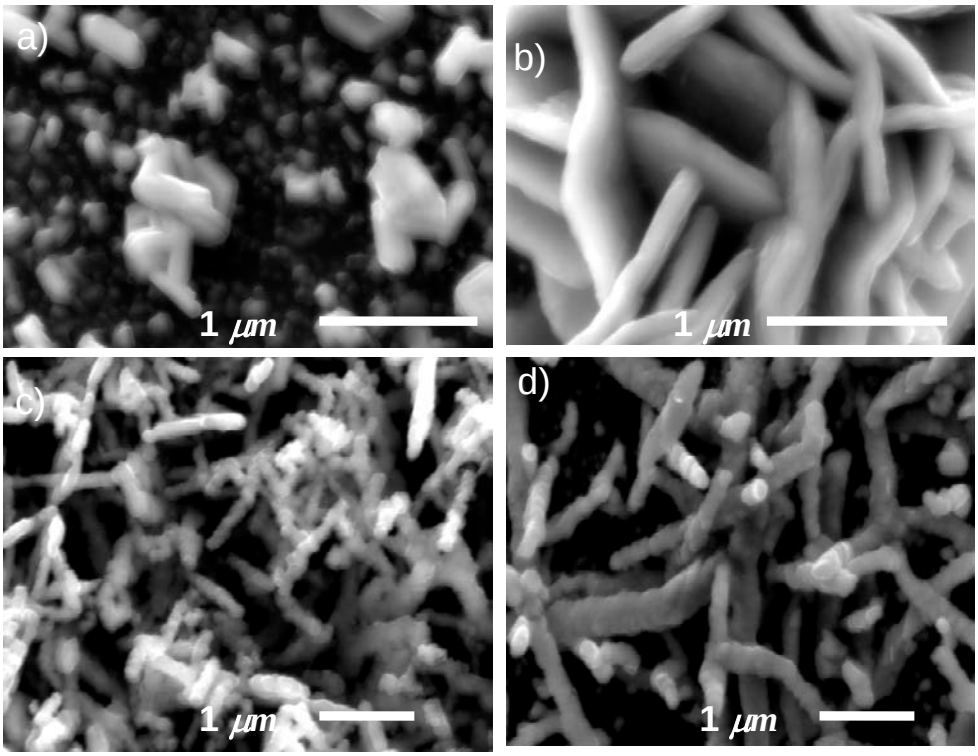

Fig. 3.5 SEM images of films deposited from $[Co(N(SCNMe_2)_2)_3]$ on glass at (a) 350 °C, (b) 400 °C (c) 450 °C and (d) 500 °C

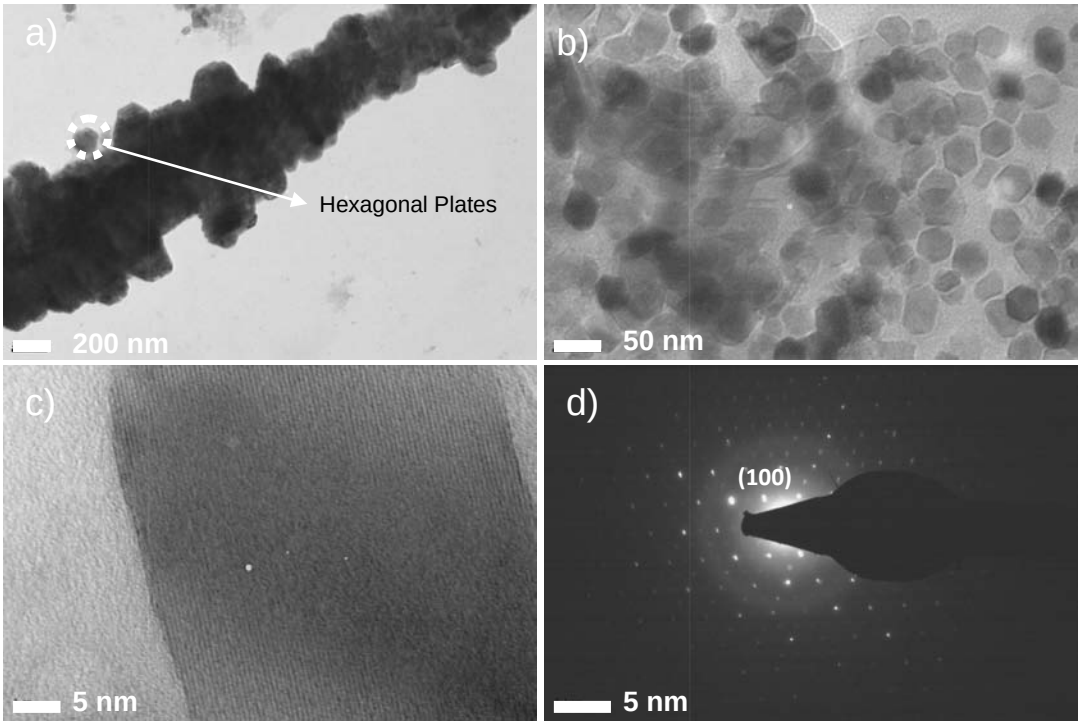

Fig. 3.6 TEM images of films deposited on glass at 500 °C (a), (b) low and high magnification (c) HRTEM image (d) SAED pattern from $[Co(N(SCNMe_2)_2)_3]$

The deposited films at 350°C consist of granular crystallites and rods whereas higher temperatures of 450°C or 500°C only rods were observed. The diameter of the rods increased from 200 to 500 nm as the deposition temperature was increased from 450 to 500 °C. EDX analysis showed the composition of the films as cobalt: sulfur 55:45 (350 or 400 °C, 53: 47 (450 °C) and 54: 46 (500 °C). The TEM image in Fig. 3.6, shows rods composed of hexagonal nanoplates. The size of the nanoplates ranged from *ca* 25-30 nm as shown in Fig. 3.6(b). The single hexagonal nanoplates have tendency to serve as the primal structure to form the secondary microrod structures. The driving force for the formation of microrods by oriented attachment mechanism has been reported as reduction in overall surface energy,[17] which can be realized by eliminating the surface at which the crystallites join. The proposed crystal growth mechanism has been described in work on ZnO,[18] TiO_2,[19] CuO,[20] ZnS[21] and CuS.[22] In this way, the oriented attached CoS will further attach to

eliminate the surface energy and form the secondary structure. Fig. 3.6(a) clearly shows the sidewise attachment of hexagonal nanoplates stacked together to form micro-sized rods. The SAED pattern in Fig. 3.6(d) shows the single crystalline nature of nanoplates. The diffraction spot can be indexed to the (100) plane of the hexagonal phase.

3.4.8 The AA-CVD deposition of cobalt sulfide thin films from $[Co(N(SCNEt_2)_2)_3]$ (4)

Film deposition was carried out at substrate temperature from 350 – 500 °C with argon flow rate of 160 sccm. No films deposition occurred below 350 °C. Black adherent films were obtained at the higher temperatures.

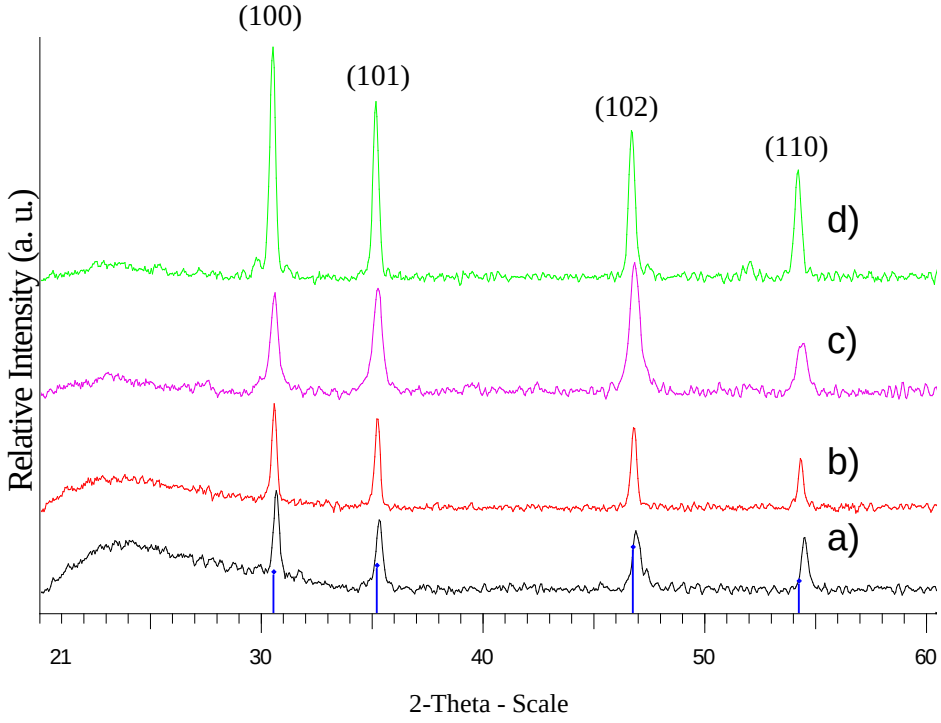

Fig. 3.7 XRD pattern of CoS films deposited from $[Co(N(SCNEt_2)_2)_3]$ on glass at (a) 350 °C,(b) 400 °C (c) 450 °C and (d) 500 °C. Solid lines are for hexagonal $Co_{1-x}S$ (ICDD-042-0826)

The XRD patterns of the deposited films at 350-500°C show formation of polycrystalline cobalt sulfide films, which could be indexed to NiAs type-hexagonal

phase of $Co_{1-x}S$ (Fig. 3.7). Higher intensities peaks were obtained for the films deposited at 450 or 500 °C.

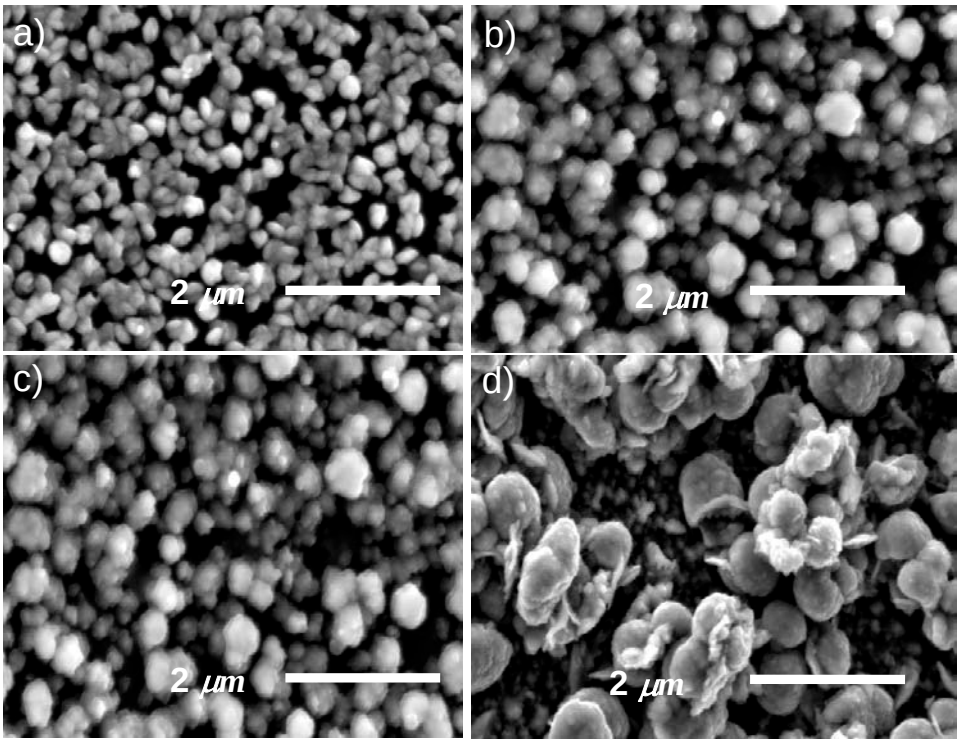

Fig. 3.8 SEM images of films deposited from $[Co(N(SCNEt_2)_2)_3]$ on glass at (a) 350 °C, (b) 400 °C (c) 450 °C and (d) 500 °C

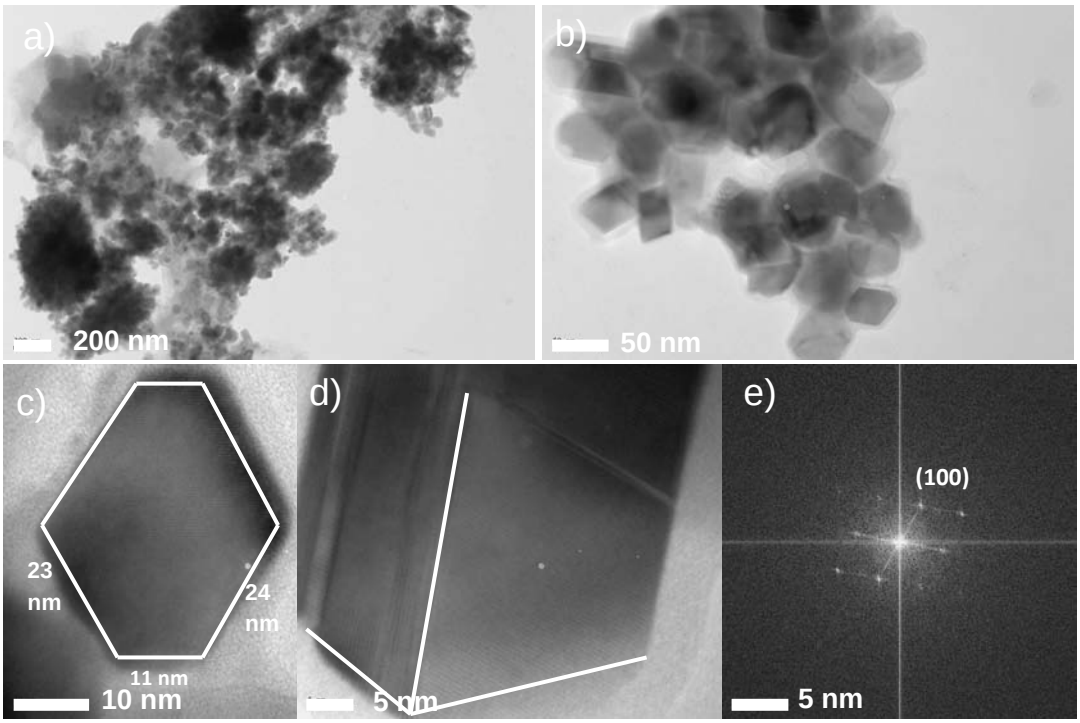

Fig. 3.9 TEM images of films deposited on glass at 500 °C (a), (b) low and high magnification (c), (d) HRTEM image (e) SAED pattern from $[Co(N(SCNEt_2)_2)_3]$

The dominant peaks can be assigned to the CoS(100), (101), (102) and (110) reflections of hexagonal $Co_{1-x}S$ as with the films grown from complex (**3**). The SEM images in Fig. 3.8, show that the growth of smaller individual granular crystallites (size 300-350 nm) at 350°C and 400°C, whereas granular clusters (size 450 – 500 nm) were formed in the films grown at 450 °C. Films deposited at 500 °C showed a flower like morphology (size 1-1.5 µm). EDX analysis shows that the films are composed of cobalt: sulfur 55: 45 (350 °C), 53: 47 (400 °C), 54: 46 (450 and 500 °C) 54:46. The Co: S ratio is closer to 1: 1 in the films deposited at temperatures higher than 350 °C. The TEM images (Fig. 3.9) of the samples from thin films grown at 500 °C showed flower-like crystallites composed of hexagonal nanoplates and nanocubes with sizes ranging from 30 to 35 nm. The growth of flower-like shape differs from the growth with complex (**3**) and may reflect imperfect oriented attachment growth of nanoplates. It is well known that the oriented attachment is not constrained to single structure, the only requirement is that the surface of the attaching particles be dimensionally similar.[23] The formation of dislocations at the bonding interface of may be the driving force for formation of imperfect oriented attachment. The SAED pattern in Fig. 3.9(e) shows the single crystalline nature of the nanoplates. The diffraction spot can be indexed to the (100) plane of the hexagonal phase. The complex (**3**) is structurally similar to complex (**4**), with an ethyl substituent rather than methyl. Thermo-gravimetric analysis of both complexes (**3**) and (**4**) gave residues of CoS_2. The XRD pattern of thin films deposited from both complexes (**3**) and (**4**) show the same phase ($Co_{1-x}S$) but with differing in morphology.

3.4.9 The AA-CVD deposition of cobalt sulfide thin films from $[Co(SON(CN^{i}Pr_2)_2)_2]$ (5)

Film deposition was carried out at substrate temperature from 280 to 400°C with an argon flow rate of 160 sccm. No deposition was obtained below 280°C.

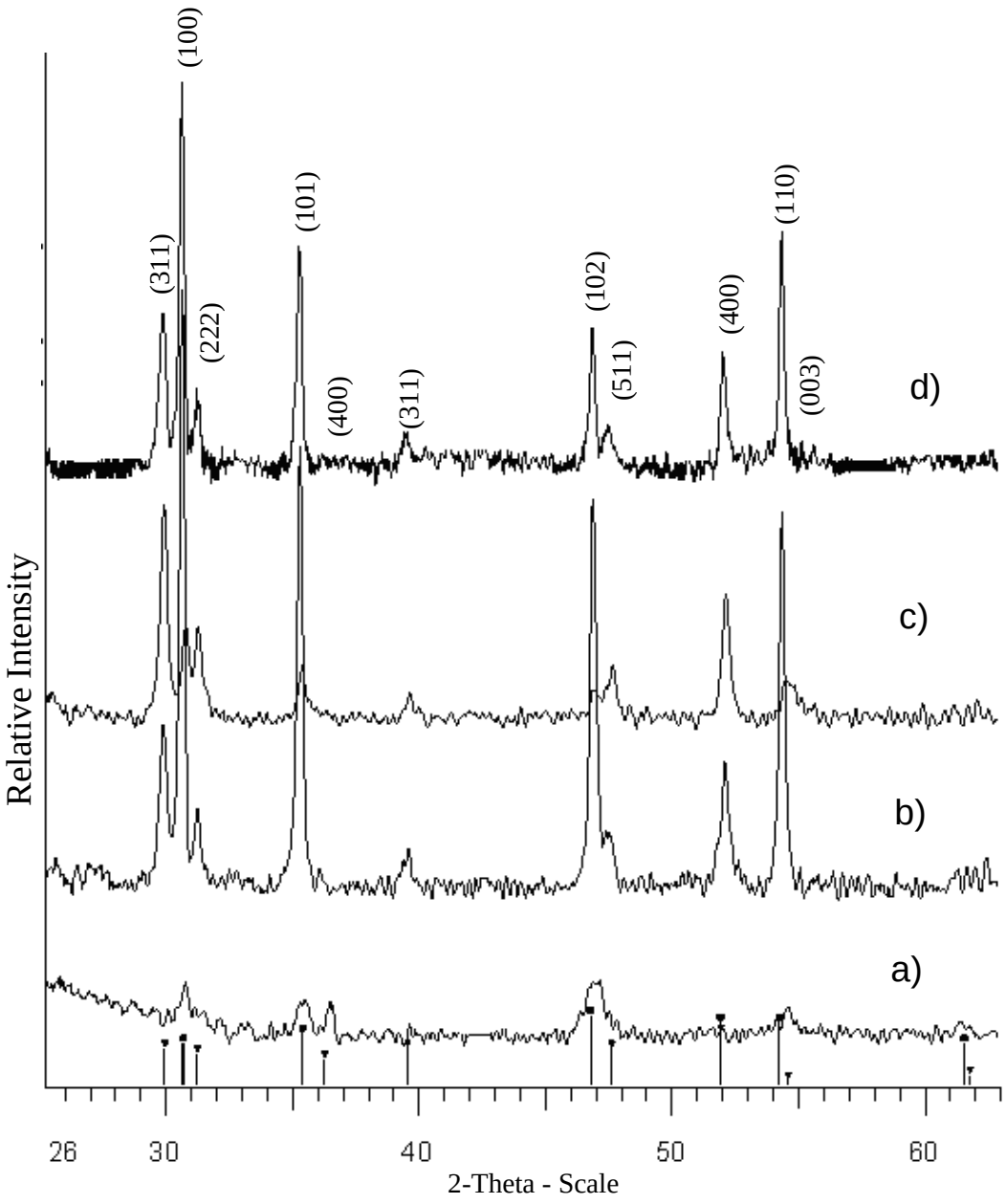

Fig. 3.10 XRD pattern of Cobalt sulfide films deposited on glass at (a) 280 °C, (b) 320 °C, (c) 360 °C and (d) 400 °C from $[Co(SON(CN^{i}Pr_2)_2)_2]$. Symbols (▼) indicating cubic (ICDD-02-1338) and (■) indicating hexagonal (ICDD-02-1458) Co_4S_3 phases.

Black, adherent films were deposited at 280°C and 320°C, whereas uniform, reflective, black films were deposited at 360 °C and 400 °C. The XRD pattern of the deposited films at 280-400 °C (Fig. 3.10) shows the formation of mixed-phase cobalt sulfide indexed to cubic and hexagonal phase of Co_4S_3. No characteristic XRD

peaks arising from possible impurities were detected. The X-ray diffraction peaks of films deposited at 280 °C show almost same intensities of cubic and hexagonal phase.

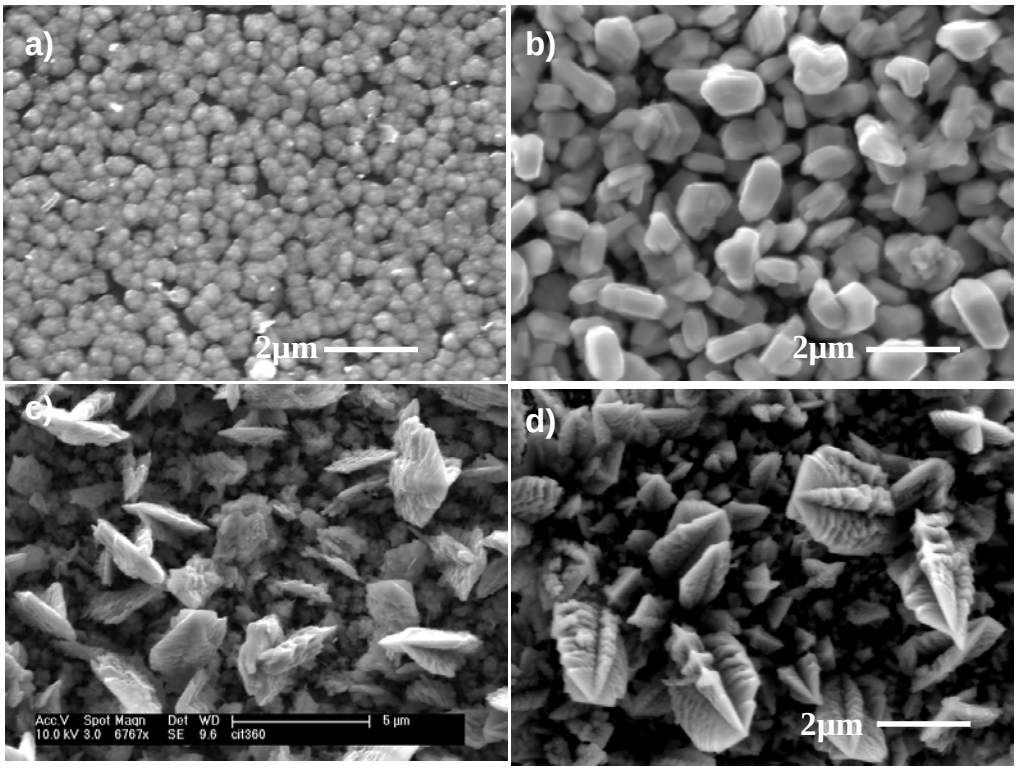

Fig. 3.11 SEM images of films deposited on glass at (a) 280 °C, (b) 320 °C, (c) 360 °C and (d) 400 °C from $[Co(SON(CN^{i}Pr_2)_2)_2]$ (**5**).

At higher temperature, hexagonal peaks are dominant. This shows formation of bigger hexagonal crystallites at higher temperatures. The XRD peaks can be assigned to the cobalt sulfide (100), (101), (102) and (110) reflections of hexagonal and (311), (222), (400), (331), (511) and (440) of cubic Co_4S_3 as shown in Fig. 3.10. The SEM images of the films (Fig. 3.11) show that the morphology of the cobalt sulfide is dependent on the growth temperature. Films deposited at 280°C consist of spherical crystallites with an average size of 250 nm and films at 320°C show the growth of cuboids. The same images from higher temperature films 360 or 400°C show as tree-like crystallites similar to stalagmite structures growing in the *z*-direction, which probably is due to stacking of the many smaller crystallites. EDX

analysis show composition of the films as cobalt: sulfur 60: 40 (280 and 320 °C), 61: 39 (360 °C) and 62: 38 (400 °C). The TEM images of the ground crystallites from the films grown at 400˚C show nanocubes of the size ranging from ca 25 to 30 nm as shown in Fig. 3.12(a).

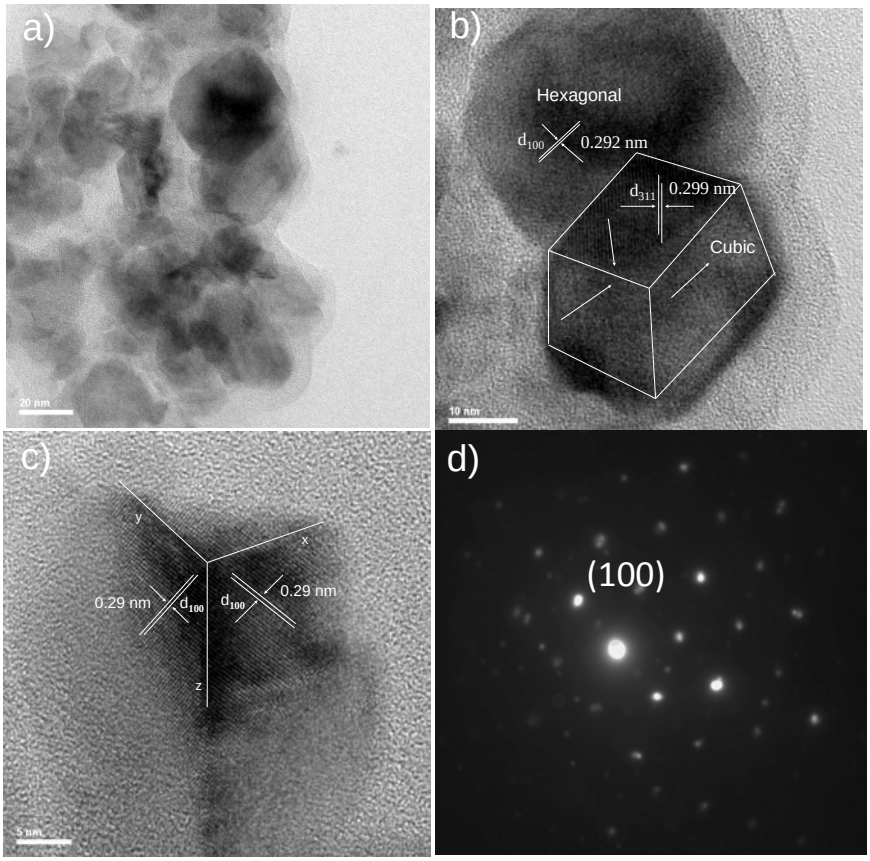

Fig. 3.12 (a) TEM images of cobalt sulfide films deposited from $[Co(SON(CN^{i}Pr_2)_2)_2]$ on glass at 400 ^{o}C, (b) and (c) HRTEM images. (d) SAED pattern.

HRTEM images of the nanocube (Fig. 3.12(b) and (c)) shows the lattice fringes with a d-spacing 0.292 nm corresponding to (100) reflection of hexagonal Co_4S_3 and 0.299 nm corresponding to (311) reflection of cubic Co_4S_3. The single nanocubes have a tendency to serve as the primal structure to form the secondary microcuboids structure. The SAED pattern in Fig. 3.12d shows single crystalline nature of nanoplates. The diffraction spot can be indexed to the (100) plane of the hexagonal phase.

3.4.10 Mechanistic studies by Py-GC-MS

Pyrolysis GC-MS is a useful technique to identify the decomposition behavior of the metal organic complexes.[24] We were able to propose the possible decomposition pathways from the relatively stable charged fragments observed in GC-MS. In Scheme 3.2 a plausible decomposition mechanism is presented for the complexes (**3**)**,** (**4**) and (**5**), summarizing the main intermediates and products. Each intermediate species can be rationalised through the observation of a corresponding fragment in the pyrolysis MS experiment and each species in Scheme 3.2 is presented with the m/z value corresponding to the fragment, if observed in one of the GC-MS experiments. The proposed mechanism involves common decomposition steps for complexes (**3**) and (**4**) whereas for complex (**5**) a slightly different pathway leads to the cobalt sulfides. In the first step the elimination of the dialkylamine occurs with the observed m/z value of 42 (**3**) and 73 (**4**) leading to the formation of common deaminated intermediate ***A*** for complexes (**3**) and (**4**). The second step involves the reductive elimination of a thiazolium group with the predominant m/z value of 102 for complexes (**3**) and (**4**), which is not observed for complex (**5**). This process is followed by elimination of CS group leading to the formation of bidentate S, N–donated cobalt complex ***C*** with a stable peak at 175 leading to the formation of cobalt sulfide (90.0).

The complex (**5**) also follows a similar decomposition pathway to that of (3) and (4) in first step, which involves the elimination of di-*iso*-propylamine with an observed mass value of 101. In the second step cleavage of Co-S bond occurs instead of a Co-O bond, leading to the formation of intermediate ***E***. The most significant aspect of the formation of intermediate ***E*** can be explained by the little observable difference in the bond-lengths Co-O 1.918, Co(1)-S(2) 2.149 therefore Co-S bonds are likely to be weaker. So the fragmentation would most likely result in preferential dissociation of the Co-S bond, ultimately resulting the formation of

intermediate ***E*** with an observed mass of 143. The decomposition of ***E*** leads to the formation of CoO or CoN (72), which is in contrast to the results obtained from AACVD, which show the deposition of cobalt sulfide films without any nitride or oxide impurities. This observation also shows that the GC/MS pyrolysis does not exactly provide the conditions under which a AACVD experiment works, although it gives us some clues to the decomposition pathways leading to the final product.

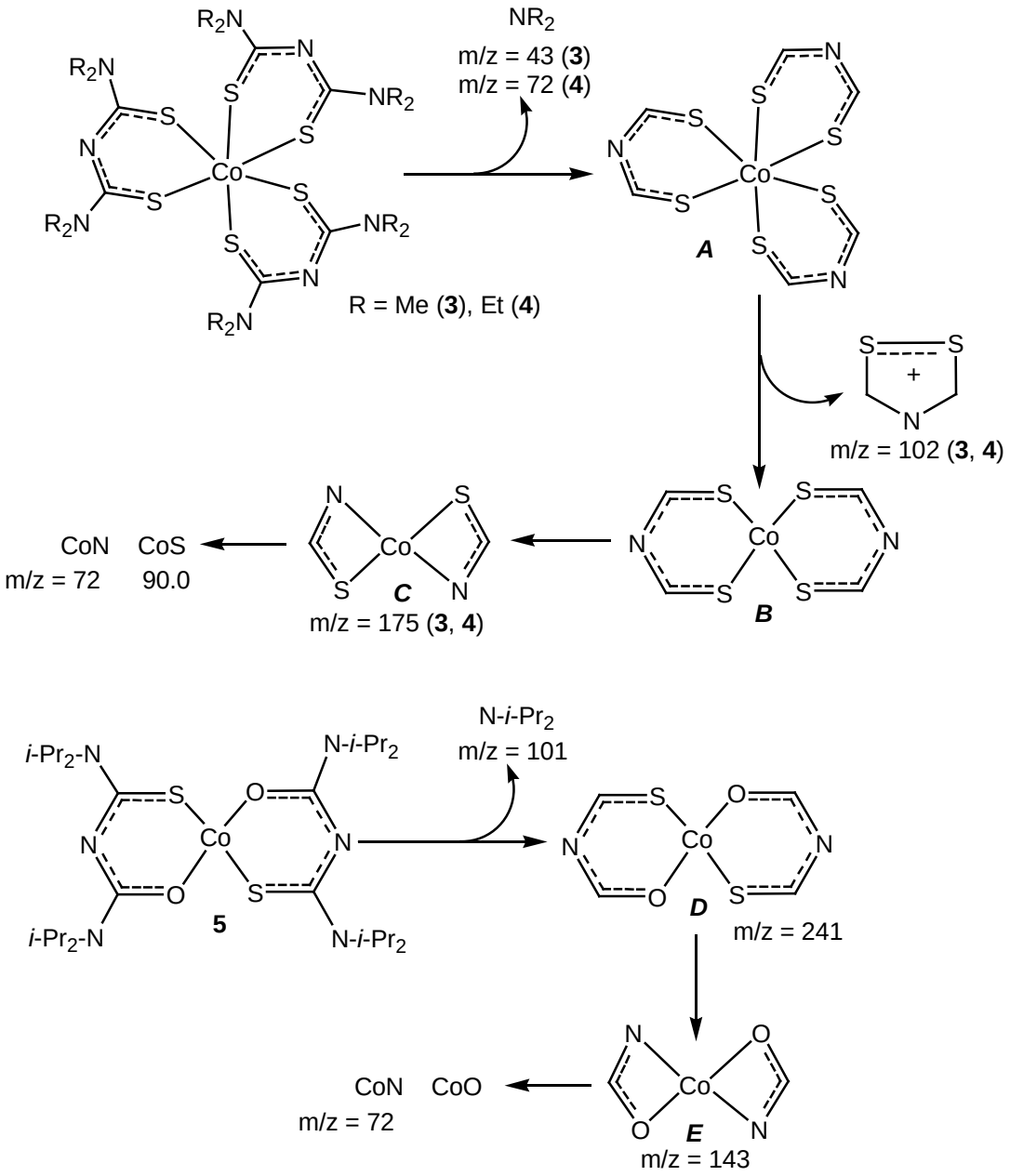

Scheme. 3.2 Plausible decomposition mechanism for (**3**), (**4**) and (**5**) from pyrolysis GC-MS studies.

3.4.11 Magnetic measurement of cobalt sulfide thin films

The electrons in cobalt sulfide occupy in partially filled d-subshells. From the magnetic measurement it should be possible to evaluate phase relationships which exist in cobalt sulfide systems. DC magnetization plot of $Co_{1-x}S$ thin films deposited on GaAs substrate at 400 ºC from complex (**3**) is shown in Fig. 3.13 (a). Magnetization versus temperature for ZFC and FC experiments at 1-kOe magnetic fields are given in Fig. 3.13 (a). It shows that the ZFC and FC curves superimpose to each other and increase with decreasing temperature which indicates the paramagnetic behavior of $Co_{1-x}S$ crystallites. The same paramagnetic nature was observed for the films deposited from complex (**4**). This result is in good agreement with the literature report for the same phase of nanoparticles.[25] On the other hand films of Co_4S_3 deposited from complex (**5**) showed ferromagnetic behavior. Heidelberg *et al.*[26] investigated the magnetic properties of various phases of cobalt sulfur systems, and reported that the composition region of Co_4S_3 was ferromagnetic below 1070 K. Magnetization versus field curves shows no measurable magnetization at 300 K. However on decreasing the temperature to 5 K, the increase in magnetization linearly observed as peculiar for paramagnetic substances with the highest magnetization value of 23.2 M(emu/g) for the $Co_{1-x}S$ films deposited from complex (**3**) (Fig. 3.13a, inset). 31.7 M (emu/g) for the $Co_{1-x}S$ films deposited from complex (**4**) (Fig. 3.13b, inset) and for Co_4S_3 films deposited from complex (**5**) is 2.1 M (emu/g). It suggests that the difference in the magnetization value of films deposited from complex (**4**), (**5**) and (**6**) due to shape anisotropy would exert a tremendous influence on their magnetic behavior.

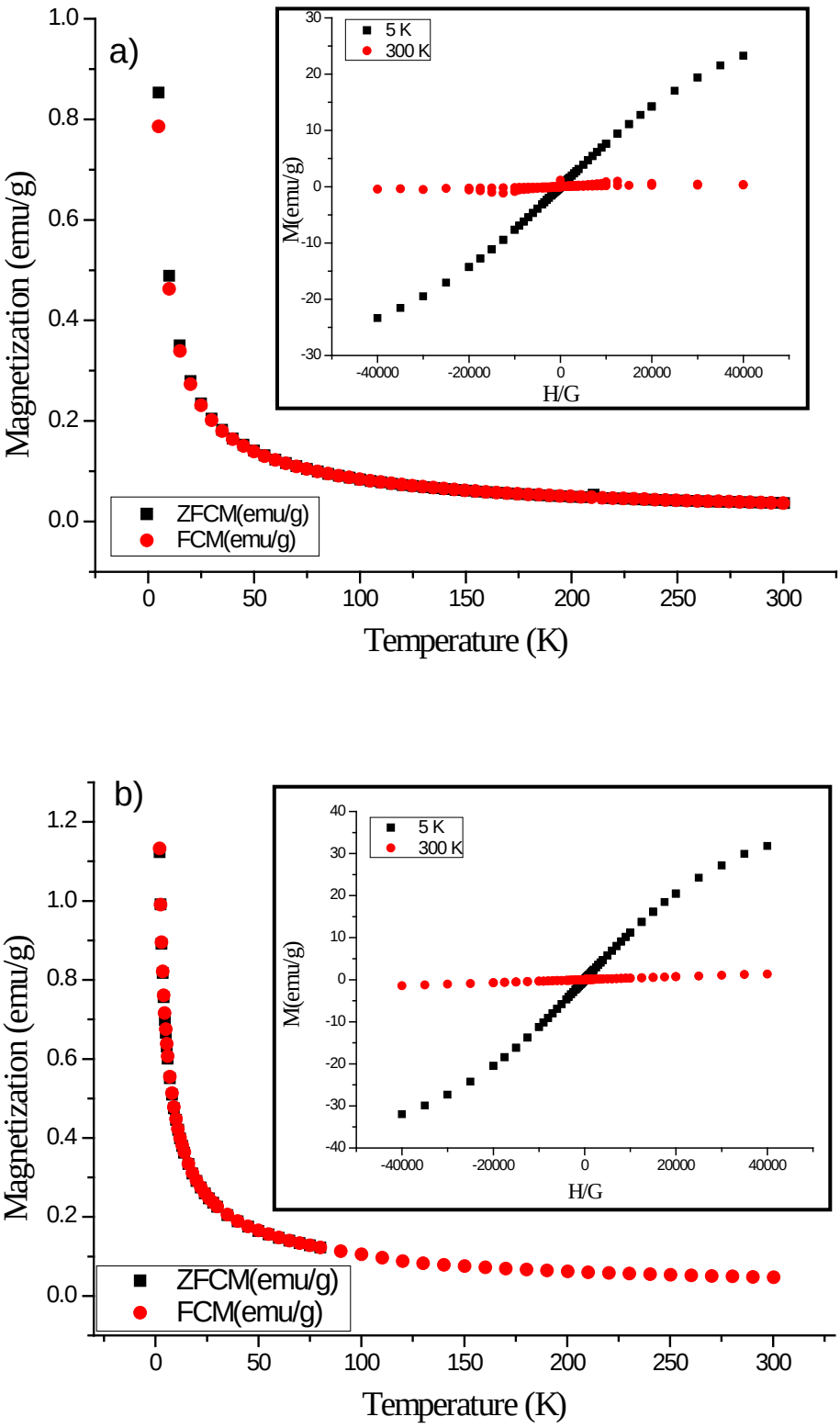

Fig. 3.13 Magnetic measurements of cobalt sulfide thin films deposited from a $[Co(N(SCNMe_2)_2)_3]$ and b) $[Co(N(SCNEt_2)_2)_3]$

3.4 Conclusion

Cobalt(III) complexes of 1,1,5,5-tetramethyl [$Co(N(SCNMe_2)_2)_3$], 1,1,5,5-tetraethyl-2,4-dithiobiuret [$Co(N(SCNEt_2)_2)_3$] and cobalt(II) complex of 1,1,5,5-tetra-iso-propyl-2-thiobiuret [$Co(SON(CN^iPr_2)_2)_2$] have been synthesized. The X-ray single crystal structures of complexes (**3**) and (**4**) contain one octahedral cobalt(III) centers, whereas the cobalt(II) in complex (**5**) is tetrahedral geometry. Thermogravimetric analysis shows all the complexes decompose in a single step to cobalt disulfide. AACVD from complexes (**3**) and (**4**) gave $Co_{1-x}S$ films whereas films of Co_3S_4 from (**5**). SEM images of the thin films deposited from complex (**3**) show rod-like morphology, granular and flower like films were deposited from complex (**4**) whereas cuboids and stalagmite structures from complex (**5**). TEM images of ground samples for the thin films from complex (**3**) showed hexagonal nanoplates stacked together to form rods. Similar TEM images from complex (**4**) gave flower-shaped crystallites composed with hexagonal nanoplates and nanocubes, whereas nanocubes are building blocks for the stalagmite like structures obtained from complex (**5**). SAED pattern confirms the single crystalline nature of nanoplates. Magnetic measurements showed the para or ferro-magnetic behavior of the $Co_{1-x}S$ and Co_4S_3 crystallites.

3.5 References:

1. G. B. Smith, A. Ignatiev, G. Zajac, *J. Appl. Phys.,* 1980, **51**, 4186.

2. T. M. Whitney, J. S. Jiang, P. Searson, C. Chien, *Science*, 1993, **261**, 1316.

3. G. H. Yue, P. X. Yan, X. Y. Fan, M. X. Wang, D. M. Qu, Z. G. Wu, C. Li, D. Yan, *Electrochem. Solid State Lett*., 2007, **10**, D29.

4. Y. G. Feng, T. He, N. Alonso-Vante, *Chem. Mater*., 2008, **20**, 26.

5. X. Y. Chen, Z. J. Zhang, Z. G. Qiu. C. W. Shi. X. L. Li, *J. Colloid Interface Sci.,* 2007, **308**, 271.

6. A. Wold, K. Dwight, Solid State Chemistry, 1993, Chapman and Hall, Inc. New York.

7. C. N. R. Rao, K. P. R. Pisharody, *Prog. Solid State Chem*., 1976, **10**, 207.

8. Z. Yu, J. Du, S. Guo, J. Zhang, Y. Matsumoto, *Thin Solid Films*, 2002, **415**, 173.

9. J. Ge. Y. Li, *Chem. Comm.*, 2003, 2498.

10. X. Luo, Z. Zhang, Y. Liang, *Langmuir*, 1994, **10**, 3213.

11. F. Srouji, M. Afzaal, J. Waters, P. O'Brien, *Chem. Vap. Deposition*., 2005, **11**, 91.

12. A. Paneerselvam, 2008, PhD thesis submitted to the University of Manchester.

13. K. Ramasamy, W. Maneerprakron, M. A. Malik, P. O'Brien, *Phil. Trans. R. Soc A.,* 2010, **368**, 4249.

14. K. Ramasamy, M. A. Malik, P. O'Brien, J. Raftery, *Dalton Trans*., 2010, **39**, 1460

15. L. Menabue, G. C. Pellacani, *J. C. S. Dalton*, 1976, 455.

16. R. Köhler, J. Sieler, R. Richter, E. Hoyer, L. Beyer, *Z. anorg. allg. Chem.,* 1989, **576**, 203.

17. R. L. Penn, J. F. Banfield, *Geochim*, *Cosmochim. Acta,* 1999, **63**, 1549.

18. B. Liu, H. C. Zeng, *J. Am. Chem. Soc*., 2003, **125**, 4430.

19. A. Chemseddine, T. Moritz, *Eur. J. Inorg. Chem.,* 1999, 235.

20. Z. P. Zhang, H. P. Sun, X. Q. Shao, D. F. Li, H. D. Yu, M. Y. Han, *Adv. Mater*., 2005, **17**, 42.

21. F. Huang, H. Z. Zhang, J. F. Banfield, *J. Phys. Chem. B.,* 2003, **107**, 10470.

22. H. Xu, W. Wang, W. Zhu, *Chem. Lett.,* 2006, **35**, 264.

23. R. L. Penn, J. F. Banfield, *Science,* 1998, **281**, 969.

24. M. Chunggaze, M.A. Malik, P. O'Brien, *J. Mater. Chem.,* 1991, **9**, 2433.

25. D. P. Dutta, G. Sharma, I. K. Gopalakrishnan, *Mater. Lett.,* 2008, **62**, 1275.

26. H. F. Heidelburg, A. H. Luxem, S. Talhouk, J. J. Banewicz, *Inorg. Chem*., 1966, **5**, 194.

Chapter 4
Nickel Sulfide Nanostructured Thin films*

4.1 Summary

This chapter describes the synthesis of nickel(II) complexes of several 1,1,5,5-tetraalkyl-2-thiobiurets (R = methyl (**1**); methyl, ethyl (**2**); ethyl (**3**); isopropyl (**4**)) and 1,1,5,5-tetraalkyl-2,4-dithiobiurets (R = methyl (**5**); methyl, ethyl (**6**); ethyl (**7**)). The single crystal X-ray structures of complexes (**1**), (**3**), (**4**), (**6**) and (**7**) were determined. Thermogravimetric analysis shows all seven complexes decompose in a single step to one or another form of nickel sulfide. The complexes were used as single-source precursors for the deposition of nickel sulfide thin films by aerosol assisted chemical vapor deposition (AACVD) at temperatures between 320 and 480 °C. Complex (**1**) gave orthorhombic Ni_7S_6 at all temperatures with spherical tipped, wire like crystallites at 320°C, and plates and wires at other temperatures. Complex (**2**) gave mixtures of hexagonal $Ni_{17}S_{18}$ and orthorhombic Ni_7S_6 with wires and plates. Complex (**3**) also led to mixture of hexagonal $Ni_{17}S_{18}$ and orthorhombic Ni_7S_6 phases but with plate-like crystallites. In contrast, complex (**4**) gave orthorhombic Ni_9S_8 with flower-like crystallites at 320 and 360°C and branched structures at 400°C. Complex (**6**) gave hexagonal $NiS_{1.03}$ at 360 and 400°C and orthorhombic Ni_7S_6 phase at 440 and 480°C with wires and rods composed of spherical particles. Complex (**7**) also led to hexagonal $NiS_{1.03}$ at 360 and 400°C and orthorhombic Ni_7S_6 at 440 and 480 °C, with rods composed of hexagonal plates. The composition of films deposited from all these complexes was confirmed by EDX analysis. The influence of the precursors on the nature of the deposited films is discussed.

*Part of the work has been published in *Dalton Trans.,* 2010, **39**, 1460 and *Chem. Mater.,* 2010 (doi:10.1021/cm102140t)

4.2 Introduction

The phase diagram for Ni-S system is more complex than that of the Fe or Co sulfides. In this system many crystalline phases and stoichiometries have been reported including: $Ni_{3+x}S_2$, Ni_3S_2, Ni_4S_{3+x}, Ni_6S_5, Ni_7S_6, Ni_9S_8, NiS, Ni_3S_4 and NiS_2.[1-3] Some compounds e.g. NiS and NiS_2 have been studied extensively, whilst for others only limited information is available.

NiS_2 (Vaesite) is a *p*-type semiconductor with a band gap of 0.5 eV. It is potentially useful in: photo electrochemical solar cells;[4,5] IR detectors;[6] catalysts;[7] and sensors.[8] It is also used as a hydrodesulfurisation catalyst and as a cathode material in rechargeable lithium batteries.[9] Nickel sulfide is considered as an "Achilles heel" in toughened glass, since it is responsible for glass cancer or spontaneous glass fracture.

Rhombohedral Ni_3S_2 (heazlewoodite) is yellow in colour and exhibits metallic properties. It has a slightly distorted body-centered cubic arrangement of sulfurs with the metal atoms in some of the pseudo-tetrahedral holes.[10] At temperature above 556 °C, it converts to $Ni_{3+x}S_2$, with an fcc structure.[11] In this phase a sub-stoichiometric number of metal atoms is randomly distributed in a cubic close-packed structure of sulfur atoms, with vacancies. The spinel-structured Ni_3S_4 (polydymite), at higher temperatures >400 °C, decomposes into NiS and NiS_2. At about 350 °C and 400 bar, Ni_3S_4 is converted into a hexagonal "NiAs-type" structure.[12,13]

Ni_7S_6 has been reported to exist in two polymorphic forms,[1] at higher temperature orthorhombic and at lower ones hexagonal, the phase transformation between these two polymorphs being sluggish. The crystal structure probably changes from hexagonal through monoclinic to orthorhombic as the stoichiometry changes, from Ni_9S_8 (through Ni_7S_6) to Ni_6S_5.[14]

NiS (millerite) has two polymorphs with unique properties.[15] At temperatures below 347 ºC, NiS has rhombohedral symmetry (millerite) and at high temperature it has the "NiAs- type" structure. In the rhombohedral form, the Ni atom is surrounded by five sulfur atoms in tetragonalpyramidal coordination, while in NiAs, each Ni is octahedrally coordinated. Rhombohedral NiS is a semimetal with temperature independent paramagnetism, whereas hexagonal NiS undergoes a first-order phase transition from a semiconducting antiferromagnetic phase to a metallic phase.[16]

Pramanik *et al*. have prepared nickel sulfide (NiS) films by solution growth on glass[17] or polymer substrates,[18] and Anuar *et al*. have electrodeposited this material.[5] In addition to the above techniques, nickel sulfide (NiS) films have been grown by successive ionic layer adsorption and reaction (SILAR),[19] laser ablation (NiS),[20] hydrothermal (Ni_3S_2, NiS),[21] soft solution-processing (Ni_3S_2, NiS_2, Ni_3S_4)[22] and CVD methods (NiS, NiS_2, Ni_7S_6).[23-26] Cheon *et al*. have reported the laser-driven photochemical vapour deposition of nickel sulfide from nickel bis(isopropylxanthate).[9] Nomura *et al*. studied the growth of $NiS_{1.03}$ from $[Ni(S_2CNEt_2)_2]$ on silicon (111) substrates by low-pressure chemical vapour deposition (LPCVD).[23] Earlier, O'Brien *et al.* have reported the deposition of nickel sulfide films from dithiocarbamate compounds of the type $[Ni(S_2CNRR')_2]$ where RR' = Et_2, MeEt, Me^{n}Bu or Me^{n}Hex, by AA[24] and LPCVD methods[25] and also from xanthate compounds of the type $[Ni(S_2COR)_2]$ where R = Et or ^{i}Pr by AACVD.[26] Recently Alam *et al*. have used pyridine adducts of nickel(II) xanthates as single source precursors for the deposition of nickel sulfide thin films by AACVD.[27]

There are no reports to deposit nickel sulfide thin films from nickel complexes of thiobiuret or dithiobiuret, except our preliminary report.[28] In this chapter the synthesis of the nickel(II) complexes of 1,1,5,5-tetraalkyl-2-thiobiuret (alkyl = methyl (**1**); methyl, ethyl (**2**); ethyl (**3**); isopropyl (**4**) and 1,1,5,5-tetraalkyl-2,4-dithiobiuret (alkyl = methyl (**5**); methyl, ethyl (**6**); ethyl (**7**) and the single crystal X-ray structure of complexes (**1**), (**3**), (**4**), (**6**) and (**7**) are reported. These

compounds were used as single source precursor for deposition of nickel sulfide thin films at relatively low temperature by AACVD

4.3 Experimental

4.3.1 Synthesis of [Ni(SON(CNMe$_2$)$_2$)$_2$] (1)

A solution of dimethylcarbamoyl chloride (1.0 g, 9 mmol) and sodium thiocyanate (0.75 g, 9 mmol) in acetonitrile (25 mL) was heated to reflux with continuous stirring for 1 h, during which time a fine precipitate of sodium chloride formed. To the cooled reaction mixture was added dimethylamine (40 % in water) (2.24 mL, 18 mmol) followed by stirring for 30 min and addition of nickel acetate tetrahydrate (1.15 g, 4.5 mmol). The crude product precipitated as a violet powder and was recrystallised from tetrahydrofuran to give suitable crystals for X-ray crystallography. Yield 1.89 g (50 %). Mpt: 286 °C. Mass (MS-APCI) (major fragments, m/z): 406 [M^+, Ni($C_6H_{12}N_3OS)_2$], 174 [NSO($CNMe_2$)$_2$]. IR (ν_{max} /cm^{-1}): 1531(b), 1481(s), 1456(b), 1346(s), 1255(b), 1193(b), 1110(b), 1028(s), 908(b), 828(s). Elemental analysis (%): Calc. For $C_{12}H_{24}N_6S_2O_2Ni$: C 35.4; H 5.9; N 20.6; S 15.7; Ni 14.4. Found: C 35.3; H 6.0; N 20.6, S 15.4; Ni 14.1.

4.3.2 Synthesis of [Ni(SON(CNMe$_2$CNEt$_2$))$_2$] (2)

Complex (**2**) was synthesized by method described for complex (**1**) using diethylamine. The crude product precipitated as a violet powder and was recrystallised from tetrahydrofuran. Yield 1.54 g (36 %). Mpt: 238 °C. Mass (MS-APCI) (major fragments, m/z): 462 [M^+, Ni($C_8H_{16}N_3OS)_2$], 202 [NSO($CNMeEt)_2$]. IR (ν_{max} /cm^{-1}): 1529(b), 1481(s), 1388(b), 1351(s), 1256(b), 1198(b), 1115(b), 1032(s), 922(b). Elemental analysis (%): Calc. For $C_{16}H_{32}N_6S_2O_2Ni$: C 41.5; H 6.9; N 18.1; S 13.8; Ni 12.6. Found: C 40.7; H 6.3; N 17.6; S 13.2; Ni 12.2.

4.3.3 Synthesis of $[Ni(SON(CNEt_2)_2)_2]$ (3)

Complex (**3**) was synthesized by method described for complex (**1**) using diethylcarbamoyl chloride (1.0 g, 7 mmol) and diethylamine (1.5 mL, 14 mmol). The solution kept aside overnight in room temperature gave violet crystals suitable for X-ray crystallography. Yield 1.32 g (35 %). Mpt: 140 °C. Mass (MS-APCI) (major fragments, m/z): 518 [M^+, $Ni(C_8H_{16}N_3OS)_2$], 258 [$NSO(CNEt)_2$]. IR (ν_{max} /cm^{-1}): 1539(b), 1514(s), 1474(s), 1474(s), 1428(b), 1401(b), 1370(s), 1350(s), 1296(b), 1253(s), 1222(b), 1174(b), 1107(s). Elemental analysis (%): Calc. For $C_{24}H_{48}N_6S_2O_2Ni$: C 46.2; H 7.7; N 16.2; S 12.3; Ni 11.2. Found: C 46.2; H 8.0; N 16.1; S 11.9; Ni 11.9.

4.3.4 Synthesis of $[Ni(SON(CN^iPr_2)_2)_2]$ (4)

Complex (4) was synthesized by method described for complex (**1**) using di-*iso*-propylcarbamoyl chloride (1.0 g, 6 mmol) and di-*iso*-propylamine (1.49 mL, 12 mmol). The solution kept aside overnight in room temperature gave violet crystals suitable for X-ray crystallography. Yield 1.78 g (46 %), mpt 177 °C; MS (APCI) major fragments: m/z = [M+] 631; $[Ni(C_{14}H_{28}N_3OS)_2]$, $[NSO(CN^iPr_2)_2]$ 284. IR (ν_{max} /cm^{-1}): 2966(s), 2927(s), 2361(s), 2336(s), 1520(s), 1494(m), 1428(m), 1356(m), 1285(m), 1262(m), 1209(m), 1148. Elemental analysis (%): Calc. For $C_{28}H_{56}N_6S_2O_2Ni$: C, 53.2; H, 8.8; N, 13.3; S, 10.1; Ni, 9.2 %. Found: C, 53.2; H, 9.0; N, 13.2; S, 9.9; Ni, 9.0.

4.3.5 Synthesis of $[Ni(N(SCNMe_2)_2)_2]$ (5)

A solution of dimethylthiocarbamoyl chloride (1.23 g, 10 mmol) and sodium thiocyanate (0.81 g, 10 mmol) in acetonitrile (25 mL) was heated to reflux with continuous stirring for 1 h, during which time a fine precipitate of sodium chloride formed. To the cooled reaction mixture was added 40 % solution of dimethylamine

(1.49 mL, 12 mmol) followed by stirring for 30 min and addition of nickel acetate tetrahydrate (0.76 g, 3 mmol). The crude product was isolated as brown powder. Yield 2.24 g (51 %). Mpt: 250 °C. Mass (MS-APCI) (major fragments, m/z): 438 [M^+, $Ni(C_6H_{12}N_3S_2)_2$], 190 [$N(SCNMe_2)_2$]. IR (ν_{max} /cm^{-1}): 1491(s), 1392(b), 1353(b), 1318(s), 1112(s), 1047(b), 977(b), 909(s). Elemental analysis (%): Calc. For $C_{12}H_{26}N_6S_4Ni$: C 32.6; H 5.8; N 19.0; S 29.0; Ni 13.3. Found: C 32.3; H 6.1; N 18.6; S 28.5; Ni 13.1.

4.3.6 Synthesis of $[Ni(N(SCNMe_2SCNEt_2))_2]$ (6)

Complex (**6**) was synthesized by method described for complex (**5**) using diethylamine. The crude product was isolated as brown powder. Diffusion from hexane and dichloromethane gave brown needles suitable for X- crystallography. Yield 1.65 g (35 %). Mpt: 191 °C. Mass (MS-APCI) (major fragments, m/z): 465 [M^+, $Ni(C_8H_{16}N_3S_2)_2$], 218 [$N(SCNMeEt)_2$]. IR (ν_{max} /cm^{-1}): 1484(s), 1417(b), 1371(b), 1346(s), 1325(s), 1263(s), 1231(b), 1126(s), 1076(s). Elemental analysis (%): Calc. For $C_{18}H_{32}N_6S_4Ni$: C 41.2; H 6.8; N 18.0; S 27.4; Ni 12.5. Found: C 40.4; H 6.5; N 17.1; S 26.0; Ni 12.2.

4.3.7 Synthesis of $[Ni(N(SCNEt_2)_2)_2]$ (7)

Complex (**7**) was synthesized by method described for complex (**5**) using diethylthiocarbamoyl chloride (1.0 g, 6 mmol) and diethylamine (0.68 mL, 12 mmol). The solution kept aside overnight in room temperature and brown crystals obtained suitable for X-ray crystallography. Yield 2.32 g (70 %). Mpt: 160 °C. Mass (MS-APCI) (major fragments, m/z): 550 [M+, $Ni(C_{12}H_{24}N_3S_2)_2$], 246 [$N(SCNEt_2)_2$]. IR (ν_{max} /cm-1): 1484(s), 1425(s), 1404(b), 1376(s), 1332(s), 1247(s), 1126(s), 1071(s), 992(b). Elemental analysis (%): Calc. For $C_{24}H_{48}N_6S_4Ni$: C 43.6; H 7.2; N 15.2; S 23.2; Ni 10.6. Found: C 43.7; H 7.5; N 15.2; S 22.8; Ni 10.2.

4.4 Results and discussion

The series of symmetrical and unsymmetrical nickel(II) complexes of 1,1,5,5-tetraalkyl-2-thiobiuret (alkyl = methyl, $[Ni(SON(CNMe_2)_2)_2]$ (**1**); methyl, ethyl, $[Ni(SON(CNMe_2CNEt_2))_2]$ (**2**); ethyl, $[Ni(SON(CNEt_2)_2)_2]$ (**3**); *iso*-propyl $[Ni(SON(CN^iPr_2)_2)_2]$ (**4**) and 1,1,5,5-tetraalkyl-2,4-dithiobiuret (alkyl = methyl, $[Ni(N(SCNMe_2)_2)_2]$ (**5**); methyl, ethyl $[Ni(N(SCNMe_2SCNEt_2))_2]$ (**6**); ethyl $[Ni(N(SCNEt_2)_2)_2]$ (**7**) were synthesised by the reaction of excess dialkylamine with *in situ* generated dialkylcarbamoylthiocyanate in acetonitrile.[29] A schematic representation for the synthesis of complexes shown in Scheme 4.1. All the complexes are air- and moisture- stable. Complexes 1-4, 6, 7 are soluble in most of nonpolar solvents. Complex (**5**) was seemingly insoluble in all common solvents, which makes the complex unsuitable for AACVD experiments.

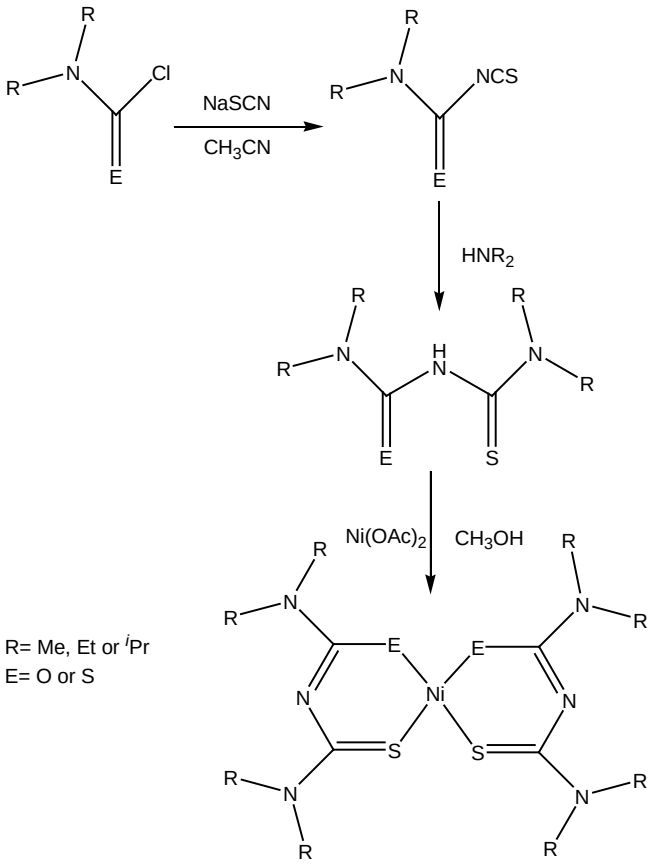

Scheme 4.1 Schematic representation of the synthesis of ligands and complexes

4.4.1 Single crystal X-ray structure of [Ni(SON(CNMe$_2$)$_2$)$_2$] (1)

The single crystal X-ray structure of [Ni(SON(CNMe$_2$)$_2$)$_2$] (**1**) shows the nickel(II) ion as square planar with an S_2O_2 donor set (Fig. 4.1(a)). The sulfur atoms are mutually *cis.* Both thiobiuret ligands of each unit chelate to form two six membered rings (NC_2OS-Ni). The crystal lattice shows the presence of monomeric independent units, which are separated by normal van der Waals distances. The average N-C-O and N-C-S angles are 129.8(4)° and 127.8(3)°. In both ligands, the pattern of bond distances indicates that the formal negative charge is predominately localized on the S atom. The relatively long C-S and short C-O average distances of 1.751(4) and 1.262(6) Å are consistent with predominantly single and double bond character respectively. This bond localization is also reflected in the average C-N bond distances to the central N atom: 1.327(5) Å in the (*iso*)thiourea group and 1.346 (6) Å in the urea group. The urea C(4)–N(2) bond within the chelate ring is substantially shorter than the exocyclic C–NMe_2 bond of 1.368(8) Å, but the thiourea C(3)-N(2) bond 1.334(7) Å is somewhat longer than the exocyclic C-NMe_2 bond 1.316(7) Å. The average metal to sulfur bond (2.139(1) Å) is longer than metal to oxygen bond (1.855(3) Å). The bond angles of O(1)-Ni(1)-S(1) and (2)-Ni(1)-S(2) are 94.98(2) and 95.59(1) respectively which are slightly larger than perfect square planar angle. Selected bond angles and bond lengths are listed in caption to Fig. 4.1. Structure refinement is listed Table A5.

4.4.2 Single crystal X-ray structure of [Ni(SON(CNEt$_2$)$_2$)$_2$] (3)

The single crystal X-ray structure of (**3**) shows nickel(II) ion is square-planar with an S_2O_2 donor set (Fig. 4.1(b). The sulfur and oxygen atoms are mutually *cis* at the edges of a square as observed in complex (**1**). The presence of the ethyl group leads to some deviation from planarity. The average N-C-O and N-C-S angles are

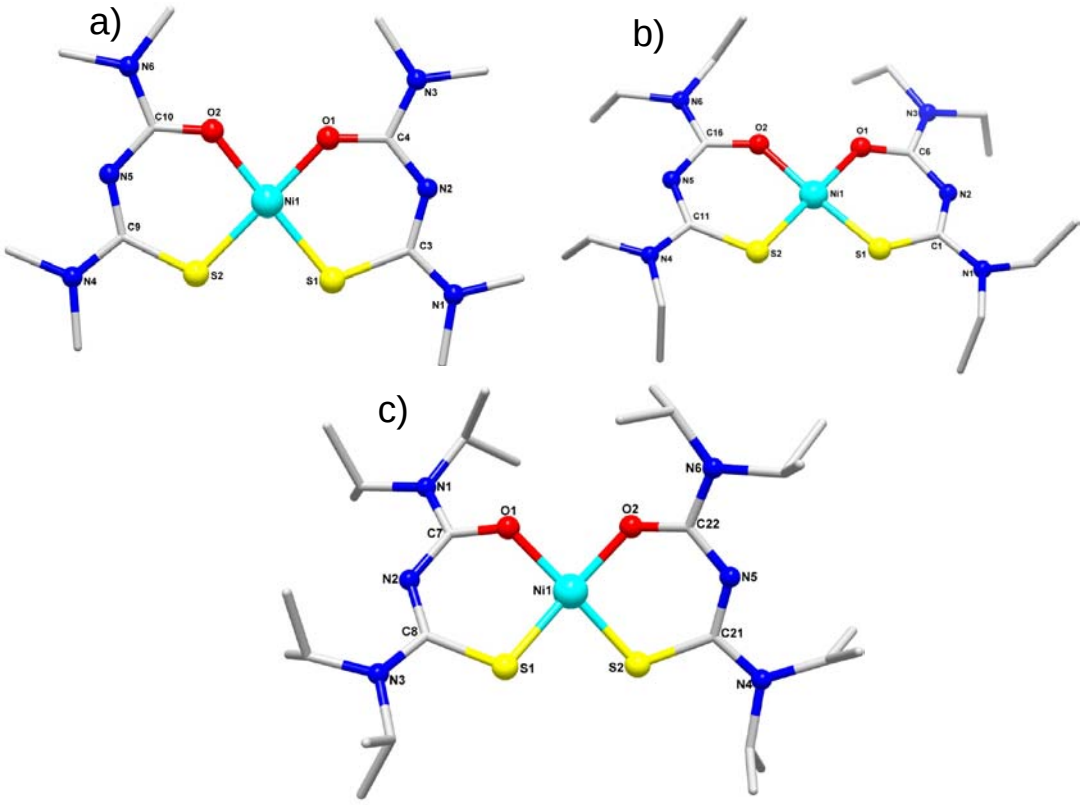

Fig. 4.1 (a) X-ray structure of (**1**). Selected bond lengths (Å) and bond angles (°): Ni1-O1 1.838(4), Ni1-S1 2.140(2), S1-C3 1.758(6), O1-C4 1.266(8); O1-Ni1-O2 83.89(2), O2-Ni1-S1 94.980(2). (b) X-ray structure of (**3**). Selected bond lengths (Å) and bond angles (°): Ni1-O1 1.872(1), Ni1-S1 2.136(6), S1-C1 1.744(2), O1-C6 1.267(2); O1-Ni1-O2 83.76(5), O1-Ni1-S1 94.520(4). (c) X-ray structure of (**4**). Selected bond lengths (Å) and bond angles (°): Ni1-O1 1.882(2), Ni1-S1 2.132(1), S1-C8 1.760(4), O1-C7 1.273(4); O1-Ni1-S2 168.81(9), O2-Ni1-S2 93.790(8)

are 129.2(1)° and 129.6(1)°. In both ligands, the pattern of bond distances indicates that the formal negative charge is predominately localized on the S atom. The relatively long C-S and short C-O average bond lengths of 1.745(1) and 1.273(1) Å are consistent with mostly single and double bond character as observed for complex (**1**), but the C-S bond is slightly shorter than the analogous distance observed in the crystal structure of complex (**1**). This bond localization is also reflected in the average C-N bond distances to the central N atom: 1.323 (1) Å in the (*iso*)thiourea group and 1.348(1) Å in the urea group, which are also shorter than the bond lengths observed for complex (**1**). The average metal to sulfur bond

(2.138 Å) is longer than metal to oxygen bond (1.859 Å). The bond angles of O(1)-Ni(1)-S(1) and (2)-Ni(1)-S(2) are 94.52(2) and 95.26(1) respectively which are slightly larger than perfect square-planar angle. Selected bond angles and bond lengths are given in the caption to Fig. 4.1. Structure refinement is listed Table A6.

4.4.3 Single crystal X-ray structure of [Ni(SON(CN^{i}Pr$_2$)$_2$)$_2$] (4)

The single crystal X-ray structure of [Ni(SON(CN^{i}Pr$_2$)$_2$)$_2$] (**4**) shows nickel as square planar with S_2O_2 donor set (Fig. 4.1(c)). The sulfur and oxygen atoms are *cis.* However, both thiobiuret ligands show significant deviation from planarity due to twisting about the central N atom; The average N-C-O and N-C-S angles are 128.2(2) and 125.9(2)°. In both ligands, the pattern of bond distances indicates that the formal negative charge is predominately localized on the S atom. The relatively long C-S and short C-O average bond lengths of 1.750(3) and 1.272(3) Å are consistent with predominantly single and double bond character respectively. This bond localization is also reflected in the average C-N bond distances to the central N atom: 1.324 (4) Å in the (*iso*)thiourea group and 1.346 (3) Å in the urea group. One of the *iso*-propyl groups in the ligand is disordered over two conformations in the ratio of 62:38. Selected bond angles and bond lengths are given in caption to Fig. 4.1. Structure refinement is listed Table A6. The effect of different alkyl groups on the ligand geometries in complexes (**1**), (**3**) and (**4**) is insignificant. However, there does seem to be a slight shortening of the Ni-S bond lengths, and lengthening of the Ni-O bond lengths in the series of complexes (**1**), (**3**) and (**4**), with the alkyl group changing from methyl to isopropyl.

4.4.4 Single crystal X-ray structure of [Ni(N(SCNMe$_2$SCNEt$_2$))$_2$] (6)

The single crystal X-ray structure of (**6**) shows that the nickel ion is in similar square planar environment to (**1**) and (**3**) with an S_4 donor set. The NiS_2C_2N rings adopt a slightly distorted chair conformation with dimethyl groups that are mutually *trans* (Fig. 4.2(a)). The average N-C-S angle is 129.0(2)° which is consist with complexes (**1**), (**3**) and (**4**). In both ligands, the pattern of bond distances indicates that the formal negative charge is delocalized over the NiS_2C_2N rings. The relatively long C(5)-S(1) and C(6)-S(2) bond lengths of 1.749(4) and 1.740(4) Å are consistent with mostly single bond character. The average thiourea C–N (1.329(4) Å bonds within the chelate ring are substantially shorter than the exocyclic C–NMe_2 (1.349(4) Å) bonds. The metal to sulfur bond (2.178(1) Å) is somewhat longer than observed for complex (**1**) (2.139(1) Å) and (**3**) (2.138(4) Å).

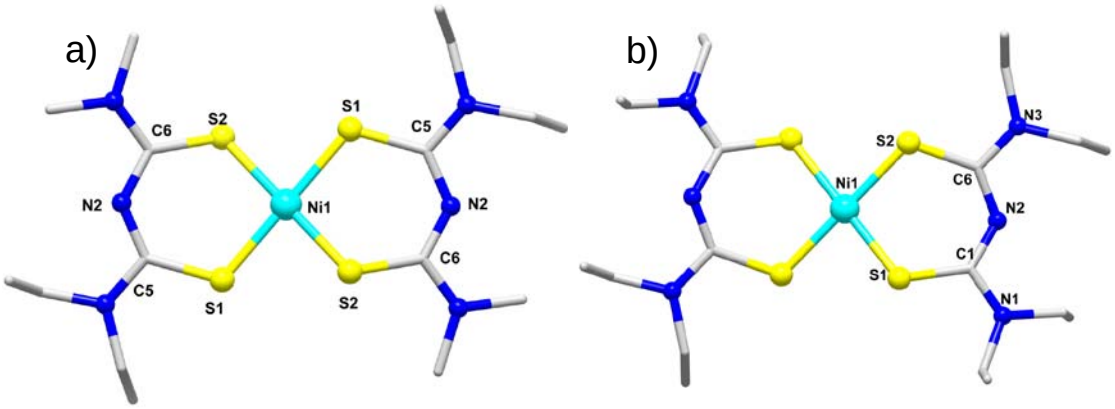

Fig. 4.2 (a) X-ray structure of (**6**). Selected bond lengths (Å) and bond angles (°): Ni1-S1 2.173(1), C6-S2 1.740(4), C5-S1 1.749(4), C6-N2 1.329(5); S1-Ni1-S2 96.51(4), N2-C5-S1 115.70(3). (b) X-ray structure of (**7**). Selected bond lengths (Å) and bond angles (°): Ni1-S1 2.164(1), C6-S2 1.740(3), C1-S1 1.741(3), C6-N2 1.332(4); S2-Ni1-S1 95.65(3), N2-C1-S1 129.40(3).

4.4.5 Single crystal X-ray structure of [Ni(N(SCNEt$_2$)$_2$)$_2$] (7)

The single crystal X-ray structure of (**7**) shows the nickel ion is in similar square planar environment to (**6**) with an S_4 donor set. The NiS_2C_2N rings adopt a

nearly perfect chair conformation (Fig. 4.2). The average N-C-S angle is 129.4(2)° which is consistent with complex (**6**). In both ligands, the pattern of bond distances indicates that the formal negative charge is delocalized over the NiS_2C_2N rings. The relatively long C(1)-S(1) and C(6)-S(2) bond lengths of 1.741(3) and 1.740(3) Å are consistent with mostly single bond character as observed for complex (**1**). The thiourea C–N bonds within the chelate ring are substantially shorter than the exocyclic C–NEt_2 (1.332(4) Å) bonds as like (**6**). The metal to sulfur bond (2.163(5) Å is somewhat longer than observed for complex (**1**) (2.139(1) Å), (**2**) (2.138(4) Å and (**4**) (2.129(1) Å) but shorter than bond distance observed for complex (**6**) (2.178(1) Å). The crystal lattice shows the presence of two monomeric independent units. Selected bond angles and bond lengths are given in caption to Fig. 4.2. Structure refinement is listed Table A7.

The above structural analyses show that all five thio and dithiobiuret complexes are monomers with nickel(II) in a square planar geometry. In complexes (**1**), (**3**) and (**4**) thiobiuret ligand coordinated through S_2O_2 donor set with two sulfur and two oxygen atoms are each mutually *cis.* The change in the alkyl group from methyl to isopropyl shortens the metal to sulfur bond in the thiobiuret complexes; in the dithiobiuret, the average metal to sulfur bond shortens on changing the alkyl groups from mixed methyl and ethyl in (**6**) to all in ethyl (**7**). In overall, metal to sulfur bond is shorter in thiobiuret complexes than dithiobiuret complexes.

4.4.6 Thermogravimetric analysis of thiobiuret complexes (1)-(4)

Thermogravimetric analysis (TGA) provides information about the decomposition processes and above the volatility of the precursors under study. TGA of the complexes $[Ni(SON(CNMe_2)_2)_2]$ (**1**), $[Ni(SON(CNMe_2CNEt_2))_2]$ (**2**), $[Ni(SON(CNEt_2)_2)_2]$ (**3**) and $[Ni(SON(CN^iPr_2)_2)_2]$ (**4**) indicated a single step decomposition with a rapid weight loss between 255-319 °C, 299-316 °C, 280-313

°C and 234-255 °C respectively (Fig. 4.3). The solid decomposition residue amounts to 24 % for (**1**), which is in agreement with the calculated value of 22.3 % for NiS

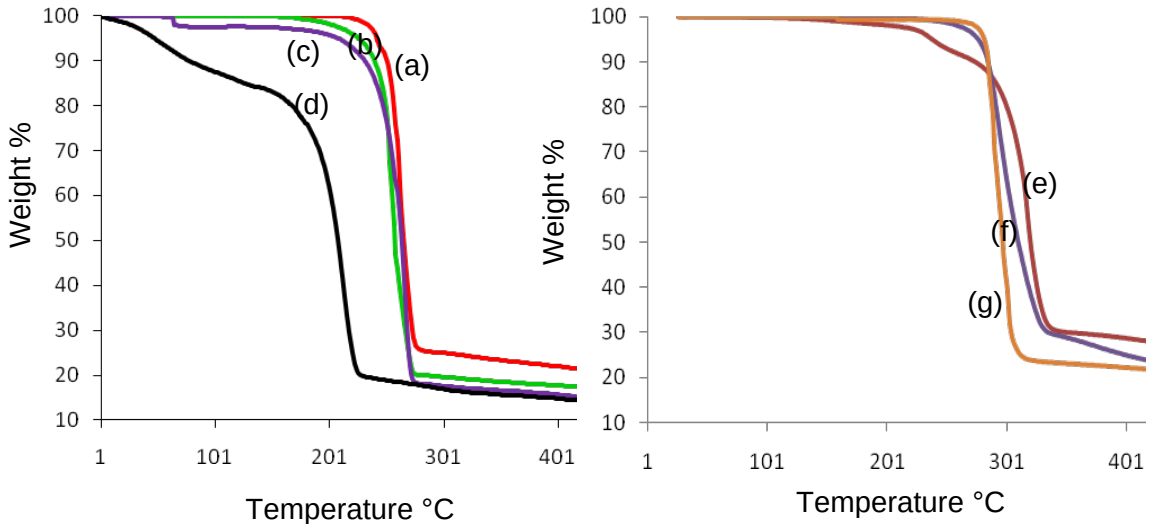

Fig. 4.3 TGA of complexes (a) $[Ni(SON(CNMe_2)_2)_2]$ (**1**), (b) $[Ni(SON(CNMe_2CNEt_2))_2]$ (**2**), (c) $[Ni(SON(CNEt_2)_2)_2]$ (**3**), (d) $[Ni(SON(CN^iPr_2)_2)_2]$ (**4**), (e) $[Ni(N(SCNMe_2)_2)_2]$ (**5**), (f) $[Ni(N(SCNMe_2SCNEt_2))_2]$ (**6**) and (g) $[Ni(N(SCNEt_2)_2)_2]$ (**7**)

Similarly, the observed final residues of 20.3 % for (**2**) 18.0 % for (**3**) which are in good agreement with the calculated values of NiS for 19.6 % and 17.4% respectively. Whereas the final residue observed for complex (**4**) of 21.4% is close to the calculated value of 19.4 % for nickel disulfide (Fig. 4.4)

4.4.7. Thermogravimetric analysis of dithiobiuret complexes (5)-(7)

The complexes $[Ni(N(SCNMe_2)_2)_2]$ (**5**), $[Ni(N(SCNMe_2SCNEt_2))_2]$ (**6**) and $[Ni(N(SCNEt_2)_2)_2]$ (**7**) decomposes in a single step with a loss of mass at temperatures between 257- 332 °C, 278-326 °C and 269-309 °C respectively (Fig. 4. 3). The observed final residue of 30.3 % for (**5**) is close to the calculated value of 28.0 for nickel disulfide. The final residue of 28.3 % for (**6**) is closer to the calculated value of 26.3 for nickel disulfide. Similarly the final residue obtained in decomposition of complex (**7**) is 23.2 %, in good agreement with the calculated

value of 22.2 % for nickel disulfide. The above thermogravimetric analysis show that thiobiuret complexes (**1**), (**2**), and (**3**) decomposes to NiS, but in contrast, the mass

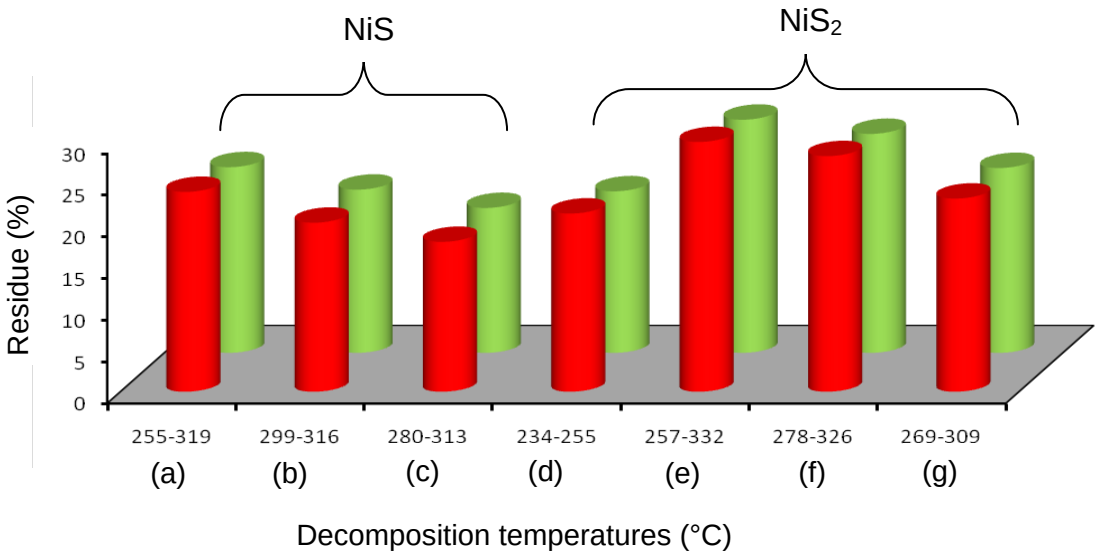

Fig. 4.4 Graph showing decomposition of precursors (a) $[Ni(SON(CNMe_2)_2)_2]$ (**1**), (b) $[Ni(SON(CNMe_2CNEt_2))_2]$ (**2**), (c) $[Ni(SON(CNEt_2)_2)_2]$ (**3**), (d) $[Ni(SON(CN^iPr_2)_2)_2]$ (**4**), (e) $[Ni(N(SCNMe_2)_2)_2]$ (**5**), (f) $[Ni(N(SCNMe_2SCNEt_2))_2]$ (**6**) and (g) $[Ni(N(SCNEt_2)_2)_2]$ (**7**). Calculated residue (red), observed residue (green)

of the final residue obtained from complex (**4**) is closer to that for NiS_2. The dithiobiuret complexes (**5**), (**6**) and (**7**) decompose in a single step into NiS_2.

4.4.8 The AA-CVD deposition of nickel sulfide thin films from $[Ni(SON(CNMe_2)_2)_2]$ (1)

The PXRD pattern of the deposited films at 320 - 440 °C (Fig. 4.5) show the deposition of Ni_7S_6 nickel sulfide, indexed as the orthorhombic phase of Ni_7S_6 (ICDD : 024-1021). The X-ray diffraction pattern of the films deposited at 320 °C showed amorphous materials with weak diffraction peaks. At 360 °C sharper peaks for (044) and (200) of Ni_7S_6 were obtained. Films deposited at 400 and 440 °C gave intense peaks of (121), (131) and (056) reflections. The major peaks (042), (121), (131), (312), (062) and (056) can be assigned to orthorhombic Ni_7S_6. The SEM images of

the films (Fig. 4.6) show that the morphology of the nickel sulfide is dependent on the growth temperature and growth period. Films deposited at 320 °C consist of wire-like crystallites with spherical tips. The average width of the wires was 200 ± 20 nm.

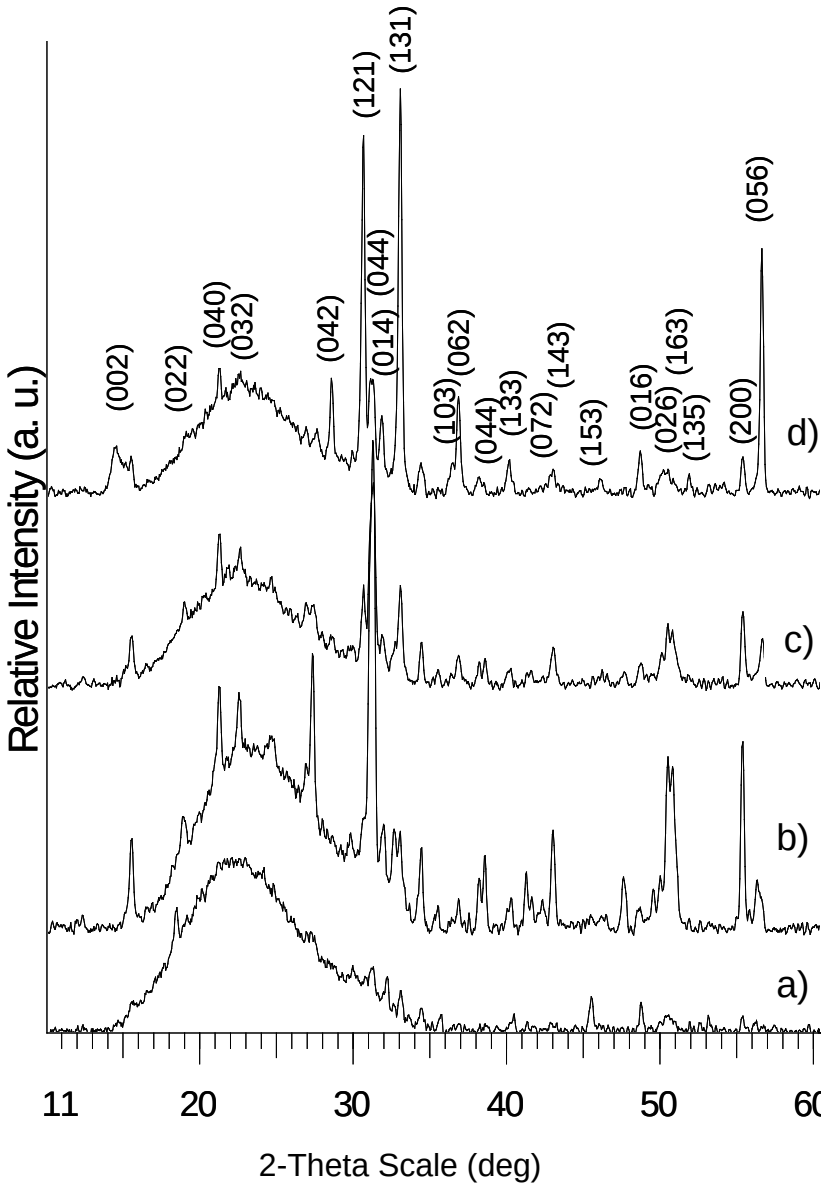

Fig. 4.5 PXRD pattern of nickel sulfide thin films deposited from $[Ni(SON(CNMe_2)_2)_2]$ (**1**) on glass at (a) 320 °C (b) 360 °C (c) 400 °C and (d) 440 °C.

Tilted SEM (45°) image showed an average length of 2 ± 0.1 μm (Fig. 4.7(a)). In order to identify the growth pattern of tipped wires, the deposition was stopped after 5 minutes and the SEM image of corresponding films showed initial formation of spherical crystallites (Fig. 4.7(b)). The films deposited at 360 and 400 °C consist of

wires and plates, whereas at 440 °C a pillar-like morphology composed of wires was obtained. EDX analysis of the films confirms the composition as Ni:S ratios : 55:45 (320 and 360 °C), 54:46 (400 °C) and 53:47 (440 °C).

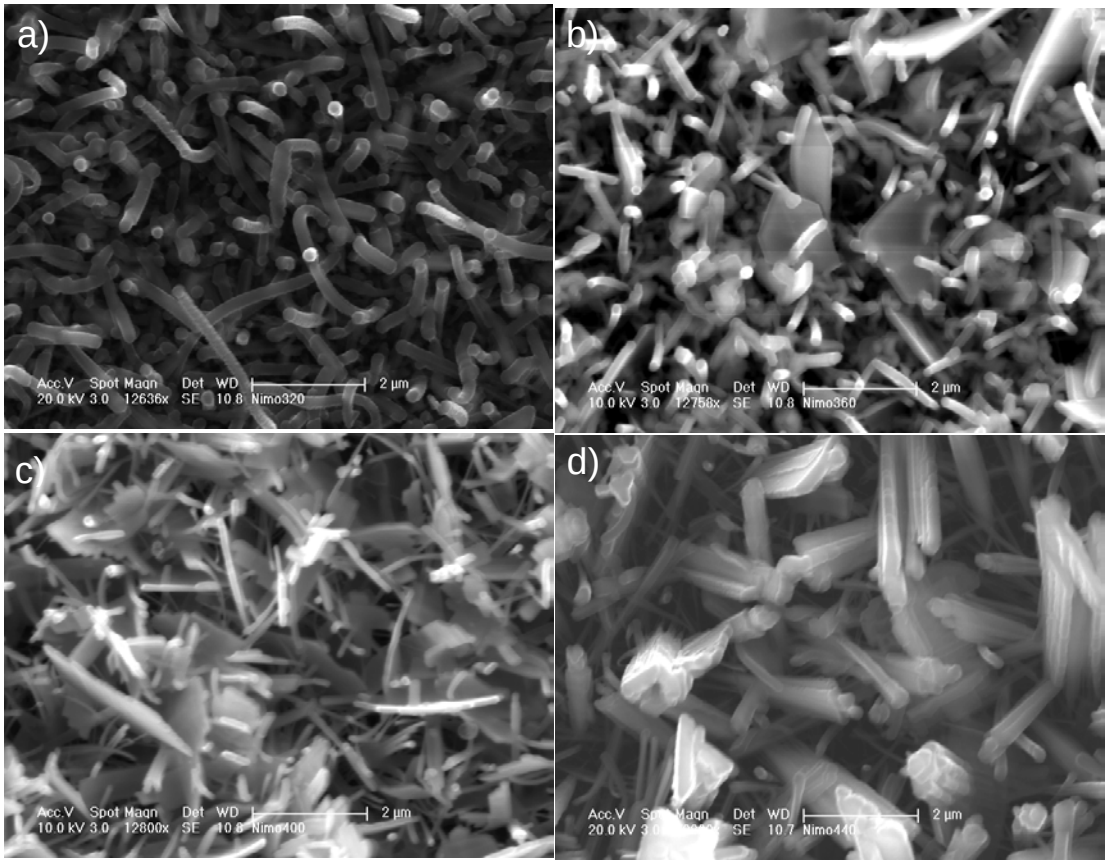

Fig. 4.6 SEM images of films deposited from $[Ni(SON(CNMe_2)_2)_2]$ (**1**) on glass at (a) 320 °C (b) 360 °C (c) 400 °C and (d) 440 °C.

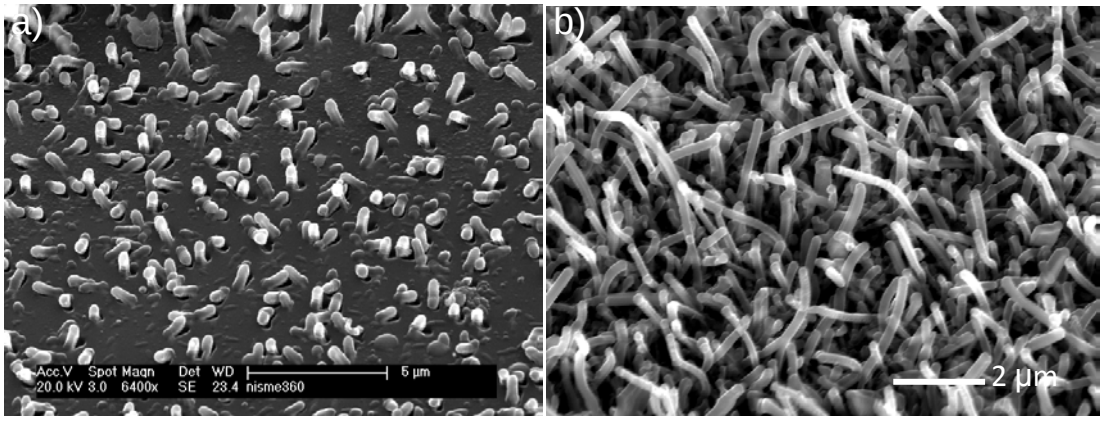

Fig. 4.7 Tilted SEM (45^o) images of films deposited from $[Ni(SON(CNMe_2)_2)_2]$ (**1**) on glass at 320 °C (a) 5 min (b) 60 min

The TEM images of scratched crystallites from the films grown at 440 °C show the width of nanobelts ranging from *ca* 20 to 30 nm as shown in Fig. 4.8(a).

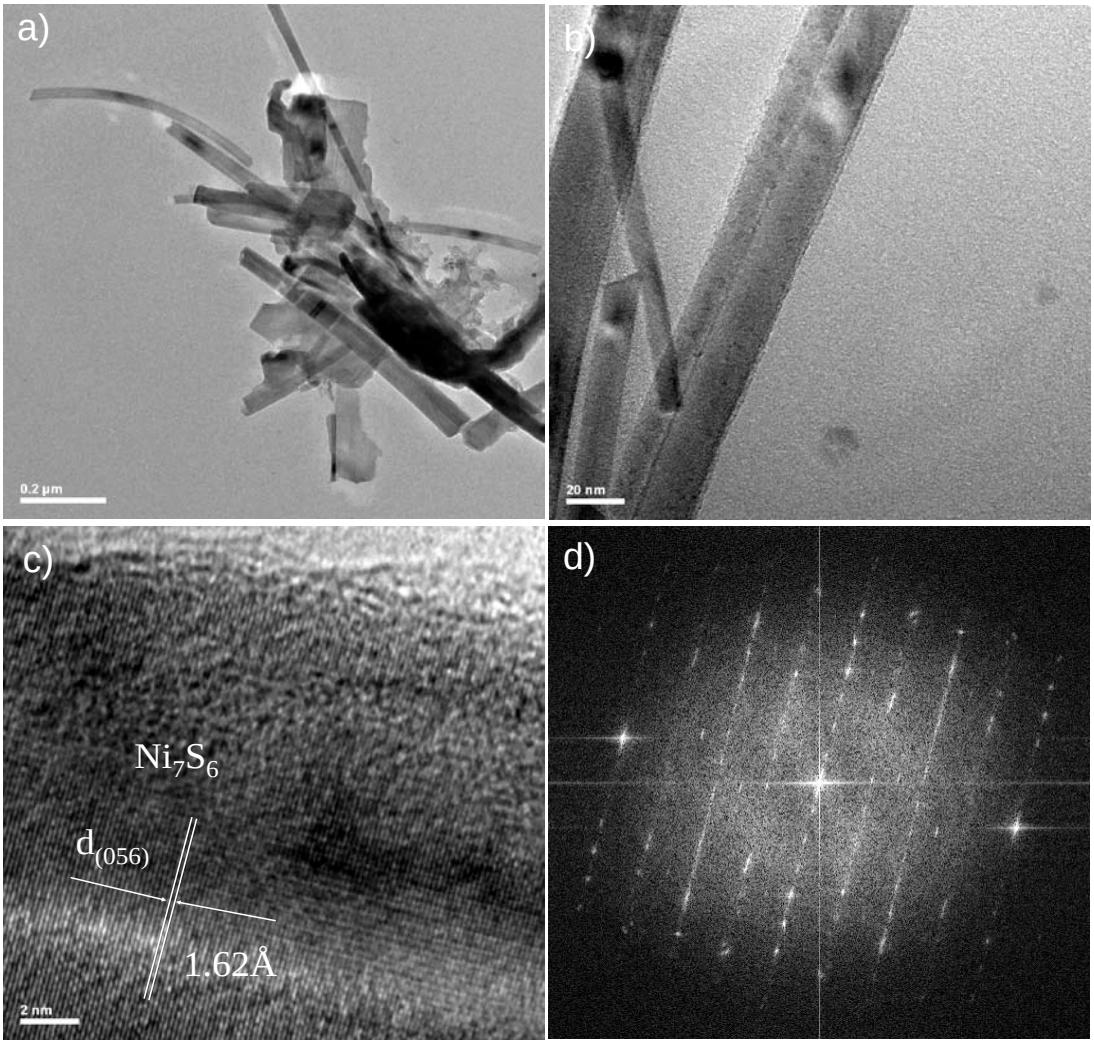

Fig. 4.8 a) and b) TEM images of nickel sulfide deposited from $[Ni(SON(CNMe_2)_2)_2]$ (**1**) on glass at 440 °C and (c) HRTEM images (d) SAED pattern.

HRTEM images of the nanobelts (Fig. 4.8(c) show the lattice fringes with d-spacing of 0.162 nm corresponding to (056) reflection of orthorhombic Ni_7S_6. The SAED pattern in Fig. 4.8(d) shows single crystalline nature of nanoplates. The diffraction spot can be indexed to the (121) plane of the orthorhombic phase.

4.4.9 The AA-CVD deposition of nickel sulfide thin films from [Ni(SON(CNMe$_2$CNEt$_2$))$_2$] (2)

Nickel sulfide film deposition was achieved in the temperature range between 320 - 440 ˚C. At 320 and 360 °C black, adherent films were deposited whereas at 400 and 440 °C uniform, black films were deposited. The powder X-ray

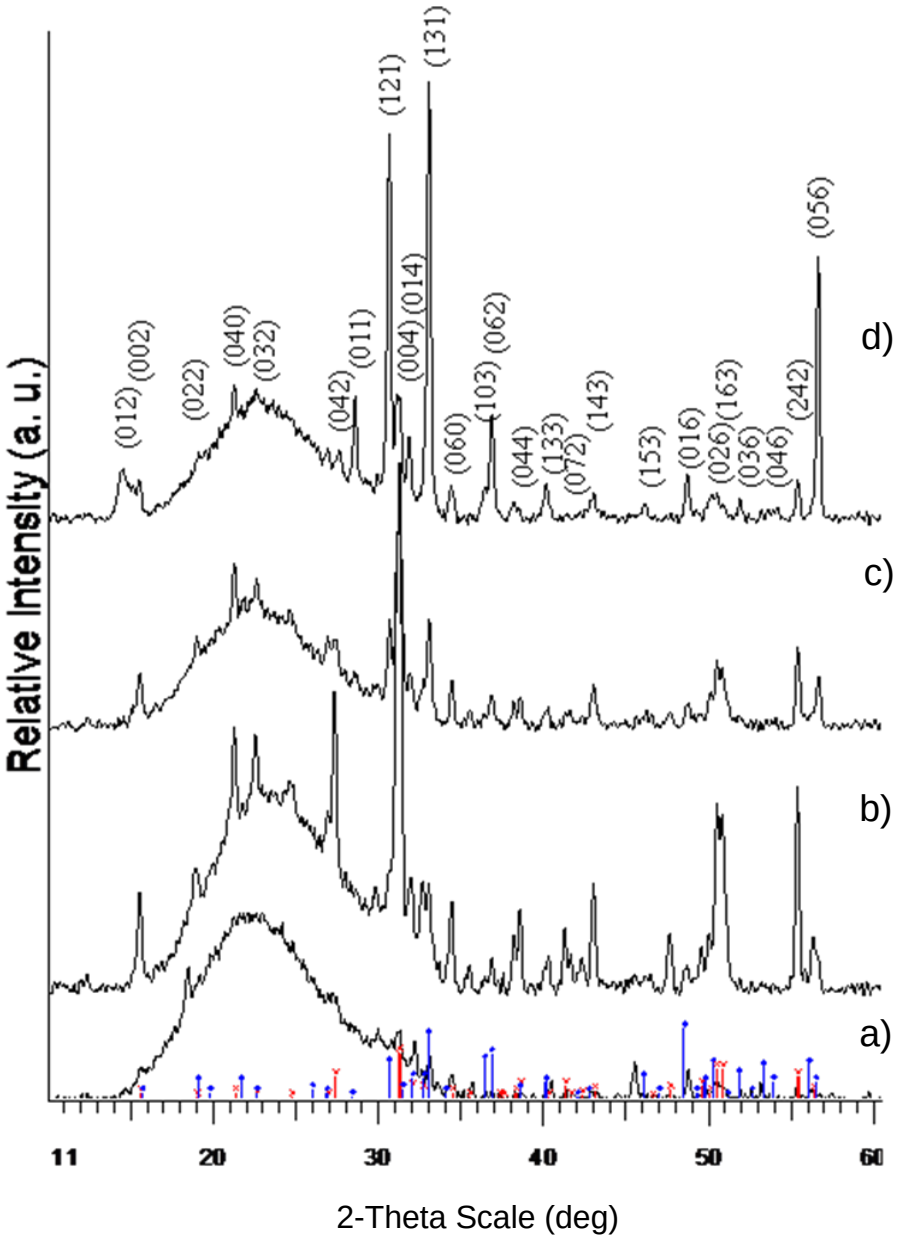

Fig. 4.9 PXRD pattern of nickel sulfide thin films deposited from [Ni(SON(CNMe$_2$CNEt$_2$))$_2$] (**2**) on glass at (a) 320 °C (b) 360 °C (c) 400 °C and (d) 440 °C. Red lines indicating or orthorhombic Ni_7S_6 and blue lines indicating hexagonal $Ni_{17}S_{18}$.

diffraction (PXRD) pattern of the deposited films at 320 - 440 °C from complex (**2**) show the mixture of hexagonal $Ni_{17}S_{18}$ (ICDD: 070-2306) and orthorhombic Ni_7S_6 phases (ICDD: 024-1021). The PXRD pattern obtained from the films deposited at 320°C show less intense peaks with almost the same ratio of orthorhombic and hexagonal phases. At 360°C the hexagonal phase was observed predominantly with high intensity peaks of (042), (004), (026), (163) and (242). At 400 °C almost the same ratio of both phases was obtained. Whereas PXRD pattern of films deposited at 440 °C show the deposition of higher amount of orthorhombic Ni_7S_6 with major diffraction peaks of (121), (131), (062) and (056) planes (Fig. 4.9). The transformation of the sulfur-rich hexagonal $Ni_{17}S_{18}$ phase to the sulfur deficient orthorhombic Ni_7S_6 phase when increasing deposition temperature, could be explained by the loss of sulfur at higher deposition temperature.

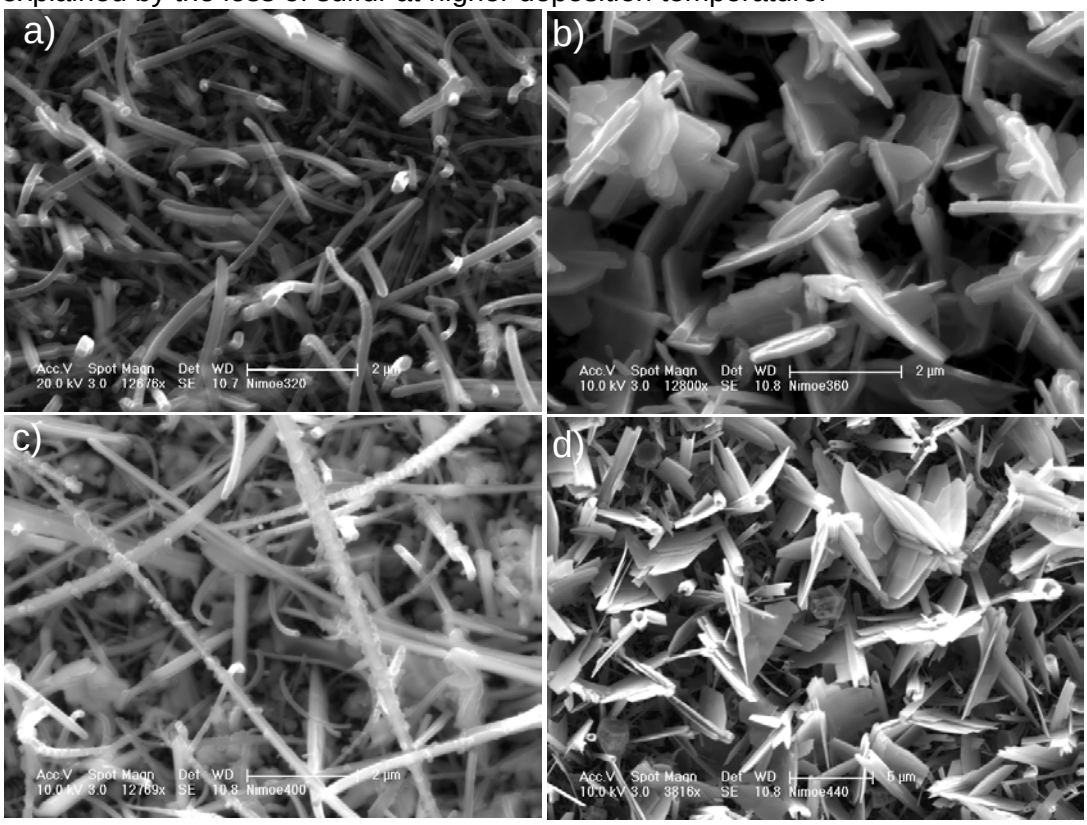

Fig. 4.10 SEM images of films deposited from [Ni(SON(CNMe$_2$CNEt$_2$))$_2$] (**2**) on glass at (a) 320 °C (b) 360 °C (c) 400 °C and (d) 440 °C

The SEM images of nickel sulfide thin film deposited from complex (**2**) are shown in Fig. 4.10. The morphology of the film is dependent on growth temperature.

At 320°C almost-uniform wires of crystallites were obtained with an average width of 200 ± 20 nm and several microns length. At 360°C plate-like crystallites with an average thickness of 200 ± 15 nm were obtained. At 400°C wire crystallites with a rough surface were deposited. The average width of the wires was 300 ± 20 nm, with a length of several microns, whereas at 440 °C plates of crystallites stacked together one over another were seen.

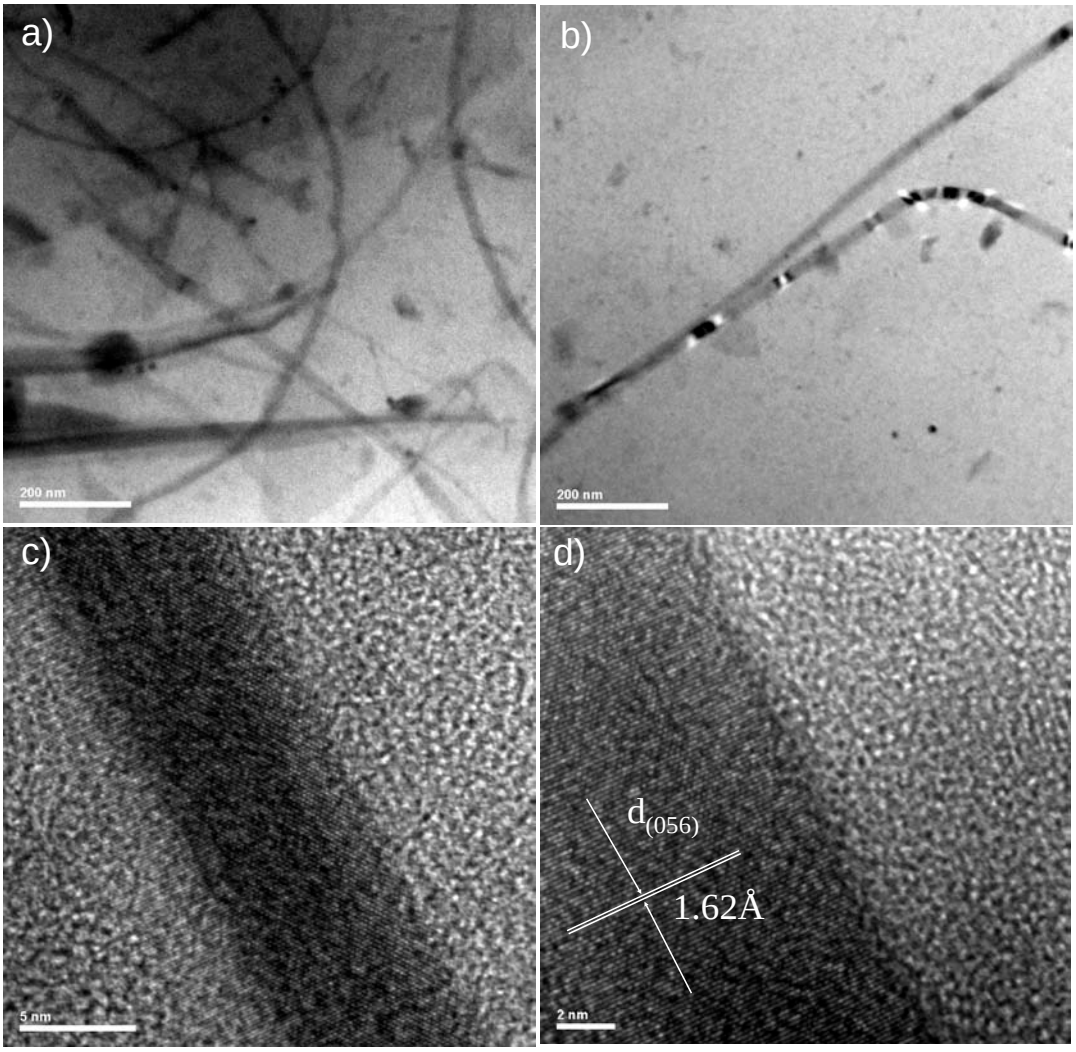

Fig. 4.11 a) and b) TEM images of nickel sulfide deposited from $[Ni(SON(CNMe_2CNEt_2))_2]$ (**2**) on glass at 440 °C and (c) and (d) HRTEM images.

The average thickness of plates could be measured as 150 ± 10 nm. The morphology of films deposited from complex (**2**) is entirely different from the morphology of films deposited from complex (**1**). This observation may be explained

by the presence of the diethyl group on complex (**2**) altering the decomposition of complex inside the CVD reactor. The composition of films deposited from complex (**2**) confirmed by EDX analysis as Ni:S ratios : 52.6:47.4 (320 °C), 53.6:46.4 (360 °C), 54.6:45.4 (400 °C) and 54.3:45.7 (440 °C). The TEM images show the scratched crystallites from the films grown at 400 °C consist of nanobelts with an average width of 15 ± 2 nm (Fig. 4.11(a)). HRTEM images of the nanobelts (Fig. 4.11(d)) show the lattice fringes with d-spacing of 0.162 nm corresponding to (056) reflection of orthorhombic Ni_7S_6.

4.4.10 The AA-CVD deposition of nickel sulfide thin films from $[Ni(SON(CNEt_2)_2)_2]$ (3)

Thin films of nickel sulfide have been deposited from complex (**3**) in the temperature range of 320 to 440 °C on glass substrate. Black, adherent, uniform films were deposited at all temperatures. The powder X-ray diffraction (PXRD)

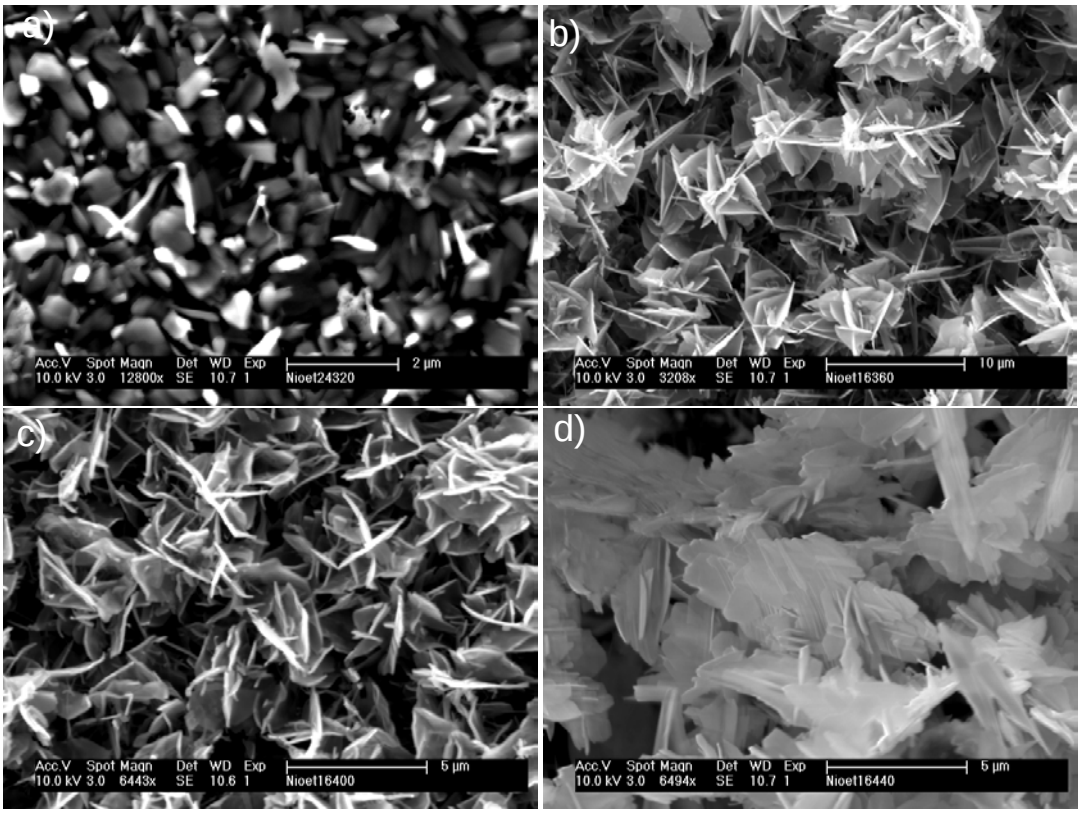

Fig. 4.12 SEM images of films deposited from $[Ni(SON(CNEt_2)_2)_2]$ (**3**) on glass at (a) 320 °C (b) 360 °C (c) 400 °C and (d) 440 °C

pattern of as deposited films at 320 - 440 °C from complex (**3**) show a mixture of hexagonal $Ni_{17}S_{18}$ (ICDD: 070-2306) and orthorhombic Ni_7S_6 (ICDD: 024-1021).

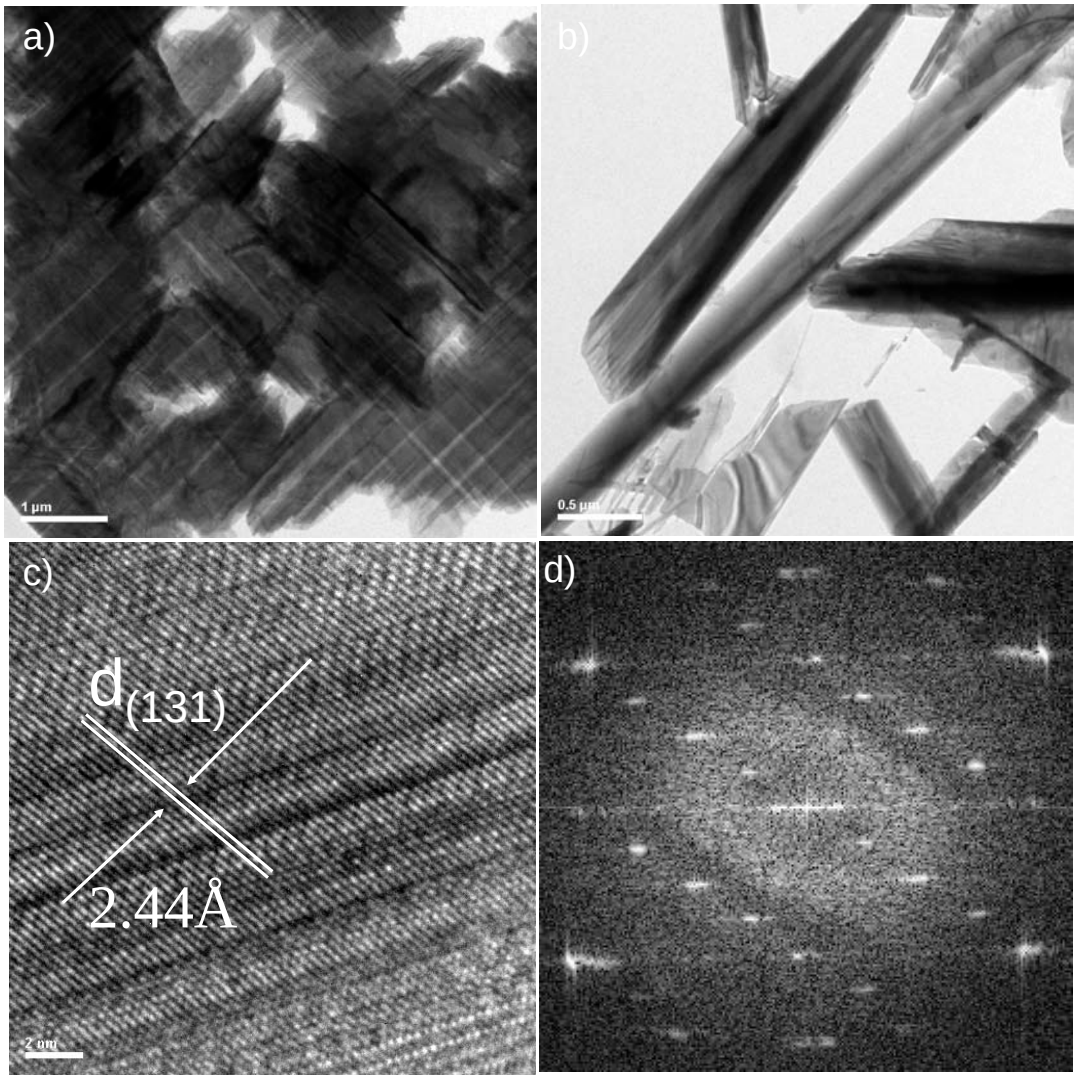

Fig. 4.13 a) and b) TEM images of nickel sulfide deposited [$Ni(SON(CNEt_2)_2)_2$] (**3**) on glass at 440 °C and (c) HRTEM images (d) FFT pattern.

The PXRD pattern obtained from the films deposited at 320 °C show intense reflections for the hexagonal $Ni_{17}S_{18}$ phases. At 360 and 400 °C almost almost the same intense of reflections from both phases obtained, whereas PXRD pattern of films deposited at 440 °C show the deposition of higher amount of orthorhombic Ni_7S_6 with major diffraction peaks of (042), (004) and (163) planes. The SEM images of nickel sulfide thin film deposited from complex (**3**) are shown in Fig. 4.12. It shows the morphology of films dependent on growth temperature. At 320 °C

irregular crystallites deposited with an average size of 300 ± 20 nm. At 360 and 400 °C cross linked plate like crystallites with an average thickness of 300 ± 35 nm and 350 ± 25 nm obtained, whereas at 440 °C group of plates stacked together one over another. The average thickness of plates could be measured as 100 ± 10 nm. The morphology of films deposited from complex (**3**) was different from the morphology of films deposited from complex (**1**) and (**2**). The composition of films deposited from complex (**2**) was confirmed by EDX analysis as Ni:S ratios : 52.1:47.9 (320 °C), 53.7:46.3 (360 °C), 54.5:45.5 (400 °C) and 56.0:44.0 (440 °C). The TEM images show the scratched crystallites from the films grown at 440 °C consist of nanobelts with an average width size of 415 ± 10 nm (Fig. 4.13(a)). HRTEM images of the nanobelts (Fig. 4.13(c)) show the lattice fringes with a d-spacing of 0.244 nm corresponding to (131) reflection of orthorhombic Ni_7S_6. FFT image in Fig. 4.13(d) confirms the single crystalline nature of crystallites.

4.4.11 The AA-CVD deposition of nickel sulfide thin films from [Ni(SON(CN^{i}Pr$_2$)$_2$)$_2$] (4)

Film deposition was carried out at substrate temperatures between 320 to 400 °C with argon flow rate of 160 sccm. No deposition was obtained below 320 °C. Black, adherent films were deposited at 320 °C and 360 °C but uniform black films were deposited at 400 °C. PXRD pattern of as deposited films at 320 - 400 °C (Fig. 4.14) show the formation of Ni_9S_8 phase nickel sulfide indexed as the orthorhombic phase of Ni_9S_8 (ICDD : 04-007-0778). No significant PXRD peaks from impurities were observed. The X-ray diffraction pattern of films deposited at 320 °C show peaks sharper than those deposited at 360 °C or 400 °C. The major peaks (310), (113), (023), (312), (060) and (135) are assigned to orthorhombic Ni_9S_8. The SEM images of the films (Fig. 4.15) show that the morphology of the nickel sulfide is dependent on the growth temperature. Films deposited at 320 and 360 °C consist of

flower like crystallites with average size of 4 ± 0.2 μm and 15 ± 1 μm respectively where as film deposited at 400 °C showed branched structures. EDX analysis of the films show the composition as Ni:S ratio of 49.0:51.0 (320 °C), 50.2:49.8 (360 °C) and 52.4:47.6 (400 °C).

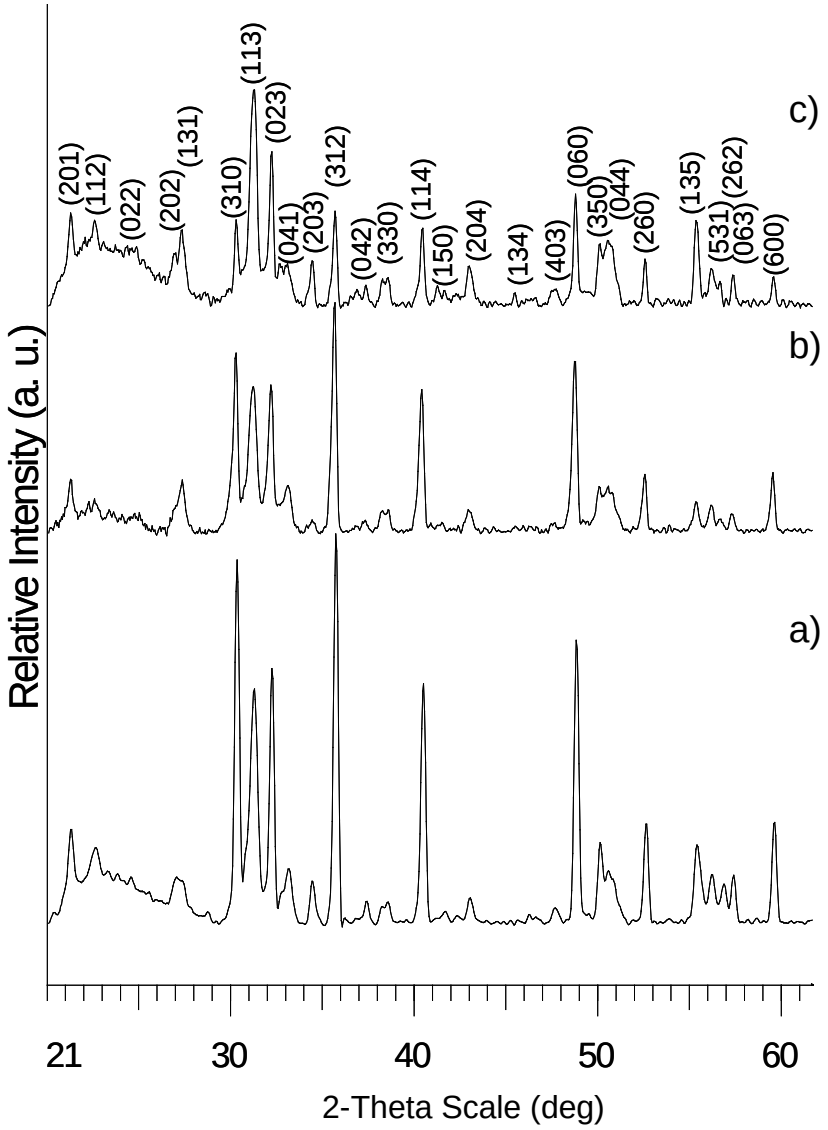

Fig. 4.14 PXRD pattern of NiS films deposited from [Ni(SON(CN^{i}Pr$_2$)$_2$)$_2$] (**4**) on glass at (a) 320 °C (b) 360 °C and (c) 400 °C

The TEM images show the scratched crystallites from the film grown at 400 °C consist of nanobelts size ranging from ca 200 to 300 nm (Fig. 4.16(a)). HRTEM images of the nanobelts (Fig. 4.16(b) and (c)) show the lattice fringes with a d-spacing 0.299 nm corresponding to (310) reflection of orthorhombic Ni_9S_8 and the

FFT pattern in Fig. 4.16(d) shows single crystalline nature of nanoplates. The diffraction spot can be indexed to the (310) plane of the orthorhombic phase.

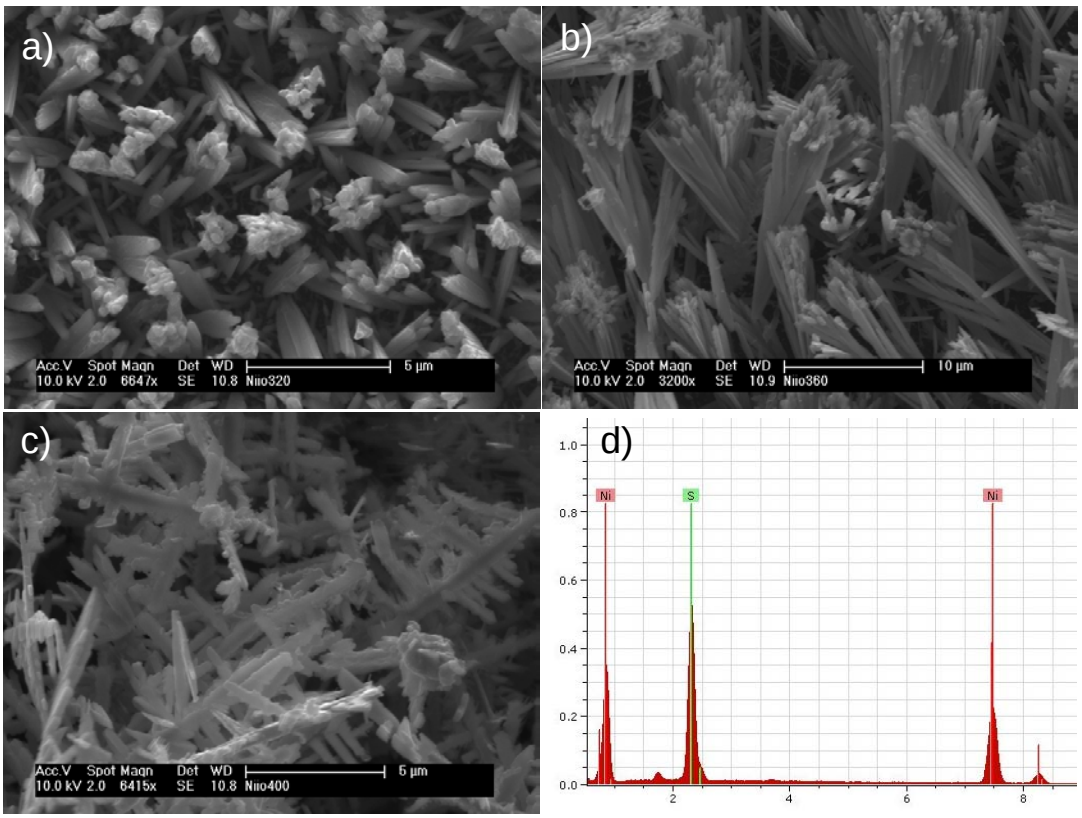

Fig. 4.15 SEM images of films deposited from [Ni(SON(CN^{i}Pr$_2$)$_2$)$_2$] (**4**) on glass at (a) 320 °C (b) 360 °C and (c) 400 °C (d) EDX graph.

4.4.12 The AA-CVD deposition of nickel sulfide thin films from [Ni(N(SCNMe$_2$SCNEt$_2$))$_2$] (6)

Film deposition was carried out at substrate temperatures between 360 to 480°C with an argon flow rate of 160 sccm on glass substrate using complex (**6**). No deposition was obtained below 360 °C and above 480 °C. Black, adherent, uniform films were deposited at all temperatures. The powder X-ray diffraction (PXRD) pattern of as deposited films at 360 - 480 °C from complex (**6**) is shown in Fig. 4.17. At 360 and 400 °C NiAs type hexagonal $NiS_{1.03}$ phase obtained with major diffraction peaks of (100), (002), (101), (102) and (110) planes (ICDD: 002-1273). The PXRD pattern from films deposited at 440 and 480 °C show diffraction peaks

from hexagonal $NiS_{1.03}$ and also peaks of (121), (103), (016), and (200) planes from orthorhombic Ni_7S_6 phase (ICDD: 024-1021).

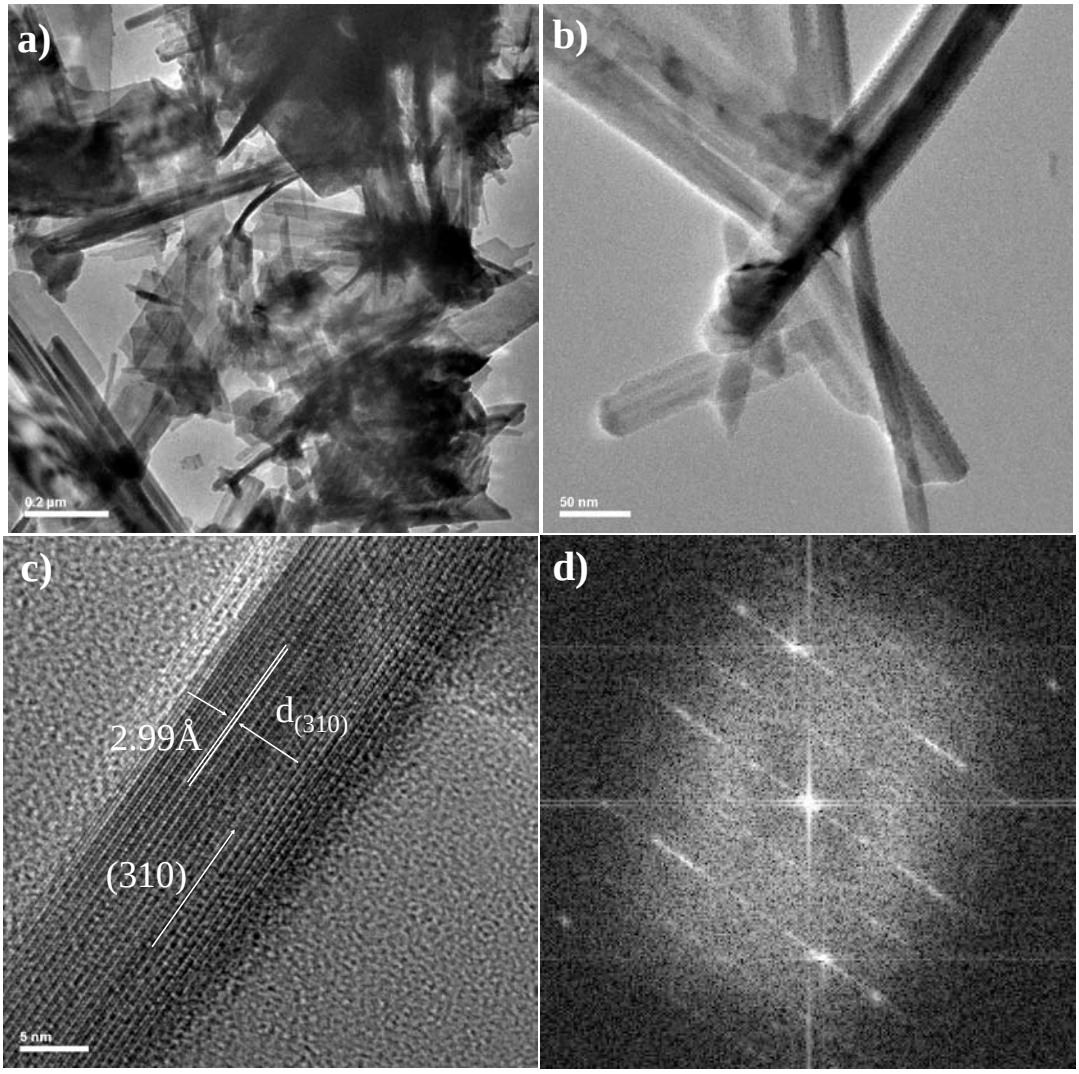

Fig. 4.16 a) and b) TEM images of nickel sulfide deposited from $[Ni(SON(CN^iPr_2)_2)_2]$ (**4**) on glass at 400 °C and (c) HRTEM images (d) FFT pattern.

The deposition of sulfur deficient Ni_7S_6 phase at high temperature could be related to volatility of sulfur at these temperatures. The SEM images of the films (Fig. 4.18) show that the morphology of the nickel sulfide is dependent on the growth temperature. Films deposited at 360 °C consist of worm-like crystallites with an average length of 5 ± 1 µm and width of 500 ± 25 nm. At 400 °C the films composed of 4 ± 0.3 µm sized plates 200 nm in width. Whereas at 440 and 480 °C smaller, uniform, rod-like crystallites were deposited. The width size of 200 ± 30 nm rods

deposited at 440 °C and 250 ± 25 nm rods deposited at 480 °C. EDX analysis of the films show the composition as Ni:S ratio of 49.1:50.9 (360 °C), 49.3:50.7 (400 °C), 53.2:46.8 (440 °C) and 54.9:45.1 (480 °C).

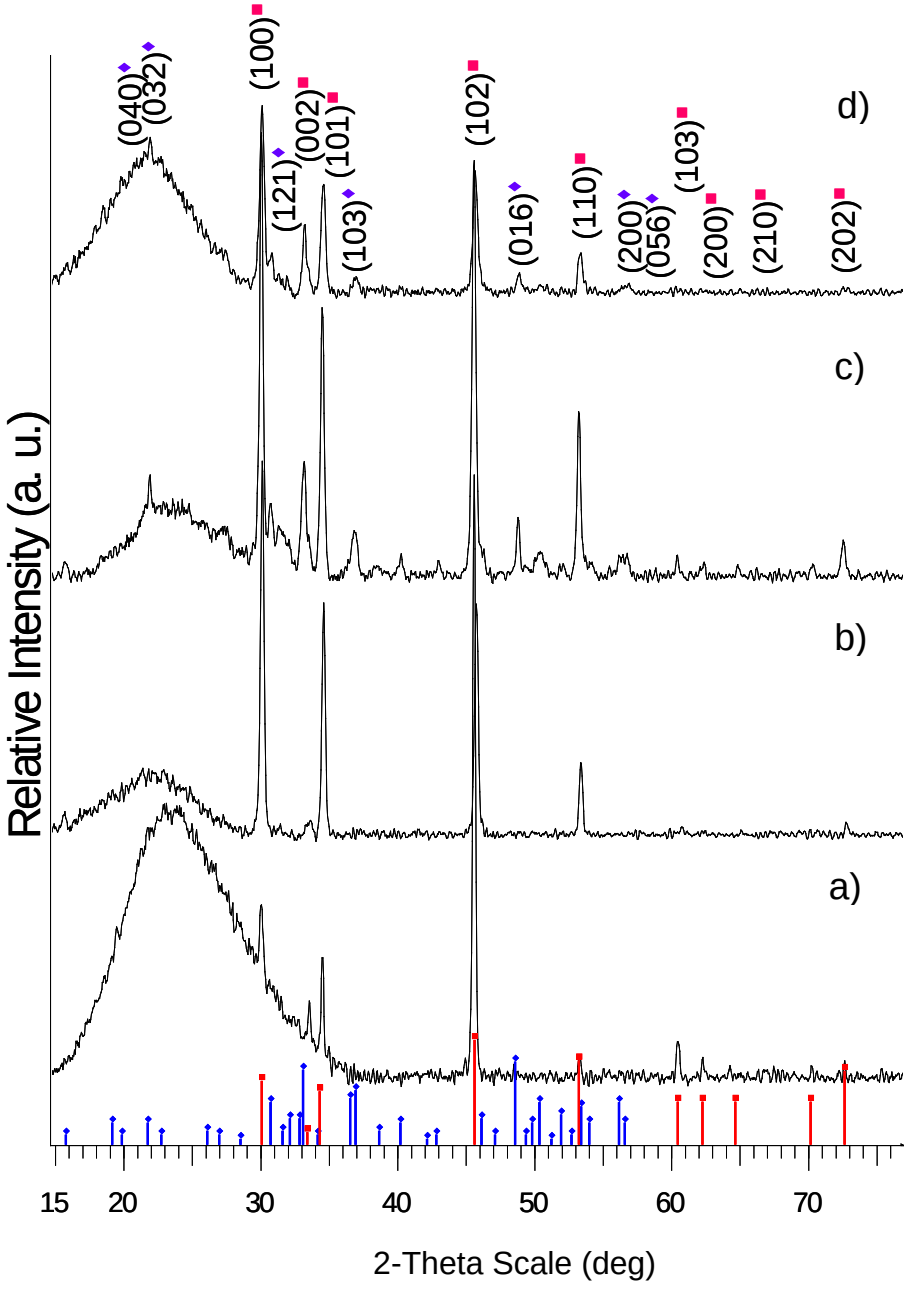

Fig. 4.17 PXRD pattern of nickel sulfide thin films deposited from $[Ni(N(SCNMe_2SCNEt_2))_2]$ (**6**) on glass at (a) 360 °C (b) 400 °C (c) 440 °C and (d) 480 °C. Symbol (♦) indicating orthorhombic Ni_7S_6 and (■) indicating hexagonal $NiS_{1.03}$

The TEM images show the scratched crystallites from the film grown at 400 °C consist of nanobelts size ranging from ca 150 to 200 nm (Fig. 4.19(b)). HRTEM

images of the nanobelts (Fig. 4.19(c)) show the lattice fringes with a d-spacing of 0.199 nm corresponding to the (102) reflection of hexagonal $NiS_{1.03}$. The FFT pattern in Fig. 4.19(d) shows the single crystalline nature of nanoplates.

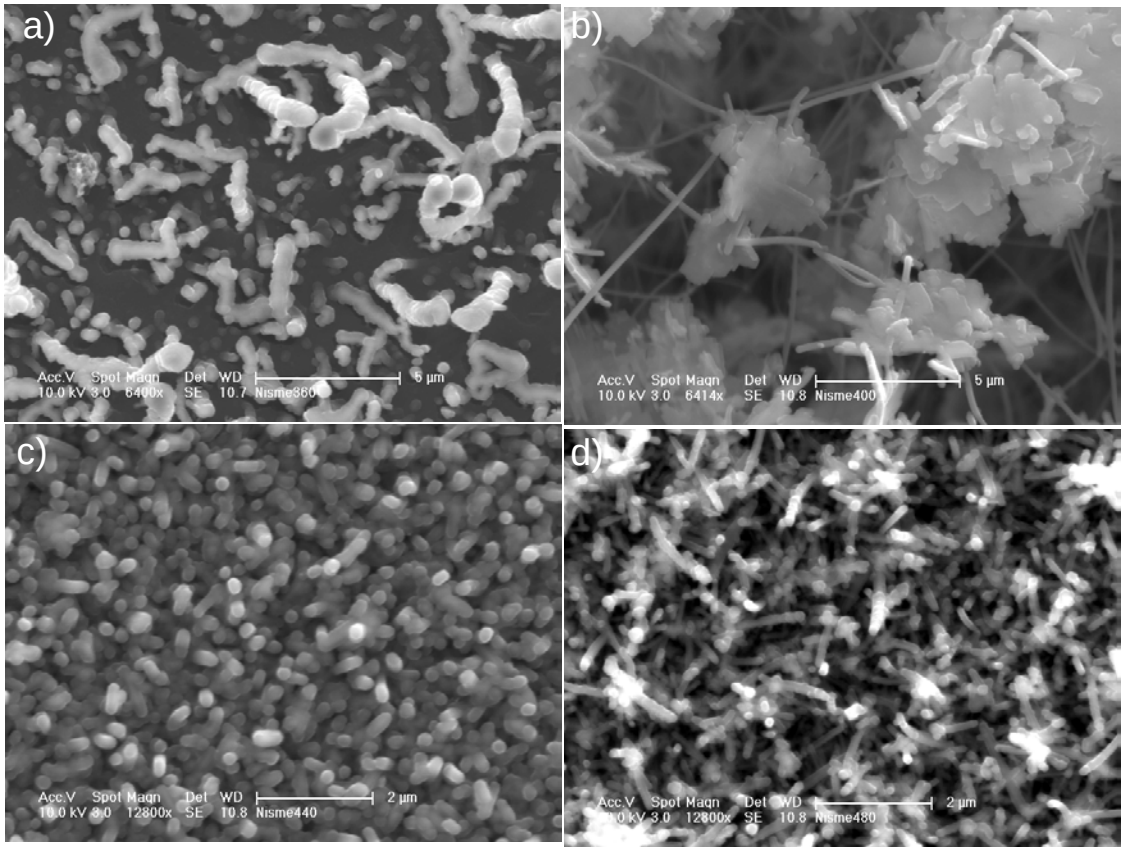

Fig. 4.18 SEM images of films deposited from $[Ni(N(SCNMe_2SCNEt_2))_2]$ (**6**) on glass at (a) 360 °C (b) 400 °C (c) 440 °C and (d) 480 °C

4.4.13 The AA-CVD deposition of nickel sulfide thin films from $[Ni(N(SCNEt_2)_2)_2]$ (7)

Thin films of nickel sulfide have been deposited from complex (**7**) in the temperatures range of 360 to 480 °C on glass substrate. Black adherent uniform films were deposited at all temperatures. The powder X-ray diffraction (PXRD) pattern of the deposited films at temperatures between 360 and 480 °C is shown in Fig. 4.20. At 360 and 400 ˚C NiAs hexagonal $NiS_{1.03}$ obtained with major diffraction peaks of (100), (002), (101), (102) and (110) planes (ICDD: 002-1273). The PXRD pattern from films deposited at 440 and 480 show diffraction s of hexagonal

$NiS_{1.03}$ and also major peaks of (004), (121), (103), and (133) planes from orthorhombic Ni_7S_6 (ICDD: 024-1021) similar to films deposited from complex (**6**)

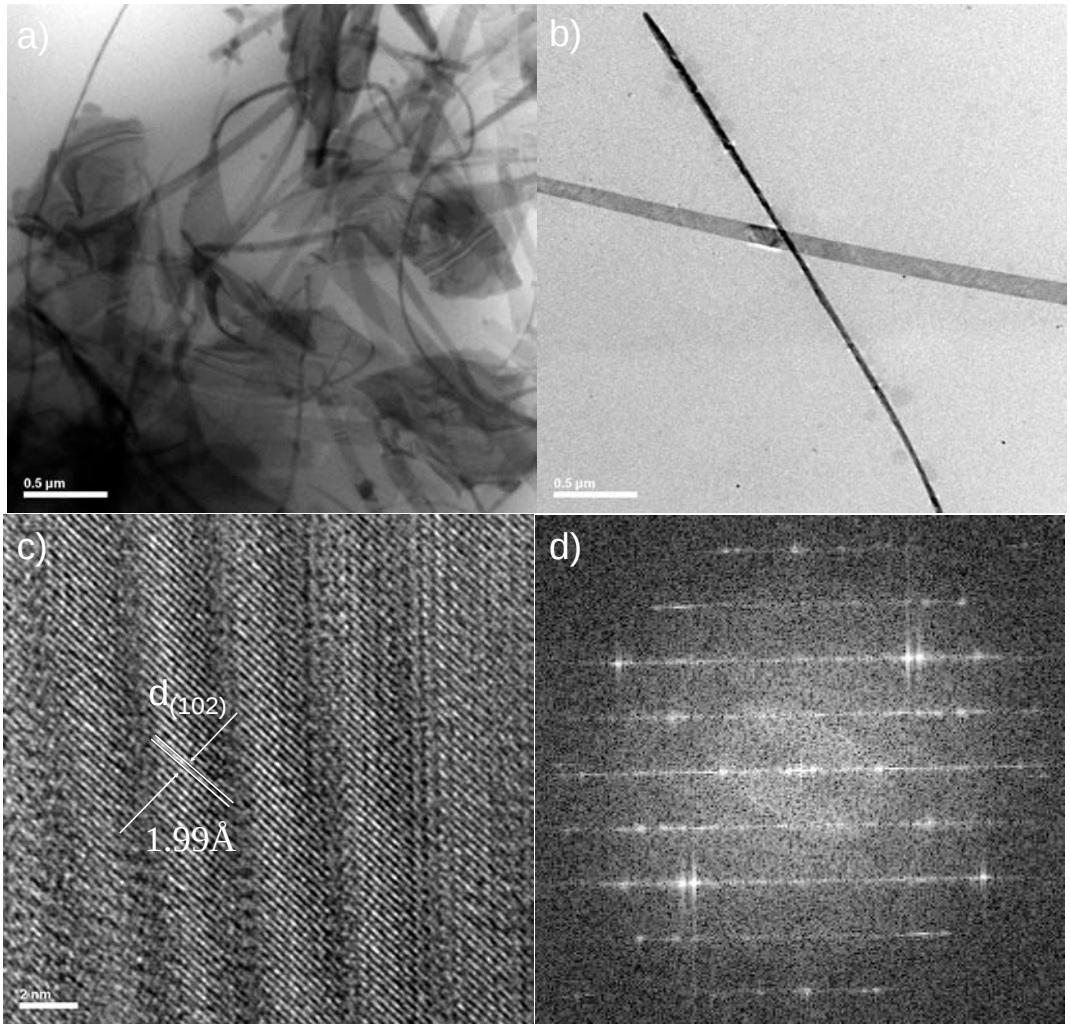

Fig. 4.19 a) and b) TEM images of nickel sulfide deposited from $[Ni(N(SCNMe_2SCNEt_2))_2]$ (**6**) on glass at 440 °C and (c) HRTEM images (d) FFT pattern.

The SEM images of the films (Fig. 4.21) show that the morphology of the nickel sulfide deposited at 360 °C consists of irregular rod-like crystallites with an average length of 6 ± 1 µm and width of 600 ± 50 nm. At 400 and 440°C films of 4 ± 0.3 µm sized plates and 200 nm width sized wires deposited, whereas at 480 °C smaller uniform rod like crystallites deposited with an average width size of 200 ± 20 nm.

EDX analysis of the films show the composition as Ni:S ratio of 49.2:50.8 (360 °C), 49.3:50.7 (400 °C), 55.5:44.5 (440 °C) and 56.1:43.8 (480 °C).

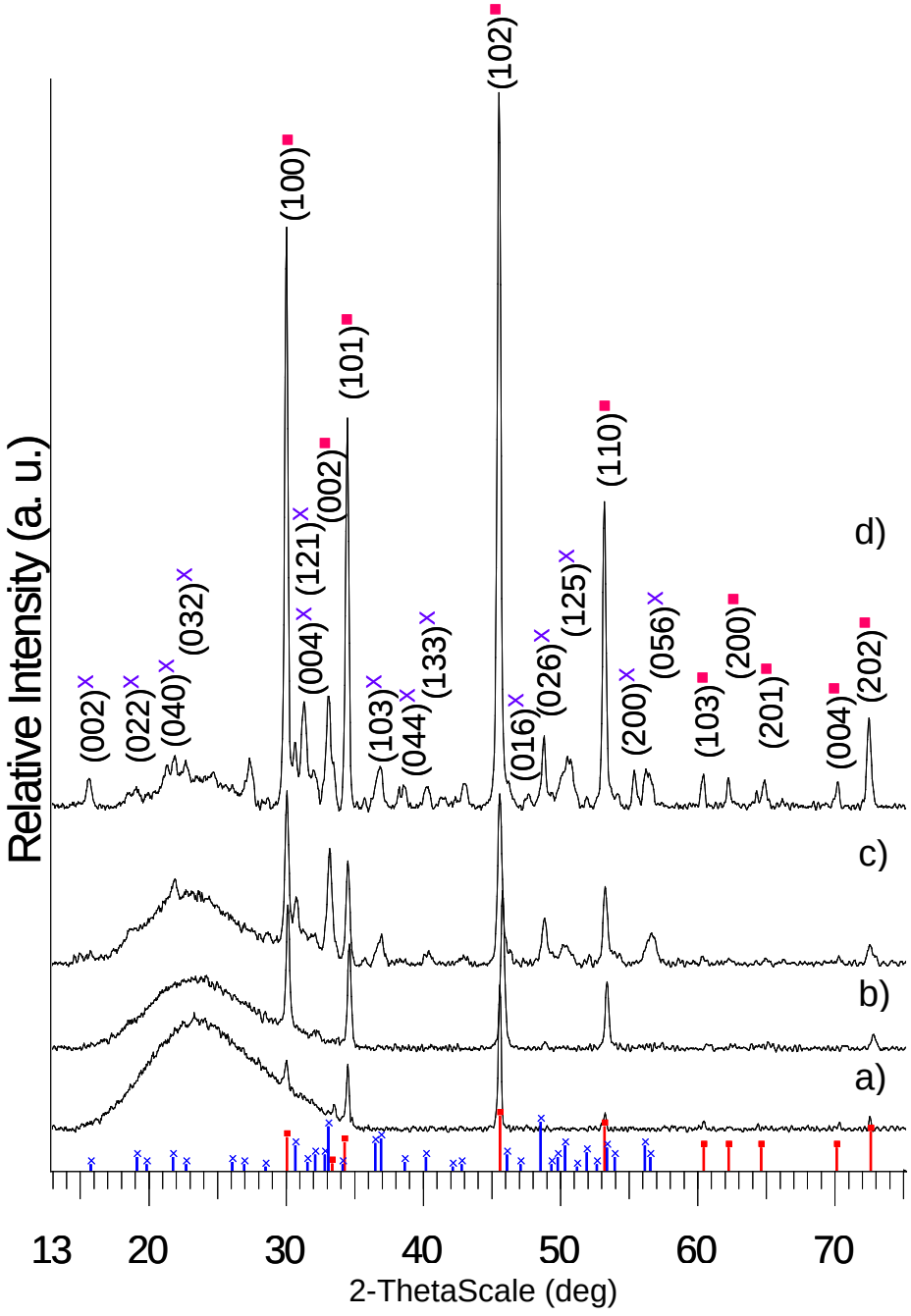

Fig. 4.20 PXRD pattern of nickel sulfide thin films deposited from $[Ni(N(SCNEt_2)_2)_2]$ (**7**) on glass at (a) 360 °C (b) 400 °C (c) 440 °C and (d) 480 °C. Symbol (X) indicating orthorhombic Ni_7S_6 and (■) indicating hexagonal $NiS_{1.03}$

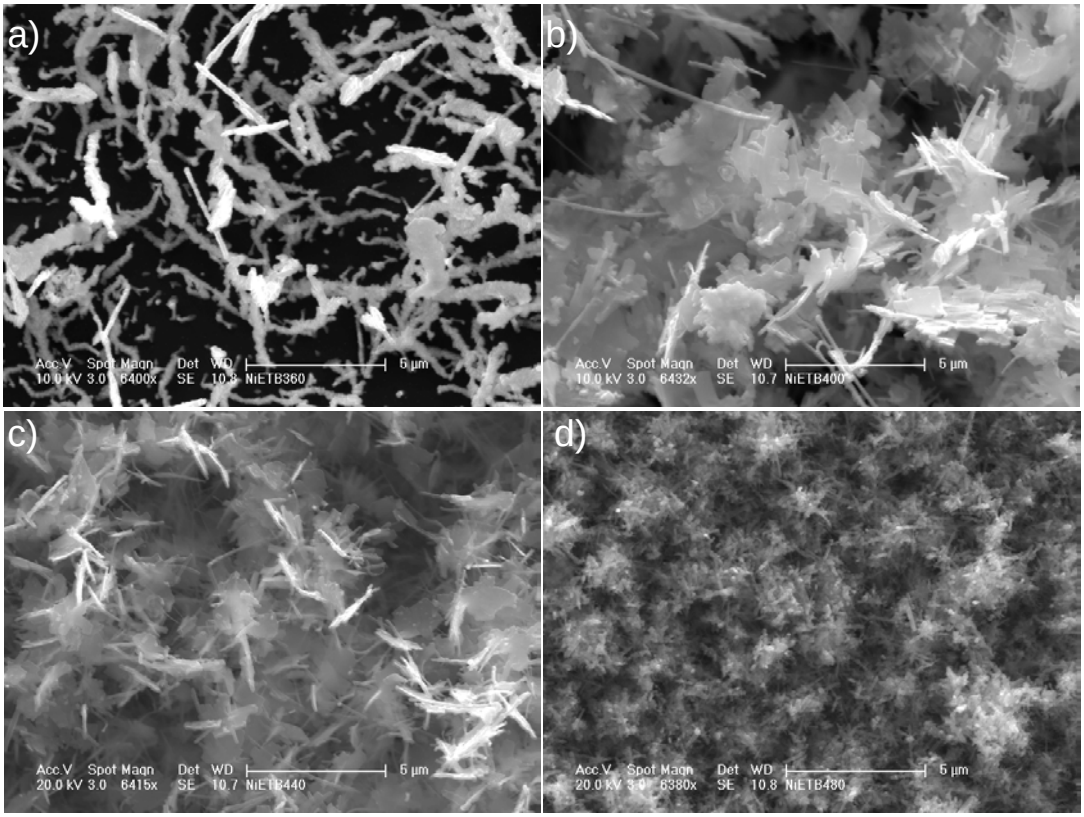

Fig. 4.21 SEM images of films deposited from $[Ni(N(SCNEt_2)_2)_2]$ (**7**) on glass at (a) 360 °C (b) 400 °C (c) 440 °C and (d) 480 °C

The TEM images show that the scratched crystallites from the film grown at 480 °C consist of hexagonal nanoplates with sizes ranging from ca 35 to 40 nm (Fig. 4.22(a)). This primary hexagonal structure attached together to form a secondary structure containing rod-like crystallites. HRTEM images of the hexagonal plates (Fig. 4.22(b) and (c)) show the lattice fringes with a d-spacing 0.266 nm corresponding to (101) reflection of hexagonal $NiS_{1.03}$ and the FFT pattern in Fig. 4.22(d) shows single crystalline nature of hexagonal plates.

4.5 Conclusion

The synthesis of nickel (II) complexes of 1,1,5,5-tetraalkyl-2-thiobiurets (R = methyl (**1**); methyl, ethyl (**2**); ethyl (**3**); isopropyl (**4**) and 1,1,5,5-tetraalkyl-2,4-dithiobiurets (R = methyl (**5**); methyl, ethyl (**6**); ethyl (**7**) are reported. The single crystal structure of complexes (**1**), (**3**), (**4**), (**6**) and (**7**) were determined. In the

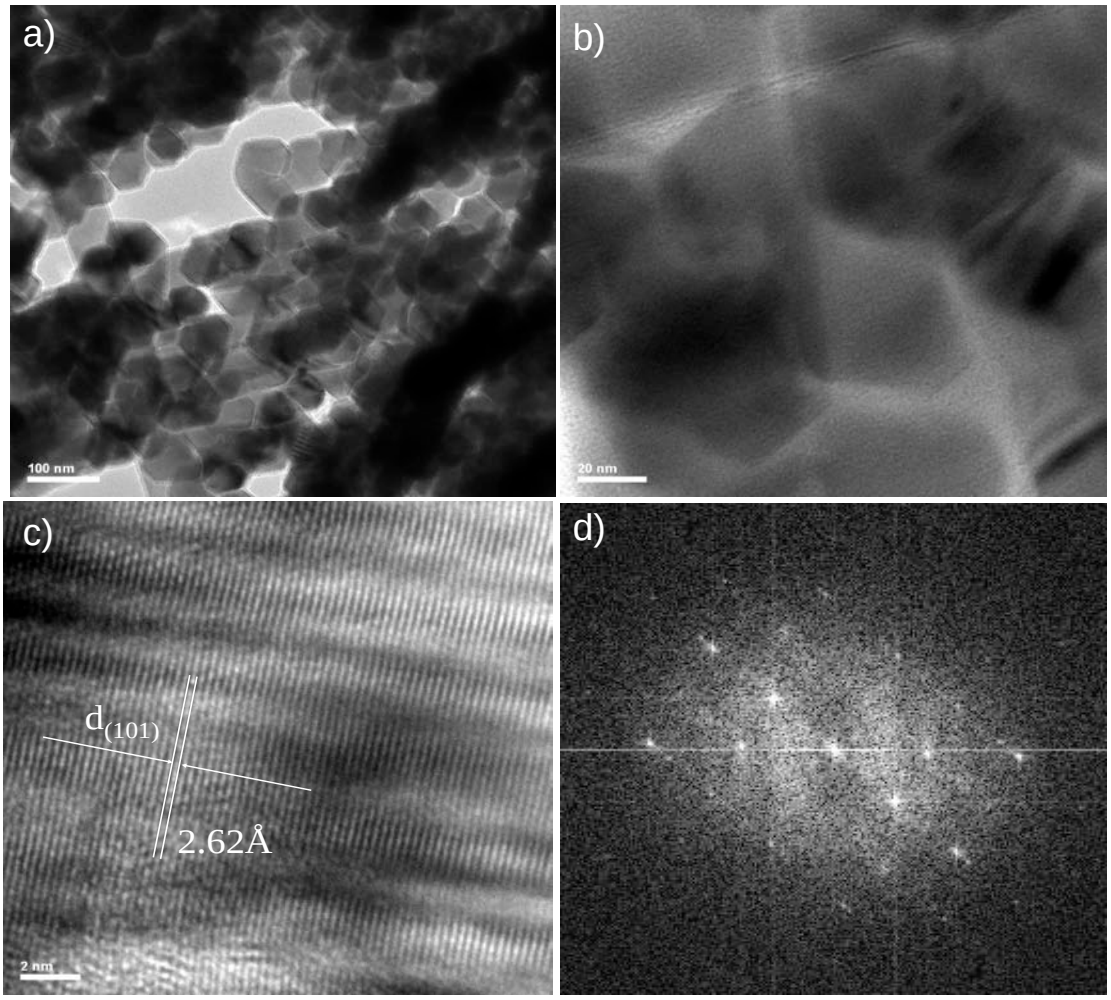

Fig. 4.22 a) and b) TEM images of nickel sulfide deposited from $[Ni(N(SCNEt_2)_2)_2]$ (**7**) on glass at 440 °C and (c) HRTEM images (d) SAED pattern.

case of the thiobiuret complexes the ligands coordinated through an S_2O_2 donor set with the two sulfur atoms being mutually *cis.* Nickel is in a square planar coordination environment in all seven thio and dithiobiuret complexes. AACVD from complex (**1**) deposited orthorhombic Ni_7S_6 phase at all temperatures with spherical tipped wire like crystallites at 320 °C, plates and wires at other temperatures. Complex (**2**) deposited a mixture of hexagonal $Ni_{17}S_{18}$ and orthorhombic Ni_7S_6, with wires and plates of crystallites. Similarly complex (**3**) also deposited mixture of hexagonal $Ni_{17}S_{18}$ and orthorhombic Ni_7S_6 phases but with plates-like crystallites. Whereas complex (**4**) deposited orthorhombic Ni_9S_8 phase with flower-like crystallites at 320 and 360 °C, branched structures at 400 °C. Complex (**6**) gave

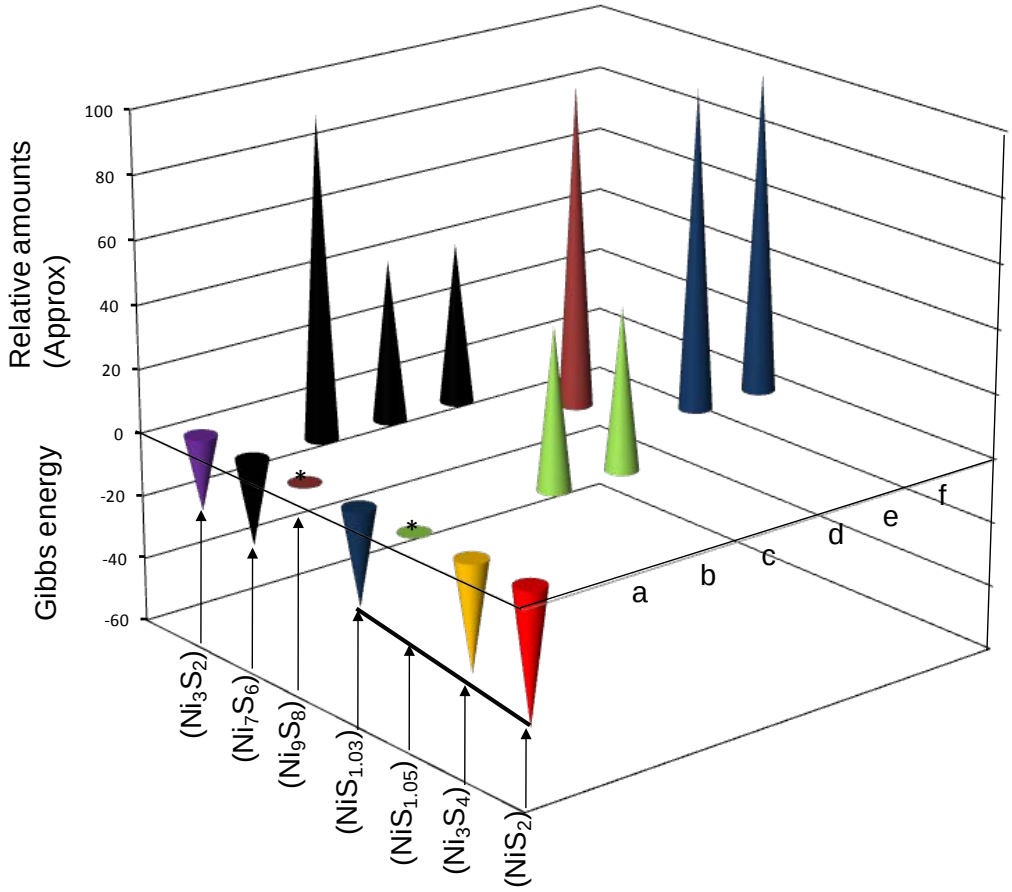

Fig. 4.23 The phases nickel sulfide thin films deposited at 400 °C from a) $[Ni(SON(CNMe_2)_2)_2]$ (**1**), b) $[Ni(SON(CNMe_2CNEt_2))_2]$ (**2**), c) $[Ni(SON(CNEt_2)_2)_2]$ (**3**), d) $[Ni(SON(CN^iPr_2)_2)_2]$ (**4**), e) $[Ni(N(SCNMe_2SCNEt_2))_2]$ (**6**) and f) $[Ni(N(SCNEt_2)_2)_2]$ (**7**), compared to the relative thermodynamic stabilities (ΔG) of the various phases of nickel sulfides calculated using heat of formation (ΔH) and entropy (ΔS) values taken from Ref.28.Symbol (*) indicating unavailable thermodynamic data.

NiAs – hexagonal $NiS_{1.03}$ at 360 and 400 °C, orthorhombic Ni_7S_6 phase at 440 and 480 °C with wires of spherical particles. Similarly complex (**7**) also deposited hexagonal $NiS_{1.03}$ at 360 and 400 °C, orthorhombic Ni_7S_6 phase at 440 and 480 °C, but with rods of crystallites composed of hexagonal plates. The composition of films deposited from all complexes were confirmed by EDX analysis.

The relative stabilities of various phases of nickel sulfide are shown in Fig. 4.23. The height of the cones on the negative z-axis represents the free energy of formation of each phase at 400 °C calculated using heat of formation and entropy

values taken from Mills.[28] The phase deposited from the thiobiuret precursors (**1**-**4**) was Ni_7S_6 and Ni_9S_8, whereas the dithiobiuret precursors (**6**,**7**) deposited $NiS_{1.03}$. In the composition range NiS to NiS_2 are most stable in a thermodynamic sense. The deposition of the 'sub-sulfide' Ni_7S_6 ([Ni]:[S] = 1:0.86) from thiobiuret probably reflects the lower sulfur content than in the dithiobiuret which leads to $NiS_{1.03}$. These observations are in stark contrast to the related tris-chelated iron complexes, which deposit FeS or FeS_2, the two thermodynamic stable members of the series running from FeS to FeS_2.[29] None of the nickel precursors lead to the thermodynamically stable phase (NiS_2). However the kinetic phase Ni_7S_6 was observed in this system.

4.6 References:

1. G**.** Kullerud, R. A. Yund, *J. Petrology*, 1962, **3**, 126

2. M. V. Swain, *J. Mater. Sci*., 1981, **16**, 151.

3. J. C. Barry, S. Ford, *J. Mater. Sci*., 2001, **36**, 3721

4. M. Sharon, G. Tamizhmani, C. Levy-Clement, J. Rioux, *Sol. Cells,* 1989, **26**, 303.

5. (a) Z. Zainal, N. Saravanan, H. L. Mien, *J. Mater. Sci: Mater. Electron.* 2005, **16**, 111. (b) K. Anuar, Z. Zainal, N. Saravanan, A. R. Kartini, *AJSTD*, 2004, **21,** 19. (c) K. Anuar, Z. Zainal, N. Saravanan, A. Zuriyatina, R. Sharin, M*aterials Science*, 2004, **10**, 157. (d) K. Anuar, Z. Zainal, N. Saravanan, S. N. Hamizi, *J. Indian Chem.Soc*., 2005, **82**, 526.

6. S. Leitz, G. Hodes, R. Tenne, J. Manassen, *Nature*, 1987, **326**, 863.

7. S. T. Oyama, *J. Catal.,* 2003, **216**, 343.

8. R. S. Mane, C. D. Lokhande, *Mater. Chem. Phys*., 2000, **65**, 1.

9. J. Cheon, D. Talaga, J. I. Zink, *Chem. Mater*., 1997, **9**, 1208.

10. A. Wold, *Adv. Chem. Series*, 1971, **98**, 17.

11. G. Line, M. C. R. Huber, *Acad. Sci*., 1963, **256**, 3118.

12. D. Lunovist, *Arkiy. Mineral. Geol.*, 1947, **A21**, 21.

13. G. Kullerud, *Carnegie Inst. Washington Year Book,* 1967, **67**, 179.

14. F. Gronvold, R. Molleurd, E. Rost, *Acta. Chem. Sacnd.,* 1966, **20**, 1997.

15. T. Sparks, T. Komoto, *Phys.Lett.,* 1967, **A25**, 398.

16. E. Barthelemy, O. Gorochov, H. McKinzie. *Mat. Res. Bull*., 1973, **8**, 1401.

17. P. Pramanik, S. Biswas, *J. Solid State Chem.,* 1986, **65**, 145.

18. P. Pramanik, S. Bhattacharya, *J. Mater. Sci. Lett.,* 1987, **6**, 1105.

19. S. D. Sartale, C. D. Lokhande, *Mater. Chem. Phys*., 2001, **72**, 101.

20. H. Lee, M. Kanai, T. Kawai, S. Kawai, *Jpn. J. App. Phys*., 1993, ***32***, 2100.

21. L. Zhang, J. C. Yu, M. Mo, L. Wu, Q. Li, K. W. Kwang, *J. Am. Chem. Soc*., 2004**,** **126**, 8116.

22. S. H. Yu, M. Yoshimura, *Adv. Funct. Mater*., 2002, **12***,* 277.

23. R. Nomura, H. Hayata, *Trans. Mater. Res. Soc. Jpn*., 2001, **26**, 1283.

24. P. O'Brien, J. Waters, *Chem. Vap. Deposition.*, 2006, **12**, 620.

25. P. O'Brien, J. H. Park, J. Waters, *Thin Solid Films.*, 2003, **431-432**, 502.

26. P. L. Musetha, N. Revaprasadu, M. A. Malik, P. O'Brien, *Mater. Res. Soc. Symp. Proc.,* 2005, **879E**, Z7.4.

27. N. Alam, M. S. Hill, G. Kociok-Kohn, M. Zeller, M. Mazar, K. C. Molloy, *Chem. Mater.,* 2008, **20**, 6157. 2001.

28. K. C. Mills, Thermodynamic data for inorganic sulphides, selenides and tellurides, Butterworth & Co., (Ltd), London, England. 1974.

29. K. Ramasamy, M. A. Malik, M. Helliwell, F. Tuna, P. O'Brien, *Inorg.Chem.,* 2010*,* **49**, 8495.

Chapter 5

Zinc Sulfide, Cadmium Sulfide and Zinc Cadmium Sulfide Thin films*

5.1 Summary

This chapter describes the synthesis of zinc and cadmium complexes of 1,1,5,5–tetraalkyl-2-4-dithiobiurets [$M(N(SCNR_2)_2)_2$] (M = Zn, R = methy (**1**), ethyl (**2**)) and (M = Cd, R = methyl (**4**), ethyl (**5**)) and 1,1,5,5–tetraalkyl-2-thiobiurets $M(SON(CNR_2)_2)_2$ (M = Zn, R = isopropyl (**3**) and M = Cd, R = isopropyl (**6**). The single crystal X-ray structure determination of complexes (**2**), (**3**), (**4**) and (**5**) are reported. Thermogravimetric analysis confirmed that all six complexes decomposed in a single step to their corresponding metal sulfides. The complexes were used as single source precursors for the deposition of zinc sulfide (ZnS), cadmium sulfide (CdS) and zinc cadmium sulfide ($Zn_xCd_{1-x}S$) thin films by aerosol assisted chemical vapour deposition (AACVD). The zinc complexes (**1**) and (**3**) deposited cubic ZnS films with small rods and granular crystallites at 300 and 350°C, whereas at 400 and 450 °C hexagonal ZnS with granular crystallites were apparent. Complex (**2**) gave granular hexagonal ZnS films at all deposition temperatures. Cadmium complexes (**4**), (**5**) and (**6**) gave granular hexagonal CdS films at all deposition temperatures. $Zn_xCd_{1-x}S$ films were deposited by varying the relative concentration of precursors (**1**), (**4**); (**2**), (**5**) and (**3**), (**6**) at 400°C. The formation of solid solution was confirmed by UV-Vis spectroscopy and powder X-ray diffraction. The morphology of the films was studied by scanning electron microscopy (SEM) and atomic force microscopy (AFM). The elemental composition of films was confirmed by energy dispersive X-ray spectroscopy (EDX).

*Part of the work has been published in *Dalton Trans.,* 2010, **39**, 1460, *Mater. Res. Soc. Symp. Proc.,* 2009, **1145**, MM04-40 and *Chem Mater.*, Submitted

5.2 Introduction

Zinc sulfide has two main forms the cubic (sphalerite) and hexagonal (wurtzite); in addition to these, other polytypes are known.[1-4] These forms differ in the packing arrangement of the layers. Optical studies on the polytypes indicate that the absorption edge and the birefringence can be correlated with the percentage of hexagonally stacked planes in the unit cell. The optical band gap of cubic ZnS 3.5eV shifts to higher values with increasing pressure.[5] ZnS is used as a phosphor with Cu, Mn, Ag added as activator or co-activator.[6,7]

CdS normally exists in hexagonal (greenockite) or cubic (hawleyite) forms,[8,9] at high pressure CdS transforms to an NaCl (halite) type structure.[10-12] Structural changes in CdS occur on electron irradiation.[13] CdS has interesting semiconducting and photoconducting properties. The mobility of charge carriers is strongly dependent upon temperature due to phonon scattering, and in addition to polar acoustic modes at low temperature.[14] Measurements of the photo Hall effect indicate that Hall mobility increases with increasing carrier concentration by photon excitation.[15] In the wurtzite structure, CdS has a band gap of 2.58 eV, which increases with increasing pressure. The band structure of CdS is calculated to be similar to that of ZnS. The photo-sensitivity of CdS can be altered by doping with impurities such as copper or iodide.[6]

ZnS or CdS thin films have been used for a wide variety of technological applications including in: photovoltaic cells, electro-optic modulators, sensors, electroluminescent and photo luminescent devices and anti reflection coatings.[16-19] In particular they have been widely employed in display technology as host lattices for doped phosphor materials, whose emission wavelength can be tailored as a function of the dopant metal.[17, 20-22] The size and electronic structure of the cations added are sufficiently similar to Cd and/or Zn for the formation of solid solutions.[23]

Thus, these are systems in which systematic variation of photoelectronic properties are possible simply by adjusting composition.

In the wurtzitic structure, ZnS and CdS have unit cell volumes in the ratio 0.77.[24] Because of such similarities these materials have been widely employed in p-n junction with a relatively small lattice mismatch in devices based on quaternary materials like $CuIn_xGa_{1-x}Se_2$ or $CuIn(S_xSe_{1-x})_2$.[25,26] Thin films of $Zn_xCd_{1-x}S$ have properties between those of ZnS and CdS.[27-29] ZnS has a larger bandgap than CdS so all the $Zn_xCd_{1-x}S$ ternaries have larger energy bandgaps than CdS which can make the materials attractive as windows in hetero-junction photovoltaics such as CdS/CdTe solar cells.[30-35] Recently, Wang *et al.* detailed the use of ZnCdS in memory devices.[36]

The route used to prepare or deposit a material can profoundly affect: phase composition, thermal stability and morphology; which can in turn influence the functional behavior of the material. Many techniques have been used including: sputtering,[37,38] pulsed laser ablation,[39,40] spray pyrolysis,[41,42] chemical bath deposition,[43,34] electrostatic assisted aerosol jet deposition,[44,45] sol-gel,[46,47] ion-beam deposition[48] and MOCVD.[49-57] MOCVD is well known to give high quality thin films. Various single-source precursors have been investigated including: metal complexes of dialkyldithiocarbamates,[51-54] alkyl xanthates[49] and dimorpholino dithioacetylacetonates.[50] We have recently demonstrated that thio- and dithio-biuret metal complexes can be used as single-source precursors for the preparation of various metal sulfide thin films[56-60] and nanoparticles.[61] In continuing this work, the synthesis of Zn and Cd complexes of 1,1,5,5–tetraalkyl-2-4-dithiobiurets (R = methyl or ethyl) and 1,1,5,5–tetraalkyl-2-thiobiurets (R = isopropyl) and their use as a single molecular precursors for deposition of ZnS, CdS and $Zn_xCd_{1-x}S$ thin films by AACVD methods are discussed in this chapter

5.3 Experimental

5.3.1 Synthesis of $[Zn(N(SCNMe_2)_2)_2]$ (1)

Dimethyl thiocarbamoylchloride (1.23 g, 10 mmol) and sodium thiocyanate (0.813g, 10 mmol) added to 40 ml of acetonitrile. Heated to reflux temperature and maintained for 1 h. Cooled to 25-30 $^{\circ}$C and filtered NaCl formed as side product. In filtrate 1.49 ml (20 mmol) 60 % solution of dimethylamine added and stirred for 30 mins at room temperature. Followed by zinc acetate dihydrate (1.10 g, 5 mmol) added stirring continued for 30 mins. Product formed was isolated by filtration. Recrystallisation was performed using mixture of chloroform and methanol. Yield: 1.44 g (65 %), Mpt : 210 ºC, ^{1}H NMR (300 MHz; $CDCl_3$; Me_4Si): 3.40 (s, 12 H), 3.15 (s, 12H), 4.38 (s, 2H). Elemental analysis: Calc for $[C_{12}H_{24}N_6S_4Zn]$: C, 32.3; H, 5.4; N, 18.8; S, 28.7; Zn, 13.9 % Found C, 32.1; H, 5.7; N, 18.7; S, 28.3; Zn, 14.6 %

5.3.2 Synthesis of $[Zn(N(SCNEt_2)_2)_2]$ (2)

Complex (**2**) was synthesised by method described for complex (**1**) using diethylthiocarbamoyl chloride (1.51 g, 10 mmol), diethylamine (1.91 mL, 20 mmol). The crude product was obtained as white powder. Recrystallisation from chloroform and methanol yielded colourless block crystals suitable for X-ray diffraction. Yield 1.5 g, (54%), Mpt : 120 ºC, ^{1}H NMR (300 MHz; $CDCl_3$; Me_4Si): δ 3.4 (q, 8H), 3.8 (q, 8H) 1.0 (t, 12H), 1.1 (t, 12H), Elemental analysis: Calc. for $C_{20}H_{40}N_6S_4Zn$: C, 42.9; H, 7.1; N, 15.0; S, 22.9; Zn, 11.6 %. Found: C, 42.8; H, 7.3; N, 14.9; S, 22.6; Zn, 11.5 %.

5.3.3 Synthesis of $[Zn(SON(CN^iPr_2)_2)_2]$ (3)

Complex (**3**) was synthesised by method described for complex (**1**) using diisopropylcarbamoyl chloride (1.0 g, 6 mmol), diisopropylamine (1.26

mL, 12 mmol). The crude product was isolated as white powder. Recrystallisation from chloroform and methanol yielded colourless needle crystals suitable for X-ray diffraction. Yield 1.30 g, (67 %) Mpt : 298 °C, ^{1}H NMR (300 MHz; $CDCl_3$; Me_4Si): δ 4.75 (m, 4H), 3.5 (m, 4H) 1.1 (d, 24H), 1.4 (d, 24H), Elemental analysis: Calc. for $C_{28}H_{56}N_6S_2O_2Zn$: C, 52.7; H, 8.7; N, 13.1; S, 10.0; Zn, 10.2 %. Found: C, 52.2; H, 8.3; N, 12.7; S, 9.6; Zn, 9.8 %.

5.3.4 Synthesis of $[Cd(N(SCNMe_2)_2)_2]$ (4)

Complex (**4**) was synthesised by method described for complex (**1**) using cadmium acetate dihydrate (1.33 g, 5 mmol) and obtained as white powder. Recrystallisation from chloroform and methanol yielded colourless needles suitable for single crystal X-ray diffraction. Yield 1.60 g, (65 %) Mpt : 90 °C, MS (ES), m/z = 491.9 [M+] 190.2, $[C_6H_{12}N_3S_2]$,^{1}H NMR (300 MHz; $CDCl_3$; Me_4Si): 3.4 (s, 12 H), 3.15 (s, 12H), Elemental analysis: Calc. for $C_{12}H_{24}N_6S_4Cd$: C, 29.2; H, 4.8; N, 17.0; S, 25.9; Cd, 22.8 %. Found: C, 28.8; H, 4.9; N, 16.7; S, 25.5; Cd, 22.7 %

5.3.5 Synthesis of $[Cd(N(SCNEt_2)_2)_2]$ (5)

Complex (**5**) was synthesised by method described for complex (**1**) using diethylthiocarbamoyl chloride (1.51 g, 10 mmol), diethylamine (1.91 mL, 20 mmol) and cadmium acetate dihydrate (1.33g, 5mmol). The crude product was obtained as white powder. Recrystallisation from chloroform and methanol yielded colourless block crystals suitable for X-ray diffraction. Yield 1.6 g, (52%), Mpt : 118 °C, ^{1}H NMR (300 MHz; $CDCl_3$; Me_4Si): δ 3.45 (q, 8H), 3.9 (q, 8H) 1.1 (t, 12H), 1.3 (t, 12H) Elemental analysis: Calc. for $C_{20}H_{40}N_6S_4Cd$: C, 39.6; H, 6.6; N, 13.8; S, 21.1; Cd, 18.5 %. Found: C, 39.5; H, 6.8; N, 13.8; S, 20.5; Cd, 18.1 %.

5.3.6 Synthesis of $[Cd((SON(CN^{i}Pr_2)_2)_2]$ (6)

Complex (**6**) was synthesised by method described for complex (**1**) using diisopropylcarbamoyl chloride (1.0 g, 6 mmol), diisopropylamine (1.26 mL, 12 mmol) and cadmium acetate dihydrate (0.81 g, 3 mmol). The crude product was isolated as white powder. Yield 1.49 g, (72 %) Mpt : 109 °C, ^{1}H NMR (300 MHz; $CDCl_3$; Me_4Si): δ 4.45 (m, 4H), 3.5 (m, 4H) 1.1 (d, 24H), 1.4 (d, 24H), Elemental analysis: Calc. for $C_{28}H_{56}N_6S_2O_2Cd$: C, 49.0; H, 8.1; N, 12.2; S, 9.3; Cd, 16.4 %. Found: C, 49.2; H, 7.8; N, 12.0; S, 9.1; Cd, 15.9 %.

5.4 Results and discussion

The zinc and cadmium complexes of thio- and dithio-biuret have been synthesised by the reaction of excess dialkylamine with *in situ* generated dialkylcarbamoylthiocyanate in acetonitrile. All the complexes are air and moisture stable. Complexes (**1**), (**2**), (**4**) and (**5**) soluble in toluene, tetrahydrofuran, chloroform and other organic solvents. Complexes (**3**) and (**6**) are soluble in toluene, chloroform, but are sparingly soluble in tetrahydrofuran.

5.4.1 Single crystal X-ray structure of $[Zn(N(SCNEt_2)_2)_2]$ (2)

The single crystal X-ray structure of complex (**2**) confirmed the formation of expected bis-chelate complex as shown in Fig. 5.1(a). Zinc has a distorted tetrahedral geometry with the ligand bite angle of 102.55(2)° and 103.41(2)° are slightly smaller than the perfect tetrahedral angle, but the angles are wider than those in the methyl analogue.[62] The ligand planes Zn(1)S(1) S(2) and Zn(1)S(3)S(4)

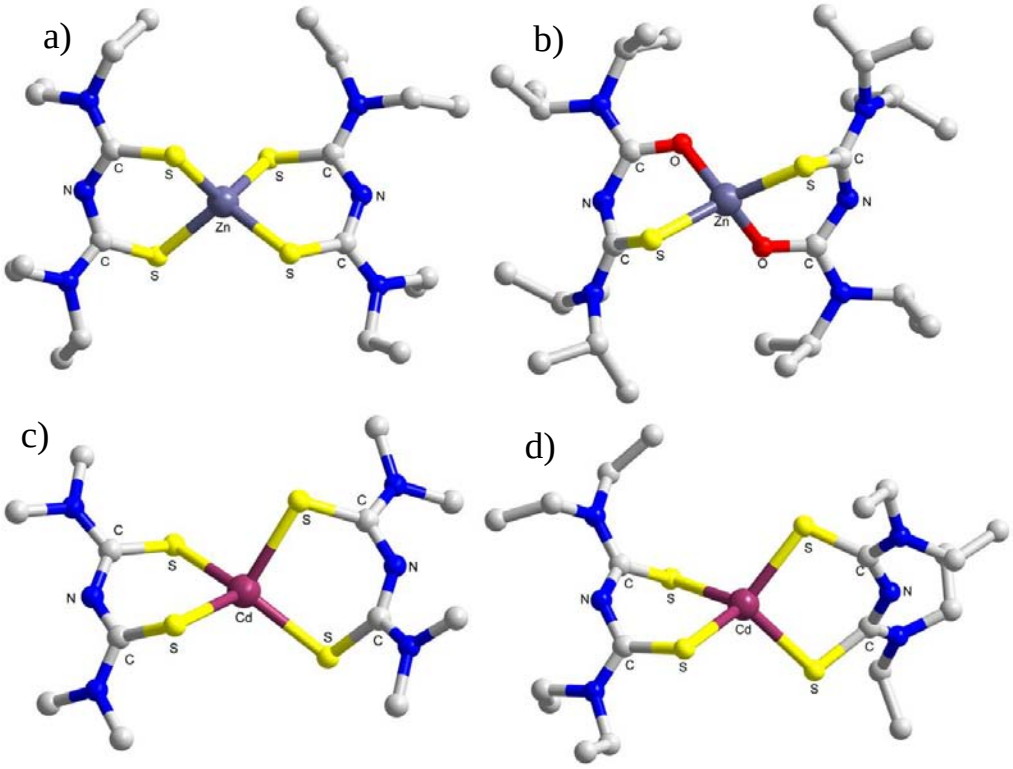

Fig. 5.1 (a) X-ray structure of (**2**). Selected bond lengths (Å) and bond angles (°): Zn1-S1 2.317(7), Zn1-S3 2.312(7), S1-C3 1.759(2), N1-C3 1.345(3); S2-Zn1-S1 102.55(2), S3-Zn1-S4 103.41(2). (b) X-ray structure of (**3**). Selected bond lengths (Å) and bond angles (°): Zn1-O1 1.972(2), Zn1-S1 2.268(1), S1-C7 1.789(4), O1-C8 1.254(4); O1-Zn1-S1 94.93(7), O2-Zn1-S2 97.28(7). (c) X-ray structure of (**4**). Selected bond lengths (Å) and bond angles (°): Cd1-S1 2.498(7), Cd1-S3 2.512(7), S1-C3 1.746(3), N1-C3 1.344(3); S2-Cd1-S1 96.46(2), S3-Cd1-S4 99.04(2). (d) X-ray structure of (**5**). Selected bond lengths (Å) and bond angles (°): Cd1-S5 2.516(6), Cd1-S7 2.499(6), S5-C23 1.752(2), N7-C27 1.464(2); S6-Cd1-S5 98.24(2), S8-Cd1-S7 97.84(2).

are almost mutually perpendicular with a torsional angle of 86.16(8). The metal to sulfur bond distances are (2.3058(7) Å) and (2.3174(7) Å). However, in order to accommodate the longer Zn-S bonds and the wide bite angle, the two ligand frameworks in the crystal structure of complex (**2**) adopt much greater torsional twists of 55.7(2)° and 56.0(2)° about the central N(2) and N(5) atoms respectively. The thiourea C-N bonds within the chelate ring are substantially shorter than the exocyclic C-NEt_2 bonds indicating that a good description of delocalisation of

electrons in the six membered (NC_2S_2-Zn) ring. Selected bond angles and bond lengths are given in caption to Fig. 5.1(a). Structure refinement is listed in Table. A8.

5.4.2 Single crystal X-ray structure of [Zn(SON(CN^{i}Pr$_2$)$_2$)$_2$] (3)

The single crystal X-ray structure of [Zn(SON(CN^{i}Pr$_2$)$_2$)$_2$] (**3**) in Fig. 5.1(b) shows zinc in distorted tetrahedral geometry with S_2O_2 donor set. The two sulfur and two oxygen atoms are at the corners of the tetrahedron. Both thiobiuret ligands of each unit are chelating to form two six membered rings (NC_2OS-Zn). The ligand bite angles of 94.93(7) and 97.28(7) are smaller than the expected perfect tetrahedral angle and angle observed for methyl analogue of similar complex. The crystal lattice shows the presence of monomeric independent units, which are separated by normal van der Waals distances. Both thiobiuret ligands are arranged in perfect planar orientation with a very slight deviation from planarity due to twisting about the central N atom observed. The angles between the two pairs of urea and thiourea 126.8(3)° are 123.4(3)°. In both ligands, the pattern of bond distances indicates that the formal negative charge is predominately localized on the S atom. The relatively long C(7)-S(1) and short C(8)-O(1) average bond lengths of 1.789(6) and 1.254(4) Å are consistent with mostly single and double bond character respectively. This bond localization is also reflected in the average C-N bond distances to the central N atom: 1.319(4) Å in the (*iso*)thiourea group and 1.367(4) Å in the urea group. The urea C(8)–N(2) bond 1.367(4) Å within the chelate ring are substantially longer than the exocyclic C–N^{i}Pr$_2$ bond 1.360(4) Å but the thiourea C(7)-N(2) bond 1.319(4) Å in coordinating ring is somewhat shorter than the exocyclic C–N^{i}Pr$_2$ bond 1.331(4) Å. The metal to sulfur bond (2.272(2) Å is longer than metal to oxygen bond (1.972(2). Selected bond angles and bond lengths are given in caption to Fig. 5.1b. Structure refinement is listed in Table. A8.

5.4.3 Single crystal X-ray structure of $[Cd(N(SCNMe_2)_2)_2]$ (4)

The single crystal X-ray structure of cadmium complex shows that cadmium has a distorted tetrahedral geometry with the ligand bite angles of 99.04(2)° and 96.46(2)° which are consistent with that reported for zinc complex (**1**), but somewhat smaller than the perfect tetrahedral angle. The bond lengths of N1-C3, N2-C3, N2-C4, N4-C4 bonds 1.315 to 1.344 Å shorter than exocyclic C-NMe_2 bonds indicating that delocalisation of electrons around all the atoms. Bond lengths of Cd-S 2.498 Å to 2.579 Å also clearly supports the involvement of cadmium on electron delocalisation although longer than the bond length observed for zinc complex (2.310 Å). Otherwise the single crystal X-ray structure of complex (**4**) is the structural analogous of zinc complex.[62]

5.4.4 Single crystal X-ray structure of $[Cd(N(SCNEt_2)_2)_2]$ (5)

The single crystal X-ray structure of complex $[Cd(N(SCNEt_2)_2)_2]$ (**5**) in Fig.5. 1(d), shows cadmium in distorted tetrahedral geometry. The complex crystallises in triclinic crystal system with P-1 space group. Two independent monomer units were observed in a unit cell. Otherwise the complex (**5**) is the structurally analogous of zinc complex (**2**). Selected bond angles and bond lengths are given in caption to Fig. 5.1(d). Structure refinement is listed in Table A9.

5.4.5 Thermogravimetric analysis (TGA)

Thermogravimetric analysis gives an idea about the decomposition and volatility of complexes. TGA of zinc complexes (**1**), (**2**) and (**3**) indicated single step decomposition with rapid weight loss of between 249-348 °C, 258-344 °C and 160-310 °C. The solid decomposition residue amounts to 21.9 % for (**1**) which is in good agreement with the calculated value of 22.0 % for ZnS. Similarly the observed

weights of final residues are 16. 6 % for (**2**) and 14.1 % for (**3**) which are close to calculated values of ZnS for 17.4 % and 15.2 % respectively.

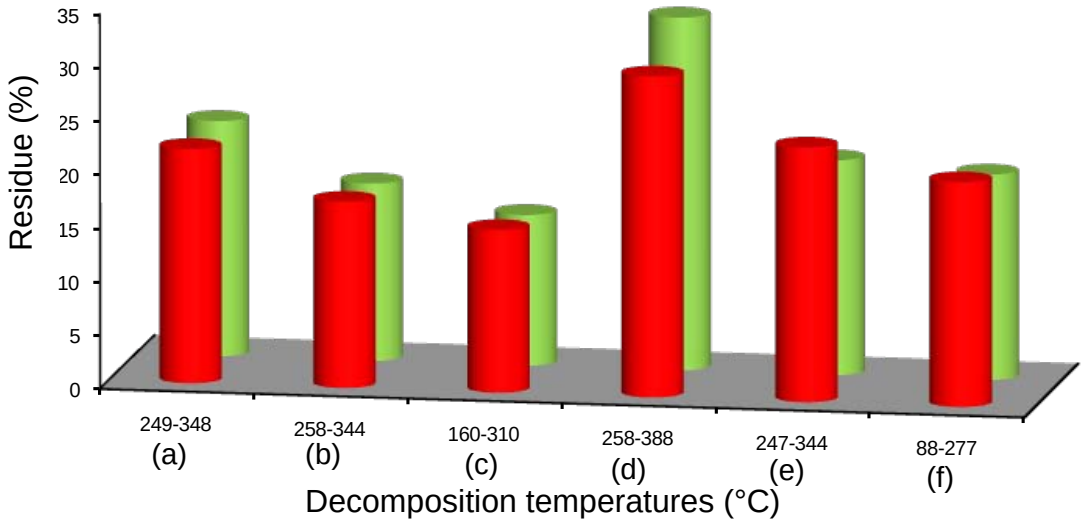

Fig. 5.2 Graph showing decomposition of precursors (a) $[Zn(N(SCNMe_2)_2)_2]$ (**1**), (b) $[Zn(N(SCNEt_2)_2)_2]$ (**2**), (c) $[Zn(SON(CN^iPr_2)_2)_2]$ (**3**), (d) $[Cd(N(SCNMe_2)_2)_2]$ (**4**), (e) $[Cd(N(SCNEt_2)_2)_2]$ (**5**) and (f) $[Cd(SON(CN^iPr_2)_2)_2]$ (**6**). Calculated residue (red), observed residue (green)

TGA of cadmium complexes (**4**), (**5**) and (**6**) showed single step decomposition with weight loss between 258-388°C, 247-344°C and 88- 277°C. The residue amounts to 33.0 % for (**4**) close to calculated value of 30.0 % for CdS. 20.1 % for (**5**) and 19.2 % for (**6**) which are close to calculated for CdS 23.8 % and 21.0 respectively (Fig. 5.2).

5.4.6 ZnS thin films

The apparatus used for the deposition of ZnS thin films is similar to that previously reported.[63] Glass substrates (2 x 2 cm, 7 or 8) were placed inside the reactor. Aerosols of thoroughly degassed solution of the precursor dissolved in THF (200 mg in 20 mL) were transported to the heated substrate using argon as a carrier gas at the flow rate of 160 sccm. ZnS thin films were deposited on glass substrates in the temperature range 300 to 450°C. Clean adhesive reflective uniform ZnS films were deposited at all temperatures from $[Zn(N(SCNMe_2)_2)_2]$ (**1**) and $[Zn(N(SCNEt_2)_2)_2]$ (**2**) whereas white, uniform, thick films were deposited from

$[Zn(SON(CN^{i}Pr_2)_2)_2]$ (**3**) at 300 and 350 °C and dark uniform films were deposited at 400 and 450 °C

5.4.6.1 Optical bandgap

The optical band gap of the deposited ZnS films can be estimated from the UV spectra. The recorded spectra closely resembled those reported in the literature for ZnS.[64] As a general rule, ZnS coatings were completely transparent throughout the visible range, with a strong absorption at ≈ λ380 nm, ascribed to electronic interband transition from the filled sulfide (S 3p) valence band to empty conduction band, with a strong Zn(II) 4s character for ZnS.

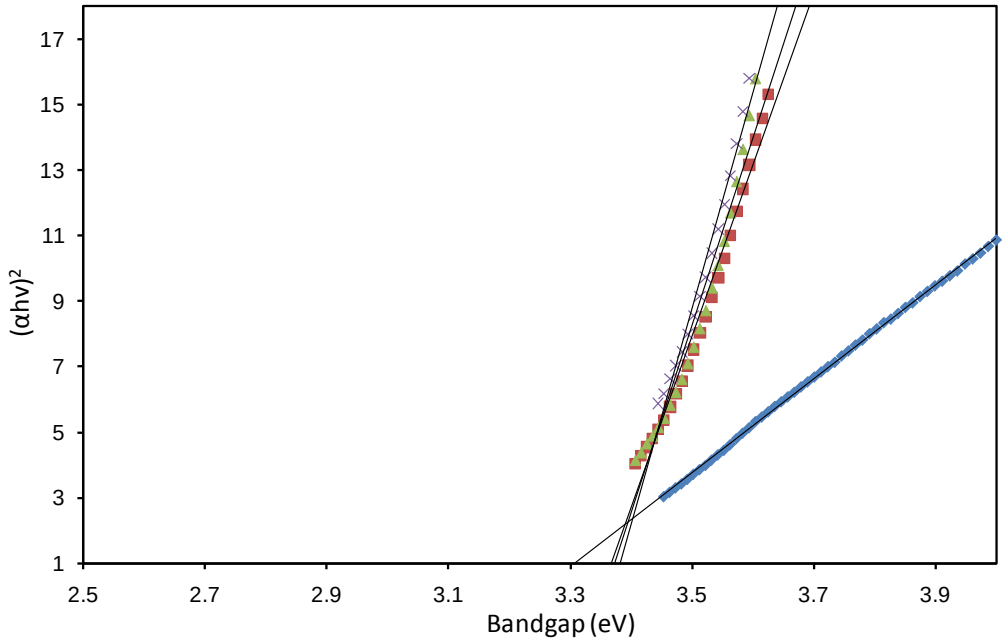

Fig. 5.3 Optical spectra of ZnS films deposited using $[Zn(N(SCNMe_2)_2)_2]$ (**1**), (♦) 300°C, (■) 350°C, (▲) 400°C and (X) 450°C

The optical bandgap of the deposited films is influenced by two factors, the inherent band gap of the material and a tail due to disorder.[65] The energy band gap of the films were measured from the dependence of absorption coefficient, α, on the photon energy, (*hv*). In the present case, a plot of $(\alpha hv)^2$ versus (*hv*) is linear, indicating the direct band nature of the films. Extrapolating the linear portion of the curve on to X-axis gives the bandgap for the film. The evaluated band gaps are 3.23

eV (300°C), 3.34 eV (350°C), 3.35eV (400°C) and 3.36 eV (450°C) for $[Zn(N(SCNMe_2)_2)_2]$ (**1**) (Fig. 5.3), 2.62 eV (300 °C), 3.07 eV (350 °C), 3.21 eV (400 °C and 450 °C) for $[Zn(N(SCNEt_2)_2)_2]$ (**2**), and 3.23 eV (300 °C), 3.29 eV (350 °C), 3.30 eV (400 °C) and 3.31 eV (450 °C) for $[Zn(SON(CN^iPr_2)_2)_2]$ (**3**). The variation of energy band gap, E_g, as a function of deposition temperature is shown in Fig. 5. 4.

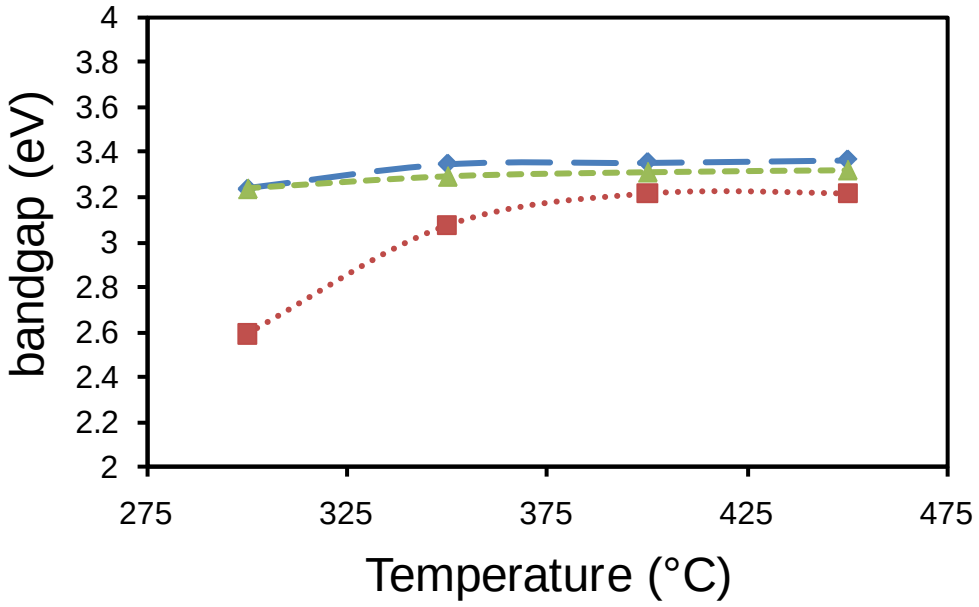

Fig. 5. 4 Graph showing variation of ZnS bandgap versus deposition temperatures using ♦) $[Zn(N(SCNMe_2)_2)_2]$ (**1**), ■) $[Zn(N(SCNEt_2)_2)_2]$ (**2**) and▲) ($[Zn(SON(CN^iPr_2)_2)_2]$ (**3**)

The band gap was found to increase with the increasing deposition temperature. It is well known that the energy band gap of a semiconductor is affected by the residual strain, defects, charged impurities, disorder at the grain boundaries and also particle size confinement.[66] In addition, the tensile strain will result in a decrease of band gap due to the elongated lattice whereas a compressional strain increases the band gap due to the compressed lattice of the film.

5.4.6.2 Structural studies

The powder X-ray diffraction patterns of zinc sulfide thin films deposited on glass substrate from precursors $[Zn(N(SCNMe_2)_2)_2]$ (**1**), $[Zn(N(SCNEt_2)_2)_2]$ (**2**) and $[Zn(SON(CN^iPr_2)_2)_2]$ (**3**) are shown in Fig. 5.5 and 5.6. The intense peak at 2θ 28.6°

(*d* = 3.12 Å) corresponds to the hexagonal (002) (ICDD: 008-7254) and/or cubic (111) reflections of ZnS (ICDD: 003-0570). The very weak lines at 2θ 51.9° (d = 1.76 Å) and 2θ 59.3° (d = 1.56 Å) correspond to the hexagonal (103) planes and the hexagonal (004) and/or cubic (222) planes respectively.

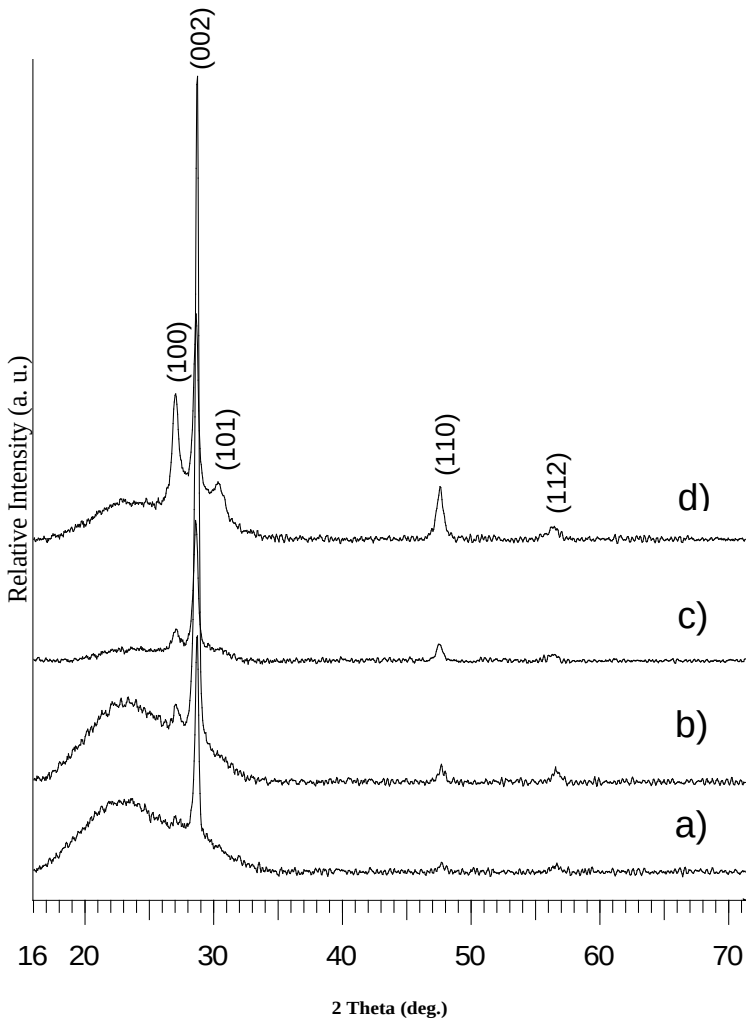

Fig. 5.5 PXRD pattern of ZnS films deposited using $[Zn(N(SCNEt_2)_2)_2]$ (**2**) at a) 300 °C, b) 350 °C, c) 400 °C and d) 450 °C on glass substrate.

Precursor (**1**) at 350 °C gives the cubic phase and above 400 °C the hexagonal phase is seen as confirmed by a second intense reflection at 2θ 47.8° (d = 1.91 Å). The reflection at d = 1.76 Å, (103) plane is unique to the hexagonal phase. A similar cubic to hexagonal phase transition above 400 °C is observed with

precursor (**3**). In contrast to these results, only the hexagonal phase of zinc sulfide films was observed using precursor (**2**) (Fig. 5.7)

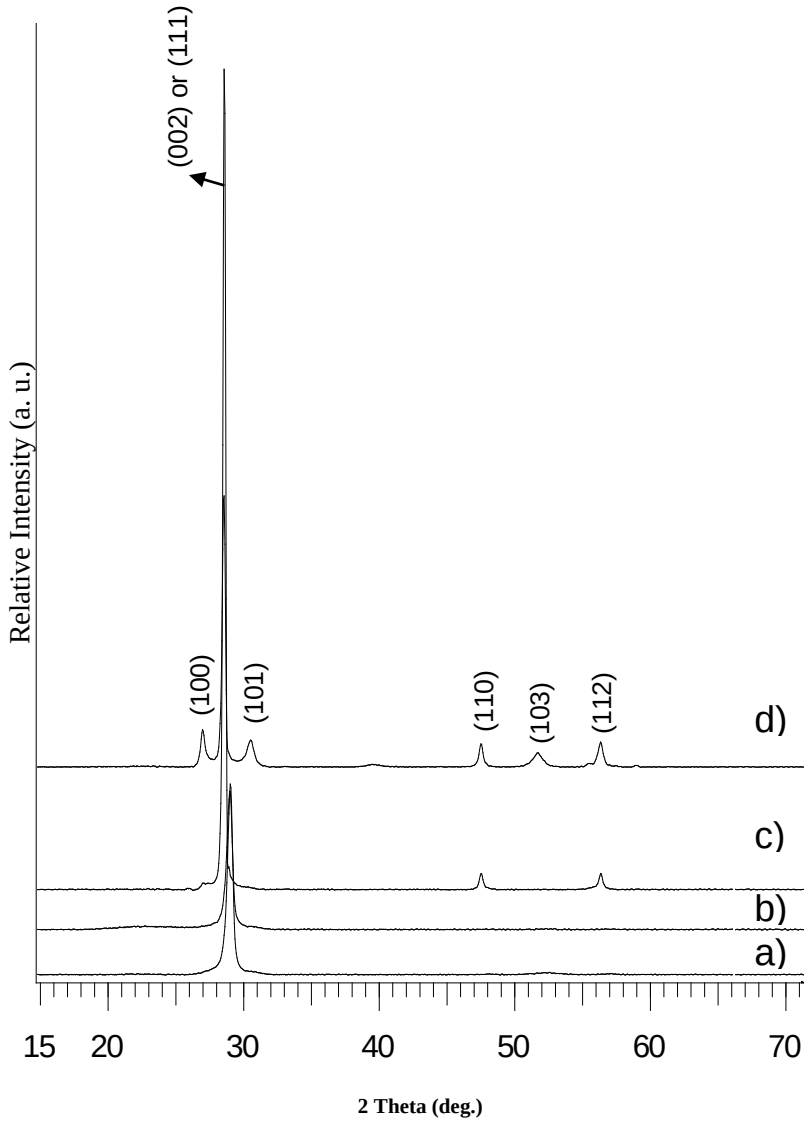

Fig. 5.6 PXRD pattern of ZnS films deposited using [Zn(SON(CN^{i}Pr$_2$)$_2$)$_2$] (**3**) at a) 300 °C, b) 350 °C, c) 400 °C and d) 450 °C on glass substrate.

Wold *et al.* reported that the temperature, sulfur fugacity and nature and orientation of substrates are the three major parameters which decide the phase cubic or hexagonal of ZnS deposition.[4] In our system the temperature or sulfiding nature of the precursors could be the reason for the deposition of cubic or hexagonal ZnS films. ZnS films deposited from precursors (**1**) and (**3**) were similar to Wold *et al.* observations. The various factors that influence the stable polycrystalline state of a material include: the lowest surface energy, the grain

boundary energy and the diffusion of surface atoms.[67] The reports by Lee *et al.*[68] reveal that the strain energy minimization and surface energy minimization would compete with one another to determine the preferred orientation of grain growth and the final texture of thin films. The extent of these energy states depends on the thickness of the films. The minimization of strain energy promotes one type of texture while the minimization of surface energy promotes another. Moreover, in thinner films surface energy dominates, whereas at greater thickness strain energy will be significant. The surface structure of the substrate forces the nuclei to grow along a specific orientation preventing the nucleation along other orientations.[69] It can be concluded from the above discussion that the interaction at the film and substrate interface could be high at lower deposition temperature. This could cause the film to grow in cubic structure. The influence of the substrate might be reduced with the increase of film thickness at higher deposition temperature.

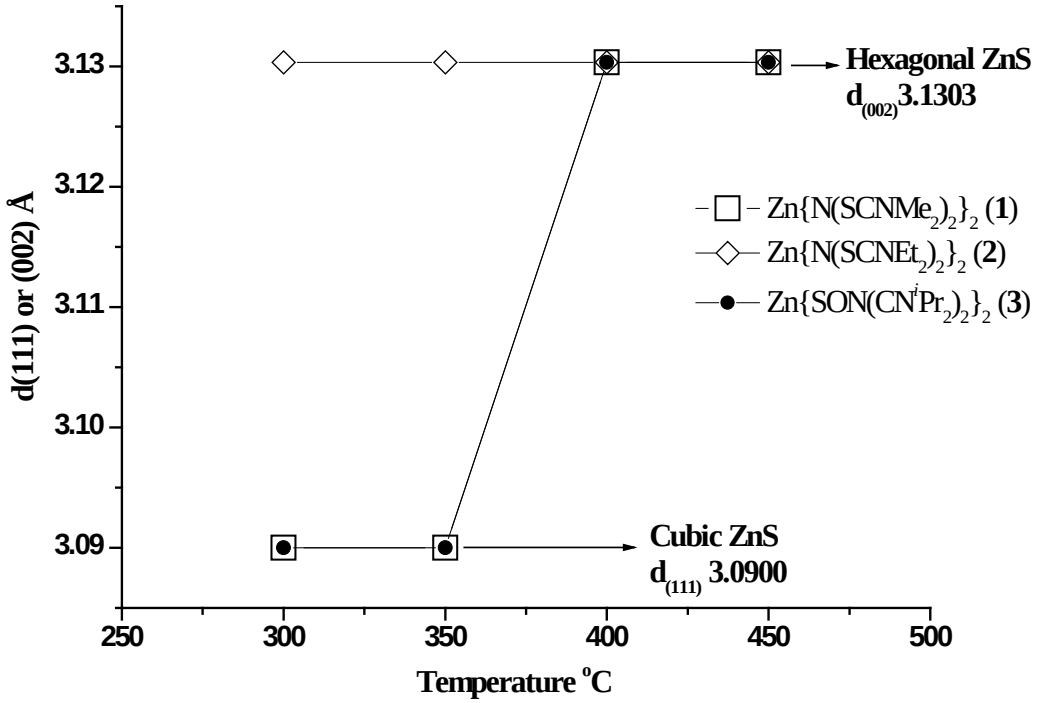

Fig. 5.7 Graph showing variation of cubic and hexagonal ZnS films deposited from complexes (**1**), (**2**) and (**3**) at temperature between 300 and 450 °C

Unequivocal characterization of the crystallographic phase is difficult for oriented ZnS films, and is often absent in the literature. The growth of hexagonal

ZnS films generally occurs at higher temperatures but can also occur at temperatures as low as 300 °C.[4] The coexistence of zinc-blende and wurtzite structure for ZnS was reported in literature.[4,70,71] Johnston *et al.*[72] and Cheng *et al.*[73] reported the hexagonal structure, while Saratale *et al.*[74] and Lee *et al.*[75] reported the cubic structure for the films prepared by chemical bath deposition. Elidrissi *et al.* reported that ZnS films grown by spray pyrolysis on glass substrates exhibited a mixture of both cubic and hexagonal phases.[76] This analysis shows that the presence of crystalline phase in ZnS films is sensitive to the method of preparation, the substrates used to prepare the films and the deposition temperature.[71] Generally in polycrystalline thin film structures, the predominant structure or orientation mainly depends on the processing parameters. The structural changes occur by surface diffusion and migration of grain boundaries during the coalescence of two differently oriented nuclei. In such cases, smaller nuclei may easily rotate on coalescence that induces the structural changes.[77]

5.4.6.3 Morphological studies

The SEM images of ZnS thin films grown on glass substrate for 1.5 h at temperature range of 300 - 450 °C, using precursors $[Zn(N(SCNMe_2)_2)_2]$ (**1**), $[Zn(N(SCNEt_2)_2)_2]$ (**2**) and $[Zn(SON(CN^iPr_2)_2)_2]$ (**3**) are shown in Fig. 5.8. Images show dense and well-arranged approx 1µm long vertical rod like crystallites were deposited from (**1**) at 450 °C, 800 ± 30 nm length of rods at 400 °C and irregular crystallites deposited at 350, and 300 °C with the size of 550 ± 25 nm, 400 ± 35 nm respectively. Highly packed spherical crystallites were deposited from precursor (**2**) at all temperatures with the size range of 300 ± 20 nm to 450 ± 30 nm. In contrast to these morphologies of crystallites deposited from precursors (**1**) and (**2**), granular crystallites deposited from precursor (**3**) with approx size range of 800 ± 35 nm to 1300 ± 50 nm at 300 - 450 °C. The increase in crystallites size with an improved crystallinity at higher temperature follows the results obtained by PXRD and UV

spectra. EDX measurement with power source of 20 kV for the films deposited on glass substrate show that the films are composed of Zn: S; 47: 53 % at 300 °C, 48: 52% at 350 °C, 50: 50% at 400 °C and at 450 °C 52: 48 from precursor (**1**), Zn: S; 48: 52 % at 300 °C, 50: 50% at 350 and 400 °C and at 450 °C 51: 49 from precursor (**2**) and Zn: S; 48: 52 % at 300 and 350 °C, 50: 50% at 400 °C and 450 °C, 51: 49 from precursor (**3**).

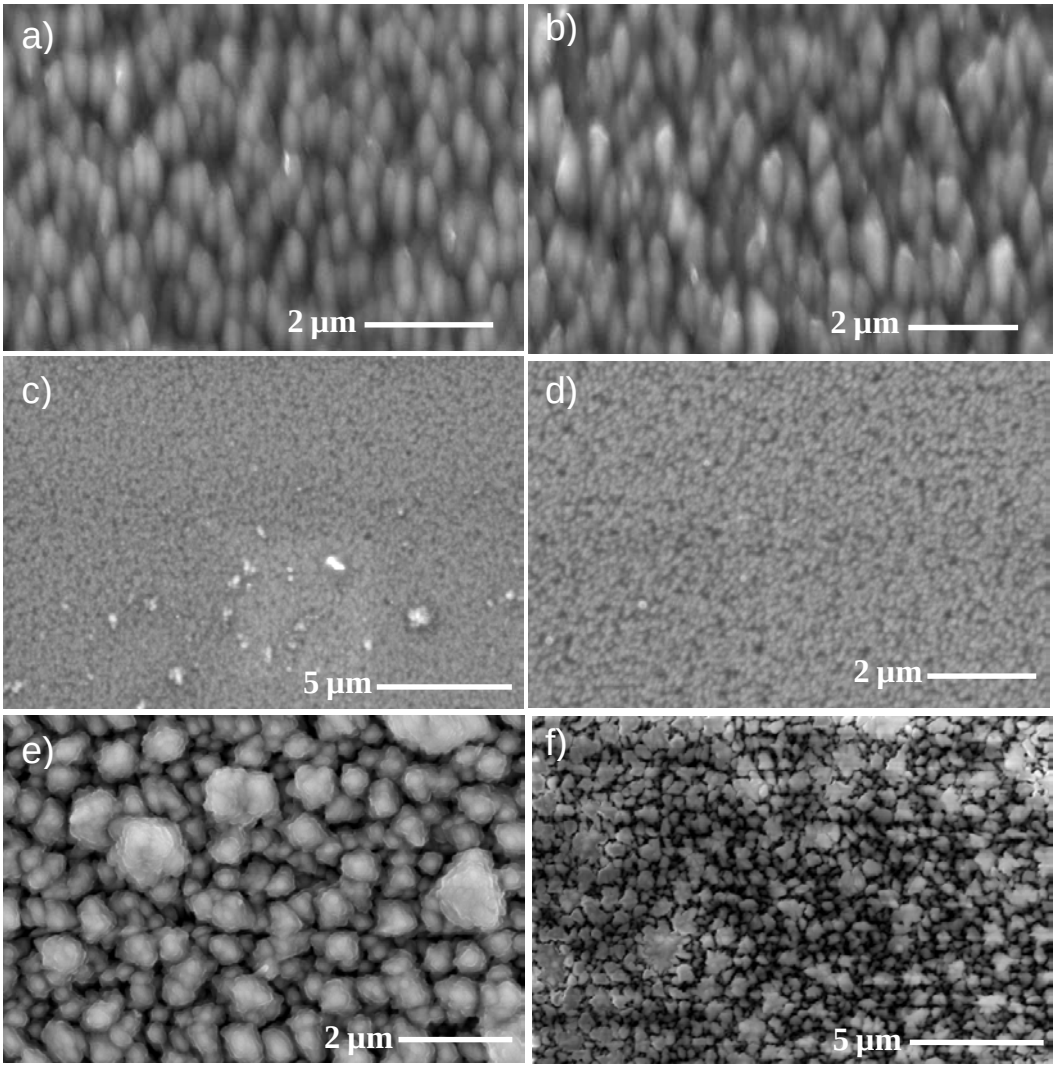

Fig. 5.8 SEM image of ZnS films deposited using $[Zn(N(SCNMe_2)_2)_2]$ at a) 400 °C, b) 450 °C, $[Zn(N(SCNEt_2)_2)_2]$ at c) 400 °C, d) 450 °C and $[Zn(SON(CN^iPr_2)_2)_2]$ e) 400 °C and f) 450 °C.

The AFM measurements were performed to analyse the topography of the as-deposited films. Fig. 5.9 shows the surface morphology of ZnS films prepared

from three different precursors. These pictures show presence of uniform and crack-free surface morphologies characterized by well interconnected rods.

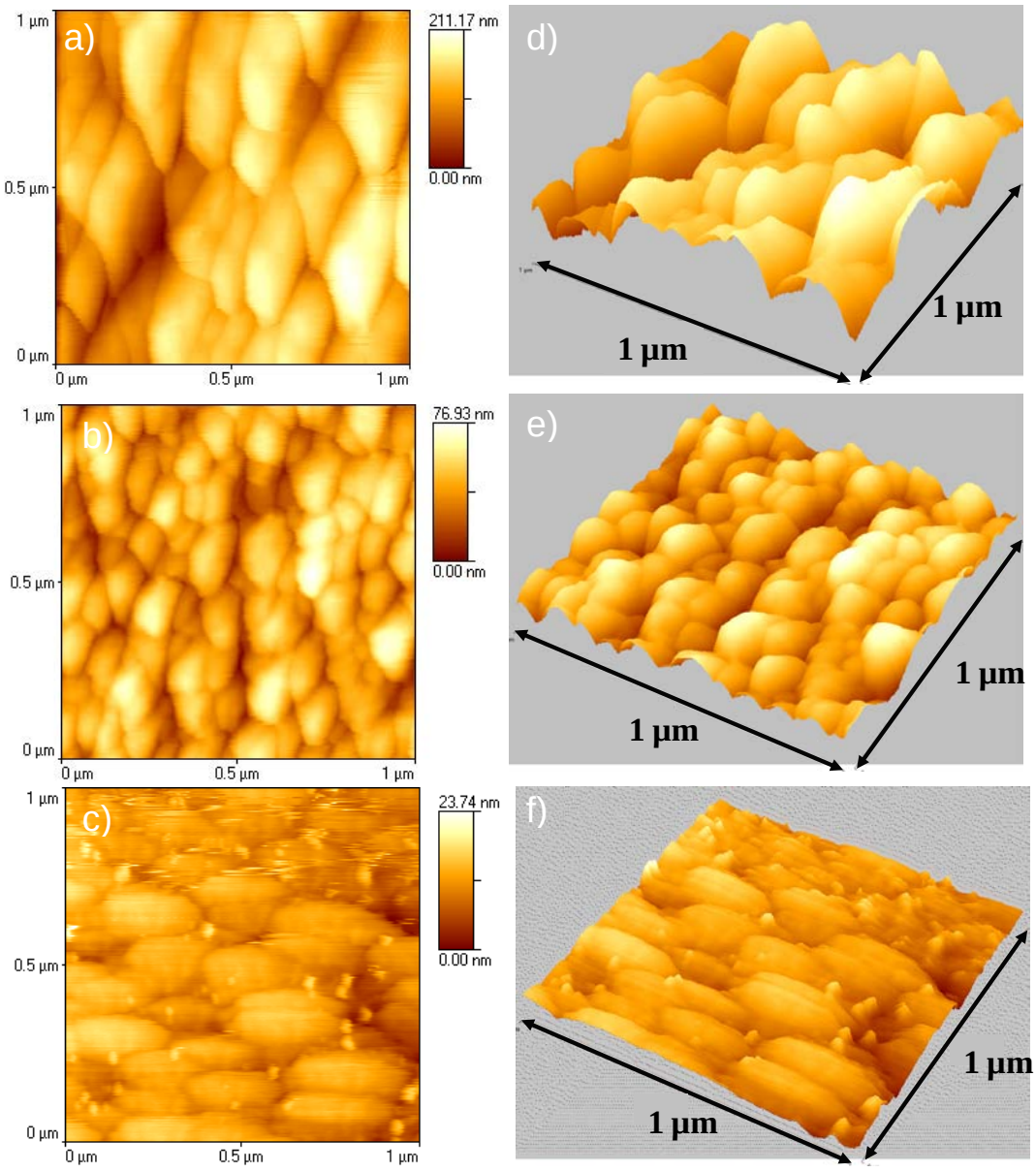

Fig. 5.9 AFM images of ZnS films deposited at 400 °C a) and d) 2D, 3D images of films from $[Zn(N(SCNMe_2)_2)_2]$, b) and e) 2D, 3D images of films from $[Zn(N(SCNEt_2)_2)_2]$ and c) and f) 2D, 3D images of films from $[Zn(SON(CN^iPr_2)_2)_2]$

The typical root mean square roughness was 25 nm to 30 nm at deposition temperature from 300 to 450 °C films deposited using precursor (**1**). Similarly well connected closely packed crystallites were seen from the AFM images of films deposited from precursor (**2**) with the typical root mean square roughness of 22 to

28 nm at temperature from 300 to 450 °C. AFM images of films deposited from precursor (**3**) show closely packed granular crystallites with the typical root mean square roughness of 34 to 40 nm at temperature from 300 to 450 °C. The increase in surface roughness with increasing deposition temperature associated with increase of grain size. As the grain grew bigger, the density of grain boundaries decreased and the grain growth took place with a large variation in the height of the grain on the film surface. Therefore it is apparent that the deposition temperature of the film changes the grain sizes as well as the surface roughness.

5.4.7 CdS thin films

The apparatus used for the deposition of CdS thin films is same as for ZnS. Glass substrates (2 x 2 cm, 7 or 8) were placed inside the reactor. Aerosols of thoroughly degassed solution of the precursors (**4**), (**5**) or (**6**) dissolved in THF (200mg in 20mL) transported to the heated substrate using argon as a carrier gas at the flow rate of 160 sccm. CdS thin films were deposited on glass substrates at temperatures ranging from 350 to 500 °C. No deposition was observed below 350 °C and above 500 °C from all three precursors. Yellowish specular CdS films were deposited on glass substrates at 350 and 400 °C. Dark yellow films were deposited at 450 and 500 °C from $[Cd(N(SCNMe_2)_2)_2]$ (**4**). Reflective yellow films of CdS were deposited on glass substrates at 350 and 400 °C, brownish films were deposited at 450 and 500 °C from $[Cd(N(SCNEt_2)_2)_2]$ (**5**) whereas uniform, thick, yellow films were deposited at 350–500 °C from $[Cd(SON(CN^iPr_2)_2)_2]$ (**6**).

5.4.7.1 Optical bandgap

The optical bandgap of the CdS films deposited from precursors (**4**), (**5**) and (**6**) were estimated from the UV spectra. The recorded band gaps are in good agreement with literature values.[43] The red shift in the fundamental absorption edge

with increasing deposition temperature indicates the growth of bigger crystallites at higher temperatures.

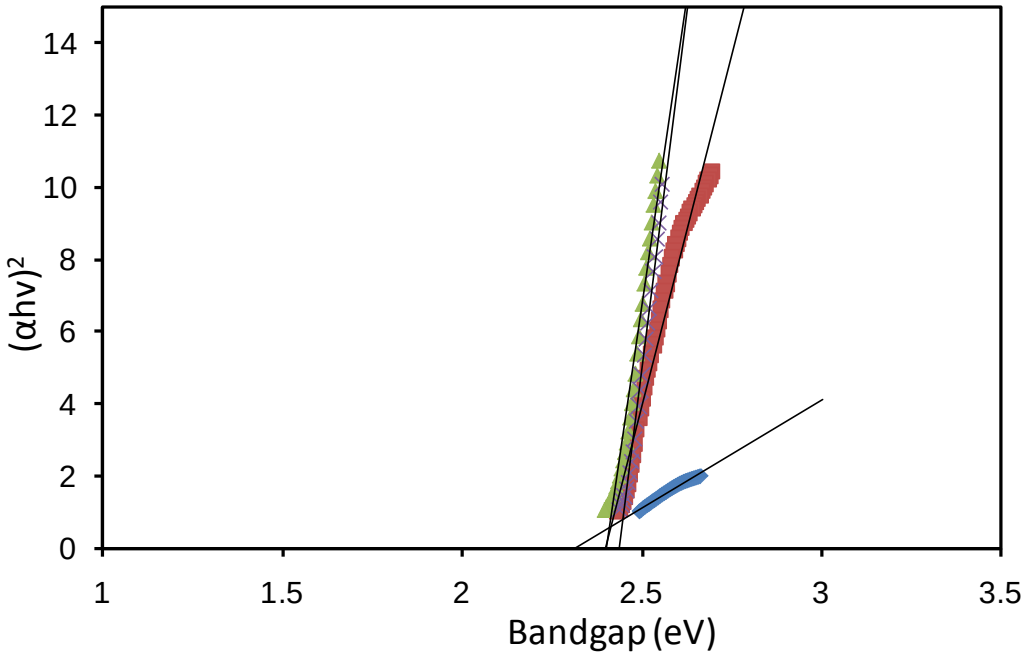

Fig. 5.10 Optical spectra of CdS films deposited using [Cd(N(SCNMe$_2$)$_2$)$_2$] (**4**); (♦) 300°C, (■) 350°C, (▲) 400°C and (X) 450°C

It is well known that the energy band gap of a semiconductor is affected by the residual strain, defects, charged impurities, disorder at the grain boundaries and also particle size confinement. Increase in absorption intensity at higher deposition temperatures also confirms the deposition of thicker films. As a general rule, CdS coatings were completely transparent throughout the visible range, and a strong absorption onset occurred at ≈ 530 nm corresponding to electronic interband transition from the filled sulfide (S- 3p) valence band to empty conduction band, with a strong Cd(II) 4s character. The type of optical transition and the energy band gap of the films were measured from the dependence of absorption coefficient (α) on the photon energy ($h\nu$). In the present case, linear plot of $(\alpha h\nu)^2$ versus ($h\nu$) indicating the direct band nature of the CdS films, and extrapolating the linear portion of the curve on to X-axis gives the band gap for the film. The evaluated energy band gaps are: 2.31 eV (350 °C), 2.39 eV (400 and 450 °C) and 2.43 eV (500 °C) for

$[Cd(N(SCNMe_2)_2)_2]$ (**4**) (Fig. 5.10), 2.32 eV (350 °C), 2.38 eV (400 °C), 2.40 eV (450 °C) and 2.41 eV (500 °C) for $[Cd(N(SCNEt_2)_2)_2]$ (**5**), and 2.34 eV (350 °C), 2.38 eV (400 °C), 2.39 eV (450 °C), and 2.41 eV (500 °C) for $[Cd(SON(CN^iPr_2)_2)_2]$ (**6**). The variation of energy band gap, E_g, as a function of deposition temperature is shown in Fig. 5. 11. The band gap was found to increase with the increasing deposition temperature.

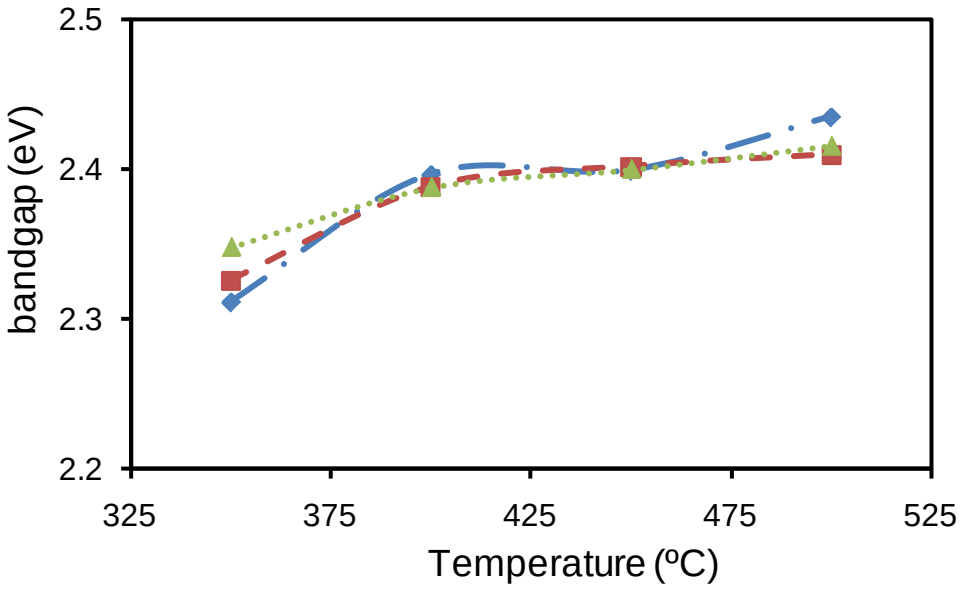

Fig. 5.11 Graph showing variation of CdS bandgap versus deposition temperatures using (♦) $[Cd(N(SCNMe_2)_2)_2]$, (■) $[Cd(N(SCNEt_2)_2)_2]$ and (▲) $[Cd(SON(CN^iPr_2)_2)_2]$

5.4.7.2 Structural studies

The powder X-ray pattern of cadmium sulfide thin films deposited on glass substrate from $[Cd(N(SCNMe_2)_2)_2]$ (**4**), $[Cd(N(SCNEt_2)_2)_2]$ (**5**) and $[Cd(SON(CN^iPr_2)_2)_2]$ (**6**) are shown in Fig. 5.12 and 5.13. PXRD patterns of CdS always show a well know complication of assigning the peaks to hexagonal or cubic polymorphs. Standard θ-2θ scans cannot reliably distinguish (111)-oriented cubic CdS from hexagonal CdS (001)-orientation.

However, in this study PXRD produced no evidence for cubic CdS in any films, and the following discussion assumes that they contain only hexagonal phase formed under most film growth conditions.[78] θ-2θ XRD scans on films deposited on glass substrate showed the intense diffraction peaks at 24.7° (*d* = 3.59 Å), 26.4° (*d* = 3.36 Å), 28.1° (*d* = 3.17 Å), 43.8° (*d* = 2.08 Å) and 47.8° (*d* = 1.90 Å) from the films deposited at 350 and 400 °C using precursors (**4**) and (**5**). Whereas the only single intense peak at 26.6° (*d* = 3.38 Å) was observed from films deposited using precursor (**6**) at 350 and 400 °C which indicates the preferred orientation along (002) plane.

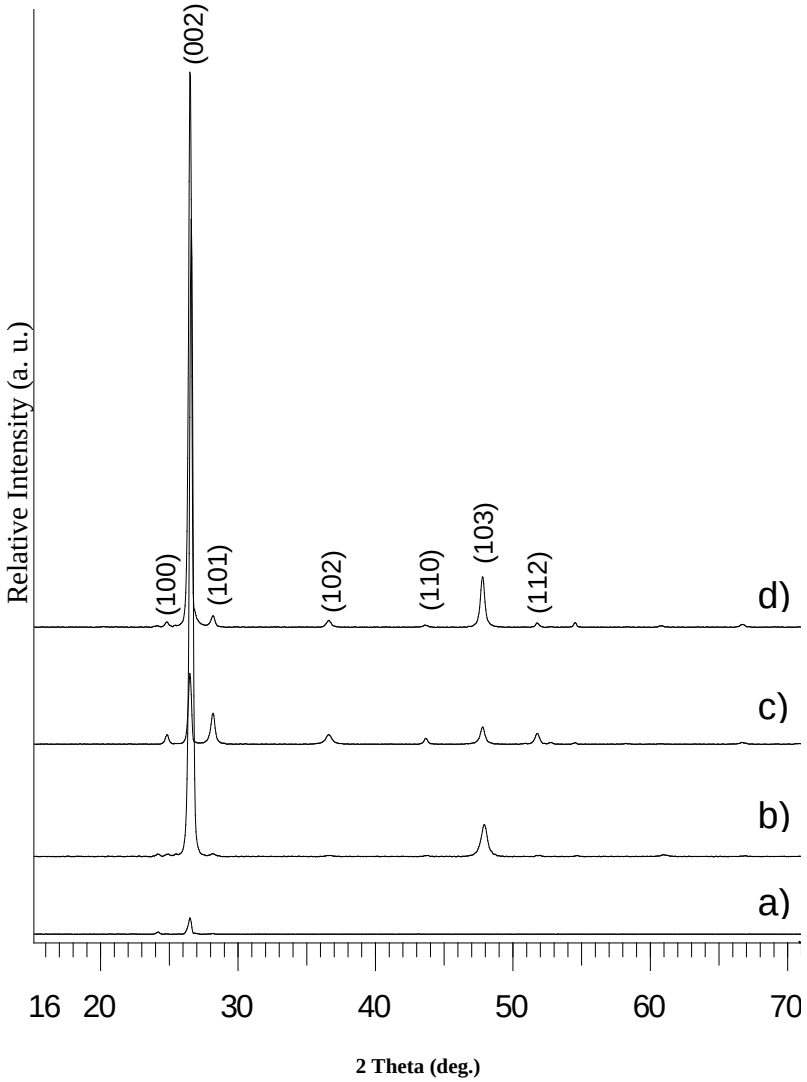

Fig. 5.12 PXRD pattern of CdS films deposited using [$Cd(N(SCNEt_2)_2)_2$] at a) 350 °C, b) 400 °C, c) 450 °C and d) 500 °C on glass substrate

The PXRD peaks from (**4**), (**5**) and (**6**) were indexed to (100), (002), (101), (110) and (103) planes of hexagonal CdS (ICDD: 01-075-1545). The lattice parameters (*c*) calculated from the largest diffraction plane (002) from the films deposited at 400 °C using precursors (**4**), (**5**) and (**6**) are 6.748, 6.763 and 6.758 respectively. The considerable increase in the *c* value from the bulk hexagonal CdS (c = 6.737) suggest the presence of a tensile strain along the *c*-axis.

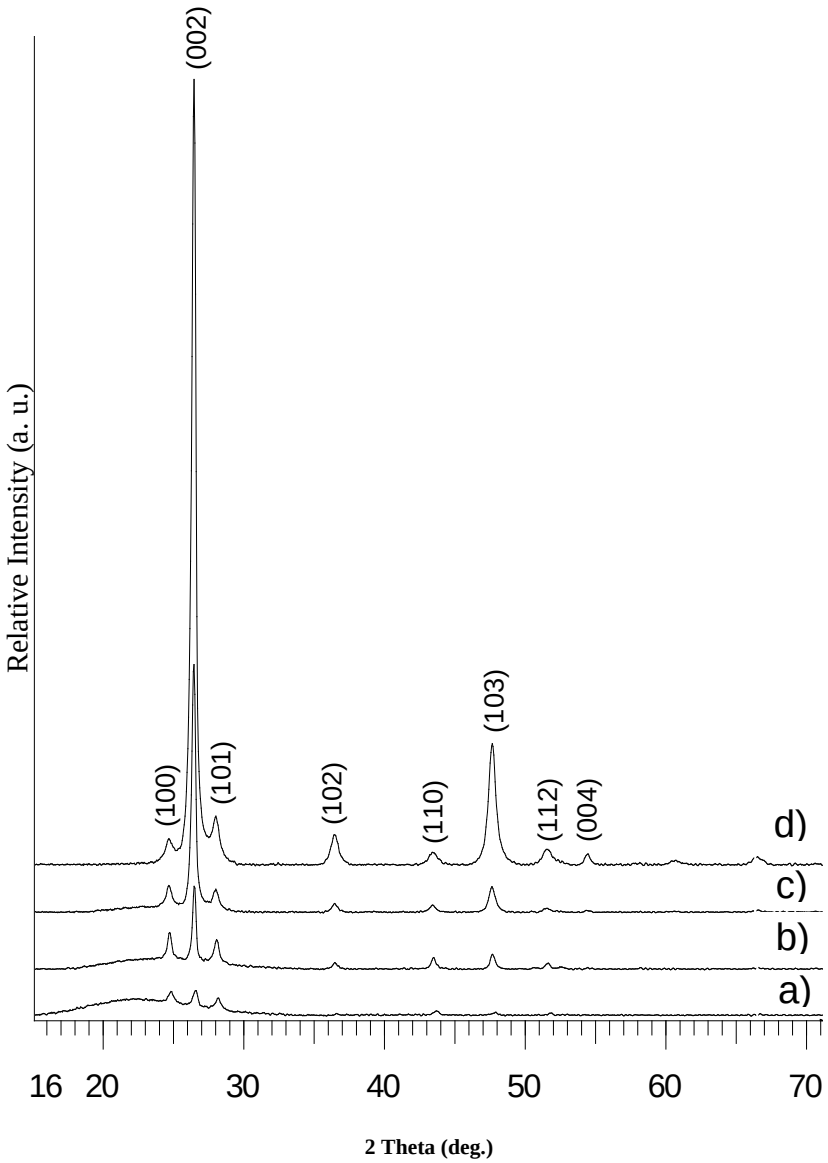

Fig. 5.13 PXRD pattern of CdS films deposited using $[Cd(SON(CN^{i}Pr_2)_2)_2]$ at a) 350 °C, b) 400 °C, c) 450 °C and d) 500 °C on glass substrate

5.4.7.3 Morphological studies

The SEM images (Fig. 5.14) of the films deposited from (**4**), (**5**) and (**6**) show growth

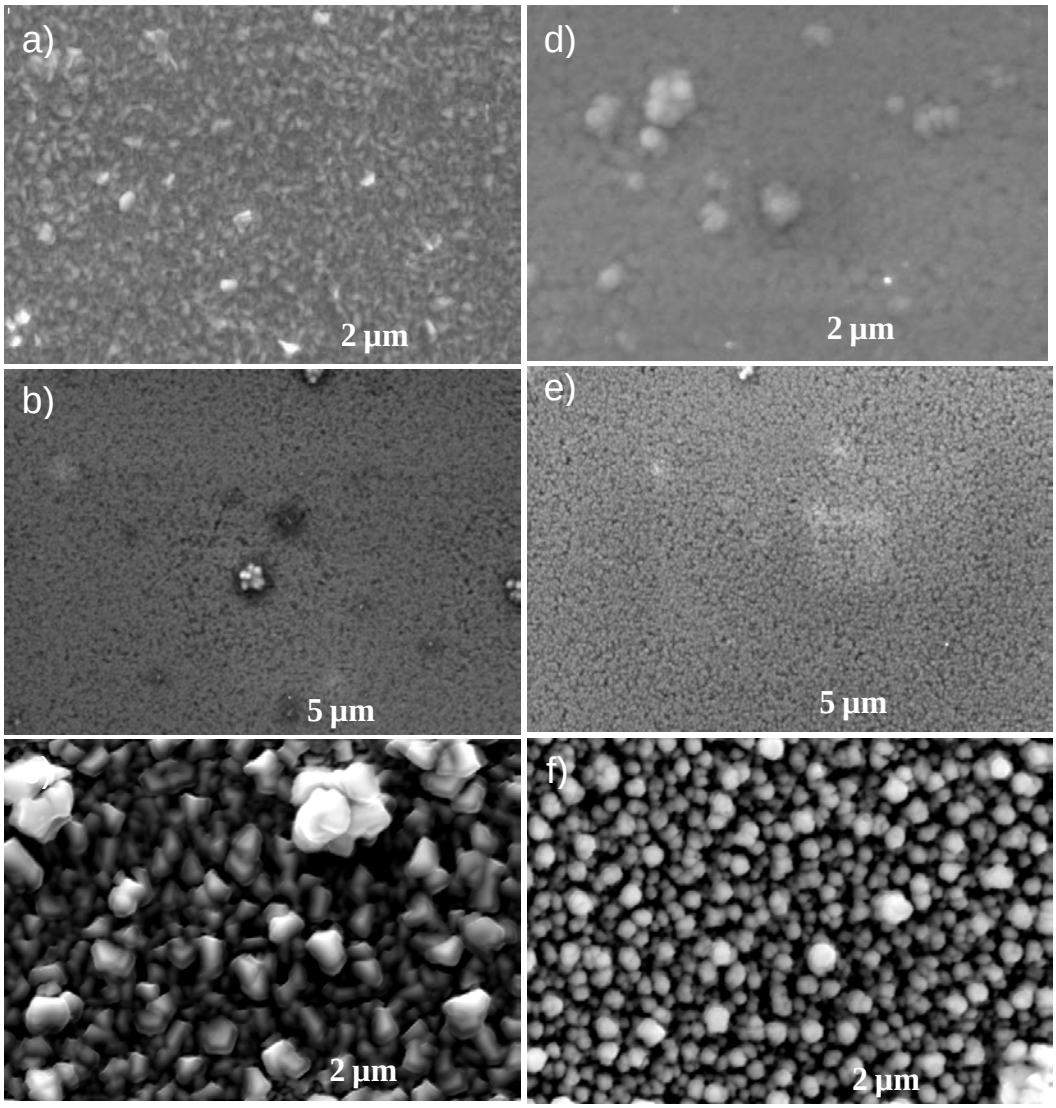

Fig. 5.14 SEM image of CdS films deposited using $[Cd(N(SCNMe_2)_2)_2]$ at a) 400 °C, b) 450 °C, $[Cd(N(SCNEt_2)_2)_2]$ at c) 400 °C, d) 450 °C and $[Cd(SON(CN^iPr_2)_2)_2]$ e) 400 °C and f) 450 °C

of granular scattered crystallites over the entire glass substrate at 350 °C whereas at 400 and 450 °C uniform bigger crystallites were observed. The deposition from precursor (**4**) at 500 °C produced clusters of granular crystallites with approx size range from 200 ± 25 nm to 350 ± 30 nm. Spherical crystallites of 400 ± 35 nm to 550 ± 30 nm observed from films deposited from using precursor (**5**) at deposition temperatures of 350 to 500 °C whereas irregular granular cluster like crystallites

were deposited from precursor (**6**) with an approx size range of 600 ± 50 nm to 1500 ± 30 nm. The composition of cadmium sulfide thin films deposited on glass substrates were analysed by EDX measurement with power source of 20 kV. The EDX analysis shows the percentage of Cd: S; 48 : 52% at 350 and 400 °C, 50 : 50 % at 450 °C and at 500 °C 52 : 48 for (**4**), Cd: S; ratio of 48 : 52 % at 350 °C, 50 : 50% at 400 and 450 °C and at 500 °C 51: 49 for (**5**) and Cd : S; ratio of 47 : 53 % at 350 and 400 °C, 50 : 50 % at 450 °C and at 500 °C 51: 49 for (**6**).

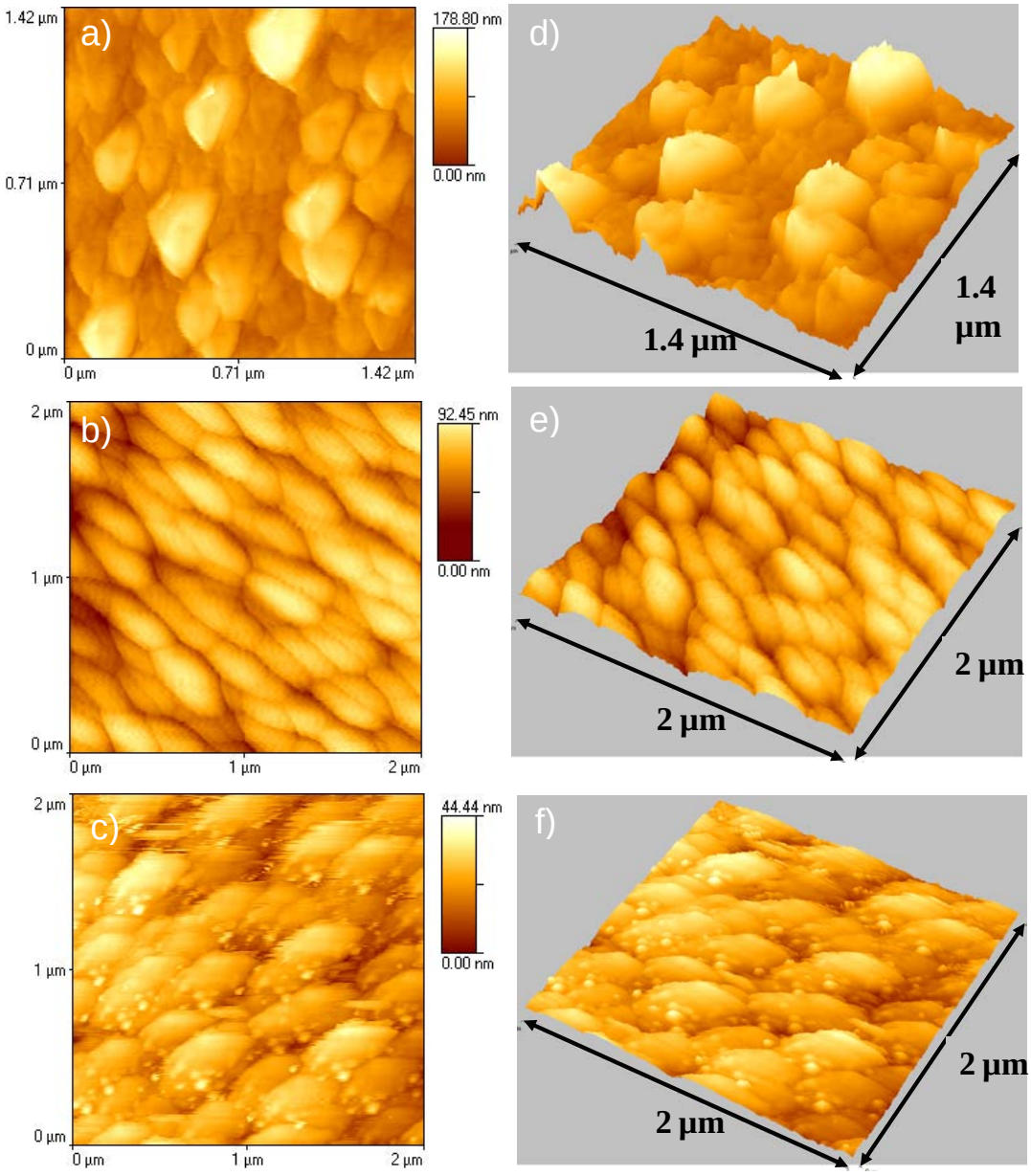

Fig. 5.15 AFM images of CdS films deposited at 400 °C a) and d) 2D, 3D images of films from [Cd(N(SCNMe$_2$)$_2$)$_2$], b) and e) 2D, 3D images of films from [Cd(N(SCNEt$_2$)$_2$)$_2$] and c) and f) 2D, 3D images of films from [Cd(SON(CN^{i}Pr$_2$)$_2$)$_2$]

The surface topography of the as-deposited films were analysed by AFM. Fig. 5.15 shows surface morphology of CdS films prepared from precursors (**4**), (**5**) and (**6**). AFM analysis from the films deposited using precursor (**4**) shows presence of uniform and crack-free surface morphologies characterized by well interconnected globular crystallites. The typical root mean square roughness was 20 nm to 27 nm at deposition temperature of 350 to 500 °C. Similarly well connected closely packed crystallites were observed from the AFM images of films deposited from precursor (**5**) with the typical root mean square roughness of 11 to 15 nm at temperature from 350 to 500 °C. AFM images of films deposited from precursor (**6**) show crack free surfaces of granular crystallites with the typical root mean square roughness of 25 to 34 nm at temperature from 350 to 500 °C. The increase in surface roughness with increasing deposition temperature associated with increase of grain size. It is apparent that the deposition temperature of the film changes the grain sizes as well as the surface roughness.

5.4.8 $Zn_xCd_{1-x}S$ thin films

Thermogravimetry confirmed that the zinc and cadmium precursors decompose to corresponding metal sulfides at similar temperatures in a single step. This data suggests that the pairs of precursors fulfill the design requirement for deposition of $Zn_xCd_{1-x}S$ by AACVD. The deposition temperature for the formation of homogeneous $Zn_xCd_{1-x}S$ was identified from the individual experiments carried out with each precursor. Films deposited at 400 °C by varying the ratio of precursors (**1**) and (**4**) in the delivery solution; x is the mole fraction of cadmium in this vessel throughout this section. The deposited films were colourless and uniform over the substrates at x=0.25 of cadmium precursor (**4**). A slightly yellowish tinge were observed at x = 0.50 and yellowish reflective films obtained at x=0.75. Similar films

were deposited using the precursors (**2**) and (**5**). Whereas films deposited using the precursors (**3**) and (**6**) thicker and uniform colourless at x = 0.25 and 0.5 to yellowish reflective at x = 0.75.

5.4.8.1 Optical bandgap

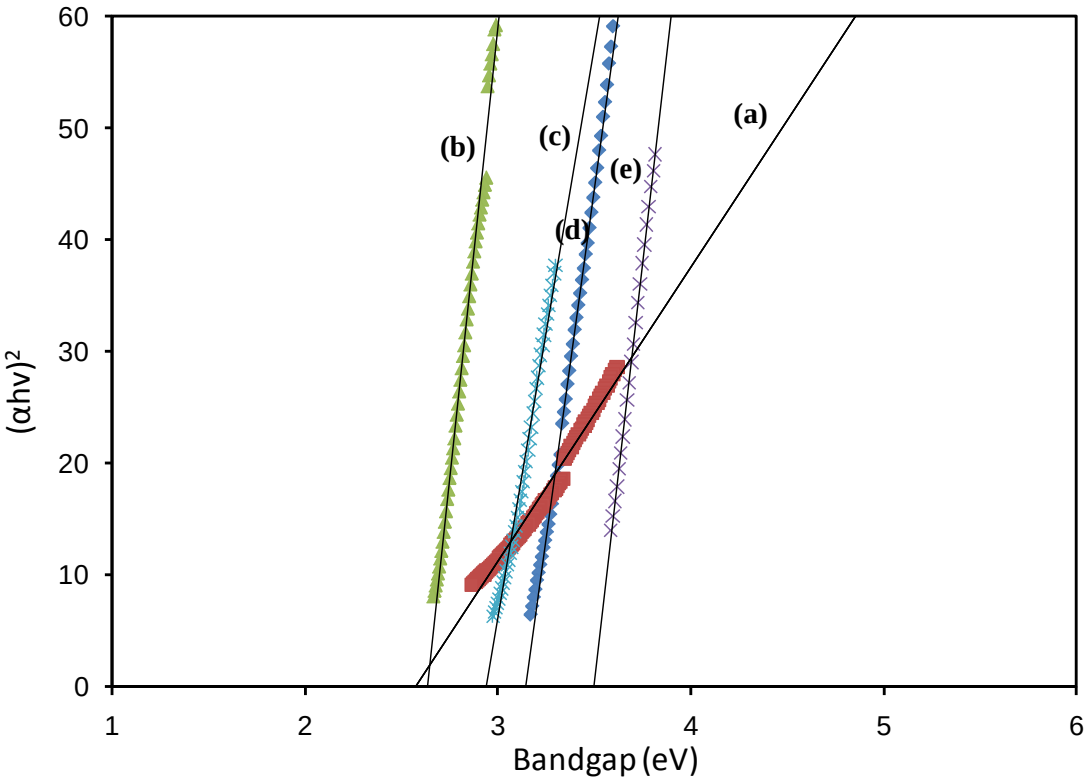

Fig. 5.16 Optical spectra of $Zn_xCd_{1-x}S$ films deposited using complexes (**2**) and (**5**). a) CdS, b) ZnS at 0.75, c) ZnS at 0.50, d) ZnS at 0.75 of cadmium precursor and e) ZnS films

The optical spectra of as-deposited films using precursors (**1**) and (**4**) were characterized by UV-visible spectroscopy. The value of the optical bandgap (Eg) is estimated by plotting $(\alpha hv)^2$ versus (hv), hv is the photon energy. Extrapolation of the linear portion of curve to $(\alpha hv)^2 = 0$ gives the optical band gap. The optical band gap of ZnS films deposited at 400 °C using precursor (**1**) is 3.35 eV and is 2.39 eV for the corresponding cadmium sulfide deposition from (**4**). The intermediate band gaps are : 3.10 eV, x= 0.25, 3.04 eV, x = 0.50 and 2.93 eV, x = 0.75. The band gaps measured for precursors (**2**) and (**5**): 2.76 eV, x = 0.25, 2.60 eV, x = 0.50 and 2.52

eV, x = 0.75 (Fig 5.16). Similarly, the band gaps of films deposited from varying the ratio of precursors (**3**) and (**6**): 3.14 eV, x = 0.25, 2.93 eV, x = 0.50 and 2.63 eV, x = 0.75. The red shift in optical absorption band edge of films shows formation of solid solution. Fig. 5.17 shows the band gap verses molar fraction of precursors in the delivery system. The variation in band gap is linear for precursor pair (**3**) and (**6**) which may indicate that these are the best matched of the three systems studied. The other pairs of precursors show positive or negative deviations from simple Vergard type behavior.

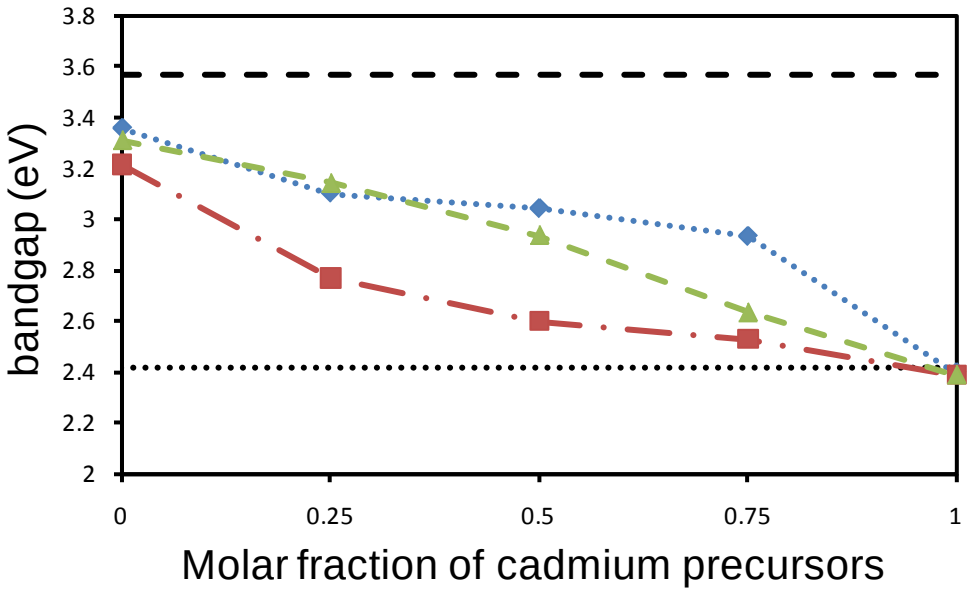

Fig. 5.17 Optical bandgap vs fraction of cadmium precursor a) $Zn_xCd_{1-x}S$ films prepared using (◆) complexes (**1**) and (**4**), (■) complexes (**2**) and (**5**), and (▲) complexes (**3**) and (**6**)

5.4.8.2 Structural Studies

The as-deposited $Zn_xCd_{1-x}S$ films were characterised by powder XRD. The X-ray diffractions confirm that all films are hexagonal. In assessing these results we need to remember that at 400°C all of the zinc precursors give predominantly hexagonal ZnS. Fig. 5.18 shows XRD patterns of $Zn_xCd_{1-x}S$ films grown on glass substrate varying the stoichiometries of precursors (**1**) and (**4**). The diffraction peak of hexagonal (002) plane shifts toward lower angle with increased concentration of

cadmium precursors. Hence the lattice expands on (002) as the bulkier cadmium substitutes for zinc.

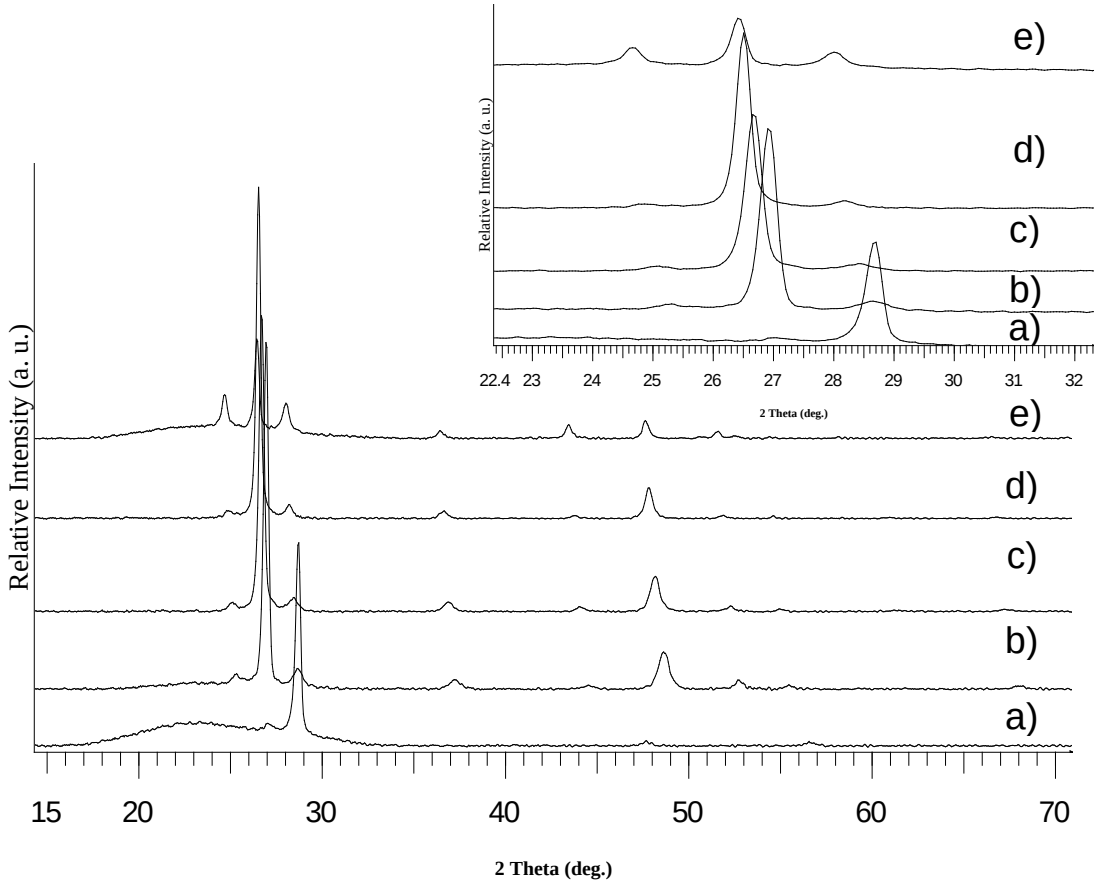

Fig. 5.18 PXRD pattern of $Zn_xCd_{1-x}S$ films deposited using complex (**2**) and (**5**). Inset shows variation of (002) plane. a) ZnS, b) ZnS at 25 %, c) ZnS at 50 %, d) ZnS at 75 % of cadmium precursor and e) CdS films

The (002) spacing plane calculated from the films deposited varying the ratio of precursors (**1**) and (**4**): 3.1882 Å, x = 0.50 and 3.3482 Å, x = 0.75. The lattice distances (*d*) for (**2**) and (**5**): 3.2507 Å, x = 0.25, 3.3406 Å, x = 0.50 and 3.3605 Å, x = 0.75. The calculated lattice distances (*d*) for precursors (**3**) and (**6**): 3.1349 Å, x = 0.25, 3.1565 Å, x = 0.50 and 3.2583 Å, x = 0.75. The shift in diffraction angle clearly indicates the formation of $Zn_xCd_{1-x}S$ solid state solution. Fig. 5.19 shows the increase in lattice distances almost consistent with increasing concentration of

cadmium precursors. The variation in lattice distances is almost linear for precursor pair (**1**) and (**4**) which confirms that these are the best matched of the three systems studied.

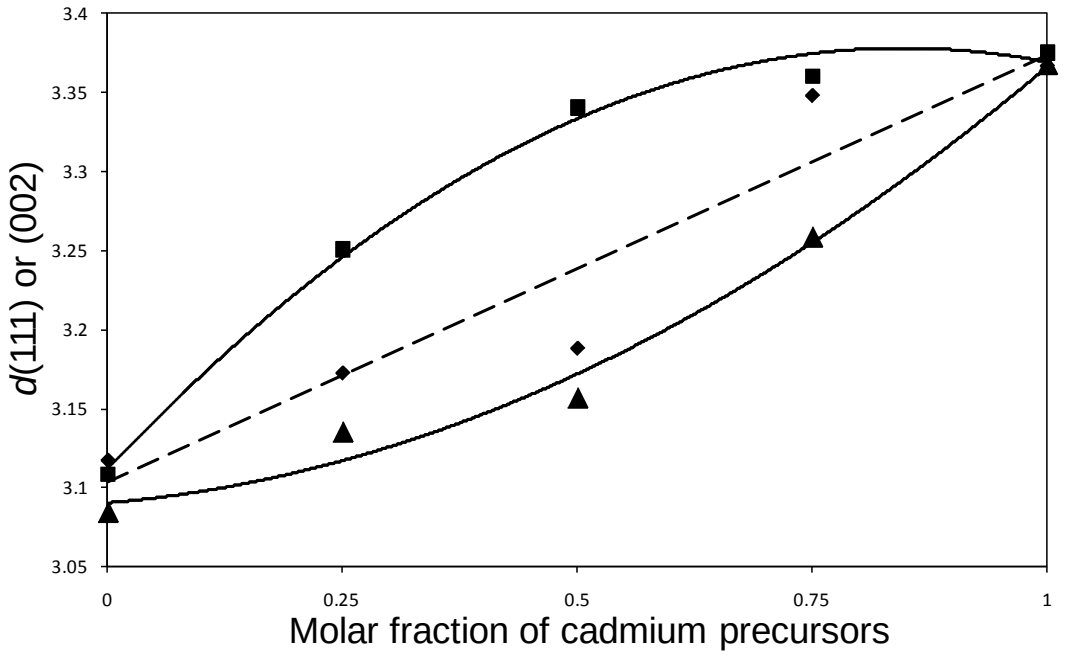

Fig 5. 19. *d*(111) or (002) vs molar fraction of cadmium precursor a) $Zn_xCd_{1-x}S$ films prepared using (♦) complexes (**1**) and (**4**), (■) $Zn_xCd_{1-x}S$ films prepared using complexes (**2**) and (**5**), and (▲) $Zn_xCd_{1-x}S$ films prepared using complexes (**3**) and (**6**)

5.4.8.3 Morphological studies

The films of $Zn_xCd_{1-x}S$ deposited by varying the ratio of the zinc to cadmium were imaged by SEM (Fig. 5.20). Granular spherical crystallites were deposited using precursors (**1**) and (**4**) with the diameter size of 235 ± 30 nm at 0.25, 255 ± 20 nm at 0.50 and 280 ± 25 nm at 0.75 molar fraction of (**4**) obtained. Granular cluster like morphology of films deposited using precursors (**2**) and (**5**) with diameter size of 550 ± 30 nm at 0.25, 570 ± 25 nm and 300 ± 25 nm at 0.5 and 0.75 molar fraction of (**5**). SEM image of films deposited using precursors (**3**) and (**6**) showed granular clusters of crystallites with diameter size of 700 ± 50 nm at 0.25, 575 ± 25 nm at 0.50 and 500 ± 30 nm at 0.75. EDX analysis of the films deposited at differing

ratios of precursor (x = mole fraction of Cd) enables an estimate of elemental composition. Precursors (**1**) and (**4**) gave Zn%, Cd%, S% are; 39.5, 13.0, 47.5 at x = 0.25; 22.0, 31.0, 47.0 %, x = 0.50 and 14.0, 38.0, 48.0 at x = 0.75.

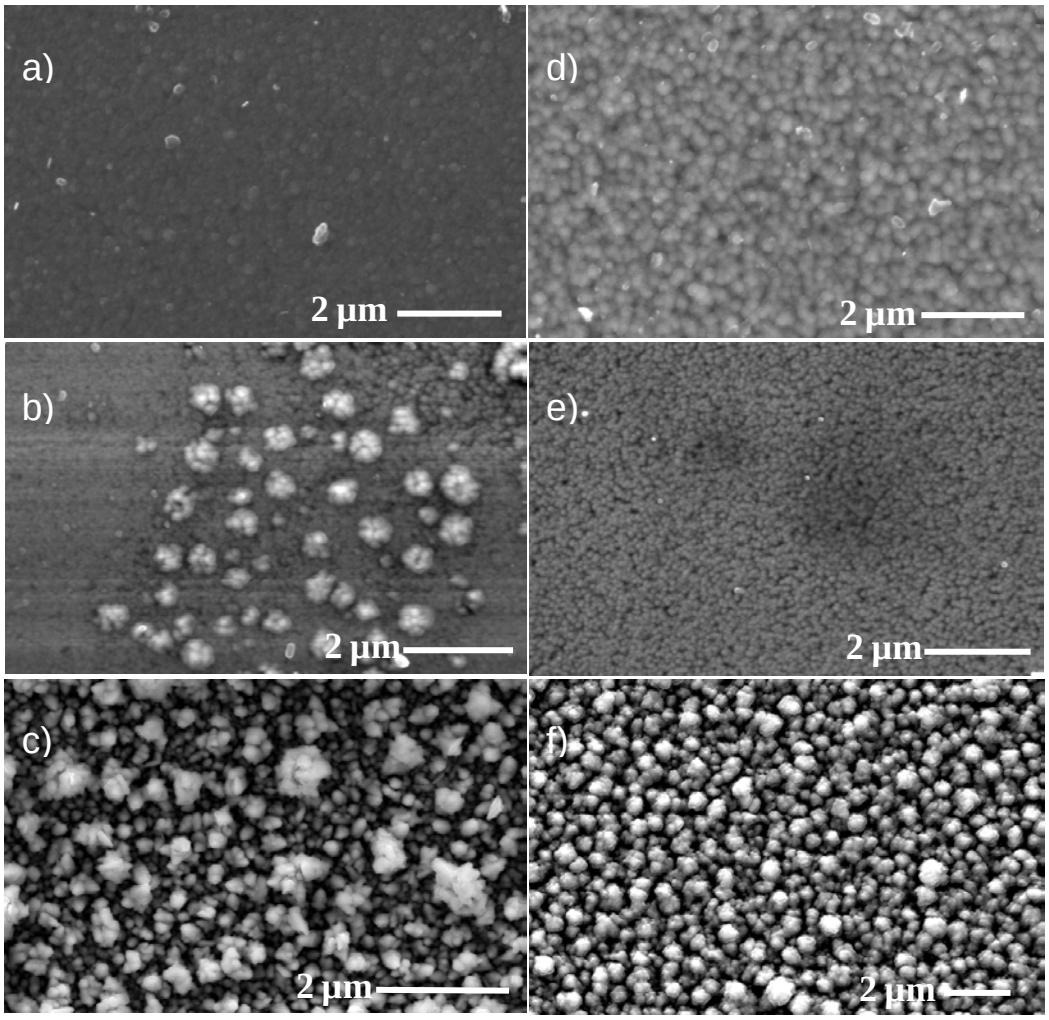

Fig. 5.20 SEM image of $Zn_xCd_{1-x}S$ films deposited at 400 °C, a, d) films prepared using complexes (**1**) and (**4**), b, e) using complexes (**2**) and (**5**) and c, f) using complexes (**3**) and (**6**)

The composition of films deposited using precursors (**2**) and (**5**) are Zn%, Cd%, S%: 24.7, 38.6, 36.5% at x = 0.25, 22.5, 36.6, 40.8 at x = 0.50 and 14.7, 42.6, 42.6 % at x = 0.75. Films deposited using precursors (**3**) and (**6**) gave Zn%, Cd%, S%: 20.4, 29.3, 50.2 at x= .25; 26.6, 26.1, 47.2 at x = 0.50 and 13.7, 34.6, 51.6 at x = 0.75. These results are illustrated in Fig. 5.21. The EDX results confirms the

variation in zinc and cadmium compositions almost linear for precursor pair (**1**) and (**4**) which is consistent with results with obtained from powder XRD results.

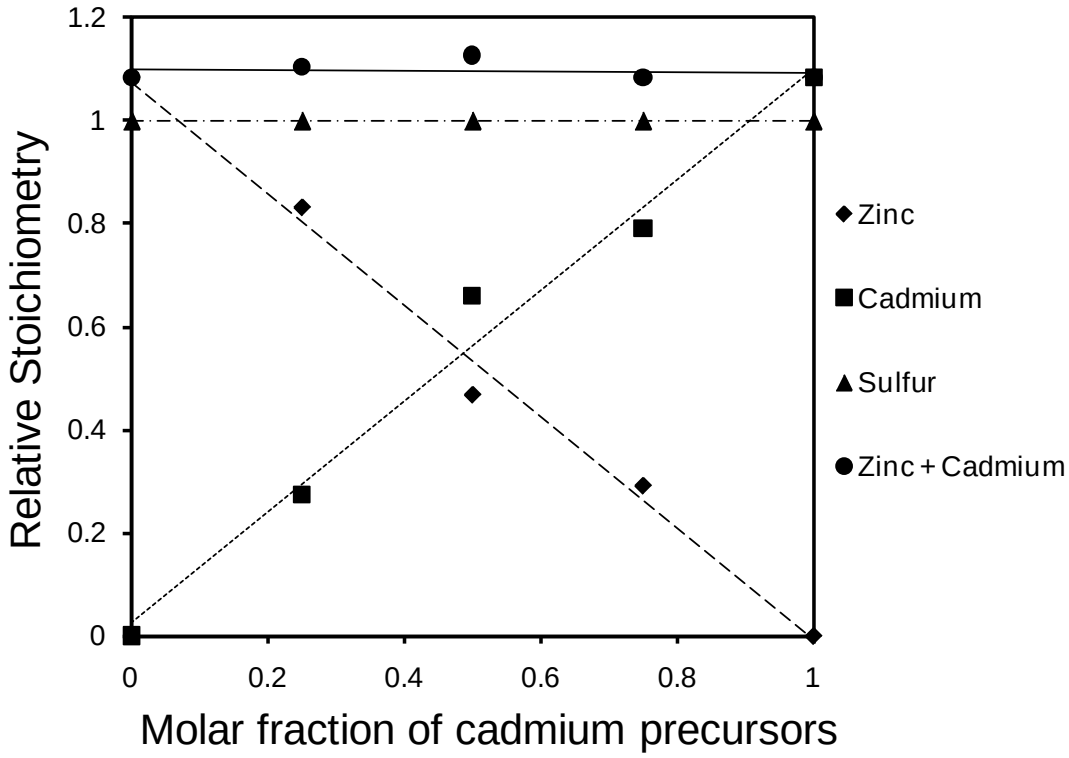

Fig. 5.21 Graph showing molar fraction cadmium precursors vs relative stoichiometry of zinc, cadmium and sulfur from films deposited using precursors (**1**) and (**4**) analysed by EDX.

AFM analysis shows presence of uniform and crack-free surfaces characterized by well interconnected globular crystallites as in Fig. 5.22. The average roughness was 35 to 45 nm appreciably higher than ZnS and CdS films deposited at 400 °C using precursors (**1**) and (**4**). AFM images show films deposited using precursors (**2**) and (**5**) consist of cluster like crystallites with an average roughness of 50 to 72 nm. Similarly the films deposited precursors (**3**) and (**6**) are composed of crack–free globular crystallites with an average roughness of 45 to 63 nm.

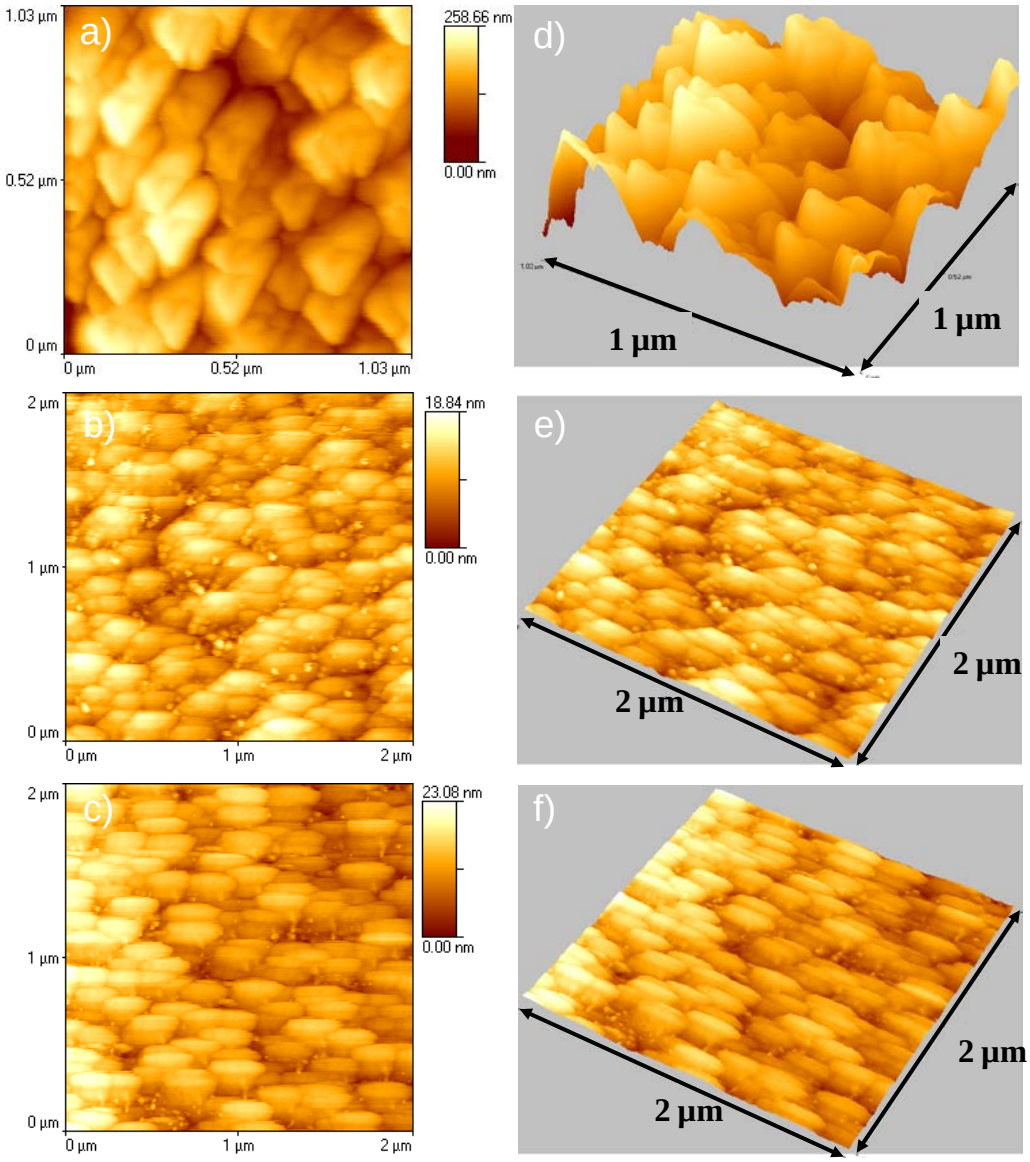

Fig. 5.22 AFM images of $Zn_xCd_{1-x}S$ films deposited at 400 °C a) and d) 2D, 3D images of films from complexes (**1**) and (**4**), b) and e) 2D, 3D images of films from complexes (**2**) and (**5**), and c) and f) 2D, 3D images of films from complexes (**3**) and (**6**)

5.5 Conclusion

The zinc or cadmium complexes of 1,1,5,5–tetraalkyl-2-4-dithiobiuret $[M(N(SCNR_2)_2)_2]$ (M = Zn, R = methyl (**1**), ethyl (**2**)) and (M = Cd, R = methyl (**4**), ethyl (**5**)) and 1,1,5,5–tetraalkyl-2-4-thiobiuret $[M(SON(CNR_2)_2)_2]$ (M = Zn, R = isopropyl (**3**) and M = Cd, R = isopropyl (**6**)) have been synthesised. The single

crystal X-ray structures of complexes (**2**), (**3**), (**4**) and (**5**) revealed Zn(II) and Cd(II) ions in tetrahedral geometries. AACVD from complexes (**1**) and (**3**) gave cubic ZnS films with small rods and granular crystallites at 300 and 350 °C, whereas at 400 and 450 °C hexagonal ZnS with granular crystallites were deposited. Complex (**2**) gave hexagonal ZnS films with granular crystallites at all deposition temperatures. Similarly the cadmium complexes (**4**), (**5**) and (**6**) gave hexagonal CdS granular films at all deposition temperatures. $Zn_xCd_{1-x}S$ films were deposited by varying molar ratio of precursors (**1**):(**4**), (**2**):(**5**) and (**3**):(**6**) at 400 °C. The optical bandgaps were measured by UV-Vis spectroscopy, powder X-ray diffraction (PXRD) and energy dispersive X-ray spectroscopy (EDX) confirmed the formation of $Zn_xCd_{1-x}S$ solid solution.

5.6 References:

1. O. Brafman, E. Alexander and I. T. Steinberger, *Acta Crystallogr.*, 1967, **22**, 347.
2. S. Mardix, O. Brafman and I. T. Steinberger, *Acta Crystallogr.*, 1967, **22**, 805.
3. L. S. Ramsdell, *Am. Miner.*, 1947, **32**, 64.
4. R. D. Pike, H. Cui, R. Kershaw, K. Dwight, A. Wold, T. N. Blanton, A. A. Wernberg and H. J. Gysling, *Thin Solid Films,* 1993, **224**, 221
5. J. L. Shay, W. E. Spicer and F. Herman, Phys. Rev. Lett., 1967, **18**, 649.
6. R. H. Bube, *Physics and Chemistry of II-VI Semiconductors*, 1967, North-Holland, Amsterdam.
7. B. Ray, *II-VI Compounds*, 1969, Pergamon Press, Oxford.
8. D. S. Boyle, P. O'Brien, D. J. Otway, O. Robbe, *J. Mater. Chem*, 1999, **9**, 725.
9. A. Bayer, D. S. Boyle, M. R. Heinrich, P. O'Brien, D. J. Otway, O. Robbe, *Green. Chem.*, 2000, 79.
10. A. N. Mariano and E. P. Warekois, *Science*, 1963, **142**, 672.
11. C. J. M. Rooymans, *Phys. Rev. Lett*., 1963, **4**, 186.
12. S. S. Kabalkina and Z. V. Troitskaya, *Dokl. Akad. Nauk SSSR.*, 1963, **151**,

1068.

13. G. Teodorescu, G. Jitanu and D. Ciomistan, *Rev. Romm. Phys.*, 1972, **17**, 71.
14. M. Fujite, *J. Phys. Soc. Jpn.*, 1965, **20**, 109.
15. A. B. Fowler, *J. Phys. Chem. Solids,* 1961, **22**, 181.
16. Y. F. Nicolau, M. Dupuy, and M. Brunel, *J. Electrochem. Soc.,* 1990, **137**, 2915.
17. M. Nyman, K. Jenkins, M. J. Hampden-smith, T. T. Kodas, and E. N. Duesler, *Chem, Mater.,* 1998, **10**, 914 and references therein.
18. M. Tsuji, T.Aramoto, H. Ohyama, T. Hibino, and K. Omura, *Jpn. J. Appl. Phys.,* part 1, 2002, **39**, 3902.
19. M. Wei and K. L. Choi, *Chem. Vap. Deposition.,* 2002, **8**, 15.
20. A. Ortiz, J. C. Alonso, and V. Pankov, *J. Mater. Sci. Mater. Electron.,* 1999, **10**, 503.
21. T. Kushida and A. Kurita, *J. Lumen.,* 2000, **87-89**, 466.
22. T. G. Kryshtab, V. S. Khomchenko, V. P. Papusha, M. O. Mazin, Y. A. Tzyrkunov, *Thin Solid Films*, 2002, **403-404**, 76.
23. A. M. Salem, *Appl. Phys. A.,* 2002, **74**, 205-211.
24. V. P. Singh, S. Singh, *Czech. J. Phys. B.,* 1976, **26**, 1161.
25. T. Yamaguchi, J. Matsufusa, A. Yoshida, *Jpn. J. Appl. Phys.,* 1992, **31**, L703.
26. T. Walter, M. Ruckh, K. O. Velthaus and H. W. Schock, Proc. 11th EC Photovoltaic Solar Energy Conf., Montrex, 1992,124.
27. R. S. Feigelson, A. N'Diage, S. Y. Yin and R. H. Bube, *J. Appl. Phys.,* 1977, **48**, 3162.
28. A. Banerjee, P. Nath, V. D. Vankar and K. L. Chopra, *Phys. Stat, Sol. (a),* 1978, **46**, 723.
29. D. S. Boyle, O. Robbe, D. P. Halliday, M. R. Heinrich, A. Bayer, P. O'Brien, D. J. Otway, M. D. G. Potter, *J. Mater, Chem*, 2000, **10**, 2439.
30. K. T. R. Reddy and P. J. Reddy, *J. Phys. D:* 1992, **25**, 1345.
31. B. M. Basol, *J. Appl. Phys.,* 1984, **55**, 601.

32. Y. K. Jun and H. B. Im, *J. Electrochem. Soc.: Electrochem, Sci. Technol.,* 1988, **135**, 1658.

33. H. S. Kim and H. B. Im *Thin Solid Films,* 1992, **214**, 207.

34. T. Yamaguchi, Y. Yamamoto, T. Taniska and H. Yoshida, *Thin Solid Films*, 1999, **516**, 343.

35. I. O. Oladeji, L. Chow, C. S. Ferikides, V. Viswanathan and Z. Zhao, *Solar Energy Mat. Solar Cells,* 2000, **61**, 203.

36. Z. Wang, P. B. Griffin, J. McVittie, S. Wong, P. C. McIntyre and Y. Nishi, *IEEE Electron Device lett.,* 2007, **28**, 14.

37. S. K. Mandal, S. Chaudhuri, and A. K. Pal, *Thin Solid Films,* 1999, **350**, 209.

38. C. T. Tsai, D. S. Chuu, G. L. Chen and S. L. Yang, *J. Appl. Phys.,* 1996, **79**, 9105.

39. M. Mclaughin, H. Sakeek and P. Maguire, *Appl. Phys. Lett.,* 1993, **63**, 1865.

40. B. Ullrich, H. Sakai and Y. Segawa, *Thin Solid Films,* 2001, **385**, 220.

41. H. H. Afifi, S. A. Mahmoud and A. Ashour, *Thin Solid Films,* 1995, **263**, 248.

42. M. C. Baykul and A. Balcioglu, *Microelectron. Eng.,* 2000, **51-52**, 703.

43. P. Nèmec, I. Nèmec, Y. Nahalkova, F. Trojaner, and P. Maly, *Thin Solid Films*, 2002, **403 – 404**, 9.

44. M. Wei and K. L. Choi, Chem. *Vap. Deposition*, 2002, **8**, 15.

45. B. Su, M. Wei and K. L. Choy. *Mater. Lett.*, 2001, **47**, 83.

46. W. Tang and D. C. Cameron, *Thin Solid Films,* 1996, **280**, 221.

47. S. Gorer, G. Hodes, Y. Sorek and R. Reisfeld, *Mater. Lett.*, 1997, **31**, 209.

48. A. Kuroyanagi, *Thin Solid Films,* 1994, **249**, 91-94.

49. D. Barreca, A. Gasparotto, C. Maragno, E. Tondello, and C. Sada, *Chemical Vapor Deposition,* 2004, **10**, 229.

50. K. Ramasamy, M. A. Malik, P. O'Brien and J. Raftery, *Dalton Trans.*, 2009, 2196.

51. O. B. Ajayi, O. K. Osuntola, I. A. Ojo, C. Jeynes, *Thin Solid Films,* 1994, **248**,

57.

52. M. B. Hursthouse, M. Azad Malik, M. Motevalli, P. O'Brien, *Organometallics*, 1991, **10**, 730.
53. D. M. Frigo, O. F. Z. Khan, P. O'Brien, *J. Cryst. Growth*, 1989, **96**, 989.
54. C. Byrom, M. A. Malik, P. O'Brien, A. J. P. White, *Polyhedron*, 2000, **19**, 211.
55. M. Nyman, M. J. Hampten-Smith, E. Duesler, *Chem. Vap. Deposition*, 1996, **2**, 171.
56. K. Ramasamy, M. A. Malik, P. O'Brien, J. Raftery, *Mater. Res. Soc. Symp. Proc,* 2009, **1145**, MM 04-40.
57. K. Ramasamy, M. A. Malik, P. O'Brien, J. Raftery, *Dalton Trans.*, 2010, **39**, 1460.
58. K. Ramasamy, M. A. Malik, M. Helliwell, F. Tuna, P. O'Brien, *Inorg. Chem*., 2010, **49**, 8495.
59. K. Ramasamy, M. A. Malik, J. Raftery, F. Tuna, P. O'Brien, *Chem. Mater*., 2010, **22**, 4919.
60. K. Ramasamy, M. A. Malik, M. Helliwell, P. O'Brien, *Chem. Mater*., In Press.
61. K. Ramasamy, M. Weerakanya, M. A. Malik, P. O'Brien, *Phil. Trans*. *R. Soc. A*, 2010, **368**, 4249.
62. K. E. Armstrong, J. D. Crane, M. Whittingham, *Inorg. Chem. Commun*, 2004, **7**, 784.
63. D. Fan, M. Afzaal, M. A. Mailk, C. Q. Nguyen, P. O'Brien, J. Thomas, *Coord. Chem. Rev.* 2007, **251**, 1878.
64. D. Barreca, A. Gasparotto, C. Maragno, E. Tondello, *J. Electrochem. Soc.,* 2004, **151**, G428.
65. M. Ichimura, F. Goto, E. Arai, *J. Appl. Phys*., 1999, **85**, 7411.
66. Y. G. Wang, S. P. Lau, H. W. Lee, S. F. Yu, B. K. Tay, H. X. Zhang, H. H. Hng, *J. Appl. Phys*., 2003, **94**, 354.
67. S. Fujihara, C. Sasaki, T. Kimura, *Appl. Surf. Sci*., 2001, **180**, 341.

68. D. N. Lee, *Thin Solid Films*, 2003, **434**, 183.

69. L. M. Nikolic, L. Radonjic, V. V. Srdic, *Ceram. Int.,* 2005, **31**, 261.

70. A. E. Hichou, M. Addou, J. L. Bubendorff, J. Ebothe, B. E. Idrissi, M. Troyon, *Semicond. Sci.Technol*,, 2004, **19**, 230.

71. S. D. Scott, H. L. Barnes, *Geochim. Cosmochim. Acta*, 1972, **86**, 1275.

72. D. A. Johnston, M. H. Carletto, K. T. R. Reddy, I. Forbes, R. W. Miles, *Thin Solid Films*, 2002, **403**, 102.

73. J. Cheng, D. B. Fan, H. Wang, B. W. Liu, Y. C. Zhang, H. Yan, *Semicond. Sci.Technol.,* 2003, **18**, 676.

74. S. D. Saratale, B. R. Sankapal, M. Lux-Steiner, A. Ennaoui, *Thin Solid Films,* 2005, **480**, 168.

75. J. Lee, S. Lee, S. Cho, S. Kim, I. Y. Park, Y. D. Choi, *Mater.Chem. Phys.*, 2002, **77**, 254.

76. B. Elidrissi, M. Addou, M. Regragui, A. Bougrine, A. Akchouane, J. C. Bernede, *Mater. Chem. Phys.*, 2001, **68**, 175.

77. K. L. Chopra, *Thin Solid Phenomena*, New York, McGraw-Hill, 1969.

78. Druz, B. L.; Dyadenko, A. I.; Evtukhov, Y. V.; Rakhlin, M. Y.; Rodionov, V. E.; *Inorg. Mater*., 1990, **26**, 24.

Chapter 6

General Experimental

6.1 Chemicals

Iron(III) nitrate, cobalt(II) chloride, cobalt(II) acetate, nickel(II) acetate, zinc(II) acetate, cadmium(II) acetate, dimethylthiocarbamoyl chloride, diethylthiocarbamoyl chloride, dimethylcarbamoyl chloride, diethylcarbamoyl chloride, di-iso-propylcarbamoyl chloride, dimethyl amine, diethyl amine, di-iso-propyl amine, sodium thiocyanate, and d-chloroform were used as purchased from Sigma Aldrich. Acetonitrile, chloroform, methanol, toluene and tetrahydrofuran were purchased from Fisher Chemicals.

6.2 Handling of air-sensitive compounds

The syntheses were carried out in an inert atmosphere using a double manifold Schlenk-line, attached to an Edwards E2M8 vacuum pump, and a dry nitrogen cylinder. All flasks were evacuated, and then purged with nitrogen at least three times prior to use, with external heat applied where deemed necessary. Solid air-sensitive compounds were handled inside a glove box under an atmosphere of dry nitrogen. Liquid air-sensitive chemicals were transferred to Schlenk type flask either by cannula or using syringes. Dry solvents, were either distilled over standard drying agents (Na/benzophenone, CaH_2 etc.) or purchased and stored in flasks over molecular sieves.

6.3 Deposition of films by AACVD

In a typical experiment 0.25 mmol of the complex was dissolved in 20 mL tetrahydrofuran in a two-necked 100 mL round-bottom flask with a gas inlet that allowed the carrier gas (argon) to pass into the solution to aid the transport of the aerosol. This flask was connected to the reactor tube by a piece of reinforced tubing. The argon flow rate was controlled by a Platon flow gauge. Seven glass substrates (approx. 1 x 3 cm) were placed inside the reactor tube, which is placed in

a CARBOLITE furnace. The precursor solution in a round-bottom flask was kept in a water bath above the piezoelectric modulator of a PIFCO ultrasonic humidifier (Model No. 1077). The aerosol droplets of the precursor thus generated were transferred into the hot wall zone of the reactor by carrier gas. Both the solvent and the precursor were evaporated and the precursor vapor reached the heated substrate surface where thermally induced reactions and film deposition took place.

6.4 Cleaning of glass substrates

The glass substrates used in this work were cleaned using the following procedure.

(a) Glass substrates were degreased in trichloroethylene and placed in acetone to remove organic residues.

(b) Then the substrates were rinsed in deionised water.

(c) The rinsed substrates were placed in 50 % nitric acid for overnight and then ultrasonicated for further 10 minutes in deionised water.

(d) Finally, they were rinsed again in deionised water and air-dried.

6.5 Characterization methods

NMR spectra were recorded using a Bruker AC300 FT-NMR spectrometer, using $CDCl_3$ as solvent. ^1H NMR spectra were referenced to the solvent signal and the chemical shifts are reported relative to Me_4Si.

Infrared spectra were recorded on a Perkin Elmer Spectrum BX FT-IR spectrometer. Mass spectra were recorded on a Micromass platform II instrument by atmospheric pressure chemical ionization (APCI) method.

6.6 Thermogravimetric analysis

Thermogravimetric analysis measurements were carried out by a Seiko SSC/S200 model under a heating rate of 10 ^{o}C min^{-1} under nitrogen. Indium metal is used as a reference to calibrate the instrument. TGA was performed by school of chemistry microanalysis team

6.7 Elemental analysis

CHNS analysis is carried out on a Carlo Erba EA 1108 elemental analyser which is calibrated with standard reference material (acetanilide). The sample is placed in a tin container which is dropped into a furnace at 1000 °C and then oxygen ejected from furnace. The sample burns and decomposes forming carbon dioxide (C), water vapour (H), nitrogen (N) and sulphur dioxide. These gases are analysed in a gas chromatography (GC) column to determine the amount of each element present in the sample. Metal (Fe, Co, Ni, Zn and Cd) analysis were carried out by adding acid to the weighed quantity of the sample placed in a tube. This is heated to the temperature at which the sample is digested and decomposed by the acid. The residue is transferred to volumetric flask conating water. This solution is analysed by Fisons Horizon ICP-OES which measures the concentration of each element in the solution. Elemental analysis were perfomed by school of chemistry microanalysis team.

6.8 Pyrolysis GC-MS

Pyrolysis GC-MS analysis was carried out using a Hewlett Packard 5890 gas chromatograph linked to a VG Trio-2000 mass spectrometer. The chromatography conditions were as follows: column BP5 (Supplied by SGE); bonded phase methyl siloxane, length 25 m, inner diameter 0.22 mm; phase thickness 0.25 µm. The temperature program employed for analysis was; initial

temperature 40 °C, initial time 2 min, 8 °C min^{-1} to 300 °C, final time 30 min. The pyrolysis injector temperature was 295 °C. The carrier gas (helium) pressure was kept at 12 psi with flow rate of 1 cm^3 min^{-1}. MS settings were 70 kV electron energy, source temperature 200 °C, 100 μA beam current and 7 kV detector voltages. Mass spectra were recorded between 40 and 800 atomic mass unit with a scan speed of 0.9 s. The complex (< 0.1 mg) was packed between the silica gel and sealed in a capillary tube.

6.9 UV/Vis spectroscopy

A Helios-Beta Thermospectronic spectrophotometer was used to carry out the optical measurements.

6.10 X-ray diffraction (XRD)

X-ray diffraction studies were performed on a Bruker AXS D8 diffractometer using Cu-Kα radiation. The samples were mounted flat and scanned between 20 to 80^o in a step size of 0.05 with a count rate of 9 sec. The diffraction patterns were then compared to the documented patterns in the ICDD index.

6.11 Scanning electron microscopy (SEM) and energy dispersive X-ray spectroscopy (EDX)

Films were carbon coated using Edward's E306A coating system before carrying out SEM and EDX analyses. SEM analysis was performed using a Philips XL 30FEG and EDX was carried out using a DX4 instrument.

6.12 Transmission electron microscopy (TEM)

TEM was performed using a Philips CM200 (200 kV) microscope. Samples were briefly ultrasonicated in toluene, which produces a suspension and then a drop of the suspension was placed on a carbon-coated copper grids.

6.13 Single crystal X-ray structure determination

Single-crystal X-ray diffraction data for the compounds were collected using graphite monochromated Mo-Kα radiation (λ = 0.71073 Å) on a Bruker APEX diffractometer. The structure was solved by direct methods and refined by full-matrix[1] least squares on F^2. All non-H atoms were refined anisotropically. H atoms were included in calculated positions, assigned isotropic thermal parameters and allowed to ride on their parent carbon atoms. All calculations were carried out using the SHELXTL package.[2] Single crystal X-ray diffraction data collection and structure determination were performed by Dr. James Raftery or Dr. Madeleine Helliwell.

6.14 Magnetic measurements

Magnetic measurements were performed in the temperature range 1.8-300 K, by using a Quantum Design MPMS-XL SQUID magnetometer equipped with a 7 T magnet. The diamagnetic corrections for the compounds were estimated using Pascal's constants, and magnetic data were corrected for diamagnetic contributions of the sample holder. Magnetic measurements were performed by Dr. Floriana Tuna.

6.15 XPS measurements

The XPS spectra were recorded using a Kratos Axis Ultra spectrometer employing a monochromated Al-Kα X-ray source and an analyzer pass energy of 80 eV for survey scans and 20 eV for elemental scans, resulting in a total energy

resolution of ca. 1.2 eV or 0.9 eV respectively. Uniform charge neutralization of the photoemitting surface was achieved by exposing the surface to low energy electrons in a magnetic immersion lens system (Kratos Ltd). The system base pressure was 1 x 10^{-9} mBar. Spectra were analysed by first subtracting a Shirley background and then obtaining accurate peak positions by fitting peaks using a mixed Gaussian/Lorenzian line shape. During fitting, spin orbit split components were constrained to have identical line width, elemental spin orbit energy separations and theoretical spin orbital area ratios. All photoelectron binding energies (BE) are referenced to C1s adventitious peak set at 285 eV BE. The analyser was calibrated using elemental references; Au 4f7/2 (83.98 eV BE), Ag 3d5/2 (368.26 eV BE) and Cu 2p3/2 (932.67 eV BE). XPS measurements were performed by Dr. Paul Wincott.

6.16 References

1. Sheldrick, G. M. SHELXS-97 and SHELXL-97, University of Göttingen, Germany, 1997.

2. Bruker, SHELXTL Version 6.12, Bruker AXS Inc., Madison, Wisconsin, USA, 2001.

Chapter 7

Conclusion and Future work

7.1 Conclusion

Metal sulfide thin films have potential applications in photovoltaics, solar cells, microelectronics, displays and opto-electronic devices. MOCVD method has been widely exploited to grow high quality thin films of metals sulfides. A variety of single source precursors have been developed for the deposition of metal sulfide thin films. Only selected single source precursors have deposited good quality thin films. Hence it is important to develop single source precursors with appropriate physico-chemical properties. In this study, a series of novel metal (Fe, Co, Ni, Zn, Cd) complexes of thio- and dithio-biurets were synthesised. The synthesised complexes were characterized by MS, IR, NMR, elemental analysis and single crystal X-ray structures. Thermal stability of the complexes were analysed by TGA. The complexes were employed as potential single source precursors for the deposition of metal sulfide thin films by aerosol assisted chemical vapour deposition. The synthetic processes of complexes are simple and use low cost chemicals. In addition, thio- and dithiobiuret complexes avoid the use of toxic and smelly CS_2 and phosphines.

The second chapter explains the synthesis, structures and magnetic properties of some new Fe(III) complexes of 1,1,5,5-tetraalkyl-2-thiobiurets. The synthesis is straight forward from the reaction of di-*iso*-propylcarbamoyl chloride, sodium thiocyanate and iron nitrate in the presence of dialkylamine produced new monomeric complexes, however in the case of diethylamine a methoxide bridged binuclear iron(III) complex was formed. Single crystal X-ray structure of complexes $[Fe(SON(CN^{i}Pr_2)_2)_3]$, $[Fe_2(\mu\text{-}OMe)_2(SON(CNEt_2)_2)_2]$ and $[Fe(SON(CNMe_2)_2)_3]$ showed a distorted octahedral geometry on iron(III) ion. Magnetic measurement for complex $[Fe_2(\mu\text{-}OMe)_2(SON(CNEt_2)_2)_2]$ confirmed its antiferromagnetic behavior.

Complex $[Fe(SON(CN^{i}Pr_2)_2)_3]$ deposited hexagonal troilite FeS films with small amount of tetragonal pyrrhotites $Fe_{1-x}S$ at 300 °C, whereas only troilite FeS was deposited at 350, 400 or 450 °C. Complexes $[Fe_2(\mu\text{-}OMe)_2(SON(CNEt_2)_2)_2]$ and $[Fe(SON(CNEt_2)_2)_3]$ deposited a mixture of hexagonal troilite FeS and cubic pyrite FeS_2 films at all temperatures. Complex (**4**) deposited very thin films of FeS at all temperatures as troilite. Scanning Electron Microscopy (SEM) images of the films deposited from all complexes showed that the morphology consisted of plates, granules, rods and sheets like crystallites.

The third chapter described the synthesis of cobalt(III) complexes of 1,1,5,5-tetramethyl- and 1,1,5,5-tetraethyl-2,4-dithiobiuret, and the cobalt (II) complex of 1,1,5,5-tetra-*iso*-propyl-2-thiobiuret. The determination of single crystal X-ray structure of the thiocyanate $[N(SCNMe_2)_2]SCN$ and tetrachlorocobaltate $[N(SCNMe_2)_2]_2[CoCl_4]$ of the parent cyclised ligand, together with complexes $[Co(N(SCNMe_2)_2)_3]$, $[Co(N(SCNEt_2)_2)_3]$ and $[Co(SON(CN^{i}Pr_2)_2)_2]$. Complexes $[Co(N(SCNMe_2)_2)_3]$ and $[Co(N(SCNEt_2)_2)_3]$ deposited NiAs type hexagonal $Co_{1-x}S$ films, whereas complex $[Co(SON(CN^{i}Pr_2)_2)_2]$ gave a mixture of cubic and hexagonal Co_4S_3. The morphology of films was characterized by scanning electron microscope (SEM) and showed rod like crystallites from $[Co(N(SCNMe_2)_2)_3]$, granular crystallites from $[Co(N(SCNEt_2)_2)_3]$ and stalagmitic structures from $[Co(SON(CN^{i}Pr_2)_2)_2]$. Transmission electron microscopy (TEM) of the samples obtained from thin films from $[Co(N(SCNMe_2)_2)_3]$ and $[Co(N(SCNEt_2)_2)_3]$ show that the films are composed of hexagonal nanoplates with nanocubes from $[Co(SON(CN^{i}Pr_2)_2)_2]$. Magnetic measurements showed the para or ferro-magnetic behavior from the crystallites. The mechanism for decomposition of precursors to the cobalt sulfide was studied by pyrolysis gas chromatography (Py-GC-MS) suggested complexes $[Co(N(SCNMe_2)_2)_3]$ and $[Co(N(SCNEt_2)_2)_3]$ followed same decomposition pathways, whereas $[Co(SON(CN^{i}Pr_2)_2)_2]$ followed slightly different decomposition pathway.

In the fourth chapter the synthesis of nickel(II) complexes of 1,1,5,5-tetraalkyl-2-thiobiurets (R = methyl; methyl, ethyl; ethyl; isopropyl) and 1,1,5,5-tetraalkyl-2,4-dithiobiurets (R = methyl; methyl, ethyl; ethyl) is reported. The single crystal structure of complexes $[Ni(SON(CNMe_2)_2)_2]$, $[Ni(SON(CNEt_2)_2)_2]$, $[Ni(SON(CN^iPr_2)_2)_2]$, $[Ni(N(SCNMe_2SCNEt_2))_2]$ and $[Ni(N(SCNEt_2)_2)_2]$ were showed nickel(II) ion in square planar coordination. In case of the thiobiuret complexes the ligands coordinated through S_2O_2 donor set with two sulfur and two oxygen atoms are each mutually *cis.* In dithiobiuret complexes the ligands coordinated to the nickel (II) ion through four sulfur atoms. AACVD from complex $[Ni(SON(CNMe_2)_2)_2]$ deposited orthorhombic Ni_7S_6 phase at all temperatures with spherical tipped wire like crystallites at 320 °C, plates and wires at other temperatures. Complex $[Ni(SON(CNMe_2CNEt_2))_2]$ deposited mixture of hexagonal $Ni_{17}S_{18}$ and orthorhombic Ni_7S_6 with wires and plates of crystallites. Similarly complex $[Ni(SON(CNEt_2)_2)_2]$ also deposited mixture of hexagonal $Ni_{17}S_{18}$ and orthorhombic Ni_7S_6 phases but with plates like crystallites. Whereas complex $[Ni(SON(CN^iPr_2)_2)_2]$ deposited orthorhombic Ni_9S_8 phase with flower like crystallites at 320 and 360 °C, branched structures at 400 °C. Complex $[Ni(N(SCNMe_2SCNEt_2))_2]$ gave NiAs – hexagonal $NiS_{1.03}$ at 360 and 400 °C, orthorhombic Ni_7S_6 phase at 440 and 480 °C with wires of spherical particles. Similarly complex $[Ni(N(SCNEt_2)_2)_2]$ also deposited hexagonal $NiS_{1.03}$ at 360 and 400 °C, orthorhombic Ni_7S_6 phase at 440 and 480 °C, but with rods of crystallites composed of hexagonal plates.

The fifth chapter described the synthesis of zinc and cadmium complexes of 1,1,5,5–tetraalkyl-2-4-dithiobiurets $[M(N(SCNR_2)_2)_2]$ (M = Zn, Cd; R = Methyl, Ethyl) and 1,1,5,5–tetraalkyl-2-thiobiurets $[M(SON(CNR_2)_2)_2]$ (M = Zn, Cd; R = isopropyl). Single crystal X-ray structures of complexes $[Zn(N(SCNEt_2)_2)_2]$, $[Zn(SON(CN^iPr_2)_2)_2]$, $[Cd(N(SCNMe_2)_2)_2]$ and $[Zn(SON(CN^iPr_2)_2)_2]$ revealed Zn(II) and Cd(II) ions in tetrahedral geometry. Thermogravimetric analysis confirms that all

six complexes decompose in a single step to their corresponding metal sulfides. AACVD from complexes $[Cd(N(SCNMe_2)_2)_2]$ and $[Zn(SON(CN^iPr_2)_2)_2]$ were deposited cubic ZnS films with smaller rods and granular crystallites at 300 and 350 °C, whereas at 400 and 450 °C hexagonal ZnS with granular crystallites were deposited. Complex $[Zn(N(SCNEt_2)_2)_2]$ gave hexagonal ZnS films with granular crystallites at all deposition temperatures. Similarly cadmium complexes $[Cd(N(SCNMe_2)_2)_2]$, $[Cd(N(SCNEt_2)_2)_2]$ and $[Cd(SON(CN^iPr_2)_2)_2]$ gave hexagonal CdS granular films at all deposition temperatures. $Zn_xCd_{1-x}S$ films were deposited by varying the concentration of zinc and cadmium precursors at 400 °C. The optical bandgap by UV-Vis spectroscopy, powder X-ray diffraction (PXRD) and energy dispersive X-ray spectroscopy (EDX) confirmed the formation of $Zn_xCd_{1-x}S$ solid solution.

Thus, a variety of new single source precursors have been synthesised and demonstrated the deposition good quality thin films of iron sulfide, cobalt sulfide, nickel sulfide, zinc sulfide, cadmium sulfide and zinc cadmium sulfide. Considerable efforts were experimented towards the synthesis of single source precursors to deposit phase selective metal sulfide thin films.

7.2 Future work

The future work will focus on synthesis of complexes of other metals including Pb, In, Ga, Cr, Mn, Sn, Ag, Au, Cu with thio- and dithiobiuret ligands. The selenium and tellurium analogous of biuret and their corresponding metal complexes will also be prepared.

The deposition of metal sulfide thin films using newly developed precursors by other chemical vapour deposition techniques such as LPCVD, APCVD etc will be investigated.

Preliminary experiments have given good quality nanoparticles of cobalt sulfide, nickel sulfide, iron sulfides by decomposing corresponding precursors in trioctylphosphine, hexadecylamine or oleylamine. More work will need to be focused on developing controllable synthesis of metal sulfide nanoparticles from newly developed precursors.

List of Publications

1. **Karthik Ramasamy**, Mohammad A. Malik, Madeline Helliwell, Floriona Tuna and Paul O'Brien, "Iron Thiobiurets: Single Source Precurosrs for Iron Sulfide Thin Films", *Inorg. Chem,* 2010**, 49,** 8495.

2. **Karthik Ramasamy,** Mohammad A. Malik, James Raftery, Floriona Tuna and Paul O'Brien, "Selective Deposition of Cobalt Sulfide Nanostructured Thin Films from Single Source Precursors", *Chem. Mater*, 2010, **22**, 4919.

3. **Karthik Ramasamy**, Weerakanya Maneerprakorn, Mohammad A. Malik and Paul O'Brien,"Single Molecular Precursor Based Approaches to Cobalt Sulfide Nanostructures", *Phil. Trans.R. Soc. A,* 2010, **368**, 4249

4. **Karthik Ramasamy**, Mohammad A.Malik, Paul O'Brien and James Raftery, "Metal Complexes of Thiobiurets and Dithiobiurets: Novel Single Source Precursors for Metal Sulfide Thin Film Nanostructures", *Dalton Trans,* 2010, **39**, 1460

5. **Karthik Ramasamy**, Mohammad A.Malik, Paul O'Brien and James Raftery, "The Synthesis and Structure of Cadmium Complex of Dimorpholino dithioacetylacetonate and their use as Single Source Precursor for CdS Thin films or Nanorods". *Dalton Trans,* 2009, 2196

6. **Karthik Ramasamy**, Weerakanya Maneerprakorn, Nasir Iqbal, Mohammad Azad Malik, Paul O'Brien, "Cobalt(II)/Nickel(II) complexes of dithioacetylacetone [$M(SacSac)_2$] (M = Co, Ni), as Single Source Precursors for cobalt/Nickel Sulfide Nanostructures", *International Journal of Nanoscience (accepted)*

7. **Karthik Ramasamy**, Mohammad Malik, Paul O'Brien, James Raftery, "ZnS, CdS and $Zn_xCd_{1-x}S$ Thin Films from Zn(II) and Cd(II) Complexes of 1, 1, 5, 5-Tetramethyl -2-4-dithiobiuret As Single Molecular Precursors", *Mater. Res. Soc Proc,* 2009, **1145**, MM, 4.40

8. **Karthik Ramasamy**, Mohammad A. Malik, Paul O'Brien and James Raftery, "Nickel Sulfide Thin Films from Thio and Dithio-biuret Precursors", *Chem.Mater.* DOI: 10.1021/cm102140t

9. **Karthik Ramasamy**, Mohammad A. Malik, Paul O'Brien and James Raftery, "Single Source Precursors for Zinc Sulfide, Cadmium Sulfide and Zinc Cadmium Sulfide". *Submitted to Chem.Mater*

10. **Karthik Ramasamy**, Mohammad. A. Malik, Paul O'Brien, "The Chemical Vapor Deposition of Cu_2ZnSnS_4 Thin Films", *Submitted to Chem.Sci*

11. Venugopal Rajendiran, **Ramasamy Karthik,** Mallayan Palaniandavar, Helen Stoeckli-Evans, Vaiyapuri Subbarayan Periasamy, Mohammad Abdulkader Akbarsha, Bangalore Suresh Srinag and Hanumanthappa Krishnamurthy, "Mixed-Ligand Copper(II)-phenolate Complexes: Effect of Co-ligand on Enhanced DNA and Protein Binding, DNA Cleavage, and Anticancer Activity", *Inorg. Chem,* 2007, **46**, 8208

12. Nanto Ziqubu, **Karthik Ramasamy**, Pullabhotla. V. S. R. Rajasekhar, Neerish Revaprasadu, Paul O'Brien, "Simple Route to Dots and Rods of PbTe Nanocrystals". *Chem. Mater,* 2010, **22**, 3817

13. Xiaoheng Liu, Mohammad Afzaal, **Karthik Ramasamy**, Paul O'Brien and Javeed Akhtar, "Synthesis of ZnO Hexagonal Single – Crystal Slices with Predominant (0001) and (000$\bar{1}$) Facets by Poly(ethyleneglycol)-Assisted Chemical Bath Deposition", *J. Am. Chem. Soc,* 2009, **131**(42), 15106

14. Arunkumar Panneerselvam, Ganga Periyasamy, **Karthik Ramasamy**, Mohammad Afzaal, Mohammad. A. Malik, John Waters, Van Dongven Bart, Paul O'Brien, Neil Burton, "Factors Controlling Material Deposition in the CVD of Nickel Sulfide, Selenides or Phosphides from Dichalcogenoimidodiphosphinato complexes: deposition, spectroscopic and computational studies". *Dalton Trans,* 2010, **39**, 6080.

15. Ncami Maseko, Neerish Revaprasadu, Rajasekhar V. Pullabhotla, **Karthik Ramasamy**, Paul O'Brien, "The Influence of the Cadmium Source on the Shape of CdSe Nanoparticles", *Mater. Lett., 2010, **64**(9), 1037*

16. P. L. Musetha, N. Revaprasadu, G. A. Kolawole, P. V. S. R. Pullabhotla, **K. Ramasamy** and P. O'Brien "Homoleptic Single Source Precursors for the Deposition of Platinum and Palladium Chalcogenide Thin Films", *Thin Solid Films,* 2010, **519**, 197.

17. **Karthik Ramasamy**, Mohammad A. Malik, Paul O'Brien and James Raftery, "The deposition of Copper Sulfide Thin Films and Nanostructures from Copper complex of 1,1,5,5-tetra-*iso*-propyl-2-thiobiuret" *Manuscript In Preparation*

18. **Karthik Ramasamy**, Nonto Ziqubu, Pullabhotla. V. S. R. Rajasekhar, Neerish Revaprasadu, Paul O'Brien, "New Route to Lead Chalcogenide Nanocrystals", *Manuscript In Preparation*

19. **Karthik Ramasamy**, Pullabhotla. V. S. R. Rajasekhar, Neerish Revaprasadu, Paul O'Brien, "New Route to Bismuth Selenide and Telluride Nanostructures", *Manuscript In Preparation*

20. **Karthik Ramasamy**, Mohammad. A. Malik, Paul O'Brien, James Raftery, "Organotin Dithiocarbamates: The Potential Single Source Precursors for Tin Sulfide Thin Films by AACVD", *Manuscript In Preparation.*

List of Presentations

1. ZnS, CdS and $Zn_xCd_{1-x}S$ Thin Films from Zn(II) and Cd(II) Complexes of 1, 1, 5, 5-Tetramethyl-2-4-dithiobiuret as Single Molecular Precursors. **Karthik Ramasamy**, Mohammad Malik, Paul O'Brien, James Raftery, Graduate Research Conference, the University of Manchester, 17th Sept, 2008.

2. ZnS, CdS and $Zn_xCd_{1-x}S$ Thin Films from Zn(II) and Cd(II) Complexes of 1, 1, 5, 5-Tetramethyl-2-4-dithiobiuret As Single Molecular Precursors. **Karthik Ramasamy**, Mohammad Malik, Paul O'Brien, James Raftery,MM.4.40, Materials Research Society Fall Meeting, Boston, MA, USA. 2-6, Dec- 2008.

3. Cobalt Sulfide Nanostructures from Single Molecular Precursors. **Karthik Ramasamy**, Mohammad Malik,Paul O'Brien, P609_004, 42nd IUPAC international congress, Glasgow, 2-7, Aug-2009.

4. A Greener Route to Metal Selenide and Telluride Nanoparticles. Neerish Revaprasadu, Olawatobi S. Oluwafemi, Nhlankipho Mntungwa and **Karthik Ramasamy**, P608_12, 42nd IUPAC international congress, Glasgow, 2-7, Aug-2009

5. The Deposition of Nickel Sulfide or Copper Sulfide Thin Film Nanostructures by AACVD. **Karthik Ramasamy**, Mohammad Malik, Paul O'Brien, P33, Nanoparticles-2009, Liverpool, 2-4, Sept-2009.

6. Novel Methods for Metal Chalcogenide Thin Films or Nanostructures, **Karthik Ramasamy**, Mohammad Malik, Neerish Revaprasadu, Paul O'Brien, NS 13, ICONSAT-2010, Mumbai, India, 17-20 Feb-2010.

Appendix

Table. A1 Structural refinement data for complexes $[Fe(SON(CN^{i}Pr_2)_2)_3]$ and $[Fe_2(\mu\text{-}OMe)_2(SON(CNEt_2)_2)_2]$

Refinement parameters	$Fe(SON(CN^{i}Pr_2)_2)_3$	$Fe_2(\mu\text{-}OMe)_2(SON(CNEt_2)_2)_2$
Empirical Formula	$C_{44}H_{87}N_{10}O_3S_3Fe$	$C_{42}H_{86}N_{12}O_6S_4Fe_2$
Formula weight	956.27	1095.17
Temperature	100(2) K	100(2) K
Wavelength	0.71073 Å	0.71073 Å
Crystal system	Monoclinic	Monoclinic
Space group	P2(1)/n	P2(1)/c
Unit cell dimensions	a = 14.341(3) Å, α = 90°	a = 10.466(2) Å, α = 90°
	b = 15.224(3) Å, β = 97.14(4)°	b = 25.355(4) Å, β = 95.44(3)°
	c = 25.725(4) Å, γ = 90°	c = 10.328(4) Å, γ = 90°
Volume	5572.9(2) A^3	2728.5(8) A^3
Z	4	2
Calculated density	1.140 Mg/m^3	1.333 Mg/m^3
Absorption coefficient	0.426 mm^{-1}	0.738 mm^{-1}
F(000)	2076	1172
Crystal size	0.35 X 0.30 X 0.20 mm	0.35 X 0.30 X 0.20 mm
Theta range for data collection	2.94 to 20.68	1.95 to 26.40°
Limiting indices	-17<=h<=17, -10<=k<=19, -32<=l<=32	-7<=h<=13, -13<=k<=31, -12<=l<=12
Reflection collected / unique	31561 / 11281 [R(int) = 0.0696]	15681 / 5558 [R(int) = 0.0313]
Data / restraints / parameters	11281/0/575	5558 / 0 /309
Goodness of fit on F^2	0.709	1.144
Final R indices [I>2σ(I)]	R1 = 0.0414, wR2 = 0.0622	R1 = 0.0510, wR2 = 0.1160
R indices (all data)	R1 = 0.0923, wR2 = 0.0674	R1 = 0.0598, wR2 = 0.1197
Largest diff. Peak and hole	0.661 and -0.409 eA^{-3}	1.677 and -0.370 eA^{-3}

Table. A2 Structural refinement data for complex $Fe(SON(CNMe_2)_2)_3$ of orthorhombic and tetragonal crystal system

Refinement parameters	$Fe(SON(CNMe_2)_2)_3$	$Fe(SON(CNMe_2)_2)_3$
Empirical Formula	$C_{23.33}H_{46.67}N_9O_{4.33}S_3Fe$	$C_{18}H_{36}N_9O_3S_3Fe$
Formula weight	674.73	578.59
Temperature	100(2) K	100(2) K
Wavelength	0.71073 Å	0.71073 Å
Crystal system	Orthorhombic	Tetragonal
Space group	Pna2(1)	P4/n
Unit cell dimensions	a = 16.978(5) Å, α = 90°	a = 25.519(1) Å, α = 90°
	b = 31.180(1) Å, β = 90°	b = 25.510(1) Å, β = 90°
	c = 18.160(5) Å, γ = 90°	c = 10.953(3) Å, γ = 90°
Volume	9613(5) A^3	11041.3(1) A^3
Z	12	16
Calculated density	1.399 Mg/m^3	1.392 Mg/m^3
Absorption coefficient	0.712 mm^{-1}	0.810 mm^{-1}
F(000)	4300	4880
Crystal size	0.45 X 0.20 X 0.15	0.30 X 0.20 X 0.06 mm
Theta range for data collection	1.37 to 23.36°	1.20 to 25.02°
Limiting indices	-17<=h<=18, -34<=k<=23, -19<=l<=12	-30<=h<=30, -30<=k<=30, -20<=l<=20
Reflection collected / unique	23094 / 11030 [R(int) = 0.1081]	78789 / 9765 [R(int) = 0.1600]
Data / restraints / parameters	11030 / 1095 / 1146	9765 / 4 / 644
Goodness of fit on F^2	1.010	0.961
Final R indices [I>2σ(I)]	R1 = 0.1006, wR2 = 0.2098	R1 = 0.0770, wR2 = 0.2120
R indices (all data)	R1 = 0.1535, wR2 = 0.2358	R1 = 0.1638, wR2 = 0.2568
Largest diff. Peak and hole	1.196 and -0.546 eA^{-3}	5.508 and -0.563 eA^{-3}

Table. A3 Structural refinement data for compounds $[N(SCNMe_2)_2]SCN$ and $[N(SCNMe_2)_2]_2[CoCl_4]$

Refinement parameters	$[N(SCNMe_2)_2]SCN$	$[N(SCNMe_2)_2]_2[CoCl_4]$
Empirical Formula	$C_7H_{12}N_4S_3$	$C_{12}H_{24}N_6S_4CoCl_4$
Formula weight	248.39	581.34
Temperature	100(2) K	100(2) K
Wavelength	0.71073 Å	0.71073 Å
Crystal system	Monoclinic	Orthorhombic
Space group	P2(1)/n	Pca2(1)
Unit cell dimensions	a = 10.409(2) Å, α = 90°	a = 13.978(2) Å, α = 90°
	b = 5.863(9) Å, β = 99.96(4)°	b = 9.226(2) Å, β = 90°
	c = 18.465(4) Å, γ = 90°	c = 18.155(3) Å, γ = 90°
Volume	1110.1(3) A^3	2341.3(6) A^3
Z	4	4
Calculated density	1.486 Mg/m^3	1.649 Mg/m^3
Absorption coefficient	0.635 mm^{-1}	1.558 mm^{-1}
F(000)	520	1188
Crystal size	0.25 X 0.18 X 0.08 mm	0.30 X 0.20 X 0.04 mm
Theta range for data collection	2.10 to 28.25°	2.21 to 28.30°
Limiting indices	13<=h<=13, -0<=k<=7, -0<=l<=24	-18<=h<=15, -10<=k<=12, -19<=l<=24
Reflection collected / unique	3193 / 3269 [R(int) = 0.0751]	13972 / 4740 [R(int) = 0.0421]
Data / restraints / parameters	3269 / 0 / 131	4740 / 1 / 252
Goodness of fit on F^2	1.101	1.022
Final R indices [I>2σ(I)]	R1 = 0.0751, wR2 = 0.1779	R1 = 0.0354, wR2 = 0.0635
R indices (all data)	R1 = 0.0835, wR2 = 0.1826	R1 = 0.0421, wR2 = 0.0655
Largest diff. Peak and hole	1.674 and -0.994 eA^{-3}	0.412 and -0.284 eA^{-3}

Table. A4 Structural refinement data for compounds $[Co(N(SCNMe_2)_2)_3]$ and $[Co(N(SCNEt_2)_2)_3]$

Refinement parameters	$[Co(N(SCNMe_2)_2)_3]$	$[Co(N(SCNEt_2)_2)_3]$
Empirical Formula	$C_{18}H_{36}N_9S_6Co$	$C_{30}H_{60}N_9S_6Co$
Formula weight	629.85	798.16
Temperature	100(2) K	100(2) K
Wavelength	0.71073 Å	0.71073 Å
Crystal system	Orthorhombic	Monoclinic
Space group	Pca2(1)	P2(1)/c
Unit cell dimensions	a = 14.872(2) Å, α = 90°	a = 9.580(8) Å, α = 90°
	b = 13.832(2) Å, β = 90°	b = 42.691(4) Å, β = 90°
	c = 13.450(2) Å, γ = 90°	c = 9.637(8) Å, γ = 90°
Volume	2767.1(7) A^3	3908.7(6) A^3
Z	4	4
Calculated density	1.512 Mg/m^3	1.356 Mg/m^3
Absorption coefficient	1.100 mm^{-1}	0.939 mm^{-1}
F(000)	1320	1704
Crystal size	0.22 X 0.18 X 0.10 mm	0.30 X 0.20 X 0.15 mm
Theta range for data collection	1.47 to 28.30°	1.91 to 28.27°
Limiting indices	19<=h<=13, -18<=k<=17, -17<=l<=17	-6<=h<=12, -53<=k<=56, -12<=l<=12
Reflection collected / unique	16614 / 6283 [R(int) = 0.0842]	24649 / 9126 [R(int) = 0.0779]
Data / restraints / parameters	6283 / 1 / 319	9126 / 0 / 427
Goodness of fit on F^2	0.676	0.891
Final R indices [I>2σ(I)]	R1 = 0.0432, wR2 = 0.0680	R1 = 0.0599, wR2 = 0.0789
R indices (all data)	R1 = 0.0890, wR2 = 0.0754	R1 = 0.1117, wR2 = 0.0918
Largest diff. Peak and hole	0.674 and -0.343 eA^{-3}	0.632 and -0.623 eA^{-3}

Table. A5 Structural refinement data for compounds $[Co(N(SOCN^{i}Pr_2)_2)_2]$ and $[Ni(SON(CNMe_2)_2)_2]$

Refinement parameters	$[Co(SON(CN^{i}Pr_2)_2)_2]$	$[Ni(SON(CNMe_2)_2)_2]$
Empirical Formula	$C_{28}H_{56}N_6O_2S_2Co$	$C_{12}H_{24}N_6NiO_2S_2$
Formula weight	631.84	407.20
Temperature	100(2) K	100(2) K
Wavelength	0.71073 Å	0.71073 Å
Crystal system	Monoclinic	Orthorhombic
Space group	C2/c	Pnma
Unit cell dimensions	a = 14.435(5) Å, α = 90°	a = 13.888(3) Å, α = 90°
	b = 18.350(6) Å, β = 91.43°	b = 6.962(1) Å, β = 90°
	c = 25.972(8) Å, γ = 90°	c = 18.451(3) Å, γ = 90°
Volume	6877(4) A^3	1784.3(6) A^3
Z	8	4
Calculated density	1.220 Mg/m^3	1.516 Mg/m^3
Absorption coefficient	0.653 mm^{-1}	1.338 mm^{-1}
F(000)	2728	856
Crystal size	0.60 X 0.15 X 0.15 mm	0.40 X 0.30 X 0.03 mm
Theta range for data collection	1.80 to 21.97°	1.84 to 26.36°
Limiting indices	-15<=h<=15, -19<=k<=19, -27<=l<=26	-16<=h<=17, -8<=k<=6, -17<=l<=23
Reflection collected / unique	18076 / 4202 [R(int) = 0.1603]	9783 / 1984 [R(int) = 0.1005]
Data / restraints / parameters		1984 / 0 /144
Goodness of fit on F^2	1.206	1.160
Final R indices [I>2σ(I)]	R1 = 0.1052, wR2 = 0.2104	R1 = 0.0643,wR2 = 0.1193
R indices (all data)	R1 = 0.1424, wR2 = 0.2261	R1 = 0.0904, wR2 = 0.1288
Largest diff. Peak and hole	0.768 and -0.551 eA^{-3}	0.745 and -0.659 eA^{-3}

Table. A6 Structural refinement data for compounds $[Ni(SON(CNEt_2)_2)_2]$ and $[Ni(SON(CN^iPr_2)_2)_2]$

Refinement parameters	$[Ni(SON(CNEt_2)_2)_2]$	$[Ni(SON(CN^iPr_2)_2)_2]$
Empirical Formula	$C_{20}H_{40}N_6NiO_2S_2$	$C_{28}H_{56}N_6NiO_2S_2$
Formula weight	519.41	631.62
Temperature	100(2) K	100(2) K
Wavelength	0.71073 Å	0.71073 Å
Crystal system	Orthorhombic	Monoclinic
Space group	Pbca	P 2_1/c1
Unit cell dimensions	a = 10.689(2) Å, α = 90°	a = 21.787 Å, α = 90°
	b = 18.763(3) Å, β = 90°	b = 13.777 Å, β = 90.99°
	c = 25.788(4) Å, γ = 90°	c = 11.925 Å, γ = 90°
Volume	5172.2(2) A^3	3578.9 A^3
Z	8	4
Calculated density	1.334 Mg/m^3	1.172 Mg/m^3
Absorption coefficient	0.939 mm^{-1}	0.690 mm^{-1}
F(000)	2224	1368
Crystal size	0.40 X 0.30 X 0.03 mm	0.30 X 0.20 X 0.04 mm
Theta range for data collection	2.17 to 26.43°	2.81 to 26.37°
Limiting indices	-13<=h<=13, -23<=k<=23, -32<=l<=31	-24<=h<=27, -16<=k<=16, -14<=l<=9
Reflection collected / unique	38878 / 5311 [R(int) = 0.0725]	16324 / 6984 [R(int) = 0.1107]
Data / restraints / parameters	5311 / 0 /288	6984 / 7 /345
Goodness of fit on F^2	0.966	0.939
Final R indices [I>2σ(I)]	R1 = 0.0295, wR2 = 0.0646	R1 = 0.0781, wR2 = 0.1718
R indices (all data)	R1 = 0.0420, wR2 = 0.0679	R1 = 0.1877, wR2 = 0.2183
Largest diff. Peak and hole	0.461 and -0.242 eA^{-3}	1.379 and -0.994 eA^{-3}

Table. A7 Structural refinement data for compounds $[Ni(NS(CNMe_2CNEt_2))_2]$ and $[Ni(N(SCNEt_2)_2)_2]$

Refinement parameters	$[Ni(N(SCNMe_2SCNEt_2))_2]$	$[Ni(N(SCNEt_2)_2)_2]$
Empirical Formula	$C_{16}H_{32}N_6NiS_4$	$C_{20}H_{40}N_6NiS_4$
Formula weight	495.43	551.53
Temperature	100(2) K	100(2) K
Wavelength	0.71073 Å	0.71073 Å
Crystal system	Monoclinic	Triclinic
Space group	P2 (1) /c	P-1
Unit cell dimensions	a = 8.143(2) Å, α = 90°	a = 9.494(2) Å, α = 89.62(3)°
	b = 17.389(4) Å, β = 110°	b = 11.455(2) Å, β = 89.72(3)°
	c = 8.304(2) Å, γ = 90°	c = 13.758(2) Å, γ = 67.54(3)°
Volume	1104.9(4) A^3	1382.9(4) A^3
Z	2	2
Calculated density	1.489 Mg/m^3	1.325 Mg/m^3
Absorption coefficient	1.271 mm^{-1}	1.023 mm^{-1}
F(000)	524	588
Crystal size	0.20 X 0.08 X 0.02 mm	0.40 X 0.40 X 0.10 mm
Theta range for data collection	2.34 to 27.10°	1.92 to 26.43°
Limiting indices	-10<=h<=10, -22<=k<=22, -10<=l<=10	-9<=h<=11, -8<=k<=14, -16<=l<=17
Reflection collected / unique	9159 / 2436 [R(int) = 0.1024]	8092 / 5529 [R(int) = 0.0221]
Data / restraints / parameters	2436 / 0 /128	5529 / 0 /291
Goodness of fit on F^2	0.915	1.112
Final R indices [I>2σ(I)]	R1 = 0.0586, wR2 = 0.0755	R1 = 0.0477, wR2 = 0.0991
R indices (all data)	R1 = 0.1060, wR2 = 0.0853	R1 = 0.0651, wR2 = 0.1037
Largest diff. Peak and hole	0.718 and -0.480 eA^{-3}	0.553 and -0.326 eA^{-3}

Table. A8 Structural refinement data for compounds $[Zn(N(SCNEt_2)_2)_2]$ and $[Zn(N(SOCN^iPr_2)_2)_2]$

Refinement parameters	$[Zn(N(SCNEt_2)_2)_2]$	$[Zn(SON(CN^iPr_2)_2)_2]$
Empirical Formula	$C_{20}H_{40}N_6ZnS_4$	$C_{28}H_{56}N_6ZnO_2S_2$
Formula weight	558.19	638.28
Temperature	100(2) K	100(2) K
Wavelength	0.71073 Å	0.71073 Å
Crystal system	Monoclinic	Monoclinic
Space group	P2 (1) /c	P2(1)
Unit cell dimensions	a = 9.092(8) Å, α = 90°	a = 11.619(1) Å, α = 90°
	b = 11.505(1) Å, β = 98.79(2)°	b = 13.397(2) Å, β = 104.16(2)°
	c = 26.955(2) Å, γ = 90°	c = 11.655(1) Å, γ = 90°
Volume	2786.4(4) A^3	1759.3(3) A^3
Z	4	2
Calculated density	1.331 Mg/m^3	1.205 Mg/m^3
Absorption coefficient	1.200 mm^{-1}	0.848 mm^{-1}
F(000)	1184	688
Crystal size	0.20 X 0.15 X 0.10 mm	0.32 X 0.30 X 0.03 mm
Theta range for data collection	1.53 to 28.29°	1.80 to 28.30°
Limiting indices	-11<=h<=11, -14<=k<=15, -35<=l<=35	-15<=h<=15, -17<=k<=17, -15<=l<=15
Reflection collected / unique	23865 / 6650 [R(int) = 0.0642]	15277 / 7922 [R(int) = 0.0588]
Data / restraints / parameters	6650 / 0 / 288	7922 / 1 / 368
Goodness of fit on F^2	0.743	0.801
Final R indices [I>2σ(I)]	R1 = 0.0360, wR2 = 0.0492	R1 = 0.0495, wR2 = 0.0646
R indices (all data)	R1 = 0.0686, wR2 = 0.0541	R1 = 0.0731, wR2 = 0.0695
Largest diff. Peak and hole	0.860 and -0.443 eA^{-3}	1.045 and -0.583 eA^{-3}

Table. A9 Structural refinement data for compounds $[Cd(N(SCNMe_2)_2)_2]$ and $[Cd(N(SCNEt_2)_2)_2]$

Refinement parameters	$[Cd(N(SCNMe_2)_2)_2]$	$[Cd(N(SCNEt_2)_2)_2]$
Empirical Formula	$C_{12}H_{24}N_6CdS_4$	$C_{20}H_{40}N_6CdS_4$
Formula weight	493.01	605.22
Temperature	100(2) K	100(2) K
Wavelength	0.71073 Å	0.71073 Å
Crystal system	Monoclinic	Triclinic
Space group	P2 (1) /n	P2-1
Unit cell dimensions	a = 12.327(1) Å, α = 90°	a = 9.183(1) Å, α = 98.79(2)°
	b = 12.021(1) Å, β = 105.49(2)°	b = 16.135(2) Å, β = 92.69(2)°
	c = 13.537(1) Å, γ = 90°	c = 19.005(2) Å, γ = 90.95(2)°
Volume	1933.2(3) A^3	2779.1(6) A^3
Z	4	4
Calculated density	1.694 Mg/m^3	1.447 Mg/m^3
Absorption coefficient	1.568 mm^{-1}	1.105 mm^{-1}
F(000)	1000	1256
Crystal size	0.25 X 0.25 X 0.06 mm	0.20 X 0.16 X 0.05 mm
Theta range for data collection	1.99 to 26.35°	1.28 to 28.33°
Limiting indices	-11<=h<=15, -13<=k<=15, -16<=l<=15	-12<=h<=10, -21<=k<=21, -25<=l<=19
Reflection collected / unique	11005 / 3943 [R(int) = 0.0338]	17772 / 12399 [R(int) = 0.0515]
Data / restraints / parameters	3943 / 0 / 216	12399 / 0 / 575
Goodness of fit on F^2	1.010	0.684
Final R indices [I>2σ(I)]	R1 = 0.0291, wR2 = 0.0633	R1 = 0.0453, wR2 = 0.0680
R indices (all data)	R1 = 0.0375, wR2 = 0.0659	R1 = 0.0902, wR2 = 0.0777
Largest diff. Peak and hole	0.466 and -0.409 eA^{-3}	1.052 and -0.983 eA^{-3}

Table. A10 PXRD data of ZnS films deposited from $[Zn(N(SCNMe_2)_2)_2]$, $[Zn(N(SCNEt_2)_2)_2]$ and $[Zn((SON(CN^iPr_2)_2)_2]$

ICDD-003-0570 cubic					$[Zn(N(SCNMe_2)_2)_2]$				$[Zn(N(SCNEt_2)_2)_2]$				$[Zn(SON(CN^iPr_2)_2)_2]$			
d	h	k	l	I	300	350	400	450	300	350	400	450	300	350	400	450
3.0900	1	1	1	100	33	0	0	0	0	0	0	0	100	100	0	0
2.7000	2	0	0	40	100	100	0	0	0	0	0	0	0	0	0	0
1.9100	2	2	0	100	0	0	0	0	0	0	0	0	0	0	0	0
1.6300	3	1	1	80	0	2	0	0	0	0	0	0	0	0	0	0
1.5600	2	2	2	40	0	0	0	0	0	0	0	0	0	0	0	0
1.3500	4	0	0	60	0	0	0	0	0	0	0	0	0	0	0	0
ICDD-008-7254 Hexagonal					$[Zn(N(SCNMe_2)_2)_2]$				$[Zn(N(SCNEt_2)_2)_2]$				$[Zn(SON(CN^iPr_2)_2)_2]$			
d	h	k	l	I												
3.3105	1	0	0	100	0	0	3	25	24	30	10	31	0	0	0	6
3.1303	0	0	2	61	0	0	100	100	100	100	100	100	0	0	100	100
2.9265	1	0	1	94	0	0	0	6	0	0	0	12	0	0	0	4
2.2745	1	0	2	33	0	0	0	0	0	0	0	0	0	0	0	0
1.9112	1	1	0	62	0	0	6	12	5	7	5	11	0	0	4	3
1.7654	1	0	3	59	0	0	0	0	0	0	0	0	0	0	0	2
1.6552	2	0	0	8	0	0	0	0	0	0	0	0	0	0	0	0
1.6313	1	1	2	36	0	0	0	0	3	5	2	3	0	0	4	3
1.6002	2	0	1	11	0	0	0	0	0	0	0	0	0	0	0	0
1.5651	0	0	4	1	0	0	1	6	0	0	0	0	0	0	0	0
1.4632	2	0	2	6	0	0	0	0	0	0	0	0	0	0	0	0
1.4150	1	0	4	1	0	0	0	0	0	0	0	0	0	0	0	0

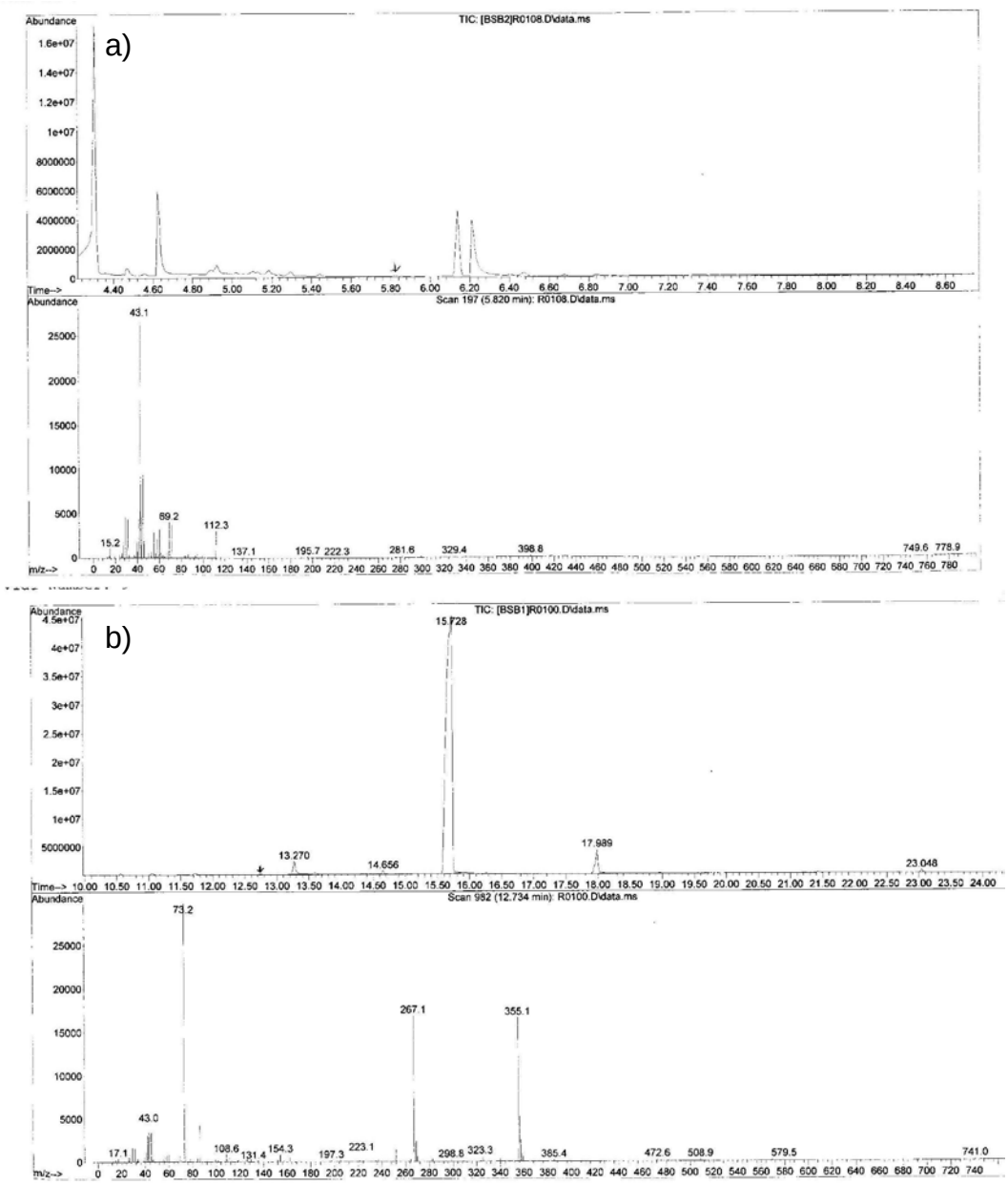

Fig. A1 GC-MS spectra of a) complex $[Co(N(SCNMe_2)_2)_3]$ b) complex $[Co(N(SCNEt_2)_2)_3]$ showing evidences for m/z value of 43 and 73

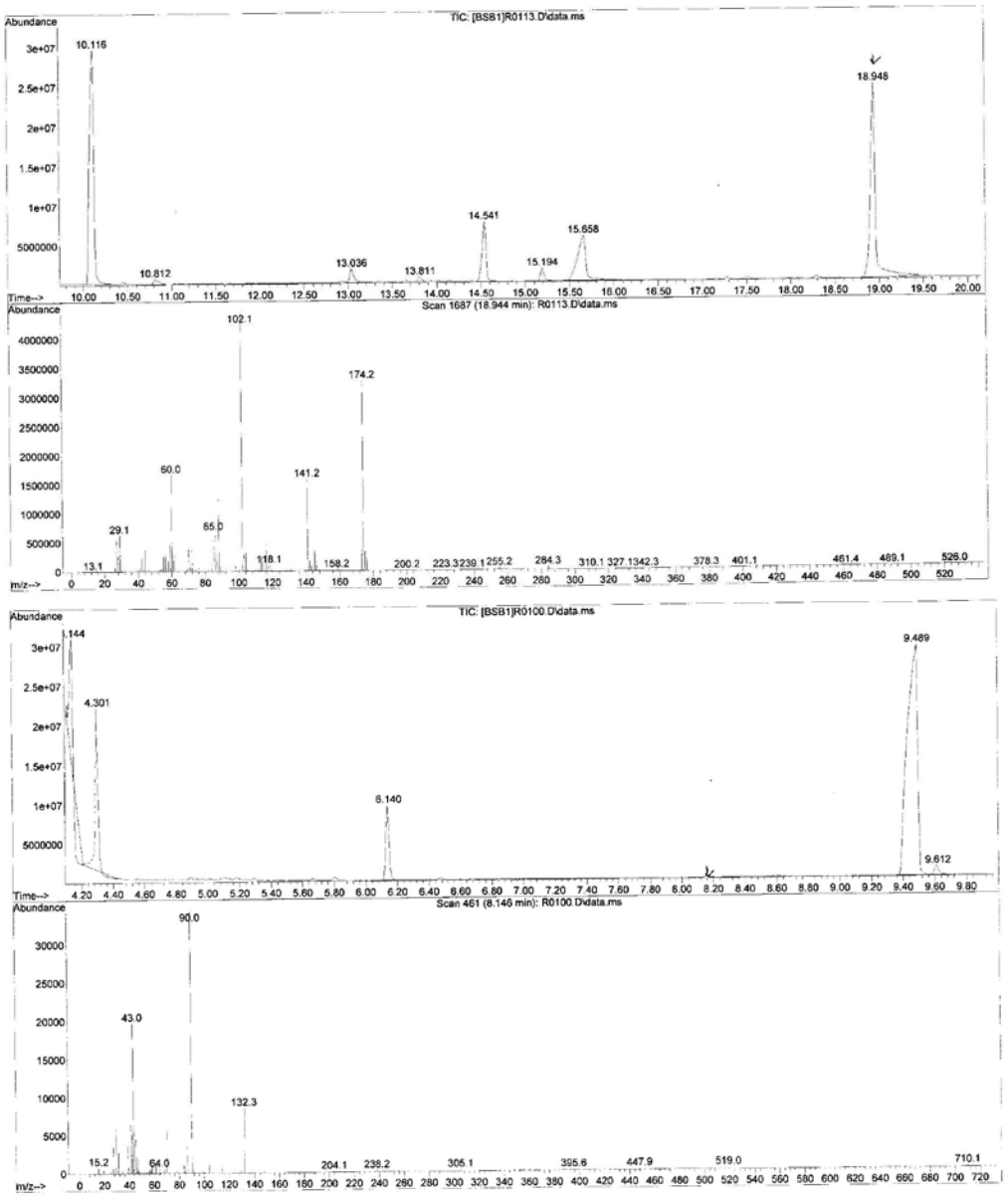

Fig. A2 GC-MS spectra of complex $[Co(N(SCNEt_2)_2)_3]$ showing evidences for m/z value of 174, 102 and 90

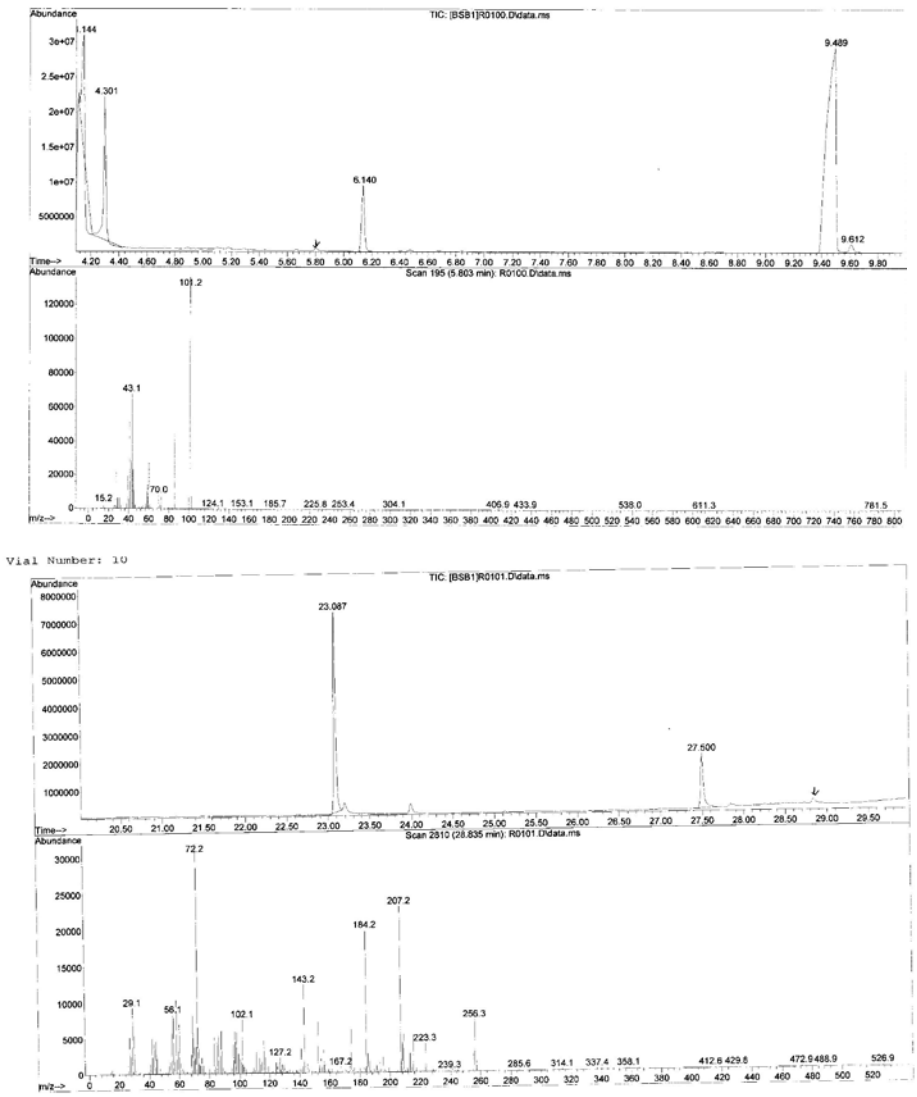

Fig. A3 GC-MS spectra of complex $[Co(SON(CN^{i}Pr_2)_2)_2]$ showing evidences for m/z value of 101, 143 and 72

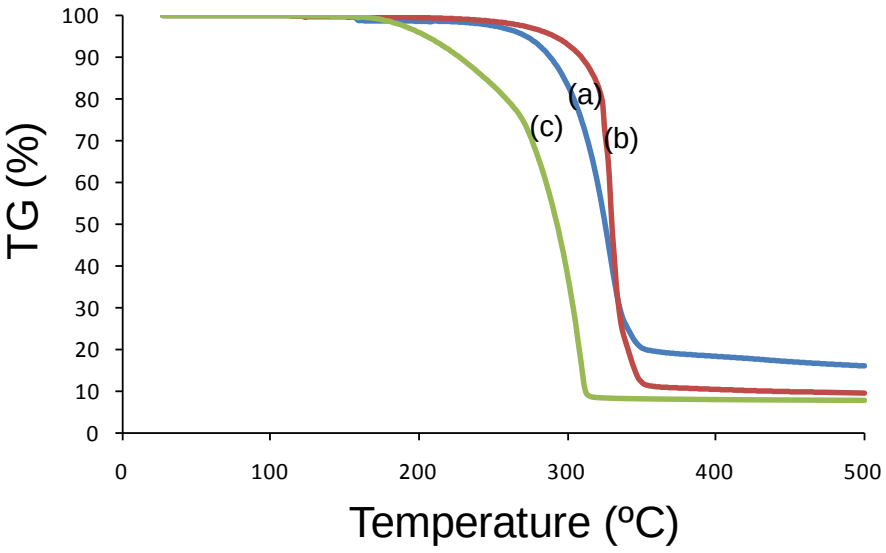

Fig. A4TGA of zinc complexes; a) $[Zn(N(SCNMe_2)_2)_2]$ b) $[Zn(N(SCNEt_2)_2)_2]$ and c) $[Zn(SON(CN^iPr_2)_2)_2]$

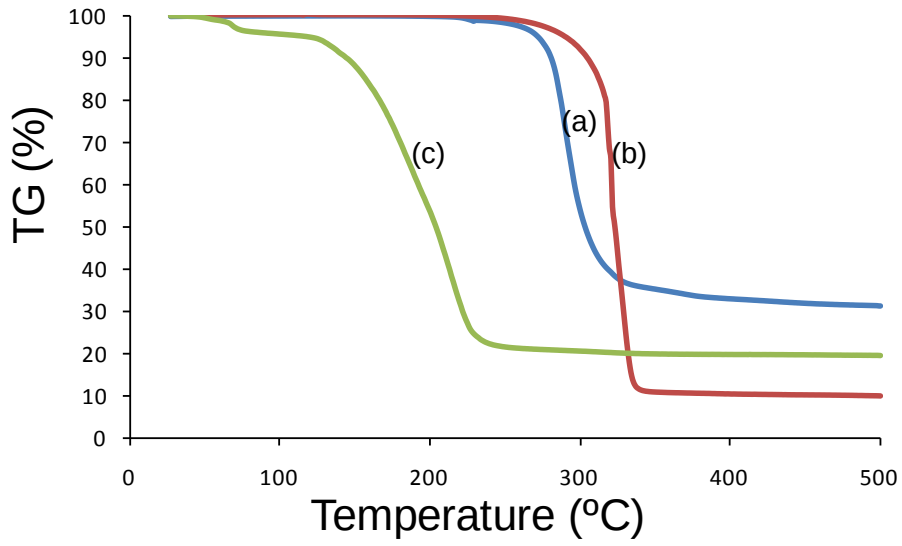

Fig. A5 TGA of cadmium complexes; a) $[Cd(N(SCNMe_2)_2)_2]$ b) $[Cd(N(SCNEt_2)_2)_2]$ and c) $[Cd(SON(CN^iPr_2)_2)_2]$

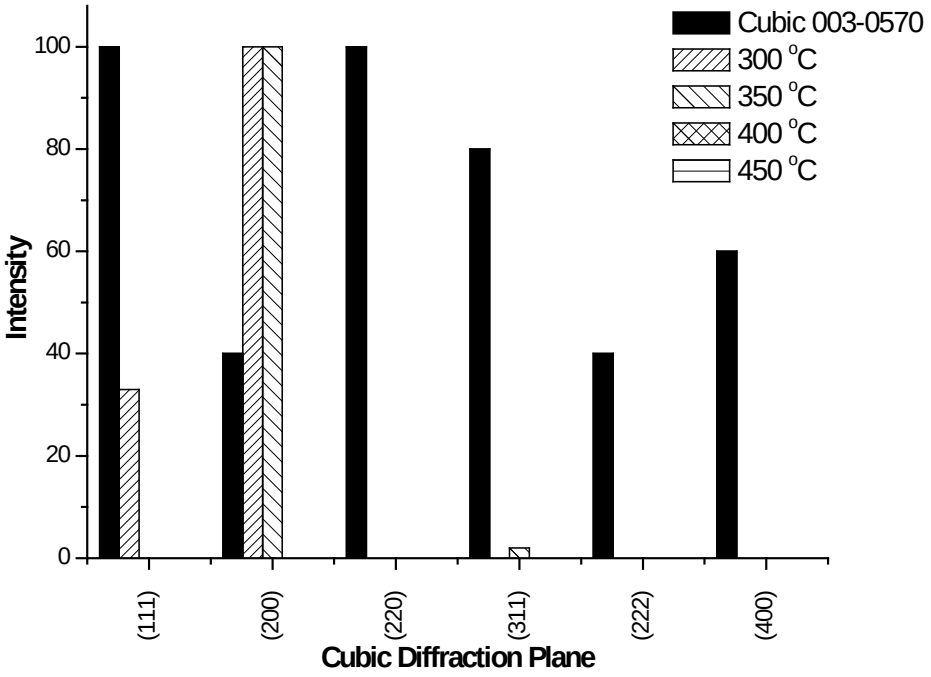

Fig. A6 PXRD pattern of cubic ZnS films deposited from $[Zn(N(SCNMe_2)_2)_2]$

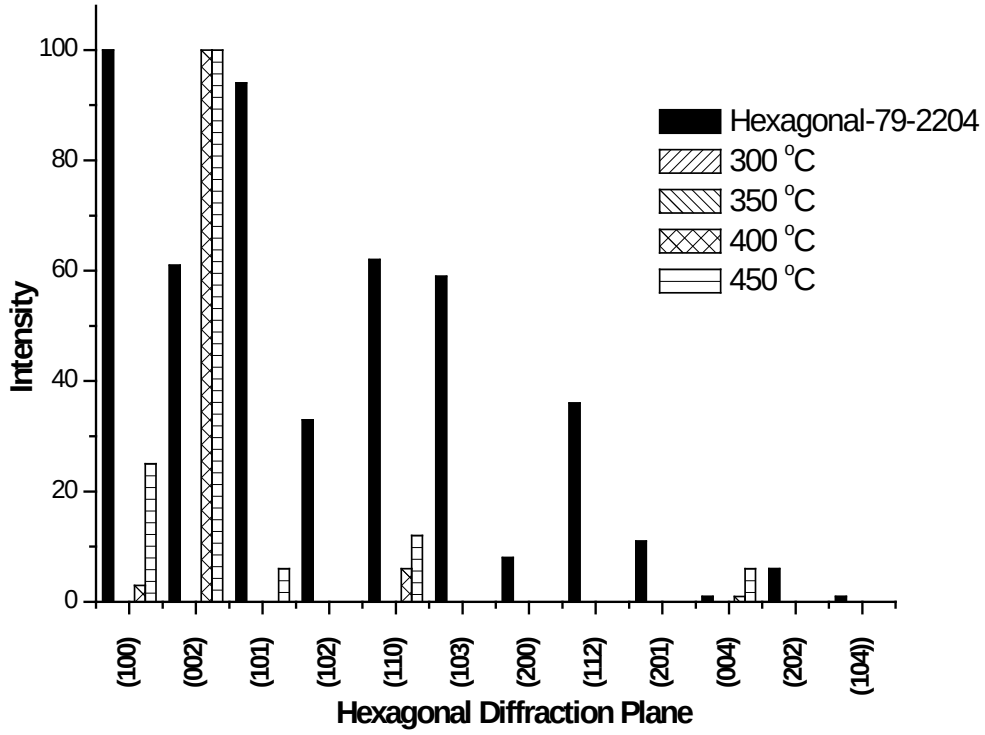

Fig. A7 PXRD pattern of hexagonal ZnS films deposited from $[Zn(N(SCNMe_2)_2)_2]$

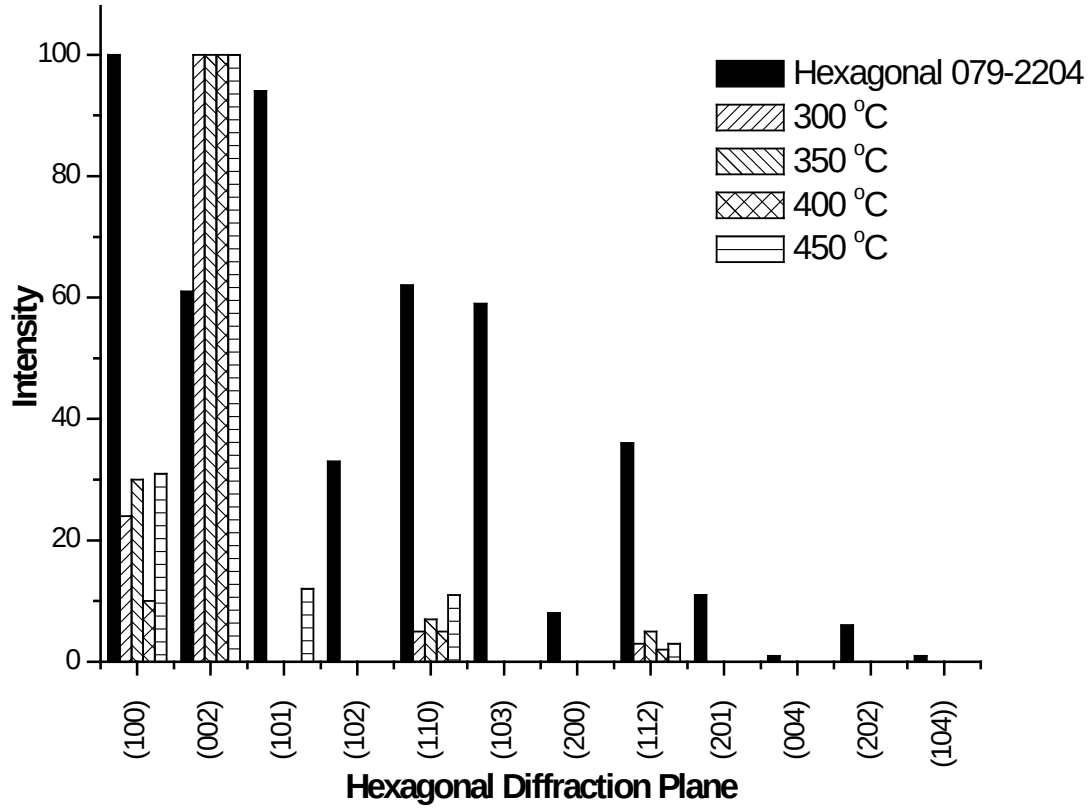

Fig. A8 PXRD pattern of hexagonal ZnS films deposited from $[Zn(N(SCNEt_2)_2)_2]$

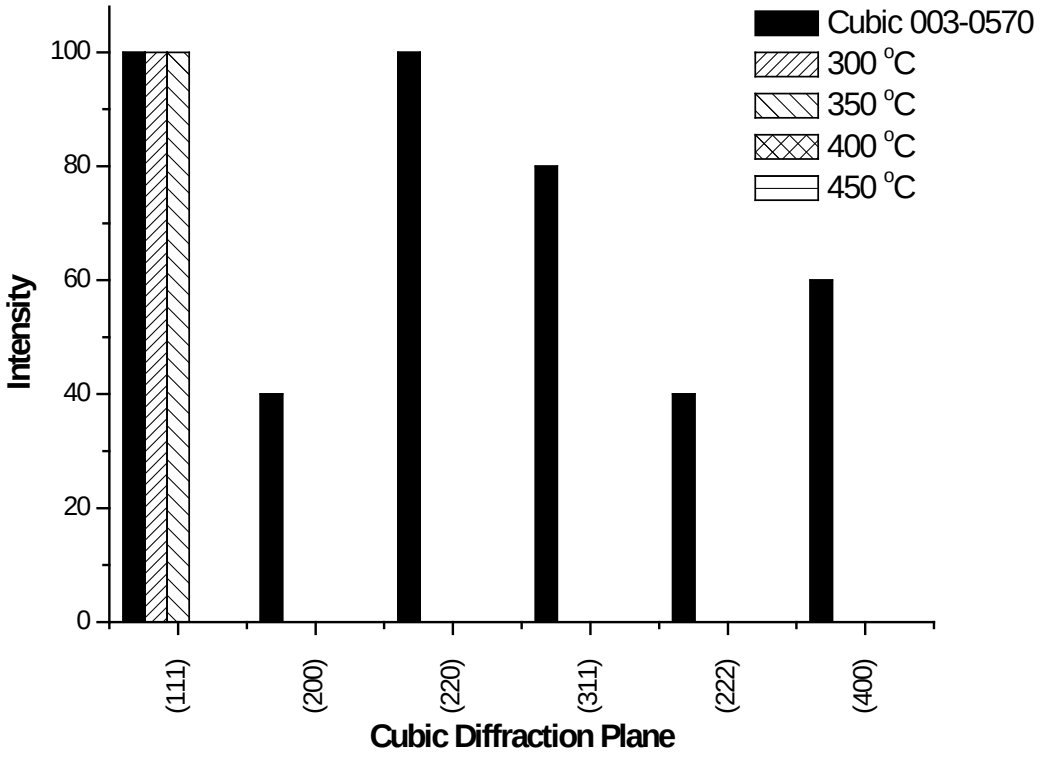

Fig. A9 PXRD pattern of cubic ZnS films deposited from $[Zn(SON(CN^iPr_2)_2)_2]$

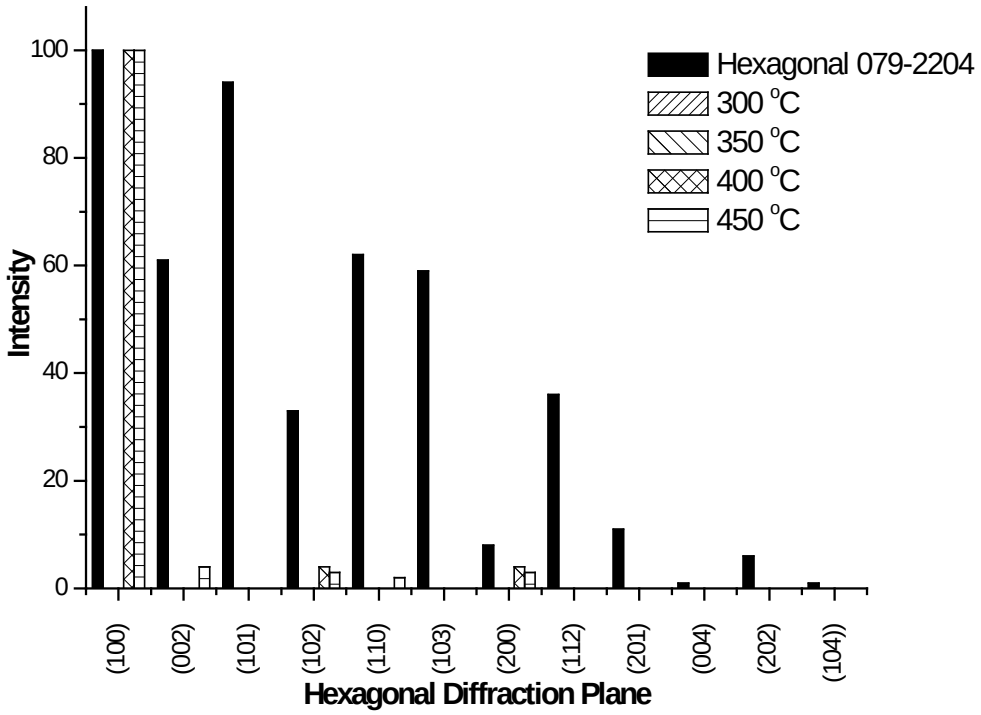

Fig. A10 PXRD pattern of hexagonal ZnS films deposited from $[Zn(SON(CN^{i}Pr_2)_2)_2]$

Table. A10 PXRD data of ZnS films deposited from [$Cd(N(SCNMe_2)_2)_2$], [$Cd(N(SCNEt_2)_2)_2$] and [$Cd(SON(CN^iPr_2)_2)_2$]

ICDD-01-075-1545					[$Cd(N(SCNMe_2)_2)_2$]				[$Cd(N(SCNEt_2)_2)_2$]				[$Cd(SON(CN^iPr_2)_2)_2$]			
d	h	k	l	I	350	400	450	500	350	400	450	500	350	400	450	500
3.5940	1	0	0	62	40	63	2	10	75	39	10	3	25	10	1	1
3.3685	0	0	2	44	100	32	100	100	100	100	100	100	100	100	100	100
3.1710	1	0	1	100	60	100	4	17	75	33	8	6	0	50	2	1
2.4577	1	0	2	25	0	26	5	6	0	5	3	4	0	10	1	0
2.0750	1	1	0	42	40	42	1	6	25	17	3	2	0	0	8	0
1.9044	1	0	3	41	30	32	18	20	25	22	10	16	0	30	0	5
1.7970	2	0	0	6	0	5	0	0	0	0	0	0	0	10	0	0
1.7667	1	1	2	30	20	26	2	6	25	5	1	2	0	0	0	0
1.7363	2	0	1	13	0	10	0	0	0	0	0	0	0	0	0	0
1.6842	0	0	4	2	0	0	2	3	0	0	0	2	0	0	0	0
1.5855	2	0	2	5	0	0	0	0	0	0	0	0	0	0	0	0
1.5250	1	0	4	2	0	0	0	0	0	0	0	0	0	0	0	0
1.4030	2	0	3	12	0	5	1	30	0	0	0	1	0	0	0	0
1.3584	2	1	0	4	0	5	0	0	0	0	0	0	0	0	0	0
1.3316	2	1	1	9	0	5	0	0	0	0	0	0	0	0	0	0

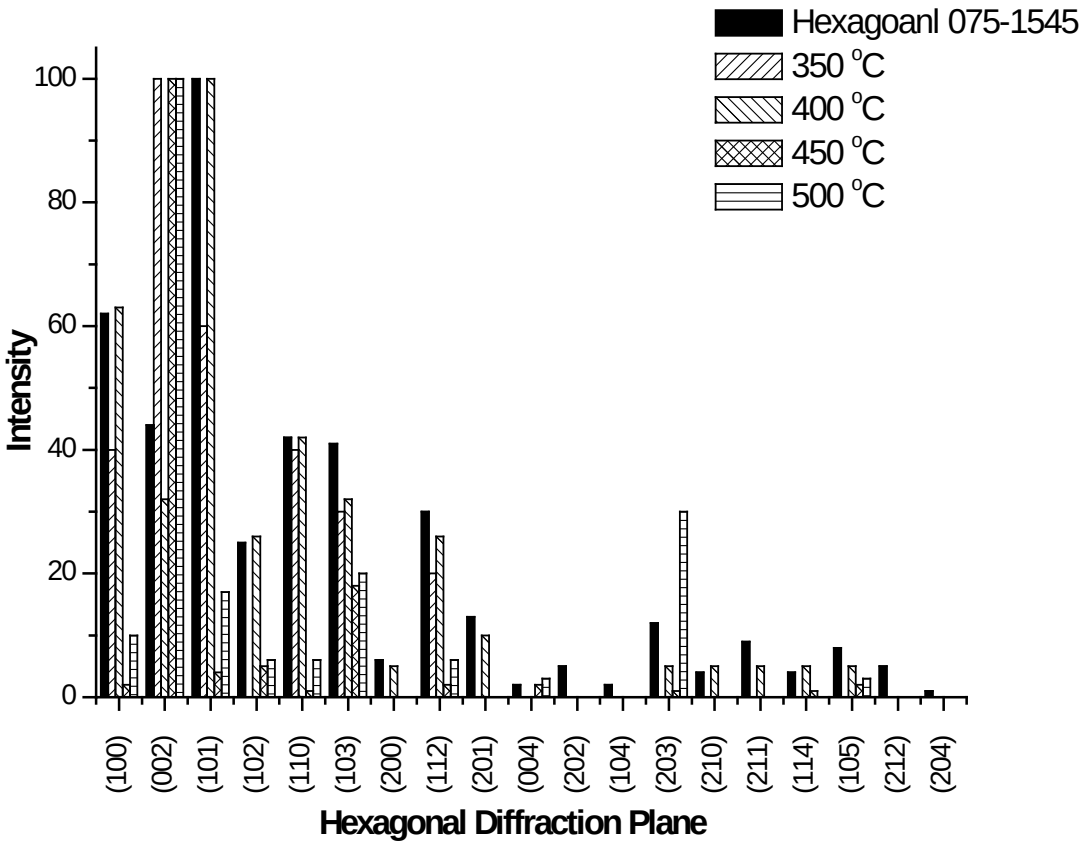

Fig. A11 PXRD pattern of hexagonal CdS films deposited from $[Cd(N(SCNMe_2)_2)_2]$

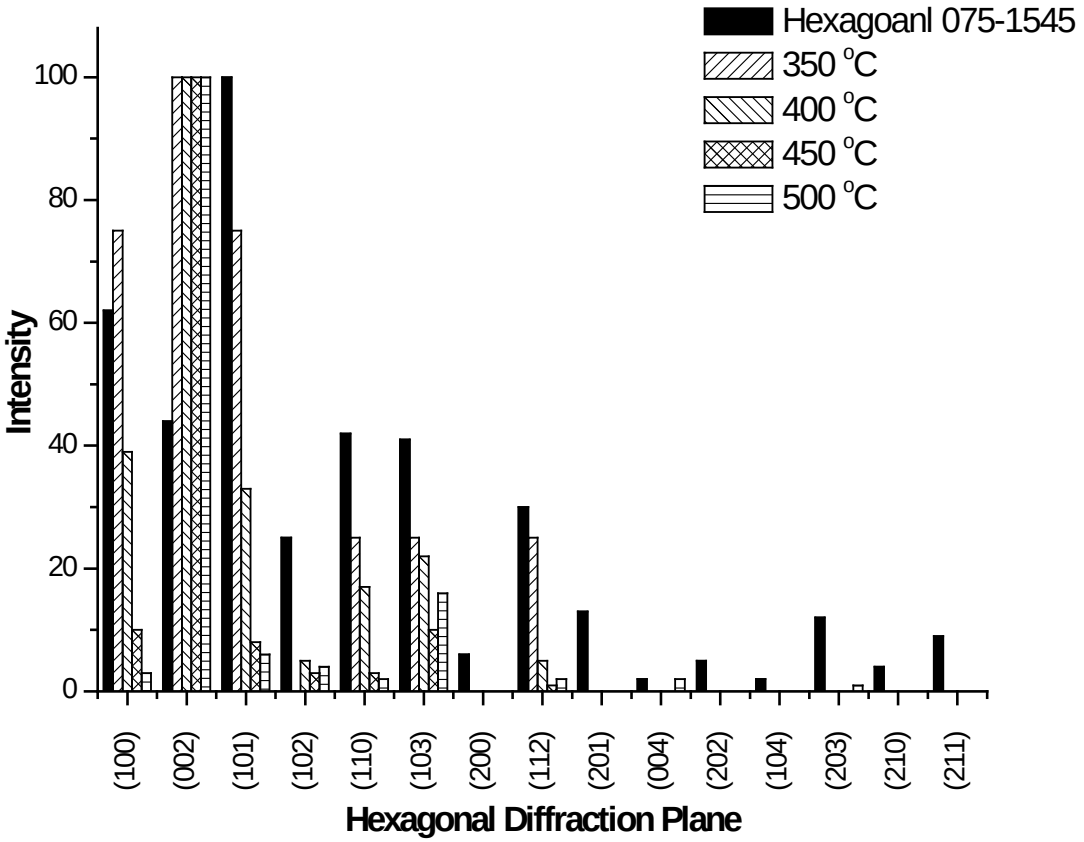

Fig. A12 PXRD pattern of hexagonal CdS films deposited from $[Cd(N(SCNEt_2)_2)_2]$

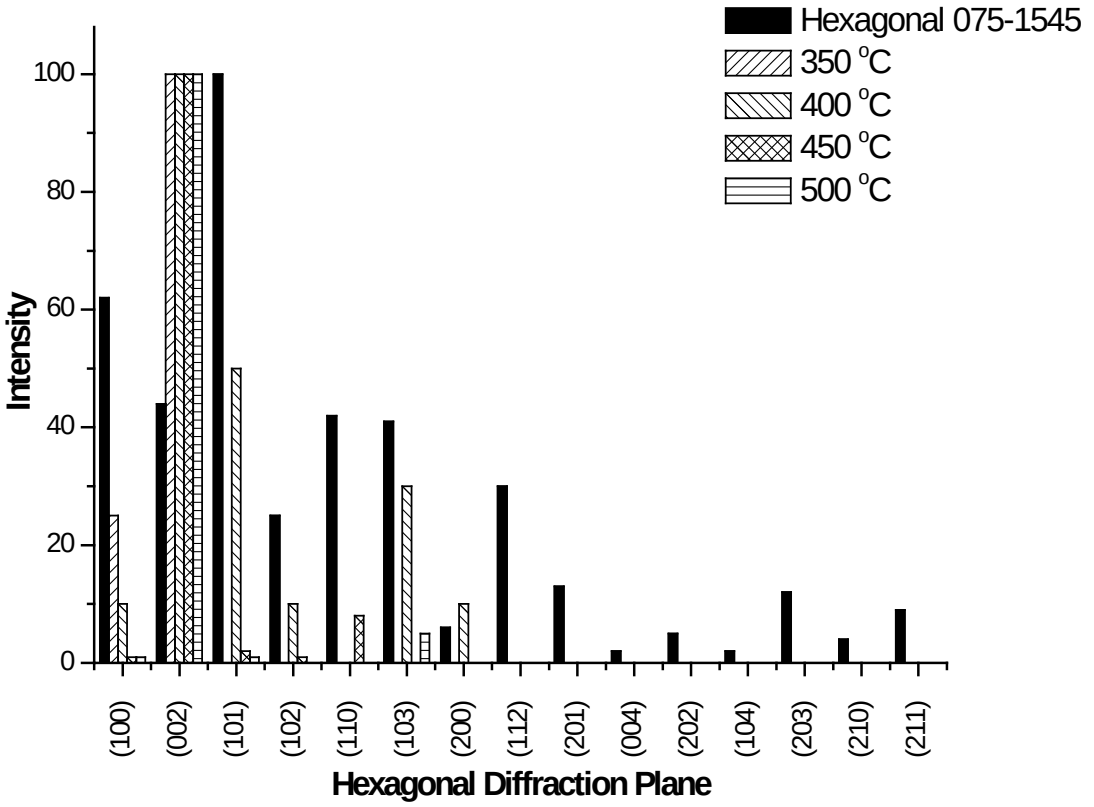

Fig. A13 PXRD pattern of hexagonal CdS films deposited from $[Cd(SON(CN^{i}Pr_2)_2)_2]$

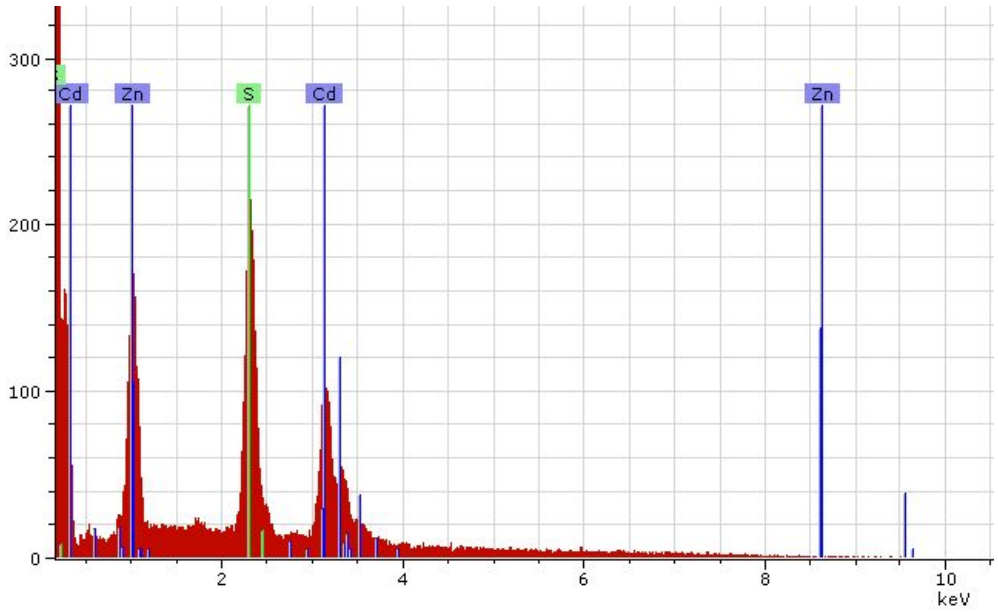

Fig. A14. EDX graph of $Zn_xCd_{1-x}S$ films prepared using $[Zn(SON(CN^{i}Pr_2)_2)_2]$ and $[Cd(SON(CN^{i}Pr_2)_2)_2]$ on glass substrate at 400 °C